

# ROCK WETTABILITY EVALUATION BY IMMERSION CALORIMETRY

D. Korobkov<sup>1</sup>, V. Pletneva<sup>1</sup>, E. Dyshlyuk<sup>2</sup>  
Schlumberger, <sup>1</sup>Moscow Research Center and <sup>2</sup>Dahran Carbonate Research

*This paper was prepared for presentation at the International Symposium of the Society of Core Analysts held in Snowmass, Colorado, USA, 21-26 August 2016*

## ABSTRACT

In the present paper, we are discussing an approach for wettability evaluation by the measurement of enthalpy variation related to the immersion process. From calorimetry it is possible to get the variation of state functions like internal energy (at constant volume) or enthalpy (constant pressure experiments) related to the wetting process. They cannot be used directly to predict wetting properties while Gibbs free energy variations can be used for that. In the immersion process, the variation of the Gibbs energy is equal to the variation of the surface energies of the system.

In the calorimetry experiments, a core sample is immersed in a liquid or a liquid vapour and the associated small heat effect (immersion enthalpy) is measured with a calorimeter. Measurements of Gibbs free energy variation at immersion of a surface (i.e. a porous media like a rock) into water and oil phases allows one to determine wettability. Feasibility study of such approach has already been done. Comparison of specific surface area measured by the proposed calorimetry approach and well known Brunauer-Emmett-Taylor (BET) method was used for verification of the approach and published in our previous SCA papers [1]. The current paper is devoted to implementation and testing of the proposed technique for wettability evaluation. Performed test experiments with immersion of pure substances demonstrated encouraging results.

## INTRODUCTION

Wettability is the major factor controlling the flow and distribution of fluids at different scales, from a single pore to oil reservoir. Wettability is determined by the physicochemical interactions of reservoir fluids with each other and with the heterogeneous surface of the formation. Due to the complexity of investigation of surface interactions no universal method for wettability determination exists up to date, which drives continuous research on this theme.

The wettability of strongly water-wet or strongly oil-wet reservoirs may in some cases be inferred from log analysis, while core analysis methods are implemented for a more accurate wettability characterization. Standard core analysis methods, such as US Bureau of Mines (USBM) and Amott-Harvey methods or a combination of them are considered as industry standards for wettability estimation in core analysis. Both of the methods simulate reservoir processes during oil recovery and are based on the measurements of

the displacement efficiency of oil by water and water by oil during spontaneous imbibition and/or forced fluid displacements in the centrifuge. As an outcome of these tests as a rule, just one number is obtained: between -1 and 1 for the Amott test and between  $-\infty$  and  $+\infty$  for the USBM test. These methods give only qualitative characteristic of wettability and have some limitation on permeability (more than 10 mD for the Amott test) and shape of the sample for analysis (cylinder made with consolidated rock).

We propose an approach for qualitative and quantitative wettability evaluation based on immersion calorimetry [1-5]. Immersion occurs whenever a solid surface is exposed to liquid or gas [6]. In the immersion calorimetry experiments, a core sample is immersed in a fluid and the associated small heat effect (immersion enthalpy) is measured with a calorimeter. The heat effect is related to the alteration of the surface energy of the rock surface during the immersion process. Depending on the choice of initial conditions of the rock surface, the associated heat effect is related either to interaction of an adsorbate molecule with the surface (i.e. wettability of the surface) or only to size of the surface, i.e. specific surface area (SSA) of the sample. As a result, two important petrophysical parameters can be measured by an accurate thermodynamic technique with calorimetry.

The total heat that evolves during an immersion experiment also known as the enthalpy of immersion  $\Delta H$  is related to the variation of Gibbs free energy  $\Delta G$  of the system by the following expression:  $\Delta H = A(\Delta G - \frac{T\partial\Delta G}{\partial T})$ , where  $A$  is the sample surface area and  $T$  is temperature. The variation of the Gibbs energy of the system is in fact equal to the variation of the surface energy of the system. If the solid is immersed from the vacuum conditions:  $\Delta G = \gamma^S - \gamma^{SL}$ , where  $\gamma^S$  is the free energy at the solid-vacuum interface (i.e. surface tension) and  $\gamma^{SL}$  is the solid-liquid interface surface tension.

It is well known that wetting deals with three materials: solid, liquid and gas or a second liquid. When we are interested in the interaction between two liquids near a surface, two independent immersion experiments should be performed with two liquids (brine and oil for example) at the same pressure and temperature. The initial state of the surface should also be the same for both experiments. Contact angle between two liquids  $L1$  and  $L2$  on a solid surface can be obtained from Young's equation [2]

$$\cos\theta = \frac{k^{L1}\Delta H_{imm}^{L1} - k^{L2}\Delta H_{imm}^{L2}}{A\gamma^{L1L2}},$$

where  $\gamma^{L1L2}$  is the liquid 1 to liquid 2 interface surface tension and

$$k = [\gamma^S - \gamma^{SL}] / [(\gamma^S - \gamma^{SL}) - \frac{T\partial(\gamma^S - \gamma^{SL})}{\partial T}] \approx \gamma^{LV} / (\gamma^{LV} - \frac{T\partial\gamma^{LV}}{\partial T}).$$

Coefficient  $k$  for each liquids can be obtained from the measurements of the liquid-vapour surface tensions  $\gamma^{LV}$  of the liquid at different temperatures, which are easily obtained from literature or measured with commercially available equipment. The surface area of the sample should be determined separately either by some other method, such as

e.g. BET method [7], or again, with the use of the differential scanning calorimetry (DSC) by the modified Harkins-Jura method [1, 8].

## EXPERIMENT DESCRIPTION

Immersion calorimetry can be performed on a wide variety of core sample types: from high permeability to low and ultra-low permeability rock, core cuttings and crushed core and/or powders.

The solids used in this study were selected to have expected wettability ranging from water-wet to oil-wet. Solids used were powders: a variety of borosilicate glass (CPG) samples of varying size (pore  $\text{\O}$ : 50 – 300 nm), carbon powder (99% purity) and calcium carbonate (99% purity). The studied samples were dried before experiments, under vacuum at  $90^{\circ}\text{C}$  during 24 hours. The fluids used were HPLC grade ( $\geq 99.9\%$ ): deionized water and cyclohexane.

Micro calorimeter [1-3] was used for measurement of the heat effect due to immersion of a rock internal surface into a liquid. For our experiments we used a specially designed cell [1] that provides: 1) a means for connecting the sample to the vacuum for pre-treating of the sample; 2) connection to a vapor source system to fill the sample with an sorptive fluid ; 3) that both the immersion liquid and the sample are in the same calorimetric cell during the experiment in order to exclude mass-heat transfer during immersion of the sample; 4) jointing of both volumes with the sample and the liquid with minimal and reproducible side heat effect (wetting of the cell itself, opening the valve, pressure drop etc.) for being systematically accounted. The cell was designed for cylindrical sample of  $\sim 1 \text{ cm}^3$  volume.

The proposed workflow includes two independent immersion experiments with the two different liquids. Prior to the experiments, the studied sample should be dried and vacuumed to remove any liquid and adsorbate from pores. After finalization of the immersion experiment with the first fluid, and prior to experiment with the second fluid, the sample should be dried and vacuumed again.

An experiment is started from “zero” pressure condition. The preliminary evacuated cell containing the sample is filled with the wetting liquid to immerse the sample surface. Immersion heat effect due to wetting of the cell itself (dark curve in Figure 1) should be removed from the measured heat effect due to wetting of the sample into the cell (red curve in Figure 1) for deriving of heat effect due to wetting of the studied sample. The heat effect due to sample immersion is immersion energy and is used for surface wettability evaluation. The duration of the immersion experiments depends on porous media permeability. From our practice, it takes several hours, typically 1 to 2 hours for immersion in cyclohexane and up to 4 hours for water immersion.

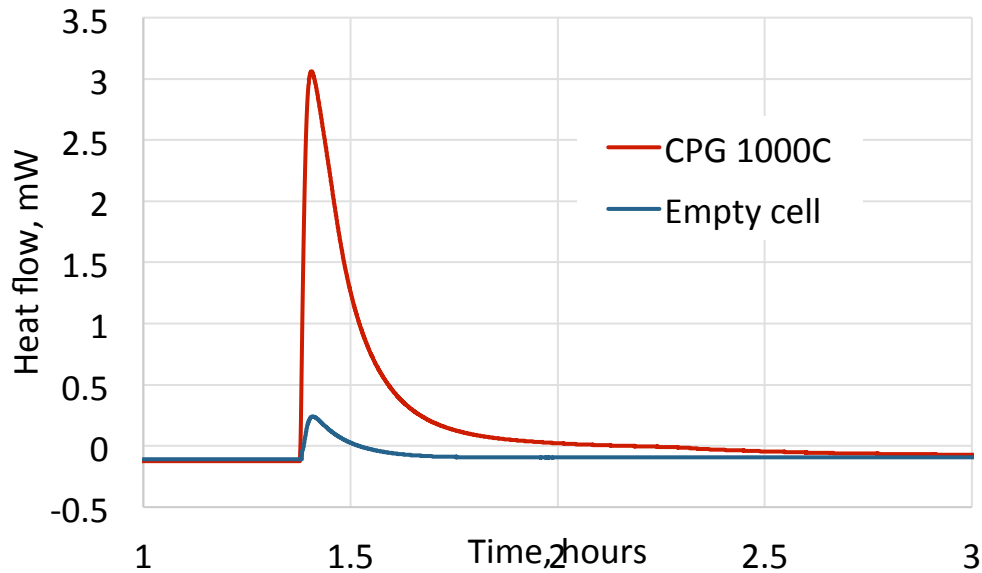


Figure 1. Typical immersion DSC heat flow curve measured with calorimeter on blank cell (dark curve) and cell with tested sample (red curve).

After completing the experiment with the first fluid (water in our case) prior to immersion into the second fluid the sample should be dried again. Drying during 24 hours at 105°C are enough if powders or core cuttings (without significant amount of clays) are used. To speed up the process, we split the sample into two portions for experiments with both fluids. The experiment with the second fluid should be performed at the same temperature and pressure.

## RESULTS

Prior to wettability experiments, we tested calorimetry method for SSA measurement [1] with cyclohexane. The obtained SSA values were in rather good agreement with BET measurements (Table 1) especially for hydrophobic carbon powder and calcium carbonate that is intermediate wet. It means that the surface of studied sample was covered by at least a monolayer of the liquid during first step of adsorption-immersion experiment. Thus, immersion calorimetry can be used for SSA of both hydrophilic and hydrophobic samples. There is no need to cool the sample in liquid nitrogen that can destroy the sample [9]. This feature is one of the main advantages of calorimetry approach over the BET gas adsorption method.

After successful determination of SSA, we tested our workflow on the same pure and homogeneous powders of calcite, carbon, and controlled pore glasses (CPG) of different pore sizes. Test results are presented in the table below.

**Table 1.** Specific surface area and wettability of powders.

Sample	Surface Area by Nitrogen Adsorption, m <sup>2</sup> /g	Surface Area by Water Adsorption, m <sup>2</sup> /g		Surface Area by Cyclohexane Adsorption, m <sup>2</sup> /g	Wettability $\cos\theta$ ( $\theta$ )
	BET method	BET method	by immersion calorimetry	by immersion calorimetry	
CPG 500C (pore Ø: 50 nm), borosilicate glass	49.2 - 54.3	45.5	43.8	51.1 - 53.7	1.80 (0°) <i>Absolutely water-wet</i>
CPG 1000C (pore Ø: 100 nm), borosilicate glass	26.6 - 27.6		23.2		1.68 (0°) <i>Absolutely water-wet</i>
CPG 3000C (pore Ø: 300 nm), borosilicate glass	8.4 - 9.5		9.3	10.1	
Calcium Carbonate	3.8	1.59	1.2; 0.96	3.1	0.46 (62°)
Carbon	1.75 – 2.0	1.47	1.0	2.3	0.31 (71°)

As it can be seen from Table 1, derived cosine of the contact angle ( $\theta$ ) calculated by Young's equation for pure hydrophilic glass powder is greater than 1. In other words:  $\gamma^{SL1} > \gamma^{SL2} + \gamma^{L1L2}$ , where L1 is cyclohexane and L2 – water. It corresponds to complete wetting described by Anthanase Dupré and Paul Dupré [10, 11] with introducing the spreading parameter  $S = \gamma^{SL1} - (\gamma^{SL2} + \gamma^{L1L2})$ . When  $S > 0$ , the liquid wets the surface completely without forming a contact angle (complete wetting). When  $S < 0$ , partial wetting occurs and Young–Dupré equation has physical solutions for  $\theta$ .

Derived contact angle of carbon is in range of intermediate wettability while we expected to obtain these values close to 95° (oil-wet range) [12]. The same tendency is observed for calcite. It can be explained by such phenomena as roughness [13] as well as possible presence of a precursor film [13]. By the way, the immersion calorimetry method provides at least qualitative information on wettability that can be estimated for any shape of studied sample (including core cutting) and types of the rock (including low and ultra-low permeable rock).

## CONCLUSION

Immersion calorimetry allows measurement of wettability of a core sample by two identical experiments with independent immersion into the two individual fluids. The main advantages of the proposed technique are possibility of evaluating wettability state of both core plugs and cuttings (including powders) with wide range of permeability: from conventional reservoir rock to micro Darcy tight rocks and nano-Darcy shales.

The technique was tested on artificial powders with known properties. Acceptable qualitative correspondence between the measured and reference contact angles was obtained for studied samples. Close values of contact angles measured on two controlled

pore glass samples with significantly different pores and SSA but the same surface properties prove the capability of the procedure.

The calorimetry technique should also be tested on a set of natural rock samples (core plugs) with wettability measured using existent commercial methods.

## REFERENCES

1. E. Dyshlyuk, D. Korobkov, V. Pletneva, "Rock Surface Characterization by Immersion Calorimetry: Wettability and Specific Surface Area," in *Society of Core Analysts*, SCA2015-059, St. John's Newfoundland and Labrador, Canada, 2015
2. E. Dyshlyuk, "Application of Differential Scanning Calorimetry to Core Analysis," in *Society of Core Analysts*, SCA2013-055, Napa Valley, California, USA, 2013.
3. E. Dyshlyuk, N. Bogdanovich, D. Korobkov and V. Pletneva, "The measurements of core sample surface wettability heterogeneity by adsorption calorimetry," in *Society of Core Analysts*, SCA2014-088, Avignon, France, 2014.
4. E. Dyshlyuk, "Method for Determining Wettability of a Surface". Russia Patent Claim # 2014109083, February 2015.
5. E. Dyshlyuk, "Method for Reservoir Wettability Properties Determination". Russia Patent 2497098, 2013.
6. Rouquerol, F., Rouquerol, J. and Sing, K. Adsorption by Powders and Porous Solids. s.l. : Academic Press, 2009.
7. S. Brunauer, P. Emmett and E. Teller, "Adsorption of Gases in Multimolecular Layers," *J. Am. Chem. Soc.*, vol. 60, p. 309, 1938.
8. S. Partyka, F. Rouquerol and J. Rouquerol, "Calorimetric determination of surface areas Possibilities of modified Harkins and Jura procedure," *Journal of Colloid and Interface Science*, vol. 68, pp. 21-32, January 1979.
9. D. Korobkov, A. Nadeev, A. Kazak, N. Bogdanovich, I. Dimitriev, S. Rudakovskaya, S. Lebedev, A. Denisenko, "Freezing of Poorly Consolidated Rock: Method of Stabilization or Alteration?" in *Society of Core Analysts*, SCA2013-093, Napa Valley, California, USA, 2013.
10. Schrader, Malcolm E. (2002-05-01). "Young-Dupre Revisited". *Langmuir* 11 (9): 3585–3589.
11. Athanase M. Dupré, Paul Dupré (1869-01-01). *Théorie mécanique de la chaleur* (in French). Gauthier-Villars.
12. W.A. Zisman. "Relation of the Equilibrium Contact Angle to Liquid and Solid Constitution." *Advances in Chemistry*; American Chemical Society: Washington, DC, 1964. 1-51.
13. Bormashenko, E. (2008). "Why does the Cassie–Baxter equation apply?" *Colloids and Surface A: Physicochemical and Engineering Aspects* 324: 47–50.

# **Analytical Gas-Oil Relative Permeability Interpretation Method for Immiscible Flooding Experiments under Constant Differential Pressure Conditions**

Hashem Nekouie, Jie Cao, L.A. James, T.E. Johansen  
Memorial University of Newfoundland

*This paper was prepared for presentation at the International Symposium of the Society of Core Analysts held in Snow Mass, Colorado, USA, 21-26 August 2016*

## **ABSTRACT**

Oil-gas relative permeability is a key parameter in evaluating gas-related EOR/IOR processes. It is normally determined from steady-state, unsteady-state gas flooding or centrifuge experiments. This paper presents an examination and further development of an analytical interpretation method for determining relative permeability from unsteady state core flooding experiments under constant differential pressure conditions. It was applied to an oil-water unsteady state core flooding experiment and this work is to further examine the method for the interpretation of relative permeability from unsteady state gas-liquid displacement. Several gas-liquid displacement experiments under constant differential pressure boundary conditions are conducted. The experimental data are interpreted using the JBN method, the newly presented method and the numerical method of history matching using software CYDAR. The performance of the new method on gas-oil displacement scenario is evaluated and compared with other methods. Since the capillary pressure is ignored in the analytical method, this technique is only valid for interpretation of viscous dominated flow; the effects of the capillary pressure still have to be corrected.

## **INTRODUCTION**

Porosity and permeability are the main properties of small and large scale porous media. Porosity of large-scale porous media has been known to have long range correlation (Dashtian et al. 2011). This makes the study of porosity straightforward comparing with the complexity of investigation of permeability in heterogeneous formations with multi-phase fluid flow. Two and three phase relative permeabilities are important parameters capturing the relative simultaneous flow of gas, oil, and water in porous media. Relative permeability data are used in commercial simulation packages, where the phase permeability is a function of liquid (water or oil) saturation. While inaccurate relative permeability data leads to a significant error in the simulation of different EOR scenarios, a good estimation of phase permeabilities helps to obtain reliable reservoir simulation models. The fluid saturation can be estimated based on both experimental data and well log data (Dashtian et al. 2015).

Generally, relative permeability data are calculated from steady state and unsteady state core flooding experiments. Although steady state experiments are the most reliable methods, they are expensive and time consuming. Unsteady state experiments are

cheaper and less time consuming. However, they are not as accurate as steady state methods and data processing is more complicated. Interpretation of unsteady state laboratory data and converting them to useable relative permeability curves is challenging. Normally, the fractional flow of different phases is calculated and then relative permeability curves are determined using an interpretation method. Although unsteady state experiments are time efficient, the accuracy depends on the interpretation method. Welge (1952) presented a method to calculate the ratio of relative permeabilities from experimental results when capillary pressure is negligible. The most popular interpretation method was developed by Johnson et al. (1959) known as the JBN method. The JBN method requires the inlet and the outlet pressure and the fluids' production data, and capillary end effects are neglected. Jones and Roszelle (1978) later presented a graphical construction method, based on the JBN method, facilitating the calculation of relative permeabilities from experimental results. Tao and Watson (1984a, 1984b) provided an error analysis for the JBN method and modified their technique to improve the accuracy of the results. Archer and Wong (1973) introduced the history matching and numerical simulation approach to calculate relative permeabilities. They matched the oil recovery and relative injectivity curves to determine the relative permeability data from core flood experiments, ignoring capillary pressure. Batycky et al. (1981) later included the effect of capillary pressure in numerical simulations and calculated the relative permeabilities. Cable et al. (1999) later applied experimental techniques to measure the relative permeabilities for gas condensate reservoirs in near wellbore regions.

In this paper, the new relative permeability interpretation method presented by Cao et al. (2014), based on the generalization of the Buckley-Leverett theory for constant pressure boundaries (Johansen and James, 2014) is presented for immiscible gas/liquid unsteady state relative permeabilities. This interpretation method applies analytical solution to fractional flow theory under constant pressure boundary, therefore reducing the need for numerical differentiation and associated errors. As an alternative to JBN method, this interpretation method was applied for water/oil displacements by Cao et al. (2015) and now is extended to immiscible gas flooding systems. In the following sections, the methodology is first explained. Then, it is demonstrated how this method is applied for gas/oil and gas/water core flooding displacements with constant pressure boundaries, when gravity forces are included. In this interpretation approach analytical techniques are employed to determine the saturation profile along the core. Afterwards, the laboratory data are also interpreted using JBN and history matching methods using software CYDAR. A comparison of three methods shows the accuracy of the presented technique.

## **METHODOLOGY**

Suppose we have immiscible two phases of gas and liquid flowing in the homogeneous and incompressible porous medium in one dimension. Assume that the liquid phase is incompressible and the gas phase has a constant compressibility inside the porous medium. Also, assume that the capillary pressure can be ignored. The fractional flow model in terms of the displacing phase (gas) can be formulated as

$$\phi \frac{\partial S_g}{\partial t} + u_T(t) \frac{\partial f}{\partial x} = 0, \quad (1)$$

where  $S_g$  is the gas saturation and  $f$  is the fractional flow function in terms of gas, defined as

$$f(S_g) = \frac{\lambda_g}{\lambda_T} - \frac{\lambda_T \lambda_g \Delta \rho}{u_T \lambda_T}; \quad \lambda = \frac{Kk_r}{\mu}; \quad \lambda_T = \lambda_g + \lambda_l. \quad (2)$$

Under constant differential pressure boundaries, the inlet and outlet pressures are kept constant while the total volumetric flux  $u_T$  is a function of time. During the displacement experiment, the breakthrough time is recorded. The breakthrough time ( $t_s$ ) of a series of saturation points ( $S$ ) are then measured based on mass balance and experimental data. The corresponding fractional function  $f(S)$  is determined based on produced volume of gas and liquid. Detailed calculation procedures are described in previous research by Cao et al. (2014). Analytical solutions to pressure and saturation distributions and derivative of fractional function can be found in Johansen and James (2014).

In this paper, two gas/liquid displacement experiments are performed and the results are interpreted using the newly proposed method, the JBN method, and the history matching method. The results from different methods are compared and the performance of the new method is discussed.

## EXPERIMENTAL DETAILS

Two phase gas/water and gas/oil core flooding experiments under constant differential pressure were conducted to examine the interpretation method proposed by Cao et al. (2014) for immiscible gas-oil and gas-water relative permeabilities. Carbon tan and Berea sandstone cores were used (see properties in Table 1).

Nitrogen (Praxair, purity > 99%) was used as the gas phase to ensure immiscibility. A synthetic brine with the salinity of 10,000 ppm, viscosity of 1.02 cP and density of 1005 kg/m<sup>3</sup>, and a dead crude oil with viscosity of 5.9 cP and density of 855 kg/m<sup>3</sup> were used. The experiments were conducted at low injection pressures. An accurate gas regulator was used to keep the pressure constant at the inlet where the pressure was supported by a high pressure gas tank. The outlet pressure was set to atmospheric pressure. The effluent was collected in a separator at the outlet. The bottom of the separator was connected to a graduated cylinder and a gas meter was connected to the top of the separator to measure the produced liquid and gas flow rates, respectively. Once the experiment began, the gas and the oil flow rates, the inlet and the outlet pressures with time were recorded, as well as the breakthrough time. In order to have accurate results, the data were recorded more often at early times. General information about the experiment and the core samples are provided in Table 1. The experimental schematic is shown in Figure 1.

## RESULTS

The interpreted results from the gas-oil and gas-water unsteady state relative permeability core flooding experiments are shown in Figures 2 and 3. The end points from each

method are the same since they are achieved in a steady state flow where no more displaced phase is produced.

The history matching method applies numerical simulation of displacement process to optimize the defined objective functions, which are the evenly weighted functions of liquid production, gas production and the differential pressure between inlet and outlet. However, the relative permeabilities obtained from history matching are in good agreement with the JBN results. The main reason is that the history matching method applies a Corey Model or a modified Corey Model fitted from JBN results and then matches the production data by modifying the coefficients in the Corey Model. This also indicates that a more flexible relative permeability model, like one using B-Splines, could improve the flexibility and accuracy in numerical matching.

The results are shown in Figures 2 and 3 for gas-oil and gas-water, respectively. Both cases show that the results from the three interpretation methods are consistent in trend; however, the liquid phase relative permeability from the new method are lower than that from the JBN method. The gas relative permeabilities from the three methods in both cases are very similar to each other. Furthermore, in both cases, the new method results lie on a smoother curve than the JBN method, with less oscillation in relative permeabilities. This is mainly because that the new method reduced the use of numerical differentiation by applying analytical solution of saturation and pressure profiles.

Figures 2 and 3 show that the oil and water phase relative permeabilities obtained from the new method are lower than those obtained from traditional the JBN and history matching approach. Therefore, these results will lead to a lower recovery factors in reservoir simulations. Thus, further research is required to examine the accuracy of the analytical methods. However, not a big difference is observed in the results obtained for the gas phase. The new method is examined as an alternative to JBN method for relative permeability interpretation from gas-liquid immiscible flooding experiments. The advantages over classical analytical methods are application of the fractional flow fundamentals under constant differential pressure boundary and the reduced use of numerical differentiation. Further experiments and research are needed to verify accuracy of the new method. Optimal differential pressure for gas-liquid flooding experiments is to be investigated.

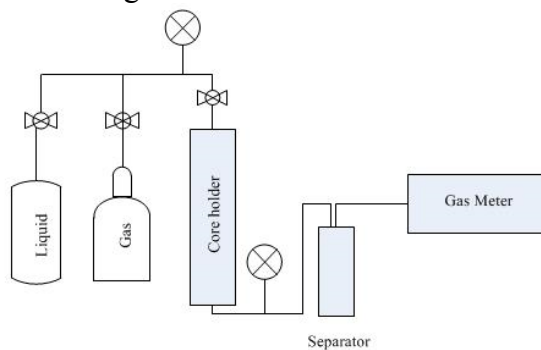


**Figure 1. Experimental Setup Schematic**

**Table 1. Core & Experimental Data**

Core sample	Carbon Tan	Berea sandstone
Displacement type	Gas/water	Gas/oil
Porosity (%)	18	15
Permeability [mD]	9	133
Differential Pressure [psi/bar]	17.98/1.16	2.18/0.15
Core Length [cm]	29.97	30.48
Core Diameter [cm]	3.81	3.81

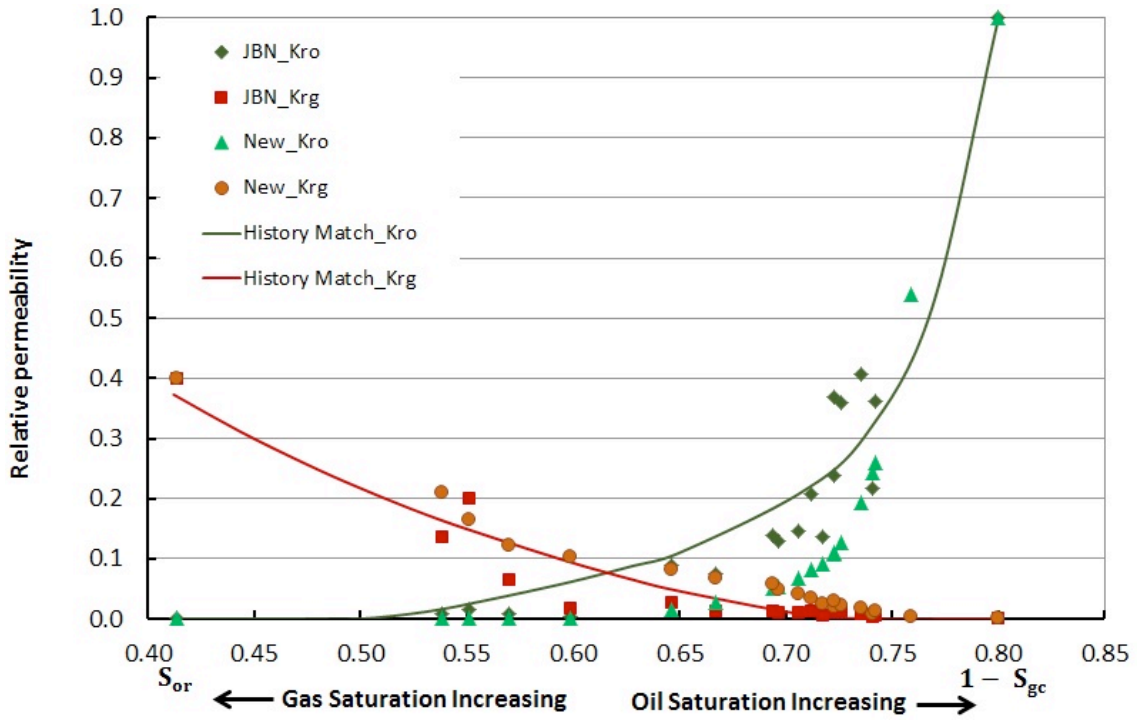


Figure 2 Gas-oil relative permeability results

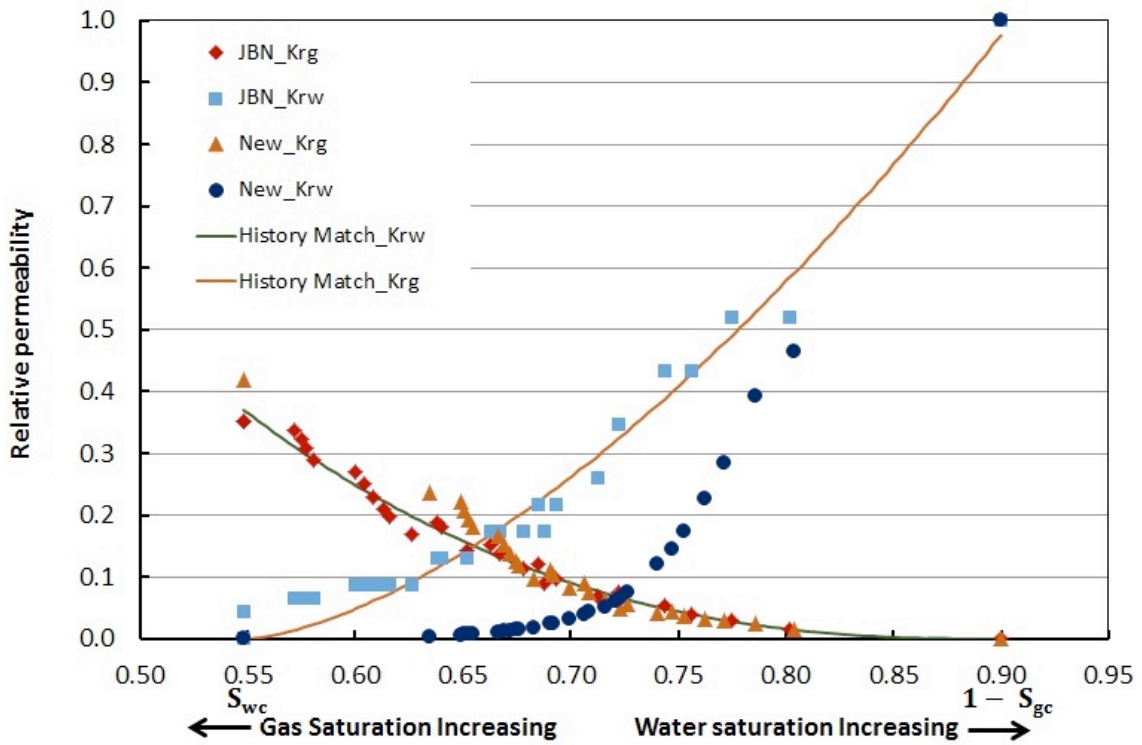


Figure 3 Gas-water relative permeability results

## CONCLUSIONS

In this research, the new analytical relative permeability interpretation method is verified through comparison with the JBN method and numerical method for same displacement experiments. The new method is examined as an alternative method for gas-liquid displacement experiment interpretations, showing a lower liquid relative permeability than JBN method. It applies fractional flow theory under constant pressure boundary and also reduces the errors associated with numerical differentiation used in other analytical methods such as JBN method. Further experiments are need for accuracy verification.

## ACKNOWLEDGEMENTS

The authors would like to thank Hibernia Management and Development Company (HMDC), Research and Development Corporation of Newfoundland and Labrador (RDC), the Natural Sciences and Engineering Research Council of Canada (NSERC), and the Hibernia EOR Research Group for technical and financial support.

## REFERENCES

1. Archer, J.S., and S.W. Wong. Use of a Reservoir Simulator to Interpret Laboratory Waterflood Data. Society of Petroleum Engineers Journal 13.06 (1973): 343-347.
2. Batycky, J.P., F.G. McCaffery, P.K. Hodgins and D.B. Fisher. Interpreting Relative Permeability & Wettability from Unsteady-State Displacement Measurements. SPEJ 21.03 (1981): 296-308.
3. Cao, J., L.A. James and T.E. Johansen, Determination of Two Phase Relative Permeability from Core Floods with Constant Pressure Boundaries. SCA, Avignon, France. 2014.
4. Cable, A., A. Mott, A. and M. Spearing. "Experimental Techniques For The Measurement Of Relative Permeability and In-Situ Saturation in Gas Condensate Near Well Bore and Drainage Studies." SCA, Golden, Colorado. 1999.
5. Dashtian, H., G.R. Jafari, M. Sahimi and M. Masihi. Scaling, Multifractality, and Long-range Correlations in Well Log Data of Large-Scale Porous Media, Physica A: Statistical Mechanics and its Applications 390 (11), 2096-2111
6. Dashtian, H., Y. Yang, and M. Sahimi. Nonuniversality of the Archie Exponent Due to Multifractality of Resistivity Well Logs, Geophysical Research Letters (2015) 42 (24).
7. Johansen, T.E. and L.A. James. Solution of Multi-Component, Two-Phase Riemann Problems with Constant Pressure Boundaries. Journal of Engineering Mathematics (2014): 1-13.
8. Jones, S.C., and W.O. Roszelle. Graphical Techniques for Determining Relative Permeability from Displacement Experiments. Journal of Petroleum Technology 30.05 (1978): 807-817.
9. Johnson, E.F., D.P. Bossler, and V.O. Naumann. Calculation of Relative Permeability from Displacement Experiments, Trans. AIME 216 (1959), 370-372.
10. Tao, T.M., and A.T. Watson. Accuracy of JBN Estimates of Relative Permeability: Part 1- Error Analysis. SPEJ 24.02 (1984): 209-214.
11. Tao, T.M., and A.T. Watson. Accuracy of JBN Estimates of Relative Permeability: Part 2- Algorithms. Society of Petroleum Engineers Journal 24.02 (1984): 215-223.
12. Welge, H.G., A Simplified Method for Computing Oil Recovery by Gas or Water Drive, Petrol. Trans AIME 195(1952), 91.

# INVESTIGATION OF IMBIBITION SATURATION EXPONENT UNDER MIXED SALINITY ENVIRONMENT

F. Pairoys, M. Alexander, V. Odu, J. Ramos, K. Bohn  
Schlumberger Reservoir Laboratories, Houston, Texas, 77041, United States

*This paper was prepared for presentation at the International Symposium of the Society of Core Analysts held in Snowmass, Colorado, USA, 21-26 August, 2016*

## ABSTRACT

An important challenge in resistivity well logging is the interpretation of electrical data to derive the water/oil saturation of an oil reservoir during sea water injection for instance. The sea water resistivity is then commonly used to obtain the water saturation from Archie's law, regardless of the potential mixing between formation brine and sea water; this is certainly valid close to the injection wellbore. However low frequency resistivity tools can have high enough depth of investigation to be affected by this mixed salinity environment. Cross-well electromagnetic (EM) resistivity method for instance, recently used to provide fluid distribution mapping at inter-well scale, can be significantly affected by the change in water resistivity during water flooding.

A core analysis program was initiated to understand the change of resistivity in mixed salinity environment using the porous plate resistivity method in imbibition cycle. Despite the known existence of hysteresis between drainage and imbibition cycles, the cementation factor  $m$  and saturation exponent  $n$ , obtained from Archie's law [1], are generally measured in the laboratory respectively before and during a primary drainage porous plate experiment with resistivity measurements. Imbibition tests are rarely performed, and when they are, no mixing effect is observed since the same formation brine is injected into the sample.

In this paper, the brine mixing effect on rock electrical properties during a porous plate imbibition test is investigated and a simple salinity model is proposed to derive the equivalent resistivity of the brine mixture for appropriate water saturation calculation.

## INTRODUCTION

In formation evaluation, unknown water salinity environment is still an obstacle to obtaining reliable reservoir saturation in a mixed salinity environment. Freeman and Fen [2] started to describe several known log analysis methods for determining reservoir saturation in a mixed water salinity environment. One of the limitations was the shallow depth of investigation of the logging tools, which were all dependent on salinity except the carbon/oxygen (C/O) method. In the last decade, many efforts were implemented to solve the mixed salinity problem. Ma *et al.* [3] gave some recommendations and fit-for-purpose logging approach using C/O logging technology for more accurate reservoir saturation monitoring and diagnosing oil displacement by brine with different salinities.

Al-Sunbul *et al.* [4] ran a pilot field test in mixed formation water salinity environment using induction tools. The multiple depths of investigation (DOI) of the slim-hole resistivity tool provided good formation resistivity data in addition to the formation water salinity determination from bottom-hole samples. Marsala *et al.* [5] showed the result of a cross-well EM technology trial project. The project objective was to map the fluid distribution and monitor the movement of the injected water; a variable formation water resistivity was used in the reservoir water saturation calculation. Ma *et al.* [6] presented a multi-well data integration approach for improved formation evaluation in a mixed salinity environment. They tackle the effect of mixing between injected fresher water and saline formation water.

In order to get a better understanding of the effect of mixed salinity on rock electrical properties, a core analysis program was initiated. It included porous plate tests with core plug resistivity measurements during imbibition cycle using two brines of different salinity. A simple salinity model is proposed to derive the equivalent resistivity of the brine mixture for appropriate water saturation calculation. This approach could be used to obtain more reliable saturations from cross-well EM technology.

## BACKGROUND

The conventional method for obtaining saturations from resistivity in a clay free rock is based on Archie's method [1]:

$$S_w = \sqrt[n]{\frac{R_o}{R_t}} = \sqrt[n]{FF} \frac{R_w}{R_t} = \sqrt[n]{\frac{R_w}{R_t} \frac{a}{\phi^m}} \quad (1)$$

Equation 1 shows the dependence of  $S_w$  to the brine salinity via the  $R_w$  parameter.

Archie's exponents are determined in the laboratory;  $m$  is measured at 100% brine saturation whereas  $n$  is obtained using the porous plate method with resistivity measurements (2-electrode configuration) made at capillary equilibrium during a primary drainage (Figure 1, left).

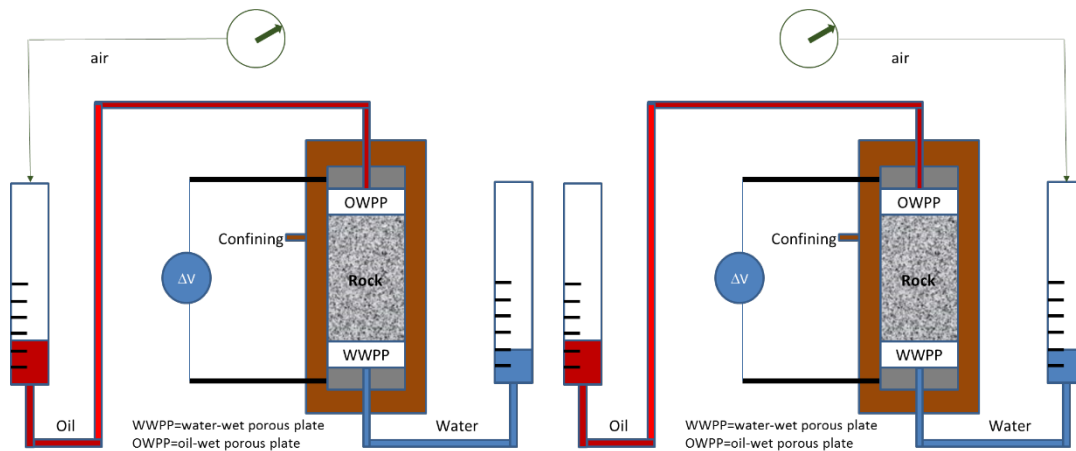


Figure 1: Porous plate and resistivity setup (drainage configuration, left – imbibition configuration, right)

The resistivity index  $RI$  curve is then plotted to obtain the drainage saturation exponent  $n_d$ , used to calculate the reservoir saturation from electrical logs. It is appropriate to calculate initial oil reserve, but imbibition saturation exponent  $n_i$  should be used to obtain a more reliable saturation from the resistivity log during water flooding (Figure 1, right).

In addition, lab data should be obtained under similar conditions to obtain more reliable saturation estimation from resistivity logs; in mixed salinity environment,  $R_t$  variation is not only due to the change in saturation and wettability, but also to the change in brine salinity. Then Equation 1 can lead to a significant error in water saturation calculation.

The porous plate resistivity method can provide information of mixing brine effect, knowing the initial formation brine volume at the end of the primary drainage and the injected brine volume during the imbibition displacement. Assuming fast brine mixing, an equivalent salt concentration  $C_{eq}$  and brine resistivity  $R_{w(eq)}$  (including Craig's approach for resistivity estimation from concentration and temperature), can be obtained :

$$a) C_{eq} = C_1 \frac{V_1}{V_t} + C_2 \frac{V_2}{V_t} \quad \text{and} \quad b) R_{w(eq)} = \left( \frac{400}{T_{ref} C_{eq}} \right)^{0.88} \quad (2)$$

Where  $C_1$  and  $C_2$  are salt concentrations of brine 1 (formation brine) and brine 2 (displacing brine in imbibition cycle) in kppm,  $V_1$  and  $V_2$  are the two brine (formation brine and displacing brine) volumes in the sample in cc,  $V_t$  is the total brine volume in cc,  $T_{ref}$  is the reference temperature for all resistivity measurements in °F.

During the porous plate resistivity experiment, water saturation  $S_w$  (frac.), 100% brine saturated rock resistivity  $R_o$  and resistivity at partial saturation  $R_t$  (in ohm.m) are measured. The saturation exponent  $n$  is obtained from the resistivity index curve  $RI$  versus brine saturation  $S_w$ . The formation factor  $FF$  measured at the beginning of the tests with the formation brine (brine 1) should be constant. Then, the equivalent 100% brine filled resistivity  $R_{o(eq)}$  and resistivity index  $RI_{eq}$  when two brines are mixed during a porous plate resistivity experiment can be obtained from Equations 3:

$$a) FF = \frac{R_o}{R_w} = cte \Rightarrow b) R_{o(eq)} = FF * R_{w(eq)} \quad \text{then} \quad c) RI_{eq} = \frac{R_t}{R_{o(eq)}} \quad (3)$$

Combining equations (2a), (2b) and (3c):

$$RI_{eq} = \frac{R_t}{FF \left( \frac{400}{T_{ref} (C_1 V_1 + C_2 V_2)} \right)^{0.88}} \quad (4)$$

Since concentration and volume of each brine are known during each test, Equation 4 can be used to calculate the equivalent resistivity index  $RI_{eq}$ .  $RI_{eq}$  versus brine saturation  $S_w$  is then plotted to obtain the imbibition saturation exponent  $n_i$  from Archie's regression.

In this study, two twin Berea sandstones were tested for resistivity (2-electrode configuration and 20 KHz of frequency) using the porous plate method in primary

drainage and imbibition cycles. During the imbibition cycle, desaturation of one sample was performed using same initial formation brine 1, whereas desaturation of the second sample was performed using a less saline brine 2 (for mixed salinity assessment).

## ROCK AND FLUID PROPERTIES

A clay free and high porosity sandstone (Berea) was tested in this program (Table 1).

Sample Id	$\rho_g$ (g/cc)	$\phi$ (%)	PV (cc)	$K_g$ (mD)	$K_{kl}$ (mD)	$FF$	$m$
S-A	2.65	25.0	10.6	698	691	16.5	2.02
S-B	2.65	25.0	11.0	592	585	16.4	2.01

Table 1: Rock properties of the two twin sandstones

As expected, the dry porosity-permeability and electrical properties at 100% brine saturation of these two samples were found to be similar.

An iso-paraffin oil (Isopar L) was used as non-conductive phase. Two brines (NaCl equivalent) of different salinity were prepared:

- Brine 1 or formation brine (200 kppm NaCl,  $R_{w1}=0.05$  ohm.m) for initial rock saturation of both samples and injected brine for imbibition of sample S-A,
- Brine 2 or injected brine (50 kppm NaCl,  $R_{w2}=0.16$  ohm.m) for the imbibition of sample S-B, simulating sea water injection for instance.

## EXPERIMENTAL RESULTS

The porous plate resistivity test was performed using four capillary pressure  $P_c$  steps (up to 20 psi maximum  $P_c$ ). Confining pressure of 800 psi was applied (ambient pore pressure and room temperature of 68°F). Brine resistivity was measured at the same room temperature. Resistivity data points were taken at transient state and capillary equilibrium.

As expected, irreducible saturation  $S_{wi}$  and saturation exponent  $n_d$  were found to be comparable for the twin plugs (Table 2).

Sample Id	$S_{wi}$ (%)	$n_d$ (equilibrium)	$n_d$ (all data points)
S-A	23.8	1.94	1.93
S-B	22.9	1.95	1.94

Table 2: Primary drainage data results

Resistivity at capillary equilibrium or at transient state lead to similar values of saturation exponent  $n_d$ .

The imbibition cycle was immediately started at the end of the primary drainage. The

spontaneous imbibition was not separately tracked but hidden in the forced imbibition. Since resistivity was the main objective, imbibition saturation exponent  $n_i$  was obtained from transient resistivity data during a one single  $P_c$  step of 5 psi. Thereby, the imbibition capillary pressure curves are not obtained.

The transient imbibition resistivity index data points were plotted versus water saturation  $S_w$  to derive the imbibition saturation exponent  $n_i$  (Figure 2). In sample S-A, the same brine 1 was used to displace oil whereas brine 2 was used to displace oil in sample S-B. Equation 4 was used to correct for mixed salinity effect on sample S-B.

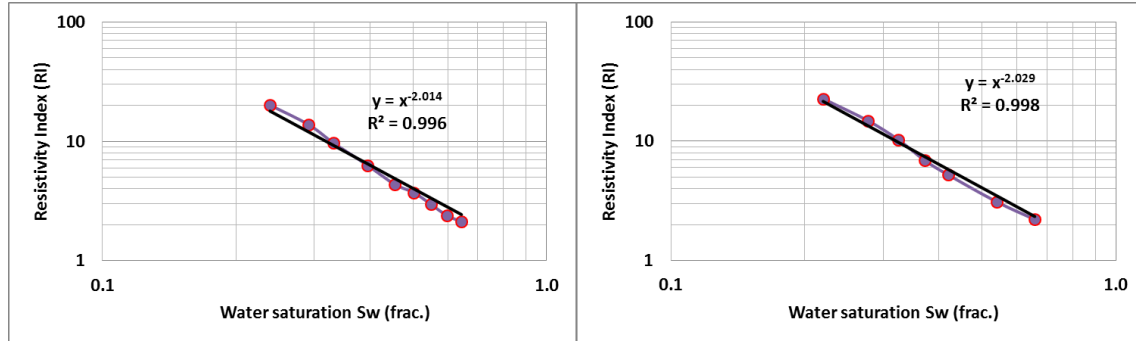


Figure 2: Transient imbibition  $RI$  curves for sample S-A (left) and for sample S-B (right)

Final water saturation  $S_w$  for both samples was very close ( $S_{w1}=64.3\%$  and  $S_{w2}=65.7\%$ ); they were confirmed by post Dean-Stark cleaning. The saturation exponent  $n_i$  obtained from sample S-B ( $n_i=2.03$ ) with mixed salinity correction using Equation 4 was found to be close to the one from sample S-A ( $n_i=2.01$ ) where same formation brine was injected. For sample S-B, if  $R_w$  from equation 1 was kept constant and equal to either  $R_{w1}$  (formation brine resistivity) or  $R_{w2}$  (displacing/injected brine), saturation exponent  $n_i$  would have been respectively higher and lower as shown in Table 3.

$R_w$ (ohm.m)	$R_t$ (ohm.m)	$\phi$ (%)	$m$	$n_i$	$S_w$ (%)
$R_w(\text{mixed})=0.08$	2.97	24.95	2.01	2.03	65.7
$R_{w1}=0.05$	2.97	24.95	2.01	2.15	54.8
$R_{w2}=0.15$	2.97	24.95	2.01	1.16	84.5

Table 3: Imbibition data results for sample S-B

Using Equation 1 with  $a=1$ , the difference in saturation exponent  $n_i$  according to brine resistivity can lead to a significant error in water saturation calculation if the correcting model in Equation 4 is not applied (Table 3). Using formation brine or injected brine resistivity can respectively overestimate or underestimate the reservoir oil saturation.

Nevertheless, Equation 1 can still be used to derive reservoir water saturation in a mixed salinity environment if the equivalent brine resistivity  $R_{w(eq)}$  obtained from the mixing law in Equation 2 is updated while water flooding the reservoir. Another advantage of

this laboratory protocol is that a more realistic residual oil saturation will be obtained during an EOR program where low salinity brine is injected for instance.

## CONCLUSION

To get a better understanding of the effect of mixed salinity on rock electrical properties, a core analysis program including porous plate tests with resistivity measurements during the imbibition cycle using two brines of different salinity was performed. A simple salinity model was proposed to derive the equivalent resistivity of the brine mixture for an appropriate water saturation calculation. Even if the lab method does not fully represent a real flooding cycle in the reservoir, the proposed mixing model can help in assessing and correcting the error induced by the change in overall brine resistivity.

It was shown that not taking into account the contrast in resistivity between the formation and the injected brines during water flooding can lead to a significant error in the estimation of oil-water saturations. In a real reservoir environment, knowing the initial formation brine saturation and its resistivity, in addition to the volume of injected brine of known resistivity in the region of investigation of the cross-well EM method (based on frequency/depth of investigation), this approach could be used to obtain more reliable inter-well saturations. Additional studies such as wettability and heterogeneity effects on the validation of the mixing model, in addition to a final field test, are required.

## REFERENCES

1. Archie, G. E.: "The Electrical Resistivity Log as an Aid in Determining Some Reservoir Characteristics", *AIME Petroleum Tech.* (1942), 1-8, 1942
2. Freeman, D.W., Fenn, C.J., "An Evaluation of Various Logging Methods for the Determination of Remaining Oil Saturation in a Mixed Salinity Environment", SPE 17976, Middle East Oil Technical Conference and Exhibition, Manama, Bahrain, 11-14 March, 1989
3. Ma, S.M., Al-Hajari, A.A., Berberian, G., "Cased-Hole Reservoir Saturation Monitoring in Mixed-Salinity Environments – A New Integrated Approach", SPE 92426, Middle East Oil & Gas Show and Conference, Bahrain, 12-15 March 2005
4. Al-Sunbul, A.H., Ma, S.M., Al-Hajari, A.A., Srivastava, A., Ramamoorthy, R., "Quantifying Remaining Oil by Use of Slimhole Resistivity Measurement in Mixed Salinity Environments – A Pilot Field Test", SPE 97489, International Oil Recovery Conference, Kuala Lumpur, Malaysia, 5-6 December 2005
5. Marsala, A.F., Ruwaili, S., Ma, S.M., Ali, Z., Buali, M., Donadille, J.M., Crary, S., Wilt, M., "Crosswell Electromagnetic Tomography: From Resistivity Mapping to Interwell Fluid Distribution", IPTC 12229, International Petroleum Technology Conference, Kuala Lumpur, Malaysia, 3-5 December 2008

6. Ma, S.M., Al-Belowi, A.R., Al-Mudhhi, M.A., Al-Ali, Z.A., Zeybek, M., “Integrated Multiwell Formation Evaluation for Diagnosing Reservoir Dynamics”, SPE 159897, Annual Technical Conference and Exhibition, San Antonio, Texas, USA, 8-10 October 2012

# The Role of Film Flow and Wettability in Immiscible Gas Assisted Gravity Drainage

H. Khorshidian, L.A. James and S.D. Butt

Memorial University of Newfoundland

*This paper was prepared for presentation at the International Symposium of the Society of Core Analysts held in Snowmass, Colorado, USA, 21-26 August 2016*

## ABSTRACT

Capillary and gravity forces control the residual saturation of liquid phases before and after gas breakthrough in Gas Assisted Gravity Drainage (GAGD). These forces are determined by the fluid and formation properties. In this research, the effects of capillary and gravity forces on oil film flow have been investigated focusing on the wettability of porous media. Experiments were conducted in oil-wet and water-wet pore network micromodels to investigate the role of wettability on oil recovery during CO<sub>2</sub> GAGD. It has been observed that the GAGD residual oil saturation profile is affected by the state of wettability. In water-wet micromodels, the irreducible water saturation was found in smaller pores (body and throats) and blocked potential pathways for oil film flow. In oil-wet micromodels, the majority of the residual oil was found in smaller pores and around the grains in micro-capillaries in the form of oil rings. In GAGD, the presence of corners and edges enable the liquid phases to maintain a stronger capillary continuity to a limited elevation. We have observed a higher oil recovery in locations with stronger capillary continuity. However, the rupture of liquid films beyond a critical capillary pressure, due to geometric constraints, can arrest liquid film flow.

## INTRODUCTION

In the Gas Assisted Gravity Drainage (GAGD) oil recovery, the differential density between the gas phase and oil phase causes the gas-oil capillary pressure to increase behind the gas front [1]. Since GAGD is a drainage process, increasing the gas-oil capillary pressure increases the number of pores invaded by gas (non-wetting phase). Consequently, the ultimate oil recovery factor becomes higher. In order to enhance the capillary pressure behind the gas front, fine capillaries must exist through which downward oil film flow can occur [2].

The role of the oil film flow in GAGD is illustrated by Fig. 1 which is a simple pattern having two pore bodies with different throat sizes. In Fig. 1A, oil (wetting phase) is displaced by gas (non-wetting phase) through the least resistant path. The capillary pressure ahead of the gas front is indicated by  $P_{cgo}^*$  (Fig. 1B). Films of oil may occupy the corners of the pattern as gas-oil interfaces with smaller radii (higher capillary pressure) can be formed in the edges. The radius of gas-oil interface at higher elevations is smaller as the capillary pressure is higher. The capillary pressure behind the gas front ( $P_{cgo}$ ) is calculated by Eq.1

$$P_{cgo} = P_{cgo}^* + \Delta\rho_{go}gH \quad (1)$$

where,  $\Delta\rho_{go}$  is the gas-oil differential density,  $g$  is the gravity acceleration,  $H$  is the elevation of the gas-oil interface behind the gas front. When an oil occupied pore throat, which is not initially invaded by gas, is located at a sufficient vertical distance ( $H_1$  in Fig. 1C) from the gas front, gas can enter the pore through the center of its throat, and oil can drain from the throat corners (Fig. 1D). Gas may enter the smaller throat similarly (Fig. 1E) when the gas front moves downward further (e.g.,  $H_2$ ). However, the roundness of the corners (pore geometry) may not allow the oil and gas to form a highly curved interface with a small radius [3]. Therefore, the oil film elevation can be terminated and the oil in the pore bodies that have a smaller throat cannot be recovered (Fig. 1F). In a three phase GAGD, the presence of water and wettability can affect the geometric constraints and the maximum obtainable capillary pressure [1].

The objective of GAGD is to inject gas to decrease mobile and immobile oil with the aid of gravity. It was found that GAGD performance was more favourable in water-wet media when oil can spread over the water surface [3, 4]. Conversely, higher GAGD oil recovery was measured in oil-wet conditions [5]. Vizika and Lombard [6] studied the effect of wettability on the residual oil saturation conducting tertiary GAGD in a 50 cm long sandpack. A low residual oil saturation was measured in a water-wet medium when the gas-water interfacial tension was high and caused spreading of oil on the surface of water. A very low residual oil saturation was also observed far from the bottom of the oil-wet sandpack (>10 cm) when the gas-water interfacial tension was low. However, the residual oil saturation at bottom the oil-wet sand pack was high due to the capillary end effect which causes the retention of the wetting phase. The gas-oil capillary pressure may drop dramatically due to exit of the gas phase through largest paths in the bottom of a porous medium.

In this research, the influence of wettability on oil recovery of secondary GAGD was studied using oil-wet and water-wet pore network micromodels. The micromodel allows detailed visualization of the gas, oil and water interfaces during GAGD. The mechanisms that affect the recovery of oil in GAGD are presented in this paper.

## EXPERIMENTAL DETAILS

A 256 x 64 mm (LxW) pore network micromodel was fabricated in the Hibernia EOR Laboratory at Memorial University. A heterogeneous pattern containing pore bodies with sizes of 1-1.6 mm and pore throats with widths of 200-800  $\mu\text{m}$ , was etched on an acrylic plate (depth: 185  $\mu\text{m}$ ) and the plate was thermally bonded to a blank plate.

A Quizix 20K series pump and three custom floating piston accumulators were used to inject the oil (red dyed Varsol) and water (blue dyed deionized water) into the micromodel at constant pressure. The fluids were produced at constant rates using another 20K pump and accumulator. Secondary GAGD experiments were conducted in the oil-wet and water-wet micromodels. The micromodel wettability was altered from oil-wet to strongly water-wet by flushing the micromodel with Hydrphil™ leaving a hydrophilic silica gel on the acrylic surface. The oil-wet micromodel oil saturation was established in two steps: 1) The fully oil saturated micromodel was aged 24 hrs and then flooded by two pore volumes of water at 10 cc/hr from bottom to top (gravity stable) of

the micromodel; and 2) Two pore volumes of red-dyed oil were injected into the micromodel at 3 cc/hr from top to bottom. In the water-wet micromodel, two pore volumes of red-dyed oil were injected (3 cc/hr) into a fully water saturated micromodel from top to bottom. GAGD tests were conducted by injecting 4 pore volumes of CO<sub>2</sub> at 0.1 cc/hr at constant temperature (20°C) and pressure (25 psig / 1.7 bar) conditions.

Saturation profiles and oil recovery were performed visually and results are presented based on 2D image analysis not accounting for the volumetric differences for larger pores being etched more deeply than more narrow pores. A Canon 6D camera and Canon EF 100mm f/2.8 USM macro lens were used to take high quality pictures every 10 minutes in order to calculate the saturation profiles during the GAGD experiments. An in-house image analysis program was used to calibrate the color of each individual pixel as red, blue, or white, depending on their colour. The oil saturation and recovery factor were then calculated knowing the number of total pixels, red pixels, and micromodel porosity.

## RESULTS & DISCUSSION

The saturation profiles in the oil-wet and water-wet micromodels are shown in Fig. 2 and 3. It was observed that the injected gas invaded the larger pores before and more quickly than smaller pores, as expected. A few fingers were formed in the gas front as the gas could not enter pores throats smaller than 500 μm. Bypassed and isolated oil occupied zones (groups of pores), especially where the pore throats were smaller than 400 μm, were created behind the gas front which may be subsequently drained in time (Fig 2B, 2C, 3B, 3C). Some of the uninvaded regions that maintained their connection to the gas front, and wetting film continuity started to drain by film flow at later times assisted by gravity. In both wettability states, the oil production, after initial piston-like drainage displacement, was driven by gravity and controlled by capillary forces.

Thick oil films, formed on rough surfaces and in the corners, played an important role in the recovery of the bypassed oil [2]. The additional oil recovery after gas breakthrough occurred only via film flow. The trapped oil occasionally moved with the assistance of film flow. The isolated oil at higher elevations flowed toward neighbouring regions by film flow increasing the local oil saturation of another bypassed zone. When the local oil saturation in the new zone is sufficiently high for the gravity forces to overcome capillary forces, the oil could flow in the direction of gravity. The flow of oil in bypassed zones occurred in a step-wise process. In oil-wet micromodels, the residual oil was observed in the smallest pore sizes and in form of films around the solid grains as shown in Fig. 2D.

In water-wet micromodels, water occupies most of the pores having throats sizes of 200 μm (pores with smallest throats) and around the solid grains. Residual oil is shown trapped in the pore bodies with throats sizes greater than 300 μm. The oil gravity drainage paths are formed through the smaller pores and capillary corners. In water-wet conditions, we observed that the pore bodies with smaller throats and around the solid grains are occupied by water, and the water blocked the formation of an oil film and subsequent drainage. The residual oil was maintained in medium size pores.

The micromodel images after GAGD (Fig. 2D and 3D) indicate that the zones near the vertical edges of the pattern in the oil-wet micromodel contain less residual oil and water phases compared to other regions of the pattern. A stronger capillary continuity existed in

the edges of both micromodels where the pattern formed a straight corner vertically. The phase interface with small radii can be formed in the edge of the micromodel which causes drainage of neighbouring pores with a higher capillary pressure. The magnified images of the oil-wet (Fig. 2D) and water-wet (Fig. 3D) micromodel edges show the difference between the oil saturation profiles of the oil-wet and water-wet micromodels. The trapped oil in the margin of the oil-wet micromodel was found in pore bodies with smallest pore throats (200  $\mu\text{m}$ ). The trapped oil in the edge of the water-wet micromodel was found in pore bodies connected to larger pore throats (400  $\mu\text{m}$ ). This difference implies that capillary continuity of the oil phase in the oil-wet micromodel is stronger.

Fig. 4 shows GAGD oil recovery in micromodels as a function of the pore volume of the injected gas. It is shown that the film flow mechanism after gas breakthrough resulted in a higher additional oil recovery factor in oil-wet rather than water-wet micromodels. Film flow contributes to an additional 6% and 2% recovery for the oil-wet and water-wet micromodels post breakthrough recovery, respectively.

Although the capillary continuity of oil in the margin of the oil-wet micromodel is stronger, the presence of oil in few pore bodies with small throats implies that the capillary pressure elevation behind the gas front is limited as the gas entry capillary pressure to these pores is higher than a critical capillary pressure that can be generated in the edge of the micromodel. The highest achievable capillary pressure depends on the geometry of capillary corners in the edge of the pattern. The enhancement of capillary pressure at higher elevations along the micromodel edge terminates when the equilibrium between capillary pressure at that corner radii can no longer be maintained. Therefore, in oil-wet micromodel, oil occupied pores with very small throats are undrainable. The critical capillary pressure, beyond which a gas-oil interface cannot form, controls the residual oil saturation. Our preliminary observations in micromodel experiments imply that maximum achievable capillary pressure in a water-wet porous medium is lower than in an oil-wet medium, as water in smaller pores interrupts the draining oil film paths.

In a water-wet porous medium, the presence of water in the smallest pores caused the residual oil to locate in small to medium sizes pores. The smallest pores maintain the wetting phase (water in water-wet condition and oil in oil-wet condition) after GAGD. Therefore, the position and saturation of post-GAGD residual oil was not only affected by the porous medium wettability, but also influenced by the pore size distribution.

The pore sizes of the micromodel are more than 10 times larger than the typical pore sizes of a sandstone. According to Eq. 1 gas-oil capillary pressure behind the gas front is determined by the breakthrough capillary pressure and elevation of gas-oil interface. It can be assumed that scaling up the pore sizes scales down both the gas breakthrough capillary pressure and the highest achievable gas-oil capillary pressure due to elevation of their interface behind the gas front. Enlargement of pore sizes, however, reduces the difference between the required gas-oil capillary pressure for drainage of oil from the largest and smallest drainable pores. Although the result of GAGD in micromodel is impacted by the poor capillary continuity condition and large scale pore sizes, it can reflect the mechanism of film flow in GAGD oil recovery effectively.

Future work should include closer examination of GAGD oil recovery mechanisms in a realistic micromodel with surface roughness to determine its effect on capillary continuity and film flow. We are developing a new micromodel with dual pore network containing coarse and fine capillaries. The presence of fine capillaries can improve the capillary continuity of the micromodel, and the quantified residual oil saturation can better represent the GAGD performance. Additionally, the interaction effects of pore size distribution and wettability on GAGD performance will be investigated in the new micromodel.

## **CONCLUSIONS**

The GAGD research in micromodels showed that gravity and capillary forces control the residual oil saturation in an immiscible vertical gas injection process. It has been found that the post-GAGD residual oil saturation profile is affected by the state of wettability and pore geometry. The gas front bypassed the smaller pores due to presence of pore-scale heterogeneities. The irreducible water saturation in the water-wet micromodel reduces the critical capillary pressure beyond which the film flow of oil cannot geometrically exist.

## **ACKNOWLEDGEMENTS**

The authors would like to thank Petroleum Research Newfoundland and Labrador (PRNL), Research and Development Corporation of Newfoundland and Labrador (RDC), the Natural Sciences and Engineering Research Council of Canada (NSERC), and the Hibernia EOR Research Group for technical and financial support.

## **REFERENCES**

1. Khorshidian, H., L.A. James, & S.D. Butt, Corner Oil Film Elevation above the Gas-Oil Interface in Water-Wet Capillaries, in International Symposium of the Society of Core Analysts, SCA, St. John's Newfoundland and Labrador, Canada, 2015.
2. Dullien, F.A., Porous media: fluid transport and pore structure. 2012: Academic press.
3. Piri, M. & M.J. Blunt, Three-phase threshold capillary pressures in noncircular capillary tubes with different wettabilities including contact angle hysteresis. *Physical Review E*, 2004. 70(6): p. 061603.
4. Chatzis, I., A. Kantzas, & F. Dullien. On the investigation of gravity-assisted inert gas injection using micromodels, long Berea sandstone cores, and computer-assisted tomography. Presented in SPE Annual Technical Conference and Exhibition. 1988.
5. Grattoni, C., X. Jing, & R. Dawe, Dimensionless groups for three-phase gravity drainage flow in porous media. *Journal of Petroleum Science and Engineering*, 2001. 29(1): p. 53-65.
6. Paidin, W.R., & Rao, D.N. Physical Model Experiments to Evaluate the Effect of Wettability and Fractures on the Performance of the Gas-assisted Gravity Drainage (GAGD) Process. Proceedings of the Society of Core Analysts Symposium, Calgary, Canada, 2007.
7. Vizika, O. & J. Lombard, Wettability and spreading: two key parameters in oil recovery with three-phase gravity drainage. *SPE Reservoir Engineering*, 1996 11(01): p. 54-60.

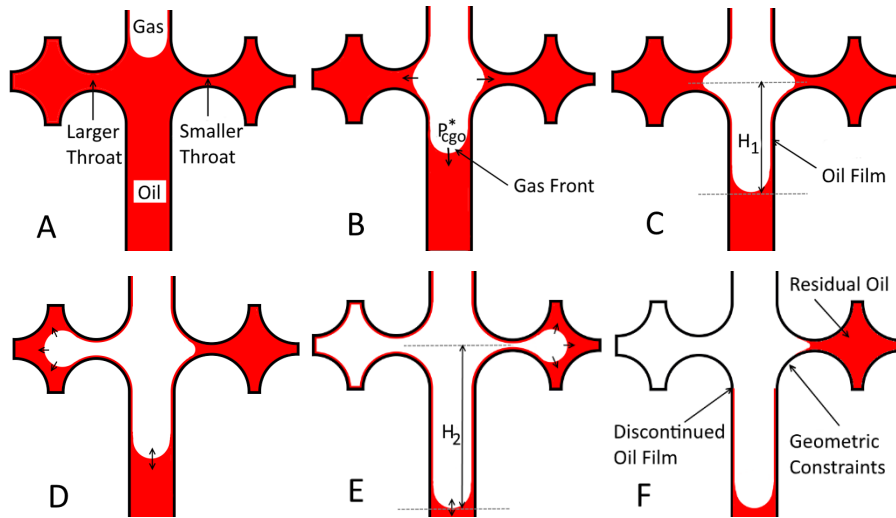


Fig. 1: Oil drainage behind the gas front through film flow in capillary corners

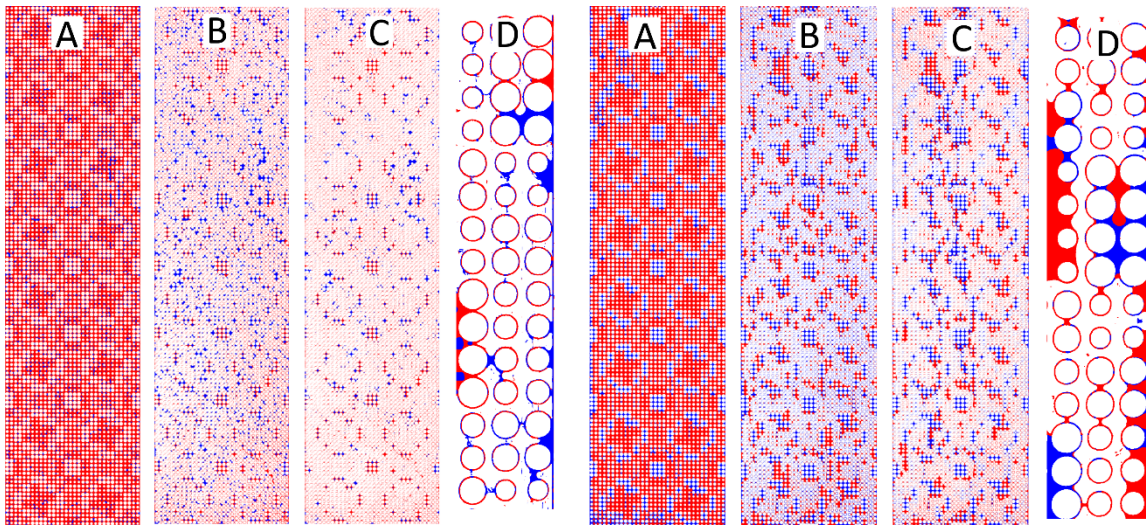


Fig. 2: GAGD in oil-wet micromodel

Fig. 3: GAGD in water-wet micromodel

(blue: water, red: oil, A: Before GAGD, B: Post breakthrough at 0.6 P.V. injected gas, C: After 4.1 P.V. injected gas, D: Magnified micromodel margin)

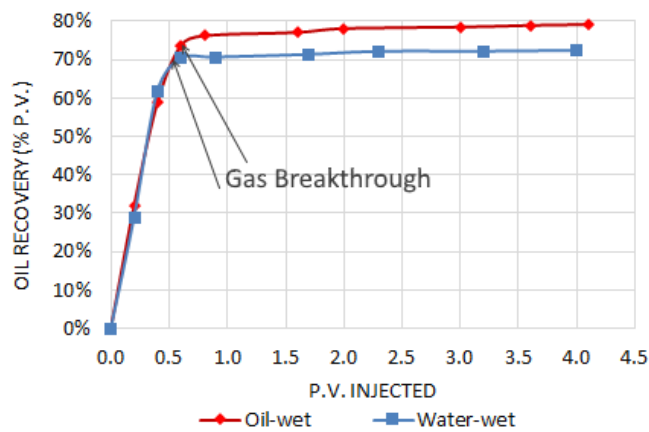


Fig. 4: Oil recovery curve in both states of wettability vs. pore volume of injected gas

## **Pore Scale Investigation of Carbonated Water Injection with and without Gravity**

S. Mahdavi, L.A James, T.E Johansen  
Hibernia Enhanced Oil Recovery Laboratory  
Memorial University of Newfoundland, Canada

*This paper was prepared for presentation at the International Symposium of the Society of Core Analysts held in Snowmass, Colorado, USA, 21-26 August 2016*

### **ABSTRACT**

In this study, the use of CO<sub>2</sub> for carbonated water injection (CWI) in pore network micromodels is investigated. Different scenarios, including water injection, secondary and tertiary CWI were performed under different oil production rates at constant temperature. The injection pressure was kept constant at 305 psi (2.1 MPa) and the production rate varied. The distribution pattern of the carbonated water in the porous media is a function of oil production rate. When the oil production rate is high, the breakthrough happens early and oil recovery is less than when production rates are lower. At a higher oil production rate, the carbonated water phase cannot sweep the oil and will not distribute in different directions of throats in the porous media. These results are analysed with respect to dimensionless analysis. The effect of gravity was verified by performing CWI injection in the presence of gravity. Pore scale events such as trapped oil are observed and seen to be affected by the production rate.

### **INTRODUCTION**

Secondary recovery techniques such as water or gas flooding help increase production by re-pressurizing the reservoirs but leave much oil trapped in place due to capillarity and/or low sweep efficiency. Enhanced oil recovery techniques can increase recovery by an additional 3-15%. The challenge is to target both pore scale and field scale (vertical and horizontal) displacement efficiency for the specific reservoir characteristics. Many field tests have demonstrated that without the benefit of vertical displacement, water flooding and gas injection operations usually result in low vertical sweep efficiency [8-10]. Water alternating gas (WAG), simultaneous WAG (SWAG) and carbonated water injection (CWI) can address the problem of efficiently recovering oil through combining advantages of both water flooding (bottom layers displacement) and gas injection operations (top layers displacement) [1-3]. CO<sub>2</sub> is more soluble in oil than the other gases, so CO<sub>2</sub> based EOR processes are more cost effective than the other gas based EOR methods as they can use less amount of CO<sub>2</sub> for the same performance. They are also environmentally friendly as they capture CO<sub>2</sub> from atmosphere [4,5]. Methods that require less CO<sub>2</sub> such as CWI, are more practical in offshore and harsh environments where the only gas/CO<sub>2</sub> supply may be CO<sub>2</sub> separated from gas cap, solution gas, a nearby gas reservoir and/or flue gas from onboard electrical generation [4,6,7]. Various studies have been conducted to macroscopically and microscopically understand the

phenomena behind the solvent injection and displacement. Pore scale interactions in visual porous media have also been studied for CWI and other EOR applications [11-14]. CWI has been found to be effective in recovering oil from complex porous media [14]. Martin [15] studied the effect of CWI on oil recovery using core samples and found a 12% improvement on oil recovery compared to water flooding. Dong et al. (2011) found that CWI recovered more oil compared to water flooding from sand packs and core samples in secondary and tertiary modes. Higher flooding rates gave optimal recovery factor [16]. Sohrabi et al. [18] recorded 24% additional oil recovery during tertiary CWI compared to water flooding in a series of core flooding experiments, and later water breakthrough in CWI than in plain water injection. The effect of CWI on oil recovery at high pressure and temperature has been investigated [14, 17]. Riazi et al. [14] compared CWI with water flooding using horizontal homogeneous micromodel at 2000 psia (13.7 MPa) and 38°C where 41, 47, and 49% recovery for water flooding, tertiary and secondary CWI, respectively. In this research the effect of CWI in vertically oriented micromodel was investigated to understand the performance of CWI on vertical oil displacement and oil distribution using different schemes.

## EXPERIMENTAL DETAILS

The injection of CWI in a pore network micromodel, with and without gravity, was examined using a pressurized micromodel setup shown in Figure 1. The injection pressure was kept constant at 305 psi (2.1 MPa) and 21°C. The homogeneous (in house etched) glass micromodels (see Table 1) were saturated with oil until no air bubbles were observed. Based on the defined scenario (see Table 3), water flooding, secondary, or tertiary CWI injection began by stabilizing the pressure difference between the inlet and outlet of the micromodel. A high resolution camera (Canon EOS 6D, 100 mm focal length) was used and images were analyzed using in-house image analysis software.

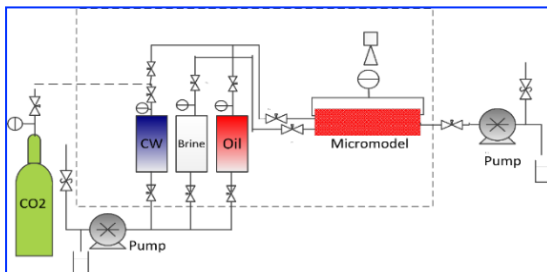


**Figure 1. Schematic of CWI experiment in pressurized micromodel setup**

**Table 1. Micromodel characteristics**

L (mm)	W (mm)	K (D)	$\phi$ (%)	Pore diameter (mm)	Throat width (mm)
270	50.7	450	30%	0.650, 0.773, 0.998	0.26, 0.33, 0.69



**Figure 2. Micromodel**

**Table 2. Fluid properties**

$\rho_o$ Kg/m <sup>3</sup>	$\mu_o$ cP	$\rho_{CW}$ Kg/m <sup>3</sup>	$\mu_{CW}$ cP	$\rho_w$ Kg/m <sup>3</sup>	$\mu_w$ cP	$\sigma_{(o-w)}$ N/m
877	14.62	1015	0.95	0.997	1.0	0.029*

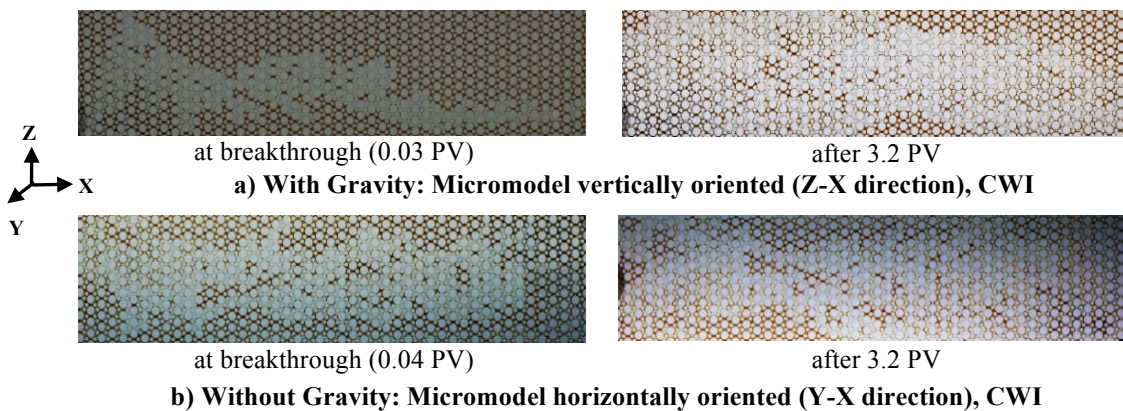
\*: The same number for oil/CW was used

$\rho$ : density,  $\mu$ : viscosity,  $\sigma$ : interfacial tension,  $o$ : oil,  $w$ : water,  $CW$ : carbonated water

The fluids are light oil, deionized water (DI) and pure CO<sub>2</sub> supplied by Praxair (99.8% purity). Their properties are given in Table 2. The viscosity of the oil was measured by VISCOLab PVT apparatus, high pressure viscometer at 21 °C and 305 psi. The viscosity and density of water and carbonated water were calculated at experimental condition (21 °C and 305 psi) using HYSYS software. The interfacial tension between oil and water was measured at 21 °C and 305 psi by VINCI IFT 700 apparatus. In order to differentiate between the oil, water, and carbonated water (CW), methylene blue was used to dye the water phase while the CW was colorless in both secondary and tertiary scenarios. The carbonated water was prepared by mixing deionized water and pure CO<sub>2</sub> at 21°C and 220 psi (1.5 MPa) for 48 hours.

## RESULTS AND DISCUSSION

**Vertical vs Horizontal CWI:** The effect of gravity on CWI injection was investigated in horizontally and vertically oriented pore network micromodels. Figure 3 shows water flooding and secondary CWI in both vertically and horizontally oriented micromodels. Please note that 1) injection is from left to right, and 2) horizontal means laid flat on a table (Y-X orientation) while vertical means standing up in landscape orientation (Z-X orientation). Figure 3a-left (and the repeat in Figure 3d-left) shows that gravity causes the carbonated water (CW) to move downward until breakthrough, whereas the CW is distributed more evenly prior to breakthrough in the horizontally oriented micromodel due to the lack of gravity effect (Figure 3b-left). The fluid distribution after 3.2 PV CWI indicates that CW phase is able to sweep the remaining oil over a large area in both vertically and horizontally oriented micromodels (Figure 3a-right/3d-right and 3b-right). However, earlier breakthrough happens in vertically oriented micromodel compared to horizontal one due to effect of gravity. Residual oil saturation in vertically oriented micromodel is decreased gradually after breakthrough, while in the horizontally oriented micromodel it remains almost constant (Figure 4). Residual oil saturation changes 35.5% and 21.7% from breakthrough up to 3.2 PV in vertically and horizontally oriented micromodels, respectively (Table 3).



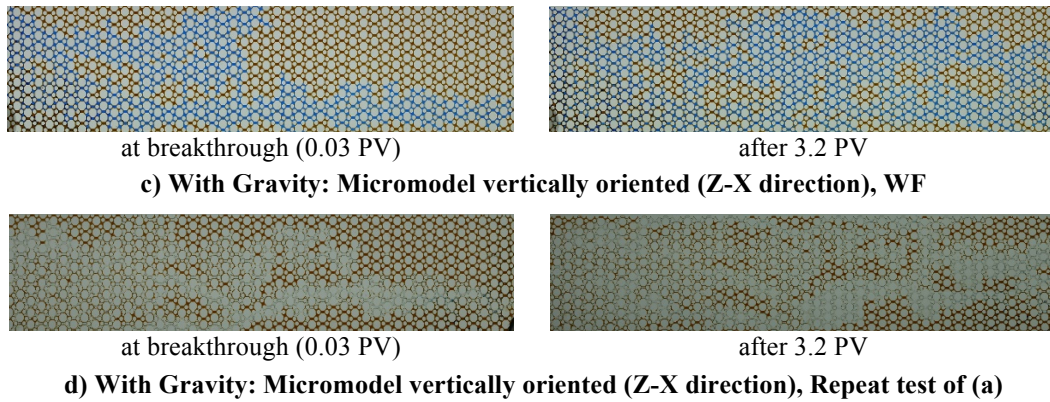


**Figure 3: Residual oil saturation from secondary CWI and WF**

**Water Flooding vs CWI:** The effect of carbonated water flooding versus water flooding on residual oil saturation is shown in Figure 4, and Table 3. We see that water breakthrough takes a little longer for water flooding (28 min) compared to CWI (24 min - average of the two replicates) possibly due to the mobility of carbonated water. Overall, CWI is more effective at reducing the residual oil saturation at all times after breakthrough (Figure 3c-right and Figure 4) while the residual oil saturation for WF is lower than CWI at breakthrough. The residual oil decreases more with CWI (84.5% to 47.5% - average of the two replicates) vs water flooding (74.3% to 63.8%) post breakthrough, resulting in significantly different residual oil saturations at ~7 PV.

**Effect of Production Rate on CWI:** The effect of production rate in secondary CWI was tested using two production rates, 0.0008 and 0.004 cc/min (Figure 4 and Table 3). The initial displacement was faster for the higher production rate and breakthrough happens earlier, as expected. At the lower production rate, the residual oil saturation profile stabilized at 3.2 PV, but at higher production rate, the oil saturation continued to decrease beyond 3.2 PV. The lower production rate yielded lower residual oil but ultimately the residual oil saturation approached ~50% irrespective of orientation or production rate.

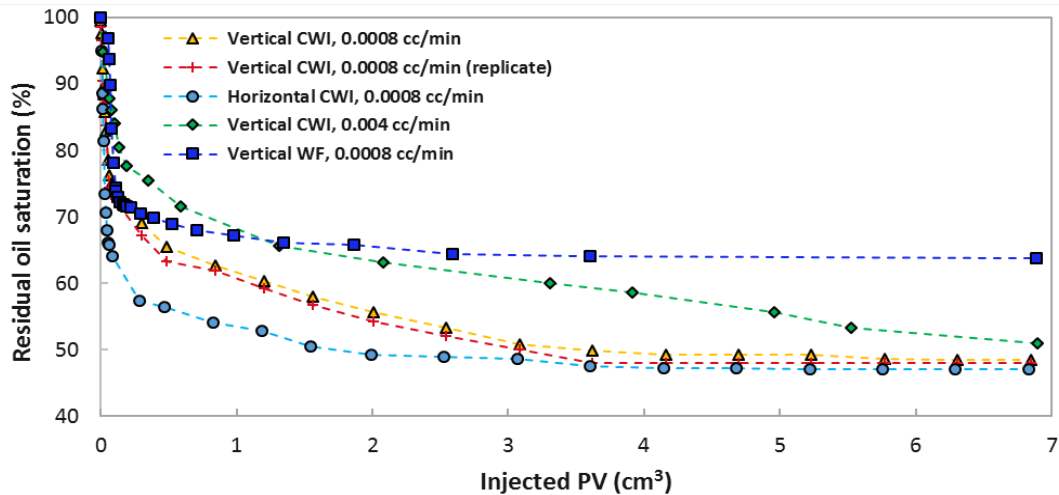


**Figure 4: Residual oil saturation in different scenarios as a function of injected pore volume**

**Table 3: Comparison of different scenarios including WF and SCWI**

Exp.	Mode	Rate (cc/min)	BT (min)	$S_{or}$ (%) at BT	$S_{or}$ (%) (1 PV)	$S_{or}$ (%) (3.2 PV)	$S_{or}$ (%) (~7 PV)	$N_{ca}$ ( $\frac{u\mu_w}{\sigma}$ )	$N_B$ ( $\frac{\Delta\rho g K}{\sigma}$ )
WF	V	0.0008	28	74.3	67.3	64.1	63.8	7.25E-8	5.82E-5
SCWI	V	0.0008	25	85.8	61.5	50.5	47.0	7.25E-8	6.50E-5
SCWI*	V	0.0008	23	83.7	58.5	48.0	48.0	7.25E-8	6.50E-5
SCWI	H	0.0008	32	70.6	53.5	48.9	47.1	7.25E-8	NA
SCWI	V	0.004	20	80.5	68.2	61.2	53.1	3.62E-7	6.50E-5

WF: water flooding, SCWI: secondary CWI, \* repeat, H: horizontal, V: vertical, BT: breakthrough,  $S_{or}$ : residual oil saturation,  $N_{ca}$ : Capillary number,  $N_B$ : Bond number,  $u$ : Darcy's velocity = actual velocity  $\times \phi \times (1 - S_{or})$ , (Riazi et al., 2011),  $g$ : gravitational force ( $m/s^2$ ),  $K$ : permeability ( $m^2$ ),  $\Delta\rho$ : density difference between displacing and displaced fluids,  $\sigma$ : Interfacial tension between displacing and displaced fluids.

**Pore scale mechanisms:** The main pore scale mechanisms of oil recovery via CWI compared to water flooding, based on the observed results of this test, are i) the redistribution of trapped oil as a result of oil film flow and ii) reconnection and fluid redistribution within the porous medium, both likely due to  $CO_2$  transfer from the water to the oil phase. Figure 5(a) shows trapped oil in the throats at the end of water flooding and Figure 5(b) shows trapped oil in the throats at the end of CWI which is less than that in water flooding.

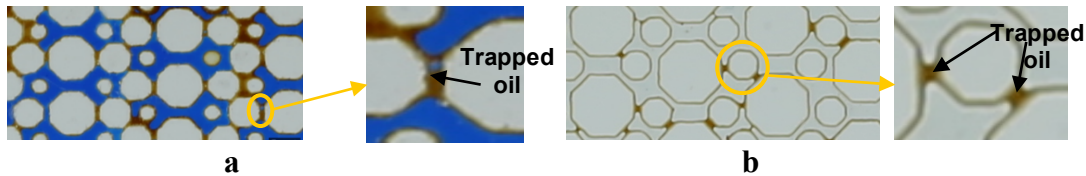


**Figure 5: Trapped oil in throats a) end of water flooding, b) end of CWI, in presence of gravity (magnified section of micromodel)**

## CONCLUSIONS

Based on the CWI pore scale micromodel experiments, the effect of gravity was verified and earlier breakthrough was observed in the presence of gravity. We observed that the distribution of the carbonated water in the micromodel depends on the oil production rate and orientation. Water flooding was shown to break through after CWI under similar conditions but CWI produces more oil after breakthrough. At lower oil production rates, the carbonated water phase sweeps a larger area and results in less residual oil saturation after breakthrough. Pore scale events such as oil film flow and oil entrapment were observed in both water flooding and CWI. It is believed that  $CO_2$  transferred from the water to the oil assisting in trapped oil recovery and film flow for CWI. After the injection of  $\sim 7$  PV, residual oil approached 50% irrespective of orientation or rate for CWI while it was significantly higher for water flooding at 64% residual oil.

## ACKNOWLEDGEMENTS

The authors would like to thank Petroleum Research Newfoundland and Labrador (PRNL), Research and Development Corporation of Newfoundland and Labrador (RDC),

the Natural Sciences and Engineering Research Council of Canada (NSERC), and the Hibernia EOR Research Group for technical and financial support.

## REFERENCES

1. Rossen, W.R. and C. Shen, "Gravity Segregation in Gas-Injection IOR", SPE 107262, SPE Europec/EAGE Annual Conference and Exhibition, United Kingdom, 2007.
2. Stone, H. L., "Simultaneous Water and Gas Flood Design with Extraordinary Vertical Gas Sweep", SPE 91724, SPE International Petroleum Conference, Mexico, 2004.
3. Stone, H. L., "Vertical Conformance in an Alternating Water-Miscible Gas Flood", SPE 11130, 57th Annual Fall Conference and Exhibition, New Orleans, LA, 1982.
4. Skauge, A., "Comparing Core Analysis Data to Field Observation for Gravity Drainage Gas Injection, SCA 9904, Society of Core Analysts Symposium, 1999, Golden Colorado.
5. James P.M., "Summary of Carbon Dioxide Enhanced Oil Recovery (CO<sub>2</sub>EOR) Injection Well Technology", American Petroleum Institute, Annual Report, 2009.
6. Bonnin, E., B. Levallois & G. Joffroy, "Full Field Tertiary Gas Injection, A Case History Offshore Abu Dhabi", Abu Dhabi, SPE 78362, 10th Abu Dhabi International Exhibition and Conference, 2002.
7. Skauge, A., Kristiansen, J.I. & Søgne sand, S., "Laboratory and Field Measurements of Residual Oil Saturation from Gas Injection at the Oseberg Field" paper number 011, proceeding from EAGE, 9th European Symposium on Improved Oil Recovery, Norway, 1997.
8. Craig, F.F. Jr., "A Laboratory Study of Gravity Segregation in Frontal Drives", Trans., AIME, Vol. 210, 275-82, 1957.
9. Sandrea, R. & Nielsen R., "Dynamics of Petroleum Reservoirs Under Gas Injection", Gulf Publishing Company, Book Division, Houston, 1974.
10. Vicente, M., D. Crosta, L. Eliseche, J. Solari and R. Castelo, "Determination of Volumetric Sweep Efficiency in Barrancas Unit, Barrancas Field", SPE 68806, SPE Western Regional Meeting, California, 2001.
11. Chatzis, I, FAL. Dullien, "Dynamic immiscible displacement mechanisms in pore doublets: theory versus experiment", Journal of Colloid and Interface Science 91 (1), 199-222, 1983.
12. Kantzas, A., I. Chatzis, FAL. Dullien, "Enhanced oil recovery by inert gas injection, SPE 17379, SPE/DOE Symposium on Enhanced Oil Recovery, Tulsa, 1988.
13. Sohrabi, M., D.H. Tehrani, A. Danesh, G.D. Henderson, "Visualisation of oil recovery by water alternating gas (WAG) injection using high pressure micromodels- oil-wet & mixed-wet systems", SPE 71494, SPE Journal 9, 290-301, 2004.
14. Riazi, M., Sohrabi, M., and Jamiolahmady, M. "Experimental Study of Pore-Scale Mechanisms of CWI", Transport in Porous Media, 86:73-86, 2011.
15. Martin, J.W. "Additional oil production through flooding with carbonated water. Producers Monthly, pp 13-15, 1951.
16. Dong, Y., C. Ishizawa, E. Lewis and B. Dindoruk, "Carbonated Water Flood: What be Observed in Sand Pack Experiments", SCA2011-34, Austin, Texas, 2011.
17. Mosavat, N. and F. Torabi, "Performance of Secondary Carbonated Water Injection in Light Oil Systems", Ind. Eng. Chem. Res., 53 (3), pp 1262-1273, 2014.
18. Sohrabi, M., Tavakolian, A. Emadi, M. Jami & S. Ireland, "Improved Oil Recovery and Injectivity by Carbonated Water Injection". SCA2012-05, Aberdeen, Scotland, August 2012.

# **A Lattice Boltzmann Approach to Wettability and Rate Effects on Relative Permeability using Digital Core Analysis**

Louis K. Gbayan and Christoph H. Arns  
University of New South Wales, Sydney, Australia

*This paper was prepared for presentation at the International Symposium of the Society of Core Analysts held in Snowmass, Colorado, USA, 21-26 August 2016*

## **ABSTRACT**

Over the last decade digital rock physics has made significant advances in particular with regard to imaging technology including multi-scale imaging. In terms of transport property calculations from tomographic images physical properties related to single component fluids are reasonably well understood when the micro-structure is well resolved. The calculation of relative permeability remains challenging; fluid distributions at partial saturations are often obtained by direct imaging, rather than fluid flow simulation and calculations of relative permeability are carried out on the individual fluid partitions using a single phase lattice Boltzmann method (LBM) when considering systems of significant size. In this paper we use a lattice Boltzmann approach to simulate multi-component flow at typical wettability [1]. We base our simulations on the Shan and Chen lattice Boltzmann model for two phase flow. The degree of wetting was approximated by the contact angle between the wetting and non-wetting phase. We demonstrate the effect of discretization and initial conditions on the pressure field distribution. The Lattice Boltzmann model was validated against literature values for wetting and non-wetting contact angles. After this validation stage, the model was applied to reconstructed Fontainebleau sandstone where we can control image resolution.

## **INTRODUCTION**

The Lattice Boltzmann method (LBM) is known to produce macroscopic behaviour of fluids by simulating the dynamics of particle ensembles on a regular lattice. The local nature of the computations and the easy implementation of boundary conditions make it particularly suitable for simulations on rock micro-structure and for multi-phase flow [2]. Various LBMs have been developed and applied to simulate real life phenomenon in different fields with varying degrees of accuracy and stability [3]. LBM models are known to be limited in their abilities to model fluid dynamics behaviour with regard to density ratios and viscosity ratios [3]. A particular question less researched is the effect of initial fluid distributions on final fluid distributions. Here we implement a Shan and Chen type LBM and a two relaxation time (TRT) approach to improve stability and accuracy.

## SAMPLES AND INITIAL SATURATION

To allow a controlled assessment of initial saturations including discretization effects, we consider in this work a reconstructed Fontainebleau sandstone. This sample has been characterised in detail in [4]. For our simulations we select resolutions of 3.66  $\mu\text{m}$  and 1.83  $\mu\text{m}$ . Initial saturations are set using distance maps; namely the Euclidean distance transform (EDT), the covering radius transform (CRT), and the capillary drainage transform (CDT) [5,6]. We note that distances of EDT and CRT are local to a pore, as opposed to the CDT, which considers the connectivity of the pore space: the CRT assigns each voxel the radius of the largest sphere which can cover it, while the CDT applies the additional condition that this sphere has to be able to intrude from the physical boundary of the sample. The initial saturation distributions for the simulations are given in Fig. 1a-c; a particular saturation is set by applying a radius cut-off on the respective distance map. Here the resulting saturations are very similar, e.g.  $S_w=53.2\%$  for CDT,  $S_w=53.0\%$  for CRT, and  $S_w=53.1\%$  for EDT for the high-resolution discretization. To avoid boundary errors in the calculations, the saturation maps were calculated on double the domain size used for flow calculations and the central  $400^3$  or  $200^3$  region selected and mirrored in flow direction for simulation of fluid flow. In all fluid flow simulations we consider the same field of view, which is  $200^3$  voxels (3.66  $\mu\text{m}$  resolution) or  $400^3$  voxels (1.83  $\mu\text{m}$  resolution) respectively.

## LATTICE BOLTZMANN METHOD

The lattice Boltzmann model is a mesoscopic numerical scheme based on a simple collide and stream algorithm. We use a Shan and Chen type lattice Boltzmann based on various accuracy improving strategies and follow the implementation of [7,2]. The LBM evolution equation is given by

$$f_a^\sigma(\mathbf{x} + \mathbf{e}_a \Delta x, t + \delta t) - f_a^\sigma(\mathbf{x}, t) = f_{eqa}^\sigma(\mathbf{x}, t) - f_a^\sigma(\mathbf{x}, t) / \tau_\sigma \quad (1)$$

with position  $\mathbf{x}$ , time  $t$ , lattice directions  $\mathbf{e}_a$ , distribution function  $f_a^\sigma(\mathbf{x}, t)$ , equilibrium function  $f_{eqa}^\sigma(\mathbf{x}, t)$ , and relaxation time  $\tau_\sigma$ , where  $\sigma$  denotes the fluid components. The equilibrium equation above is solved using the formulation below:

$$f_a^\sigma(\mathbf{x}, t) = w_a \rho^\sigma \left[ 1 + \mathbf{e}_a \cdot \frac{\mathbf{u}_\sigma^{eq}}{c_s^2} + \frac{(\mathbf{e}_a \cdot \mathbf{u}_\sigma^{eq})^2}{2c_s^4} - \frac{(\mathbf{u}_\sigma^{eq})^2}{2c_s^2} \right] \quad (2)$$

with equilibrium velocity  $\mathbf{u}_\sigma^{eq}$ . The macroscopic quantities of mass and velocities are calculated directly from there microscopic ones as:

$$\rho^\sigma = \sum_a f_a^\sigma \quad , \text{ and} \quad (3)$$

$$\rho^\sigma \mathbf{u}_\sigma^{eq} = \sum_a f_a^\sigma \mathbf{e}_a \quad . \quad (4)$$

Here  $\rho^\sigma$  is the density of component  $\sigma$ . Further implementation details can be found in [7,2]. We apply a half way bounce back boundary condition at the solid-fluid boundary. At the inlet and outlet, we mirror our image to achieve periodicity. Given the periodicity

of our domain, we apply a body force according to [7] to force each fluid. The definition of the adhesion/cohesion forces also follows [7,2]. The actual values are reported in the Figure captions.

To improve accuracy and stability of our LBM implementation, we use the TRT method as a special case of a multi-relaxation time (MRT) LBM. In the MRT relaxation rates are considered a diagonal matrix and are typically optimized for stability, conserved quantities, and accuracy. In the two relaxation time approach, the matrix reduces to two relaxation rates. Symmetric moments are relaxed with a particular choice of relaxation parameters and anti-symmetric ones are relaxed with a different one [8-10]. The optimization of these relaxation rates is not trivial particularly in a 2-phase flow simulation. It has been shown in [8] that the product of these relaxation times in the TRT  $(1/s^+ - 1/2) \times (1/s^- - 1/2)$  depends on the heterogeneity of the sample structure.

## RESULTS AND DISCUSSION

Figure 2 depicts high-resolution simulations of fluid distribution evolutions from three different initial saturation conditions set by the CDT, CRT, EDT respectively. Initial saturations across the whole domain are comparable. Two different contact angles of  $\theta = 76.8^\circ$  and  $\theta = 35.0^\circ$  are considered. The latter values is given in [1] for the case of water-wet Bentheimer sandstone, which is like Fontainebleau a rather clean water-wet sandstone. For contrast we added the case of high contact angle. Comparing the initial conditions (Fig. 1) to the LBM saturation evolution, it is clear that fluid configurations after 20,000 iterations are close to the initial conditions for the CDT and CRT. The EDT condition is less stable and approaches a saturation distribution similar to the CRT. We consider this a result of the local definition of distances (ordinary percolation) compared to the invasion percolation represented by the CDT. Furthermore, the EDT may initially provide good connectivity of both phases, while at the same time the sharp angles of the initial fluid distribution are unphysical. Comparing the rows [a-c] and [d-f] in Figure 2, we notice the clear difference in contact angle. It is apparent that the establishment of curvatures obeying contact angle settings in the simulation is relatively fast compared to approaching global equilibrium saturations—e.g., we expect that at equilibrium Fig.2d-f would show the same fluid saturation distribution, while actually after 20,000 iterations the initial saturation distribution is still visible. To explore resolution effects and consider longer simulation times, we reduced the lattice resolution by a factor of two in Figure 3. Time step  $N=10,000$  in Figure 3.a corresponds to  $N=20,000$  in Figure 2d-f. There is excellent agreement with local fluid distributions at this discretization level. Figure 3 illustrates that the convergence to global equilibrium fluid distributions is slow. It is noticeable that the fluid distributions are converging from  $N=0$  (initial condition) to  $N=80,000$ ; an order of magnitude step would be required to actually equilibrate fluids fully. We tested a further reduction in resolution to speed up the simulation. At that discretization level the evolution of fluid distributions diverged significantly with simulations at higher resolution.

## CONCLUSION

We presented an implementation of a multi-relaxation time (MRT) method, which was applied for the particular case of two relaxation times (TRT). Multiple fluid distributions for initialisation of the simulations were considered. It is clear that initial fluid distributions have a strong impact on the fluid evolution pattern. In particular, there is a very pronounced difference in initial conditions between CDT and CRT. Initialisation using the EDT appears to be similar to the CRT and also has little physical basis, thus may be discarded. In the future we will be extending the current MRT LBM to include free energy and colour gradient approaches. It is clear that application of the LBM technique to heterogeneous porous media would require high stability and computational efficiency at the same time to address representative volumes. A different route may be the combination of micro-CT fluid distribution imaging with LBM fluid relaxation techniques e.g. to consider contact angle changes and their influence on petrophysical properties.

## ACKNOWLEDGEMENTS

CHA acknowledges the ANU/UNSW Digital Core Consortium, the Australian Research Council (ARC) for a Future Fellowship, and the National Computing Infrastructure for generous allocation of computing time.

## REFERENCES

1. T. Ramstad, P.E. Oren, S. Bakke, 2009, *Society of Petroleum Engineers*, SPE124617.
2. H. Huang, L. Wang, X-Y. Lu, 2011, *Comput. Math. Appl.*, **61**, 3606-3617.
3. E.S. Boek, M. Venturoli, 2011, *Comput. Math. Appl.*, **59**, 2303 – 2314.
4. D.E. Latief, B. Biswal, U. Fauzi, R. Hilfer, 2010, *Physica A*, **389**, 1607-1618.
5. M. Hilpert, C. T. Miller, 2001, *Adv. Wat. Res.*, **24**, 243.
6. C.H. Arns, M.A. Knackstedt, N.S. Martys, 2005, *Phys. Rev. E*, **72**, 046304.
7. N.S. Martys, H. Chen, 1996, *Phys. Rev. E*, **53**(1), 743-751.
8. L. Talon, D. Bauer, N. Gland, S. Youssef, H. Auradou, I. Ginzburg, 2012, *Wat. Res. Res.*, **48**(4), W04526.
9. A. Kuzmin, I. Ginzburg, A.A. Mohammed, 2011, *Comput. Math. Appl.*, **61**, 3417-3442.
10. I. Ginzburg, F. Verhaeghe, D. d'Humières, 2008, *Comm. Comp. Phys.*, **3**(2) 427-478.

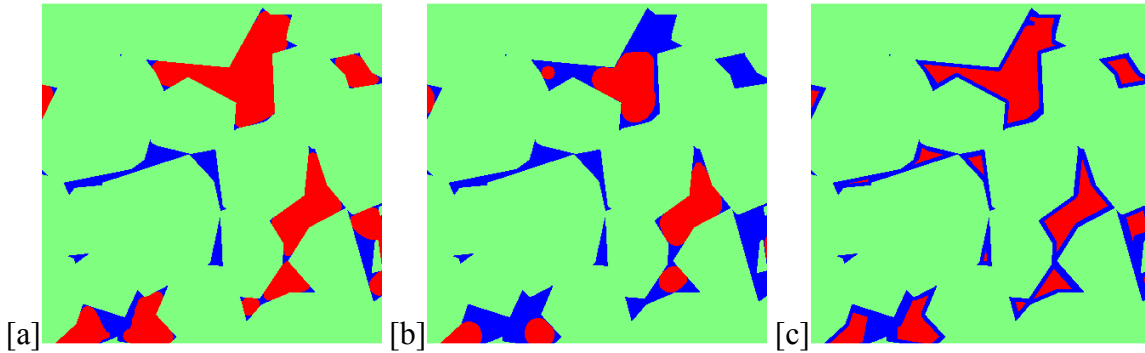


Fig.1: Slices through the initial saturation conditions for simulations on reconstructed Fontainebleau sandstone (subvolumes of  $400^3$  voxel). [a] Capillary drainage transform ( $S_w=53.2\%$ ), [b] covering radius transform ( $S_w=53.0\%$ ), [c] Euclidean distance map ( $S_w=53.1\%$ ). Saturations are given for the full domain.

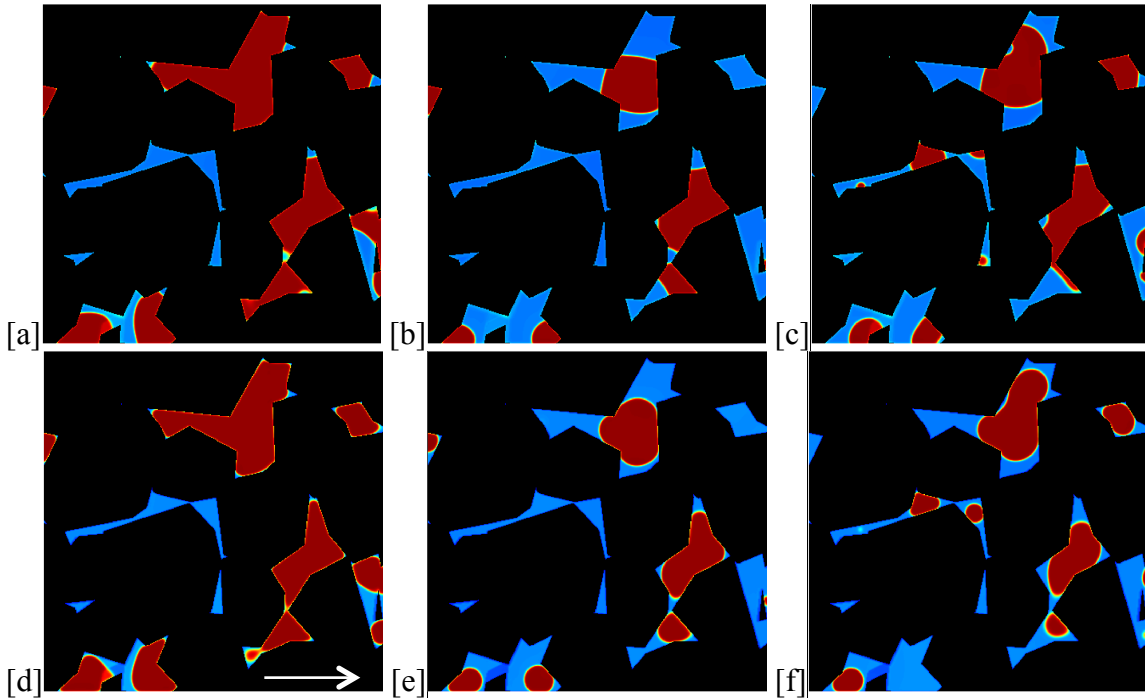


Fig.2: Slices through the density map of component one for LBM TRT simulations on reconstructed Fontainebleau sandstone corresponding to Fig. 1 (mirrored simulation domain  $800 \times 400 \times 400$ ). Depicted are saturations after 20,000 iterations. [a-c]:  $G_a = \pm 0.1$  corresponding  $\theta = 76.8^\circ$ . [d-f]  $G_a = \pm 0.3769$  corresponding  $\theta = 35.0^\circ$ ,  $G_c = 1.35$ ,  $\rho_{\text{initial}} = 4/3$  in the fluids and  $0.04$  of  $\rho_{\text{initial}}$  in the opposite fluid phase;  $\tau_i = 1$  where  $i=1,2$  are the fluid components,  $F_a = \rho_{\text{initial}} \cdot 10^{-5}$  for both fluids in x-direction (white arrow).

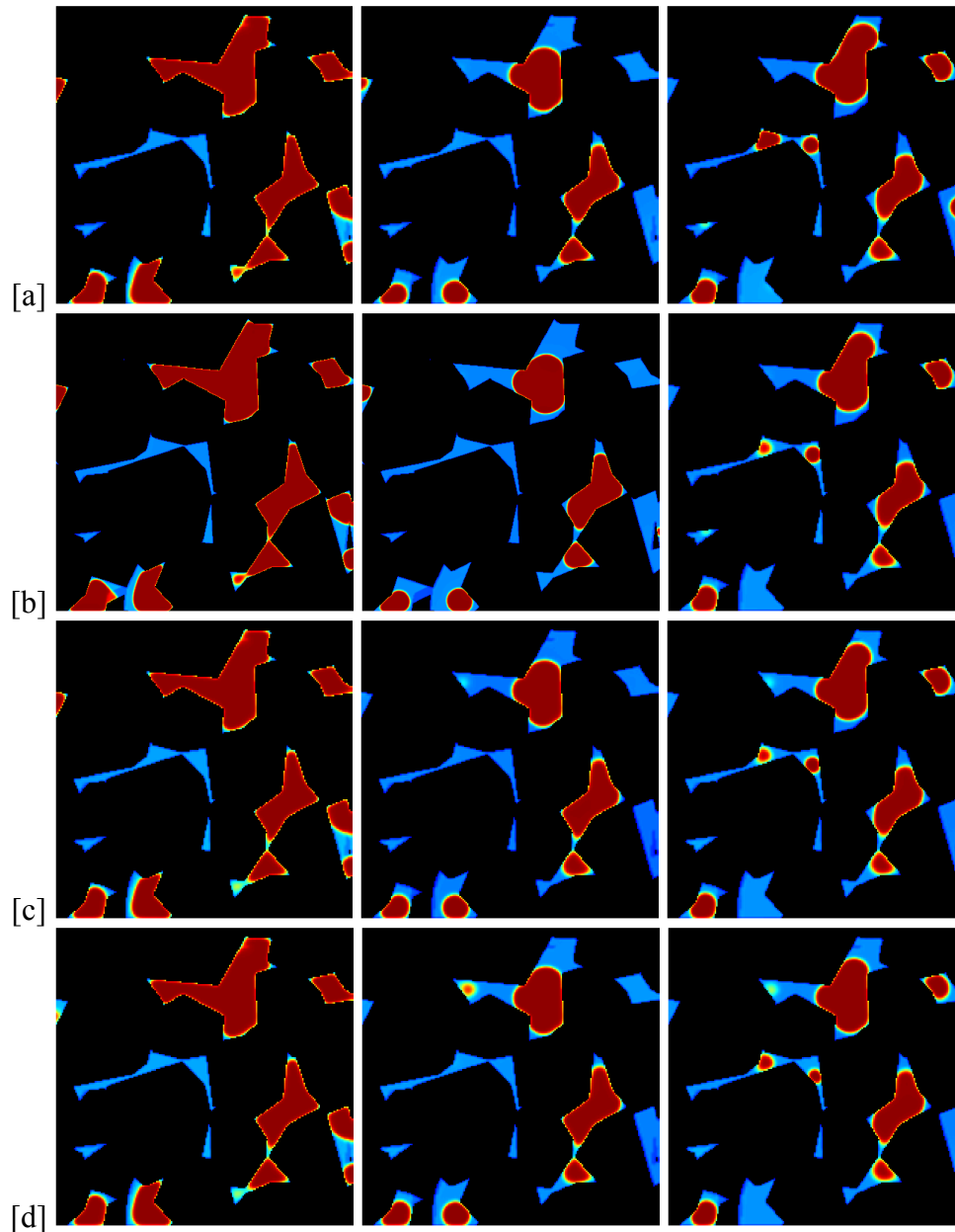


Fig.3: Slices through a time series of density maps with the same initial conditions as Fig. 2 at reduced resolution, but identical field of view (simulation domain  $400 \times 200 \times 200$ ). *Left column*: initialisation by capillary drainage, *middle*: initialisation by covering radius, *right*: initialisation by Euclidean distance. Each row corresponds to a particular number of  $N$  iterations. [a]:  $N=10,000$  (see corresponding time-step  $N=20,000$  in Fig.2d-f), [b]:  $N=20,000$ , [c]:  $N=40,000$ , [d]:  $N=80,000$ . Physical properties are as in Fig. 2, [d-f].

## **Hydrogen Index measurements of highly saline brines under pressures up to 15'000 psi and temperatures up to 300°F**

S. A. Hertel, B. C. Anger, K. Smith, M. Appel  
Shell Exploration and Production Inc., Shell Technology Center, 3333 Highway 6 South,  
Houston, TX 77082

*This paper was prepared for presentation at the International Symposium of the Society of Core Analysts held in Snowmass, Colorado, USA, 21-26 August 2016*

### **ABSTRACT**

The Hydrogen Index is routinely used as a calibration factor for NMR porosity measurements in hydrocarbon reservoirs. It accounts for the reduced density of hydrogen atoms in the different pore fluids present in the porous reservoir rock. In this contribution we present an experimental setup which allows one to measure Hydrogen Indices of brines and other chemicals under reservoir conditions. The experimental data for NaCl brines agrees with a recently published density model within experimental uncertainty of  $\pm 0.5\%$ . The model and experimental data show that the Hydrogen Index of NaCl brines can be reduced by up to 17%. Thus, failure to account for this effect may lead to unacceptable underestimations of porosity in certain hydrocarbon reservoirs.

### **INTRODUCTION**

Nuclear Magnetic Resonance (NMR) has been utilized in research laboratories of the hydrocarbon industry almost since its discovery by Bloch (1) and Purcell (2). During the 1990s NMR logging tools for downhole porosity and permeability measurements were established as standard tools for reservoir characterization (3). One essential calibration factor for the calculation of accurate porosity values from NMR data is the Hydrogen Index (HI). It accounts for the different densities of hydrogen nuclei in dependence of the pore fluid types (4; 5). Several studies were concerned with measuring the Hydrogen Indices of gases and live crude oils under reservoir conditions (6; 7). For brines it was pointed out that the Hydrogen Index can deviate substantially from unity at high salinities at standard temperature and pressure (4). For an estimation of the impact of such deviations, consider a formation porosity of 25% fully saturated with brine having a Hydrogen Index of 0.85. If the HI was wrongly assumed to be unity, the porosity of this formation would be under estimated by 4.4 porosity units. One common approach to calculate the HI of the brines under reservoir conditions is to use brine density data from thermodynamic tables such as ref. (8). However, empirical brine density models may prove to integrate more seamlessly into reservoir evaluation workflows. In this contribution we present an apparatus and measurements to validate a recently published density model as a tool to predict the HI of brines over a wide range of temperatures, pressures and salinities (9). At the same time the measurements were used to benchmark the equipment for future experiments involving more complex fluids and oversaturated brines.

## BACKGROUND

NMR logging tools are primarily sensitive to the nuclear magnetization of the hydrogen nuclei  $^1\text{H}$  of the formation fluids (10). The magnetization is given by the Curie law for spin-1/2 systems

$$M = \frac{N\gamma^2 \hbar^2 B_0}{4kT}, \quad (1)$$

where  $\gamma$  denotes the gyro-magnetic ratio,  $B_0$  is the magnetic field strength,  $k$  is Boltzmann's constant and  $T$  is the temperature in Kelvin. The number of spins  $N$  in the sensitive region is itself proportional to the number of hydrogen atoms per fluid molecule  $N_H$  as well as the density  $\rho(p, T)$  of the investigated fluids i.e.

$$N \propto \rho(p, T)N_H, \quad (2)$$

where  $p$  is the pressure. For NMR porosity measurements the Hydrogen Index is a convenient factor to account for the dependence given by eq. 2 relative to pure  $\text{H}_2\text{O}$  at Standard Temperature and Pressure (STP). Therefore, the Hydrogen Index is given by

$$\begin{aligned} HI &= \frac{\text{Amount of hydrogen in sample}}{\text{Amount of hydrogen in pure water at STP}} \\ &= \frac{\text{moles H} / \text{cm}^3}{0.111} \\ &= \frac{\rho(p, T)N_H/M}{0.111}. \end{aligned} \quad (3)$$

Here,  $M$  denotes the molecular weight of the pore fluid under study. In practice the NMR tool is immersed in a water tank at STP ( $T = 68^\circ\text{F}$ ,  $p = 14.5$  psi) before each logging run. In the water tank a reference signal is acquired. Thereafter, the NMR logging tool is lowered into the borehole, where the sensitive region of the tool extends into the porous rock of the hydrocarbon reservoir. The NMR signal amplitude is then reduced compared to the reference signal, since the rock matrix itself is NMR silent. In this case the ratio of the signal amplitude of the pore fluids to the reference signal amplitude is proportional to the porosity (10). Several calibrations have to be applied to account for the temperature and pressure difference between STP and the reservoir conditions. These differences affect the magnetization of the fluids as well as the electronic characteristics of the NMR tool (10). It can be seen from eq. 3 that with the knowledge of the density of the brine and the molality of the salts, one may calculate the Hydrogen Index. For this work, the model for brine densities of Mao and Duan (9) was chosen. The range of validity of this model for NaCl is  $T = 31.7^\circ\text{F} - 517.7^\circ\text{F}$  and  $p = 14.5$  psi - 14,500 psi. The brine density  $\rho$  is given by (9)

$$\rho = \frac{(1000 + mM_s)\rho_{\text{H}_2\text{O}}}{m v(m)}, \quad (4)$$

where  $m$  is the molality of salts (LiCl, NaCl, KCl, MgCl<sub>2</sub>, CaCl<sub>2</sub>, SrCl<sub>2</sub>, BaCl<sub>2</sub>) and  $M_s$  is the molar mass of the chlorides.  $\rho_{\text{H}_2\text{O}}$  is the density of pure water at the particular pressure  $p$  and temperature  $T$  and is calculated from the equations of the International Association for the Properties of Water and Steam (11). The specific solution volume  $v(m) = V(m)/m$  is given by

$$v(m) = \frac{V(m_r)}{m_r} + \frac{1000}{\rho_{\text{H}_2\text{O}}} \left( \frac{1}{m} - \frac{1}{m_r} \right) + v|z_+z_-|A_V[h(I_m) - h(I_{m_r})] + 2v_+v_-mRT[B_V(m - m_r) + v_+z_+mC_V(m^2 - m_r^2)], \quad (5)$$

where  $z_+$  and  $z_-$  are the charge of the cation and anion, while  $v_+$  and  $v_-$  are the number of cation and anion charges, respectively, and  $v = v_+ + v_-$ .  $A_V$  is the volumetric Debye-Hückel limiting law slope which can be found in ref. (12). Furthermore,  $I$  denotes the ionic strength  $I = 0.5 \sum_i m_i z_i^2$  and  $h(I)$  is given by  $h(I) = \log_{10}(1 + 1.2I^{0.5})/2.4$ . The reference solution volume  $V(m_r)$  and the second and third virial coefficient  $B_V$  and  $C_V$  are given by empirical polynomials in pressure  $p$  and temperature  $T$ . The equations and the involved coefficients for  $V(m_r)$ ,  $B_V$  and  $C_V$  can be found in Mao and Duan (9). For the case of NaCl the model has an average deviation from the published experimental data of  $\pm 0.025\%$ , while the experimental data considered in ref. (9) themselves have a relative uncertainty ranging from 0.001% to 0.1%.

## EXPERIMENTAL

Experiments were conducted with an Oxford Instruments GeoSpec 2 NMR spectrometer with a proton Larmor frequency of  $\nu = 2.3$  MHz and a RF-coil of diameter  $d = 53$  mm. Other NMR parameters were the duration of the 90° RF-pulses of  $p_{90} = 14.25 \mu\text{s}$ , the recycle delay of  $t_{\text{RD}} = 20$  s and the number of scans of  $NS = 128$ . The maximum signal amplitude was obtained by using the magnitude of the first data point of the Free Induction Decays (FIDs). Furthermore, the dead time before detection started was increased to  $100 \mu\text{s}$  to exclude spurious <sup>19</sup>F signals from the heating vessel.

A sketch of the custom built heating vessel is shown in Figure 1. From the top, one may see the high pressure tubing ( $OD = 1/8''$ ) that delivered pressures up to  $p_{\text{max}} = 12'000$  psi provided by a Quizix QX pump (Chandler Engineering Inc). The tubing was connected to a ceramic pressure vessel (Daedalus Innovations, LLC). The ceramic pressure vessel was immersed in Fluorinert FC-70 inside a PEEK container. The FC-70 was heated to temperatures of  $T_{\text{max}} = 300^\circ\text{F}$  in a closed loop by means of a recirculation pump (Core Laboratories Inc). During the experiments at  $T = 68^\circ\text{F}$  the recirculation pump was replaced by a thermostat in order to cool the FC-70 and to achieve a smaller temperature variation compared to the recirculating pump. In order to prevent the NMR magnet from heating beyond its preset value of  $95^\circ\text{F}$ , a cooling loop made of Teflon tubing was wound around the outside of the PEEK vessel and cold Fluorinert FC-72 was pumped continuously through the cooling loop. In addition, cold air was blown through the spectrometer bore to dissipate any remaining heat from the PEEK container. The

assembly was lowered into the NMR spectrometer using a translation stage. The temperature of the FC-70 was continuously recorded by a thermocouple at the bottom of the PEEK vessel and a variation of  $\pm 2^\circ\text{F}$  was observed over the entire duration of each experiment. However, a temperature gradient may have established between the FC-70 and the inside of the ceramic pressure vessel especially at elevated temperatures. A temperature difference of  $\pm 10^\circ\text{F}$  would contribute a relative uncertainty in the HI values of  $\pm 2\%$  due to the polarization correction with the factor  $T_{exp}/T_{ref}$  (Curie law eq. 1).

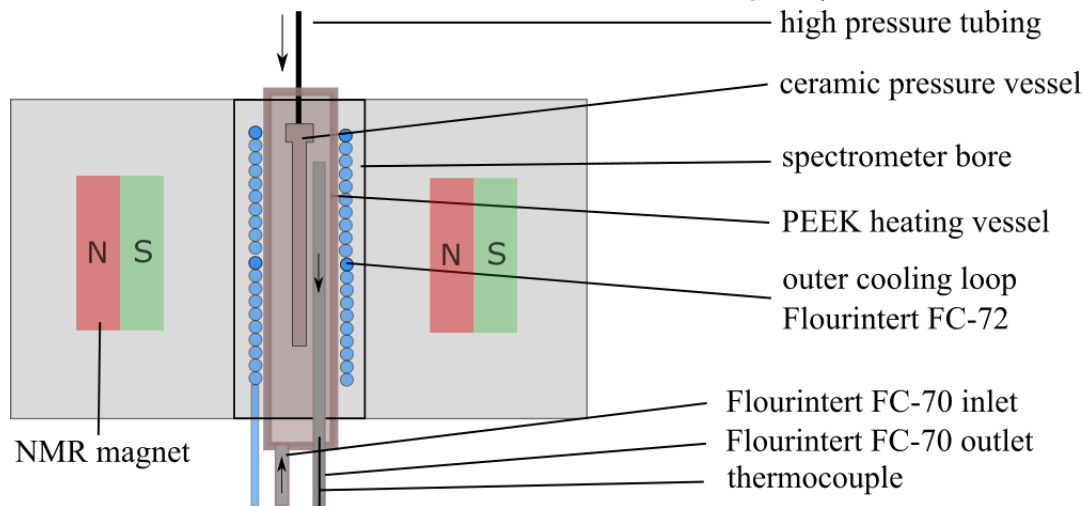


Figure 1: Sketch of the PEEK heating vessel inside the NMR spectrometer.

Six different brines were prepared with salinities of  $c_s = (47, 90, 130, 170, 200, 230, 260)$  kppm. All brines were prepared by mixing pre-calculated weight fractions of NaCl salt and pure  $\text{H}_2\text{O}$ . The salinity has been double checked using a pycnometer and comparing the measured brine densities with corresponding salinity values (8).

## RESULTS

The NMR reference signal was measured with degassed tap water at STP. Note that de-ionized water exhibited a too long relaxation time  $T_1$  making the required experimental time forbiddingly long. Figure 2 shows the predicted versus measured Hydrogen Indices for pure water and the six brines with increasing salinities. The solid line is given by evaluating eq. 9, while the dashed line is given by published values (4). The experimental data and the predicted values agree within the experimental uncertainty of  $\pm 0.5\%$ . The primary source of uncertainty for these measurements is the signal-to-noise ratio of the NMR time domain data. It can be seen that with increasing salinity the HI of NaCl brines is reduced by up to 11%, consistent with published values (4). There is a difference of no more than 0.5% between the density model (solid line) and the published data from ref. (4) (dashed line) at salinities around 100 kppm. The reason for this difference is currently unknown since the equations used to calculate the results of ref. (4) were not explicitly stated.

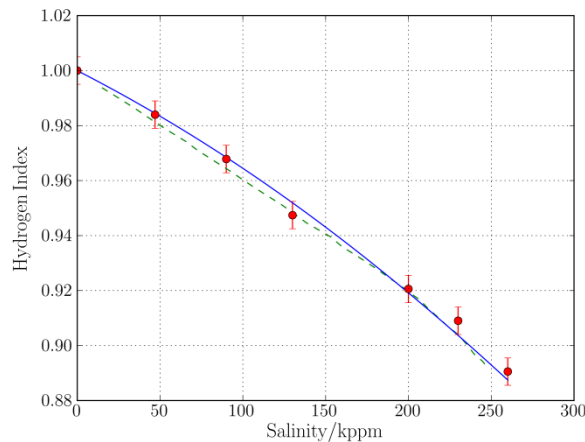


Figure 2: Plot of the Hydrogen Index versus salinity. Comparison of measured data (dots) with values predicted by the brine density model (solid line) and values taken from Kleinberg and Vinegar (4) (dashed line).

Figure 3a shows the Hydrogen Index as a function of temperature  $T$  for pure  $H_2O$  and for saturated brine with salinity of  $c_s = 260$  kppm, while the pressure was fixed at  $p = 5000$  psi to prevent the fluids from boiling.

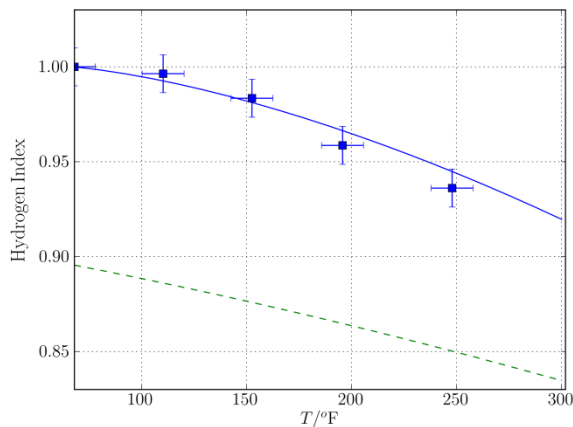


Figure 3a: Hydrogen Index versus temperature  $T$  at  $p = 5000$  psi. Calculated values of HI for pure  $H_2O$  (solid line) are compared to HI for brine with salinity of  $c_s = 260$  kppm (dashed line). Measured values for tap  $H_2O$  (squares).

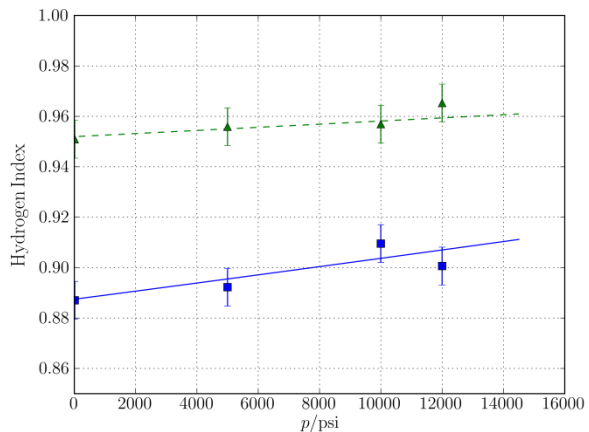


Figure 3b: Hydrogen Index versus pressure at  $T = 68^\circ F$ . Calculated values for brine with salinity of  $c_s = 260$  kppm (solid line) and measured values (squares) are compared to a brine with salinity of  $c_s = 130$  kppm (dashed line) and corresponding measured values (triangles).

The measured signal was corrected by the ratio  $T_{exp}/T_{ref}$  to account for the difference in polarization due to the Curie law given by eq. 1. The experimental data agrees with the calculated values within the relative uncertainty of  $\pm 2\%$ . The higher uncertainty is a result of the higher variation of temperature  $T$  when using the recirculating pump as compared to the thermostat and the corresponding correction using the Curie law (eq. 1). The curve of  $H_2O$  (solid line) and saturated brine (dashed line) are offset due to the

salinity effect. It is interesting to note that the HI for saturated brine is reduced to  $HI = 0.83$  at  $T = 300^\circ\text{F}$ , a 17% decrease as compared to  $\text{H}_2\text{O}$  at STP.

Figure 3b shows the HI as a function of pressure for two brines of salinities  $c_s = 260$  kppm (solid line) and  $c_s = 130$  kppm (dashed line) at a temperature of  $T = 68^\circ\text{F}$ . It can be seen that the effect of pressure on the HI is an increase of a moderate 2% over the entire pressure range of  $p = 14.5$  psi to  $p = 14,500$  psi, which is a result of the increased fluid density. A similar change of about 2% can be observed for temperatures above  $T = 68^\circ\text{F}$  (not shown). Thus, temperature and salinity of the investigated brines are the dominating effects that have to be accounted for when considering a Hydrogen Index calibration of NMR logging data.

## CONCLUSION

It was shown that the experimental setup presented in this contribution can reliably measure the Hydrogen Index of brines over a wide range of pressures and temperatures. Additionally, the brine density model may be utilized to predict the HI for NaCl brines and thus can be implemented in reservoir evaluation workflows. It remains to be evaluated whether the model can be utilized to calculate the HI of brines involving mixtures of LiCl, KCl,  $\text{MgCl}_2$ ,  $\text{CaCl}_2$ ,  $\text{SrCl}_2$  and  $\text{BaCl}_2$ . However, it may be necessary to experimentally determine the HI of more complex fluids and chemicals for which the setup has been shown to deliver sufficiently accurate results.

## ACKNOWLEDGEMENTS

We would like to acknowledge the management of Royal Dutch Shell plc. for allowing the release of these research results.

## REFERENCES

1. Bloch, F., Hansen, F. F., and Packard, M., *Physical Review* (1946), **70**, 474.
2. E. M., Torrey, H. C., and Pound, R. V. *Physical Review*, (1946), 37-38.
3. Kleinberg, R. L., Jackson, J. A., Brown, R. J. S., Chandler, R., Miller, M. N., Paltiel, Z., Prammer, M. G., *Concepts in Magnetic Resonance*, (2001), **13**, 340-411.
4. Kleinberg, R. L. and Vinegar H. J., *The Log Analyst*, (1996), 20-32.
5. Appel, M., *SPWLA Petrophysics*, (2004), **45**, 296-307
6. Zhang, Q., Lo, S. L., Huang, C. C., Hirasaki, G. J., Kobayashi, R., and House, W. V. *39th Annual Logging Symposium: SPWLA*, (1998)
7. Appel, M., van Dijk, N.P., Freeman, J.J., Perkins, R.B. Dallas, *SPWLA Annual Conference and Exhibition* (2000)
8. Weast, R.C., [ed.]. *CRC Handbook of Chemistry and Physics*, Boca Raton, Florida: CRC Press, (1982), D232-D233.
9. Mao, S., Duan, Z., *The Journal of Chemical Thermodynamics*, (2008) **40**, 1046–1063
10. Coates, G. R., Xiao, L., Prammer, M. G. *Halliburton Energy Services*, (1999)
11. Wagner, W., Cooper, J. R., *J. Eng. Gas Turbines & Power*, (2000) **122**, 150-182.
12. Bradley, D.J., Pitzer, K.S., *J. Phys. Chem.*, (1979), 1599-1603

## **EFFECT OF POROSITY CHANGES ON COMPLEX ELECTRICAL CONDUCTIVITY IN SHALY SANDS**

Frank Börner (Technical University Berlin)

Edith Müller-Huber (Technical University Berlin)

*This paper was prepared for presentation at the International Symposium of the Society of Core Analysts held in Snowmass, Colorado, USA, 21-26 August 2016*

### **ABSTRACT**

The investigation is focused on the determination of compaction of heterogeneous shaly sands. Measurements of the complex electrical rock conductivity in the frequency range from 0.05 Hz to 1 kHz are presented in order to quantify the porosity reduction in shaly sands during the step-wise compression of the samples. The measurements were carried out with a specially designed measuring cell. Overall, 10 unconsolidated shaly sand samples with varying grain size distribution were analyzed. The measured complex conductivity data of the fully water saturated samples show two co-occurring effects:

(1) Real part decreases due to the dominating Archie's law.

(2) Imaginary part increases due to the increasing contribution of interface conductivity.

The effects of compaction observed may be explained using a simple complex conductivity model that relates porosity, surface area and accompanied parameters to conductivity components. The surprisingly significant increase of the imaginary part with decreasing porosity is caused by the increase of internal surface area-to-porosity-ratio. Significance of the effect seems to depend on the cementation exponent and the porosity range under consideration. The proposed interpretation algorithm allows the determination of relative porosity variation, from a base line measurement and a single repeat measurement without knowledge of further rock characteristics, which is associated with changes of compaction and hence changes of hydraulic permeability.

### **INTRODUCTION**

Pore space properties of sedimentary rocks are of general interest for reservoir evaluation but also for special geotechnical applications. Verification and monitoring of slight porosity changes are essential for controlling processes like, e.g., the compaction by pressure drawdown in weakly consolidated reservoirs, the stimulation effects for productivity enhancement of reservoirs, or the compaction of building ground. It is well known that electrical resistivity or conductivity are closely connected with pore space geometry and are very sensitive to slight changes of pore space characterizing parameters.

The degree of compaction characterizing parameters, like porosity, pore or grain size distribution and bulk density, is commonly used for modelling fluid flow but increasingly frequently also e.g. for simulation of geotechnical stability of reservoirs, dams and embankments. A special problem is the determination of naturally or artificially induced porosity changes and accompanied changes of permeability or compaction in very heterogeneous sedimentary rocks. Electrical rock properties can provide valuable

information on porosity change. However, due to various petrophysical influences on electrical rock properties, the attempt to convert electrical conductivity variations into variations of porosity or the degree of compaction often leads to ambiguous results.

Complex electrical conductivity is sensitive to the size of the mineral-water-interface at the grain surfaces and hence, together with porosity, sensitive to changes in pore space geometry. Complex electrical measurements in the low frequency range provide besides conductivity also information on the electrical capacity and relaxation of charge carriers in the pore space. Therefore, complex measurements can reduce the petrophysical ambiguity caused by the influence of textural and state properties.

Complex conductivity phenomena and measuring techniques are reviewed by, e.g. [1], [2] or [3]. [4] presented an overview of the properties and state conditions which influence complex conductivity spectra. The complex electrical properties of shaly sands were investigated e.g. by [5] or [6]. Recently [7], [8] and [9] focused their research on unconsolidated material as well as on the dependency of complex interface conductivity on salinity, pH-value or temperature ([10], [11], [12]). Another topic is the investigation of textural effects on hydraulic and electrical conductivity of sedimentary rocks ([13], [14]) or unconsolidated sediments ([15]) due to a variation in pore radii ([13]). According to our knowledge, the effect of porosity change, especially porosity reduction, on complex interface conductivity was not yet explicitly investigated.

## FUNDAMENTALS

The complex conductivity  $\sigma^* = \sigma' + i\sigma''$  of a water-saturated shaly sand consists of a real electrolytic conductivity  $\sigma_{el}$  and a complex interface conductivity  $\sigma_{if}^* = \sigma'_{in} + i\sigma''_{in}$  (e.g. [5], [6], [9]), if water is the wetting fluid. When oil wets the rock matrix, interface conductivity is insignificant. The key question is to find an applicable parameter model to relate  $\sigma_{el}$ ,  $\sigma'_{in}$  and  $\sigma''_{in}$  to pore space characterizing parameters such as, e.g. formation factor  $F$ , surface area-to-porosity-ratio  $S_{POR}$  and compaction. If frequency dependence is negligible, then the following approach for  $\sigma'$  and  $\sigma''$  is applicable in the low frequency range (e.g. [5], [10], [16]):

$$\sigma' = \sigma_{el} + \sigma'_{in} = \sigma_w / F + f(\sigma_w)S_{POR} / F \quad (1a)$$

$$\sigma'' = \sigma''_{in} = lf(\sigma_w)S_{POR} / F \quad (1b)$$

The real part  $\sigma'$  consists of the Archie-component  $\sigma_{el}$  and the real part of interface conductivity  $\sigma'_{in}$ . The imaginary part  $\sigma''$  equals the imaginary part of interface conductivity  $\sigma''_{in}$ . The model is applicable to shaly as well as to clean sands.  $F$ , for purposes of simplicity, is the same formation factor for all conductivity components,  $f(\sigma_w)$  is a general function considering salinity and pH dependence of interface conductivity dependent on surface charge density and ion mobility in the interface region, and  $l$  is the ratio between real and imaginary part of interface conductivity that is assumed to be nearly independent of salinity and varies only slightly with porosity changes.

Recently, the model approach was modified and/or further developed by [7], [10], [11], [17] and others.

All electrical conductivity contributions in equations (1a) and (1b) are dependent on porosity  $\Phi$ . While the porosity dependence on the electrolytic conductivity in equation (1a) is well known according to the Archie-equation  $F = \Phi^{-m}$  ([18]), the relationship between interface conductivity and porosity in equations (1a) and (1b) is less thoroughly investigated. Based on equations (1a) and (1b) and  $S_{POR} = S_m d_m (1 - \Phi) / \Phi$  ( $S_m$  – surface area per mass,  $d_m$  – grain density), a dependency of interface conductivity components  $\sigma'_{in}$ ,  $\sigma''_{in}$  on porosity is expected in the form of

$$\sigma'_{in}, \sigma''_{in} \propto (1 - \Phi) \Phi^{m-1}. \quad (2)$$

This means that a porosity variation of a given rock sample with fixed specific surface area  $S_m$  results in a change of  $S_{POR}$  and consequently in a variation of the interface conductivity. Fig. 1 shows how interface conductivity depends on porosity, on the size of cementation exponent  $m$ , and on the related porosity range. The calculated curves show significant differences of the porosity effect on interface conductivity for unconsolidated and consolidated rocks, respectively.

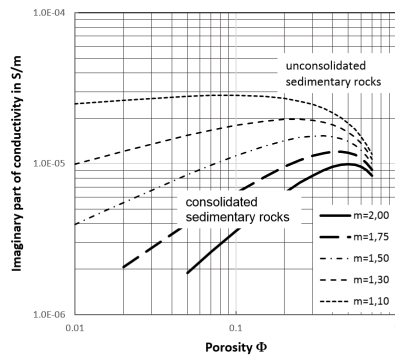


Fig. 1: Calculated curves imaginary part of conductivity vs. porosity for different cementation exponents  $m$ .

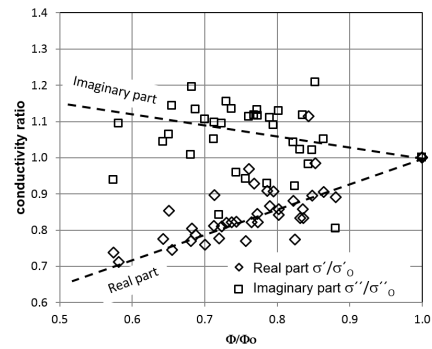


Fig. 2: Imaginary part and real part of complex conductivity vs. porosity (normalized on initial state).

## MATERIAL AND METHODS

The relationship between porosity alteration and complex conductivity has been analysed using a series of 10 different unconsolidated shaly sand samples. The mean grain diameter ranges from 0.15 to 1.35 mm. The samples were saturated with NaCl-solution of conductivities between 0.05 S/m and 0.1 S/m at 25°C. The samples were set up in a cylindrical cell with 30 mm diameter and 80 mm length. Complex conductivity was measured with a 4-electrode laboratory system (electrodes made from platinized platinum mesh or wire, respectively) in the frequency range 0.05 Hz to 1 kHz. Data acquisition and data processing was similar to that proposed by [4]. Measurements were carried out at atmospheric pressure and 25 °C. The cell was installed at a tabletop vibrator to produce a step-wise compaction of the sample. The porosity reduction was determined measuring the decrease of sample length and volume of emitted pore water. Porosity reduction was in the order of up to 10%. During compaction the pore water conductivity remained

unchanged. For comparison, data of 8 shaly sandstone samples from [6] were incorporated, which have various porosities but similar specific surface areas  $S_m$ .

### RESULTS

The expected increase of imaginary part with decreasing porosity or compaction, respectively was found experimentally. All experimental data (real as well as imaginary part), normalized on values for initial porosity  $\Phi_0$ , are plotted in Fig. 2. The high error of the imaginary part may be caused by a slight instability of the grain package and additional weak changes in pore water conductivity. Experimental results of selected unconsolidated shaly sand samples are plotted in Fig. 3 together with calculated curves of  $\sigma''=f(\Phi)$ . Curve parameter is  $S_m$  while  $m=const.=1.3$ . The shaly sandstones with only slightly varying  $S_m$  show the different behaviour of consolidated rock with lower porosities and a high cementation exponent (Fig. 4). The model curves were calculated for different  $S_m$  but fixed  $m=2$ .

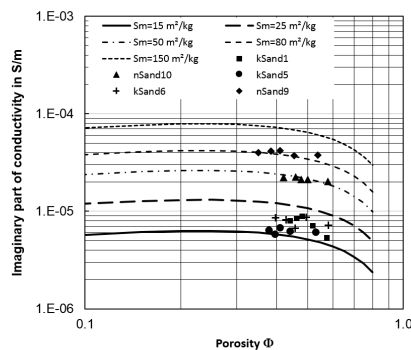


Fig. 3: Unconsolidated shaly sands – imaginary interface conductivity vs. porosity.

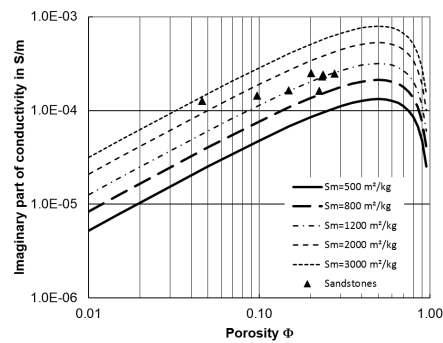


Fig. 4: Shaly sandstones – imaginary part of conductivity vs. porosity.

Imaginary interface conductivity calculated with a modified capillary tube model (see [13] or [15]) indicates that compaction of sediments leads to a decrease in the ratio of pore throat to pore body radius  $r_b/r_t$ , while pore throat radius  $r_t$  remains constant (see Fig. 5). In comparison to shaly sands, shaly sandstones seem to be characterized by lower ratios  $r_b/r_t$  and lower radius  $r_t$  (see Fig. 6).

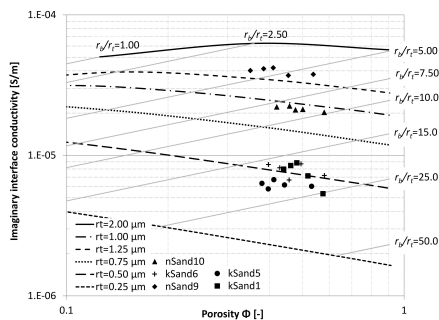


Fig. 5: Unconsolidated shaly sands – Modeled imaginary interface conductivity vs. porosity.

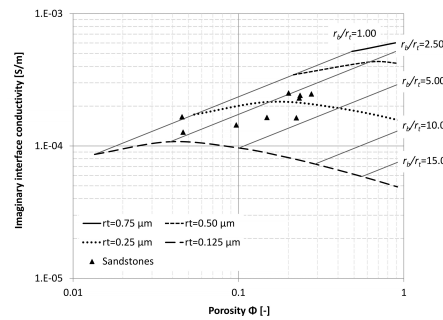


Fig. 6: Shaly sandstones – Modeled imaginary interface conductivity vs. porosity.

Porosity of the shaly sands calculated from complex conductivity data according to

$$\Phi = \left( \frac{\sigma_w}{\sigma' - \sigma''_{if}/l} \right)^{\frac{1}{m}} \quad (3)$$

versus independently determined porosity is presented for all unconsolidated samples in Fig. 7. The relative porosity change  $C$  relates the porosity  $\Phi$  to the initial porosity  $\Phi_0$ :

$$C = \frac{\Phi}{\Phi_0} = \left[ \left( \frac{\sigma'_0 - \sigma''_{if,0}/l}{\sigma' - \sigma''_{if}/l} \right)^{\frac{1}{m}} \right]^q \quad (4)$$

Using equation (4),  $C$  was then calculated from complex conductivity data alone for all unconsolidated shaly sand samples. The result is shown in Fig. 8. The exponent  $q$  was found to be about 2. It takes account of all remaining effects of changing  $m$  and  $l$ .

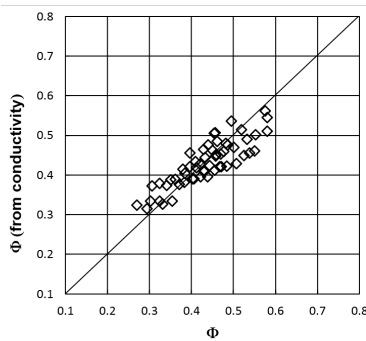


Fig. 7: Porosity from complex conductivity vs. porosity from volumetric measurement.

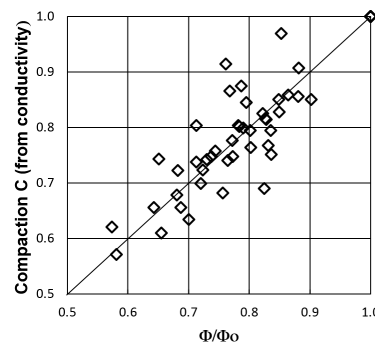


Fig. 8: Compaction  $C$  from complex conductivity vs. compaction from relative porosity decrease.

## CONCLUSION

The observed significant increase of the imaginary part with compaction is caused by the increase of internal surface area-to-porosity-ratio  $S_{POR}$  with decreasing porosity. The increase was found to be restricted to unconsolidated shaly sands with high porosities and therefore low cementation exponents. In contrast to that, a decrease of the imaginary part with decreasing porosity occurs in the case of consolidated shaly sandstones characterized by lower porosities and cementation exponents of about 2. If the surface area effect is ignored, the calculated porosity changes are reduced or not detectable due to the influence of interface conductivity. The proposed formula predicts the porosity change, which is associated with changes in permeability and bulk density (compaction), from a base line measurement and a repeated measurement without knowledge of further petrophysical properties.

## ACKNOWLEDGEMENTS

We thank the German Research Foundation for supporting the investigations with the project BO1082/12-1. Furthermore we thank Gesa Franz and Daniel Branka for their support with conducting experimental measurements in our petrophysical laboratory.

**REFERENCES**

1. Ward, S.H. “Resistivity and Induced Polarization Methods” In: Ward SH (ed) Geotechnical and Environm. Geophysics, *SEG Series Invest. in Geophysics* (1990), **5**.
2. Börner, F. “Complex conductivity measurements” In: Kirsch, R (Ed.): *Groundwater Geophysics*, Springer (2009), 119-153.
3. Schön, J. *Physical properties of rocks, Developments in Petroleum Sciences*, **65**, Elsevier (2015).
4. Olhoeft, G.R. “Low frequency electrical properties”, *Geophysics* (1985), **50**, 2492-2503.
5. Vinegar, H.J., M.H. Waxman “Induced polarization of shaly sand”, *Geophysics* (1984), **49**, 1267-1287.
6. Börner, F. “Complex conductivity measurements of reservoir properties”, *Proc Third Europ. Core Analysis Symp. Paris*, (1992), 359-386.
7. Slater, L.D., D.P. Lesmes “Electric-hydraulic relationships observed for unconsolidated sediments”, *Water Resources Research* (2002), **8**, 13.
8. Ulrich, C., L.D. Slater “Induced Polarization on unsaturated, unconsolidated sands”, *Geophysics* (2004), **68**, 762-771.
9. Weller, A., L.D. Slater, S. Nordsiek, D. Ntarlagiamis “On the estimation of specific surface per unit pore volume from induced polarization: A robust empirical relation fits multiple data sets”, *Geophysics* (2010), **75**, 4, WA105-WA112.
10. Revil, A., M. Skold “Salinity dependence of spectral induced polarization in sands and sandstones”, *Geophys. J. Int.* (2011), **187**, 813-824.
11. Skold, M., A. Revil, P. Vaudelet “The pH dependence of spectral induced polarization of silica sands: Experiment and modelling”, *Geophys. Res. Let.* (2011), **38**, L12304.
12. Börner, J.H., V. Herdegen, J. Repke, K. Spitzer “The impact of CO<sub>2</sub> on the electrical properties of water bearing porous media”, *Geophys. Prosp.* (2013), **61**, 446-460.
13. Müller-Huber, E., J. Schön, F. Börner “The effect of a variable pore radius on formation resistivity factor”, *J. of Applied Geophysics* (2015), **116**, 173-179.
14. Müller-Huber, E., J. Schön, F. Börner “Combining hydraulic and electrical conductivity for pore space characterization in carbonate rocks”, *Petrophysics* (2016), accepted.
15. Müller-Huber, E., J. Schön “Characterization of pore space characteristics in unconsolidated sediments (laboratory measurements and modified capillary tube models)”, *Grundwasser* (2014), **19**, 137-149 (in German).
16. Börner, F., J. Schopper, A. Weller “Evaluation of Transport and storage properties in the soil and groundwater zone from induced polarization measurements”, *Geophys. Prosp.* (1996), **44**, 583-601.
17. Lesmes, D.P., K.M. “Frye Influence of pore fluid chemistry on the complex conductivity and induced polarization responses of Berea sandstone”, *J. of Geophys. Research* (2001), **106**, 4079-4090.
18. Archie, G.E. “The electrical resistivity log as an aid in determining some reservoir characteristics”, *T. American Inst. Mining, Metall. and Petrol. Eng.* (1942), **146**, 54-62.

# **IMPROVING LAB NMR PETROPHYSICAL ESTIMATIONS BY INCORPORATING THE SURFACE RELAXIVITY PARAMETER**

Andre Souza, Giovanna Carneiro, Austin Boyd, Schlumberger Brazil Research and Geoen지니어ing Center; Martin Hurlimann, Schlumberger-Doll Research Center; Willian Trevizan, Bernardo Coutinho, Vinicius Machado, Petrobras Research Center; Rodrigo Bagueira, Fluminense Federal University

*This paper was prepared for presentation at the International Symposium of the Society of Core Analysts held in Snowmass, Colorado, USA, 21-26 August 2016*

## **ABSTRACT**

Nuclear Magnetic Resonance (NMR) relaxation time measurements are used routinely to evaluate the permeability ( $k$ ) of porous media. For this application, the Timur-Coates ( $k_{TC}$ ) equation is one of the most widely used  $k$  estimators. It takes into account the ratio of porosity associated with large and small pores, based on the interpretation of the transversal relaxation time ( $T_2$ ) distribution as a pore size distribution. A key parameter is the value of  $T_{2cutoff}$  that separates the free and bound fluids. It is related to a characteristic pore size by the transversal surface relaxivity ( $\rho_2$ ). However,  $\rho_2$  is not routinely measured in petrophysical NMR laboratory studies of sedimentary rock cores. In current practice, a default value of  $T_{2cutoff}$  is used. We have recently introduced a new technique to measure  $\rho_2$  directly in a given core. This allows us to calibrate the  $T_2$  distribution in terms of a distribution of  $V/S$  (the volume-to-surface area ratio) and introduce a  $V/S_{cutoff}$  to separate free and bound fluids. We demonstrate that this approach results in an improvement of over a factor of 2 in the permeability estimates based on the modified  $k_{TC}$  equation. Additionally, a correlation of  $\rho_2$  with  $S_{wi}$  is proposed, making possible the estimation of this parameter as well.

## **INTRODUCTION**

The NMR technique is routinely used to evaluate important petrophysical properties of porous media, in particular reservoir rock cores [1]. The main application relies on the measurement of  $T_2$ , and the interpretation of the resulting  $T_2$  distribution as a pseudo pore body size distribution, given by:

$$T_2 = \frac{1}{\rho_2} \cdot \left( \frac{V}{S} \right)_{pore} \quad (1)$$

Here we neglect diffusion in internal magnetic field gradients and bulk relaxation. This is a reasonable assumption for most of sedimentary rock cores when the measurement is done with proper acquisition parameters and when vuggy porosity is absent. As seen, Equation (1) depends on the pore body-to-surface area ratio ( $V/S$ ), a term proportional to pore radius and pore geometric features, and also on the surface relaxivity.  $\rho_2$  describes how efficiently the pore walls can relax the polarized saturating fluids [1], and so it is the

key parameter to relate  $T_2$  to pore size. However, in most of the routine petrophysical applications of Equation (1), it is usually assumed that  $\rho_2$  is a constant (for a given lithology). This is a common practice when estimating permeability based on  $T_2$  distributions [2,3]. Furthermore, measuring  $\rho_2$  is not simple and most of the developed methods rely on *a priori* knowledge, as pore geometry or V/S determination [1].

Recently, Souza et al. [4] have shown a significant improvement on the accuracy of permeability estimation using the classical  $k_{SDR}$  equation, when  $\rho_2$  is determined and is used together with the mean  $T_2$ . The equation is defined as  $k_{SDR} = a_{SDR} \cdot \phi^4 \cdot (T_{2LM})^2$ , being  $a_{SDR}$  a constant that depends on the lithology,  $\phi$  the porosity and  $T_{2LM}$  the logarithmic mean of the  $T_2$  distribution. The authors show an impressive gain in  $k_{SDR}$  accuracy (more than a factor of 2) when the term  $(T_{2LM})^2$  is replaced by the  $(\rho_2 \cdot T_{2LM})^2$ . The determination of  $\rho_2$  presented in that work is based on the restricted diffusion phenomena. When a fluid is diffusing in a confined geometry, its diffusion coefficient ( $D$ ) is reduced by a amount that is proportional to the pore's S/V ratio [4]. Since  $T_2$  is also dependent on this parameter (Equation 1), the correlation of  $D$  with  $T_2$ , acquired by the two dimensional  $D$ - $T_2$  experiments, allows the determination of  $\rho_2$  through a linear fitting of the measured  $D$  versus  $T_2$ . This method eliminates the need of a model for the porous system under investigation, since it does not depend on the pore's size and geometry, giving a more reliable effective  $\rho_2$  when compared to the ones given by correlations between NMR relaxation times with different techniques, like MICP derived pore throat size distribution, surface area by BET, image analysis, among others. Another problem with these methods is that each one probes different length scales of the porous system, resulting in correlations that are not reliable enough to be used in routine studies.

In 2002, Richard Sigal [5] studied the  $k_{TC}$  and  $k_{SDR}$  equations, aiming to clarify their inter-correlations. He proposes that  $k_{TC}$  can be interpreted exactly as the  $k_{SDR}$  one through the definition of a "Coates time" ( $T_{Coates}$ ), which is the product of  $T_{2cutoff}$  and the (FFI/BVI) term, if applied on fully brine saturated samples. Its general form can be written as:

$$k_{TC} = a_{TC} \cdot \phi^4 \cdot (T_{2cutoff})^2 \cdot \left(\frac{FFI}{BVI}\right)^2 \quad (2)$$

where  $a_{TC}$  is a constant that depends on lithology, FFI and BVI are defined by integrating the  $T_2$  distribution: FFI by the signal above a pre-defined  $T_2$  cutoff and the BVI, below. When  $\rho_2$  deviates from its default value, the pore size associated with the  $T_2$  cutoff value changes and will make Equation (2) less reliable. This effect was already observed for  $k_{SDR}$  as well [4]. Furthermore, the lack of unit consistency is another problem [5]. In the seminal works about permeability estimation by NMR [2-4], the authors have implicitly assumed a constant value for  $\rho_2$  for each lithology and rock type that was reflected in the values of  $a_{TC}$  and  $a_{SDR}$ . So, the explicit inclusion of  $\rho_2$  on those equations must also lead to a re-definition of those constants. This corrects the dependency of permeability (squared length) by NMR measurement, clarifying and keeping the required consistency. The general assumption when core lab calibration is not available, is to use for the  $T_{2cutoff}$  values 33 ms for sandstones and 100 ms for carbonates [1]. However, using these values

can give erroneous permeability estimates, especially in carbonates where the heterogeneity and complexity can be high. In such cases, a specific calibration procedure is often used to determine a more appropriate value of  $T_{2\text{cutoff}}$  [1].

Following Souza et al. work [4], the aim of this work is to propose a methodology that incorporates the  $\rho_2$  parameter to routine petrophysical analysis by NMR, with focus on the  $k_{\text{TC}}$  equation, cutoff definition and  $S_{\text{wi}}$  estimation. All those quantities are very important and crucial parameters for best routine oil-field decisions and operations [1].

## PROCEDURES

16 sandstones and 10 carbonate cylinders outcrop rock cores with 1.5" diameter and 2" length were studied. Helium gas porosity ( $\phi_{\text{He}}$ ) and permeability ( $k_{\text{He}}$ ) were measured applying a confining pressure of 500 psi. Cores were saturated with 20,000 ppm NaCl brine and NMR  $T_2$  relaxation times were measured using the CPMG pulse sequence, on a low-field GeoSpec spectrometer (2 MHz frequency for  $^1\text{H}$ ) from Oxford Instruments (UK). Details of the 2D  $D$ - $T_2$  experiment acquisition and signal processing can be found in [4]. Table 1 shows the basic petrophysical data ( $\phi_{\text{He}}$  and  $k_{\text{He}}$ ) and  $\rho_2$  obtained.

## RESULTS

The purpose of this work is to present a methodology that applies  $\rho_2$ , measured by the  $D$ - $T_2$  experiment, to re-define the cutoff concept widely applied in the petrophysical estimations of permeability and irreducible water saturation. As already stated,  $\rho_2$  is the parameter that provides the relationship between relaxation time and pore size distributions, so having itself a strong physical meaning.

Therefore, a cutoff on the  $(V/S)$  dimension, instead of the regular  $T_2$  dimension, is proposed. In this new approach, we have a fixed  $(V/S)_{\text{cutoff}}$  that corresponds to a variable  $T_{2\text{cutoff}}$  that depends on  $\rho_2$  (as shown in Equation 1), given by:

$$T_{2\text{cutoff}} = \frac{1}{\rho_2} \cdot \left(\frac{V}{S}\right)_{\text{cutoff}} \quad (3)$$

Figure 1 compares the error in permeability prediction ( $\sigma_k$ ) based on  $k_{\text{TC}}$  as a function of the cutoff value for the two approaches. When a traditional  $T_{2\text{cutoff}}$  is used (Figure 1a), the minimum  $\sigma_k$  for sandstones is 3.6 and occurs for  $T_{2\text{cutoff}}$  at around 50 ms, while for carbonates the minimum  $\sigma_k$  is 5.4 for a  $T_{2\text{cutoff}} = 150$  ms. This has to be compared with the new approach where the  $(V/S)_{\text{cutoff}}$  is used instead (Figure 1b). The minima in  $\sigma_k$  are significantly smaller, i.e. 2.3 for sandstone with  $(V/S)_{\text{cutoff}} = 0.4 \mu\text{m}$  and 2.6 for carbonates with  $(V/S)_{\text{cutoff}} = 1.8 \mu\text{m}$ . Figure 2(a) shows the results of  $k_{\text{TC}}$  using the optimized  $T_{2\text{cutoff}}$ 's, and Figure 2(b) shows the estimations using the corresponding  $(V/S)_{\text{cutoff}}$ 's. The accuracy, analysed via  $\sigma_k$  and considering both lithologies, shows a significant improvement of more than a factor of 2. To test the proposed estimator, 10 additional twin plugs chosen from the available samples described in Table 1 were measured and plotted on Figure 2, using the same  $T_{2\text{cutoff}}$  and  $(V/S)_{\text{cutoff}}$  values. The correlation of their estimated  $k_{\text{TC}}$  versus  $k_{\text{He}}$  was as good as the one found for the other

cores. It is notable that the new method proves to be applicable for a permeability range that spans over almost 5 orders of magnitude.

The impact of the knowledge of  $\rho_2$  that generates the achieved gain on  $k_{TC}$ , is illustrated in Figure 3 on three carbonate samples. In Figure 3(a), the regular  $T_2$  distributions for a very high  $\rho_2$  (Indiana 70, high  $k_{He}$ ), a high  $\rho_2$  rock (Austin Chalk, low  $k_{He}$ ) and a low  $\rho_2$  (Indiana 2-4, low  $k_{He}$ ), are shown. It is clear that assuming identical scaling factors for converting  $T_2$  distributions into pore size distributions is not appropriate to explain the permeability range for these samples. However, when  $(V/S)$  is plotted (Figure 3(b)), the two low  $k_{TC}$  cores lined almost perfectly at small  $(V/S)$  values, and the high one is shifted to longer values. The plots show also the cutoffs of 150 ms for  $T_2$  and 1.8  $\mu\text{m}$  for  $(V/S)$ . Clearly, the  $(FFI/BVI)$  calculated in Figure 3(b) based on  $(V/S)$  correctly reflects their permeabilities. These analyses demonstrate the improved pore size representation based on the  $(V/S)$  dimension. The gain for carbonates was greater than for sandstones, corroborating the well described high complexity of that lithology.

As a check of consistency and following Sigal's work [5], the suggestion that  $Sw_i$  can be estimated from the NMR  $T_2$  on fully saturated cores, with the *a priori* knowledge of the  $(V/S)_{cutoff}$ , was studied. Substituting Equation (3) in (2),  $k_{SDR} \approx k_{TC}$  gives:

$$a_{SDR} \cdot \phi^4 \cdot (\rho_2 \cdot T_{2LM})^2 \approx a_{TC} \cdot \phi^4 \cdot \left(\frac{V}{S}\right)_{cutoff}^2 \cdot \left(\frac{FFI}{BVI}\right)^2 \quad (4)$$

Figure 4(a) shows the plot of  $T_{2LM}$  versus  $T_{2cutoff} \cdot (FFI/BVI)$  (as described by  $k_{SDR}$  equals to Equation 2) and Figure 4(b) shows  $\rho_2 \cdot T_{2LM}$  versus  $(V/S)_{cutoff} \cdot (FFI/BVI)$  (as described by Equation 4). The correlation in Figure 4(a) is reasonably good for sandstones, with a Pearson's coefficient ( $R^2$ ) of 0.80, but very poor for carbonates, with a  $R^2$  of only 0.26. Figure 4(b) shows the notable gain in linearity for the carbonate lithology when  $\rho_2$  information is included to improve the pore size estimation, with a  $R^2$  of 0.88. Sandstones have shown an increase of only 7% ( $R^2$  of 0.87), due to its low complexity.

In conclusion, if  $T_2$  distribution,  $\rho_2$  and  $(V/S)_{cutoff}$  are measured, Equation (4) can be used to estimate  $(FFI/BVI)$ , that in turn can be used to estimate  $Sw_i$  (if total porosity,  $\phi_T$  is known). Laboratory  $Sw_i$  measurements are being conducted, in order to be compared with the estimating method of  $Sw_i$  proposed in this work.

## CONCLUSION

The methodology presented, based on the definition of a new NMR cutoff value on the  $(V/S)$  dimension (instead of the regular  $T_{2cutoff}$  widely used on petrophysical estimations), proved to be very efficient to improve: (a) by more than 2 times the permeability estimation by Timur-Coates equation, (b) the cutoff concept itself and (c) the estimation of  $Sw_i$ .  $\rho_2$  parameter can be robustly and accurately measured by the 2D  $D-T_2$  experiment, a well established technique available in most of the lab NMR machines used by the oil production and exploration industry. For this reason and considering all the deliverables that this parameter can improve, the main proposition is that  $\rho_2$  should be thought and considered when lab NMR investigations are being planned.

**REFERENCES**

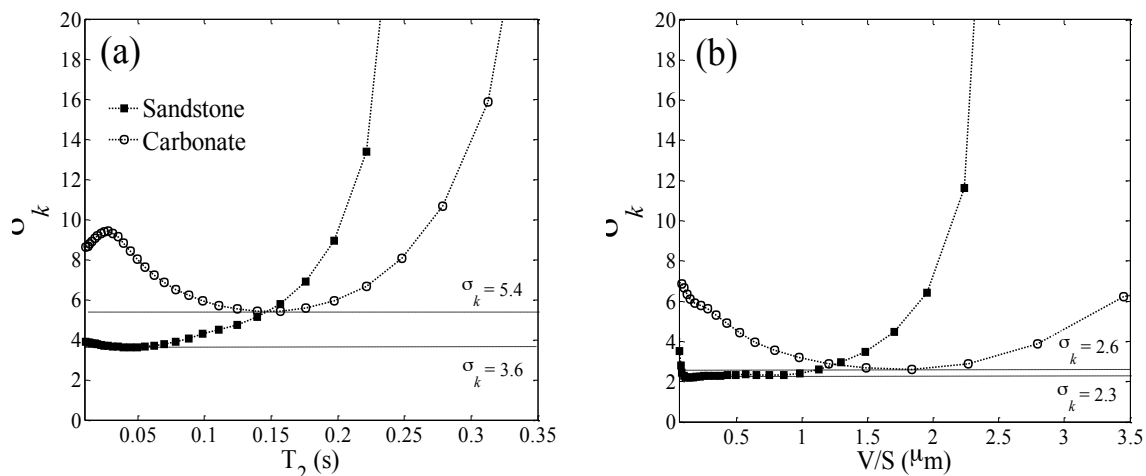
1. Dunn, K., Bergman, D., Latorraca, G. *Nuclear Magnetic Resonance: Petrophysical and Logging Applications*. Elsevier Science Ltd. The Netherlands, (2002), 71-238.
2. Timur, A., "Producible Porosity and Permeability of Sandstones Investigated Through Nuclear Magnetic Resonance Principles", *The Log Analyst*, (1969) v. 10, n. 1, 3-11.
3. Kenyon, W., Day, P., Straley, C., Willemsem, J., "A three part study of NMR longitudinal relaxation properties of water saturated sandstones", *SPE Formation Evaluation*, (1988) 3, n. 3, 622-636.
4. Souza, A., et al. "Permeability Prediction Improvement Using 2D NMR Diffusion-T2 Maps", *54<sup>th</sup> SPWLA Annual Logging Symposium*, (2013) paper U.
5. Sigal, R., "Coates and SDR Permeability: Two Variations on the Same Theme", *Petrophysics*, (2002) v. 43, n. 1, 38-46.

**Table 1.** Porosity ( $\phi_{He}$ ), permeability ( $k_{He}$ ) and effective surface relaxivity ( $\rho_2$ ), of the samples studied.

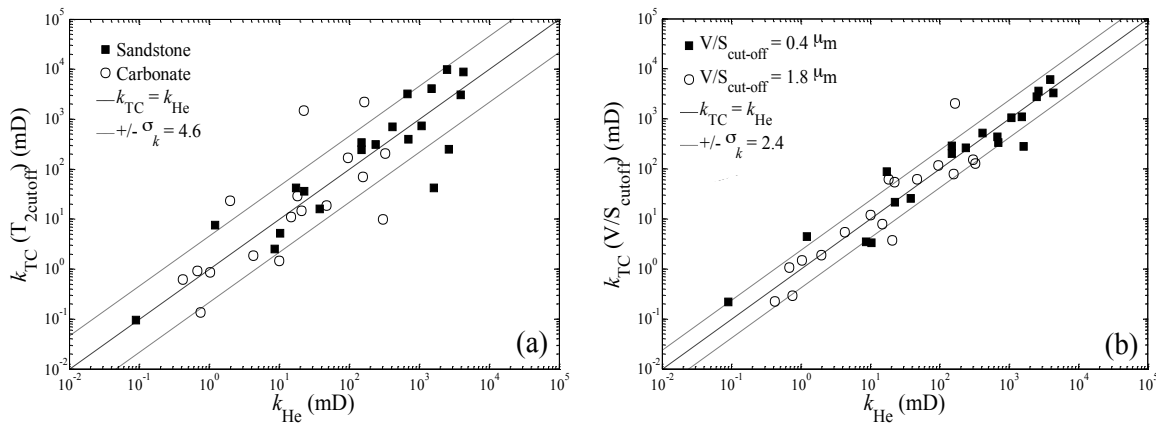
Sample	$\phi_{He}$ (p.u.)	$k_{He}$ (mD)	$\rho_2$ ( $\mu\text{m/s}$ )
Bandeira Brown	20.8	1.2	8.6
Bandera Gray	21.7	22.6	10.0
Bentheimer	23.2	2490.0	7.6
Berea	20.2	149.0	11.4
Berea Stripe	21.2	415.0	12.1
Boise Idaho Brown	27.5	1510.0	8.3
Boise Idaho Gray	29.3	4310.0	12.0
Briarhill	24.3	3900.0	16.5
Buff Berea	24.4	698.0	13.0
Carbon Tan	17.1	38.0	15.9
Castlegate	26.3	1080.0	20.0
Crab Orchard	6.5	0.1	19.6
Leopard	20.5	1610.0	55.1
Kirby	21.8	17.3	19.4
Nugget	10.8	8.6	24.7
Sister Gray Berea	20.8	149.0	12.5

Sample	$\phi_{He}$ (p.u.)	$k_{He}$ (mD)	$\rho_2$ ( $\mu\text{m/s}$ )
Austin Chalk	23.0	10.0	23.3
Desert Pink	30.5	95.5	18.8
Edwards Yellow	22.9	165.0	16.5
Guelph Dolomite	7.9	4.3	12.4
Indiana 8-10 mD	9.1	0.4	2.9
Indiana 2-4 mD	13.8	1.9	3.3
Indiana 70 mD	18.9	301.0	35.8
Leuders	16.2	1.0	10.5
Silurian Dolomite	12.4	18.3	9.5
Winsconsin	5.6	0.8	8.6



**Figure 1.** Error of Timur-Coates model considering the cutoffs: (a) from each  $T_2$  bin; and (b) each ( $\rho_2, T_2$ ) bin. The minima of  $\sigma_k$  represent the best predictions for each lithology.



**Figure 2.** Timur-Coates permeability estimations considering: (a)  $T_{2cutoff}$  of 50 ms for sandstones (black squares) and 150 ms for carbonates (open circles); and (b)  $V/S_{cut-off}$  of 0.4  $\mu\text{m}$  for sandstones and 1.8  $\mu\text{m}$  for carbonates. The gain in accuracy is notable, with a reduction in  $\sigma_k$  from 4.6 to 2.4 (in log scale).

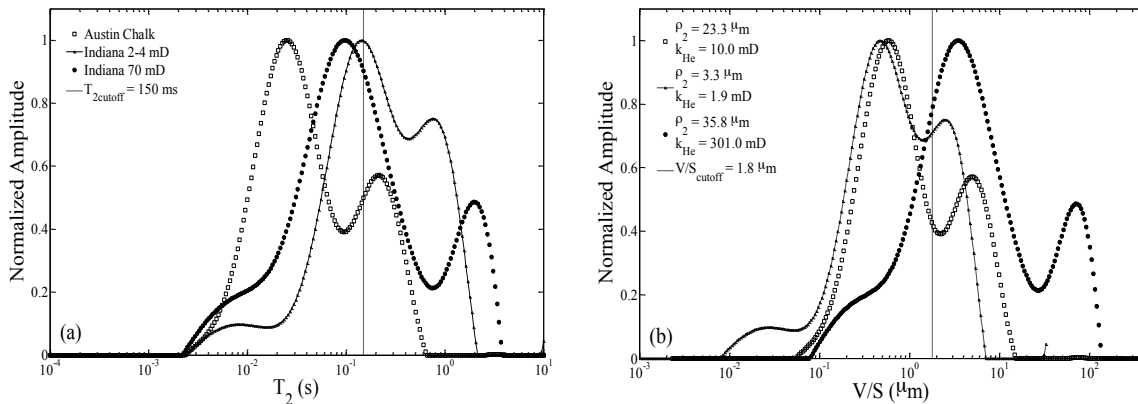


**Figure 3.**  $T_2$  (a) and  $V/S$  (b) distributions and respective cutoffs, for 3 carbonate samples with very high to low  $\rho_2$ . When  $\rho_2$  is applied, a dramatic shift properly correlates pore sizes with permeabilities.

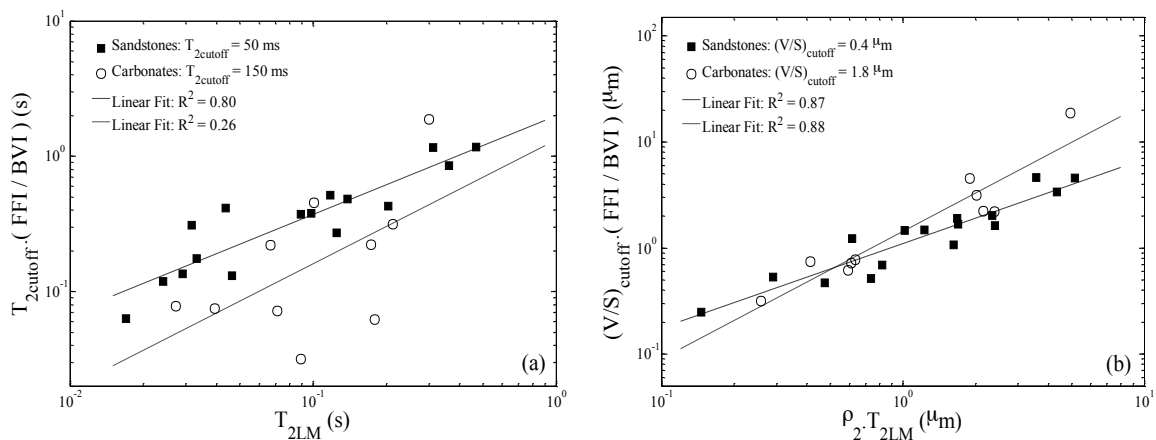


**Figure 4.** Correlation of (FFI/BVI) with: (a)  $T_{2LM}$ ; and (b)  $\rho_2 \cdot T_{2LM}$ . The y axis is multiplied by each cutoff, in order to keep the consistency. The analysis of  $R^2$  clearly indicates the gain in linearity in (b).

# NEW SATURATION FUNCTION FOR TIGHT CARBONATES USING ROCK ELECTRICAL PROPERTIES AT RESERVOIR CONDITIONS

Oriyomi Raheem and Hadi Belhaj  
The Petroleum Institute, Abu Dhabi, UAE

*This paper was prepared for presentation at the International Symposium of the Society of Core Analysts held in Snowmass, Colorado, USA, 21-26 August 2016*

## ABSTRACT

In the present study, a core analysis program including NMR measurements were performed to get a better petrophysical characterization of carbonate reservoir transition zone in the Abu Dhabi region. The results reveal three distinct rock types with average NMR-T<sub>2</sub> cutoffs of 292 ms, 164 ms and 63 ms for the topmost, middle and lowermost samples of the reservoir respectively. Electrical resistivity and capillary pressure-water saturation were also measured at ambient and reservoir (2500 psi and 85 °C) conditions using a DCI Pc-RI systems mimicking drainage and spontaneous imbibition to investigate the hysteresis and variation in saturation exponent.

It was found that the cementation exponent increases from 1.9 to 2.4 under overburden conditions and decreases in a stepwise manner during reduction of overburden, but not to the initial value due to hysteresis. This implies that the electrical parameters at ambient condition would lead to underestimation of water saturation. The saturation exponents estimated during drainage and spontaneous imbibition at reservoir conditions range from 1.5 – 4.0 for the different rock types tested in this study.

New saturation functions were developed for each rock type from the measured electrical parameters at reservoir conditions by using the modified Archie's equation for the transition zone of this carbonate reservoir. The outcomes of the present study lead to a correction of the field resistivity log data that, overestimate the water saturation and hence predictions of saturation distributions, mobility and original oil in place.

## INTRODUCTION

To understand wettability distribution variation across a particular reservoir, a meticulous understanding of the reservoir mechanisms (fluid flow behavior) is required to predict the original oil in place. Both fluid dynamic properties of reservoir and geological understanding will aid for the determination of both water saturation and wettability distribution throughout the reservoir. Electrical resistivity of a reservoir rock is a very important petrophysical attributes of log analysis. Rock electrical properties measured in the lab are widely employed in well logs interpretation and calibration. It is used to estimate the Archie's parameters which are later used in log porosity-saturation estimation. The Archie cementation factor  $m$  of reservoir rock sample is an important

parameter as it significantly influences the porosity and permeability of rocks in a carbonate reservoir. Carbonate reservoirs usually show thick transition zone which is traditionally defines as the reservoir interval that extends from the oil-water contact (OWC) up to the reservoir level where water saturation reaches its irreducible level. As transition zone contains significant volume of oil, its characterization is utmost important for reserve estimation. Therefore, estimations of electrical resistivity, and water saturation at reservoir conditions are required to better understand the saturation distribution with ultimate focus on the transition zone.

High pressure and elevated temperature are observed due to increasing depth of hydrocarbon bearing carbonate rocks in the reservoir. The effect of confining pressure on the cementation factor  $m$  have been studied by many investigators, mostly on sandstone rocks, but occasionally on carbonate rocks [1-3]. Further investigations on water saturation exponent  $n$  as well as cementation factor  $m$  are highly recommended to draw a clear concept on the variation of these parameters at reservoir conditions. Particularly carbonate samples from transition zone and their characterizations are crucial in this contest to get a better understanding of the fluid flow behavior and initial water saturation distribution. The cementation and saturation exponent values in the empirical equations of Archie are assumed to be independent of reservoir fluid, solid surface properties, temperature and pressure [3]. Longeron et al. [1] found out that sandstones reached equilibrium rather quickly after an increase in confining pressure, but carbonate samples in turn required several days to reach equilibrium. They concluded that cementation factor  $m$  increases with pressure. Several authors observed that the saturation exponent  $n$  reflected the wettability effect on rock electrical properties. While some researchers concluded that  $n$  depends on the microscopic distribution of fluids during drainage or imbibition [1,2,4], other researchers stated that  $n$  is a function of rock wettability and showed that  $n$  increases as the oil wettability of a rock increases.

The task ahead involved developing a saturation function to correct the field logs using the carbonate plug samples in the Abu Dhabi region. For this purpose, the present work uses the 2D NMR and conventional core analysis for the petrophysical characterization of transition zone plug samples. Electrical resistivity and capillary pressure-water saturation values, at ambient and reservoir conditions, were also measured using a DCI Pc-RI systems.

## **EXPERIMENTAL METHODOLOGY**

The core samples were selected at different depth domains in the transition zone of the carbonate reservoir. They were cut and trimmed to a maximum of 2 inch length and 1.5 inch diameter. The samples were cleaned by Soxhlet extraction method. NMR  $T_1T_2$  maps were used to ascertain the crude oil or tar absence from the samples before further analysis. De-ionized water and different salts were mixed in appropriate proportions to prepare the formation brine in the laboratory to recreate the aquifer brine.

The core samples were vacuumed and saturated with brine at a pressure of 2000 psi and kept pressurized for a period of 24 hours in a saturator. Nuclear magnetic resonance was

used to group the fully saturated plugs into different static rock types, based on similar pore size distributions. Centrifugation technique was used to develop air-brine capillary measurements and get irreducible water saturation and subsequent  $T_2$  cut-off values.

The effect of both confining pressure and temperature on the cementation and saturation exponents of the core samples were studied with the help of a porous plate DCI equipment that measures resistivity at  $\frac{1}{2}$  in. intervals along the core. The cementation factor  $m$  and saturation exponent  $n$  estimated from electrical resistivity measurements are tagged as 1\_2, 1\_3, 2\_3 and 1\_4 along the samples. Subsequently, the capillary pressure curves and the resulting irreducible water saturation at reservoir conditions were compared with centrifuge and NMR ambient values. The saturation exponent  $n$  was also derived during drainage and imbibition processes at 2500 psi and 85°C. A curve fitting by least squares regression was used to estimate the saturation function using the fundamental Archie's equation [5].

## RESULTS AND DISCUSSION

Carbonate rocks are dissimilar to sandstones, having more complex pore system which may due to diagenesis, compaction and stress changes thereby causing dual porosities. Figure 1 depicts the unimodal pore size distribution of the selected plug samples. The wider NMR  $T_2$  spectrum indicates large porosity and a wider pore size range. Using Centrifuge-NMR technique, Figure 2 clearly shows the cumulative NMR  $T_2$  distribution. The cementation factor  $m$  and formation factor  $FF$  of all the core samples used in this study were found to increase with confining pressure from 500psi to 2500psi and corresponding temperature variation from 25 °C to 85 °C as shown in Figure 3. The increase was slight for the rock samples closer to aquifer. From Table 1 it is confirmed that the 'm' decreases with increasing depth.

The saturation exponents,  $n$  determined from both the logarithmic slopes during drainage and imbibition cycles are shown in Figures 4, 5, 6 for three rock samples. The detailed results are shown in Table 2. The  $n$  values estimated from force fitting to cross  $(RI;S_w)=(1;1)$  samples 1\_8 and 1\_30 were greater than 2 (oil-wet) during drainage. However, the  $n$  values of samples 1\_30 and 2\_1 increased during spontaneous imbibition (more oil wet). This change in wettability was attributed to the 40 days ageing effect. During long term ageing the polar organic compounds of the crude oil are believed to be adsorbed onto the rock surface and change of wettability. The estimated  $n$  values for sample 1\_8 was initially greater than (oil-wet) during drainage but decreased further during spontaneous imbibition (less oil wet) (table 2). This confirms wettability changes with depth [4]. The average  $n$  values estimated at both frequencies (1 kHz & 10 kHz) were approximately the same during drainage and spontaneous imbibition (table 2). The  $S_{wi}$  values estimated from the capillary pressure curves were found to be 16% less than that estimated at ambient conditions, as shown in Figures 7 and 8. By substituting RRT-1 ( $m = 2.25$ ,  $n = 4.0$ ), RRT-2 ( $m = 1.95$ ,  $n = 2.6$ ) and RRT-3 ( $m = 1.95$ ,  $n = 1.1$ ) values in the equation 1 below, the saturation functions can be developed accordingly.

$$S_w = \left[ \frac{aR_w}{\phi^m R_T} \right]^{1/n} \quad (1)$$

Where  $R_w$  is the resistivity of formation brine,  $R_t$  is the true formation resistivity and  $a$  is the lithology factor. Due to the changes in pore volumes and resistivity noticed between atmospheric and 500 psi confining pressure which are assigned to poor electrode contact, the baseline for comparison were set at 500 psi and room temperature. Measurements of resistivity and saturation during the porous plate test were taken at equilibrium. In summary, electrical resistivity was influenced by changes in confining pressure and temperature. Due to the increase in brine conductivity due to temperature, the electrical resistivity across the core samples were found to decrease with temperature as shown in Figure 9. However, as the confining pressure was increased in the test cell cart, the electrical resistivity showed a reverse trend, increasing by about 56% within 500 psi and 2500 psi due to compaction or pore volume reduction (Figure 10). The results prove that electrical resistivity measurements performed in the laboratory simulating reservoir conditions are preferably more accurate.

## CONCLUSIONS

Based on the results of the present work, the following conclusions can be drawn as follows:

1. Pore size distribution by NMR  $T_2$  study indicates three different rock types along the different depth of the reservoir.
2. The estimated  $S_{wi}$  values at reservoir conditions are 16% lower than that measured at ambient conditions, underestimating oil saturation. Electrical resistivity is influenced by changes in confining pressure and temperature. By running sensitivity analysis, 17% error occurred in  $S_w$  determination when  $m$  and  $n$  are not measured at reservoir conditions.
3. The saturation exponent  $n$  values calculated during spontaneous imbibition are higher than values determined during drainage for oil-wet system and vice versa for water-wet system. Estimated saturation exponents from force fit were minimally affected by changes in frequency.
4. There is a possibility of wettability change as water saturation decreases up the transition zone which is influenced by its thickness.

## ACKNOWLEDGEMENTS

The authors would like to acknowledge the fund made available and data provided by ADNOC and its Group for this project. Also, special thanks are due to the Petroleum Institute, Abu Dhabi for hosting this study.

## REFERENCES

1. Longeron, D.G., M.J. Argaud, and J.P. Feraud, "Effect of Overburden Pressure and the Nature and Microscopic Distribution of Fluids on Electrical Properties of Rock Samples," *SPEFE* (June 1989); *Trans., AIME*, 287, 194-202.

2. Sanyal, S.K. *et al.*: "The Effect of Temp. on Electrical Resistivity of Porous Media," *Trans.*, 13th SPWLA Annual Logging Symposium, Tulsa (May 7-10, 1972) paper I.
3. Mahmood, S. M., N. L. Maerefat, and M. M. Chang. "Laboratory measurements of electrical resistivity at reservoir conditions." *SPE Formation Evaluation* 6.03 (1991): 291-300.
4. Dunlap, H.F. *et al.*: "The Relation between Electrical Resistivity and Brine Saturation in Reservoir Rocks," *Trans.*, AIME (1949) 186, 259-64.
5. Archie, G.E. 1942. The Electrical Resistivity Log as an Aid in Determining Some Reservoir Characteristics. *Trans. of AIME* 146 (1): 54-62

Table 1. Calculated values of cementation exponent ‘m’.

Sample	Depth from (ft)	Por. (%)	K <sub>air</sub> (mD)	T <sub>2</sub> CUTOFF (ms)	Amb. Cond. [AC]				Res. Cond.[RC]				[AC]	[RC]
					m 1-2	m 1-3	m 1-4	m 2-3	m 1-2	m 1-3	m 1-4	m 2-3	m <sub>av</sub>	m <sub>av</sub>
1_8	9523	17.74	1.13	156	2.1	1.9	1.9	1.8	2.3	2.3	2.3	2.3	1.9	2.3
1_9	9526	11.53	0.12	152	2.0	1.9	1.9	1.9	2.2	2.1	2.2	2.1	1.9	2.2
1_15	9547	10.88	0.12	115	1.8	1.7	1.7	1.6	2.1	2.0	2.0	1.9	1.7	2.0
1_30	9592	17.53	0.92	115	1.6	1.7	1.6	1.7	2.0	1.9	1.9	1.8	1.6	1.9
1_32	9596	17.49	0.96	115	1.9	1.7	1.7	1.6	2.1	1.9	1.9	1.7	1.7	1.9
2_1	9597	16.39	0.55	79	1.6	1.7	1.6	1.7	2.0	1.9	1.9	1.8	1.6	1.9
2_4	9606	14.24	0.31	79	1.8	1.6	1.6	1.6	2.1	1.9	1.9	1.8	1.6	1.9
2_6	9612	18.67	0.71	60	1.8	1.7	1.7	1.7	2.1	1.9	2.1	1.8	1.7	2.0

Table 2. Calculated values of saturation exponent ‘n’ at different frequencies.

DRAINAGE										
Sample	Resistivity @ 1khz					Resistivity @ 10khz				
	n 1-2	n 1-3	n 1-4	n 2-3	n avg	n 1-2	n 1-3	n 1-4	n 2-3	n avg
1_8	3.0	2.7	2.6	2.5	2.7	3.0	2.8	2.6	2.7	2.8
1_30	2.7	2.6	2.6	2.4	2.1	2.8	2.6	2.6	2.5	2.1
2_1	2.0	2.0	1.9	1.8	1.9	2.0	2.0	1.9	1.8	1.9
IMBIBITION										
Sample	Resistivity @ 1khz					Resistivity @ 10khz				
	n 1-2	n 1-3	n 1-4	n 2-3	n avg	n 1-2	n 1-3	n 1-4	n 2-3	n avg
1_8	2.8	2.6	2.4	2.3	2.5	2.9	2.7	2.4	2.6	2.6
1_30	3.0	2.9	2.9	2.7	2.7	3.2	3.0	2.9	2.8	2.6
2_1	2.7	2.4	2.4	2.2	2.4	2.7	2.5	2.4	2.2	2.5

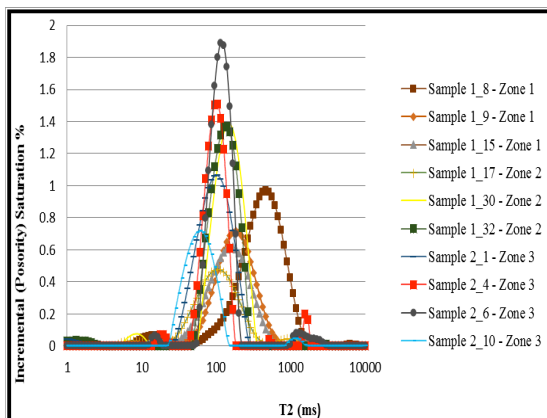


Figure 1. NMR Pore Size Distribution.

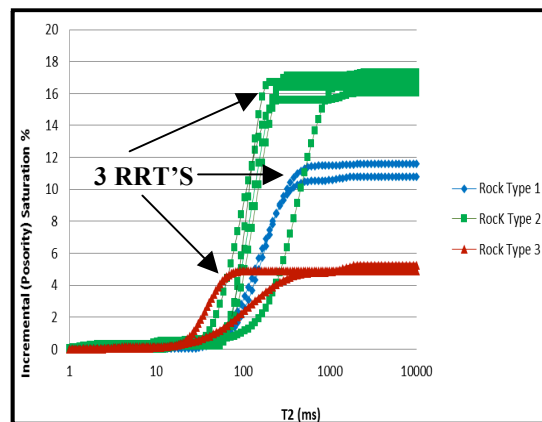


Figure 2. NMR Incremental Saturation vs. T2.

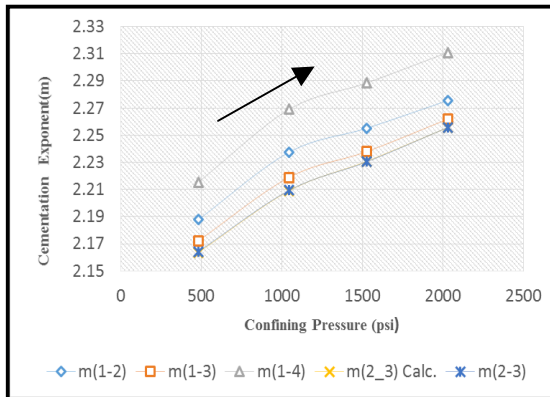


Figure 3. Plot of "m" vs. Pressure (1\_8).

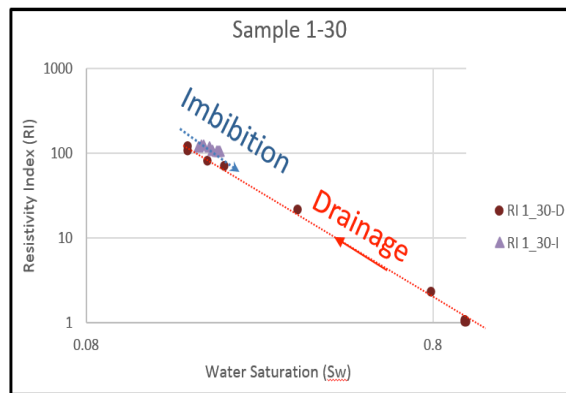


Fig. 4. Drainage & Spont. Imb in RI vs Sw (1\_30).

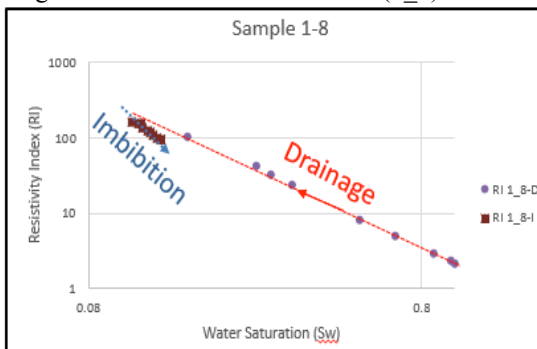


Fig. 5. Drainage & Spont. Imb. in RI vs Sw (1\_8).

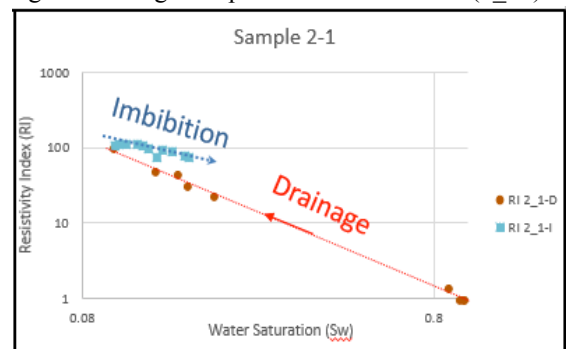


Figure 6. Drainage & Spont. Imb. in Pc vs Sw (2\_1).

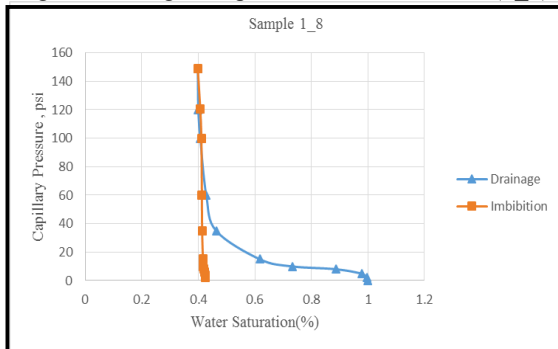


Figure 7. Drainage & Spont. Imb. in I vs Sw (1\_8).

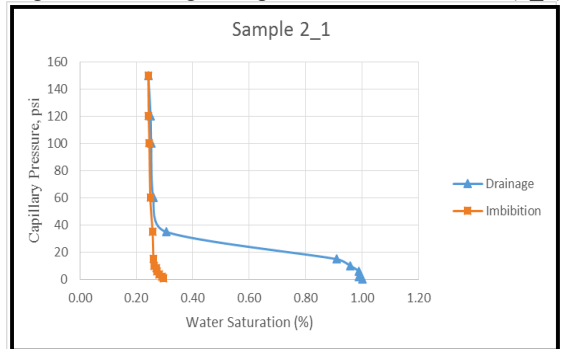


Fig. 8. Drainage & Spont. Imb. in Pc vs Sw (2\_1).

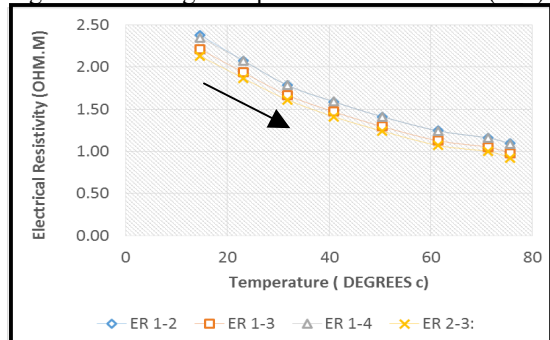


Figure 9. Plot of resistivity vs. temperature (1\_8).

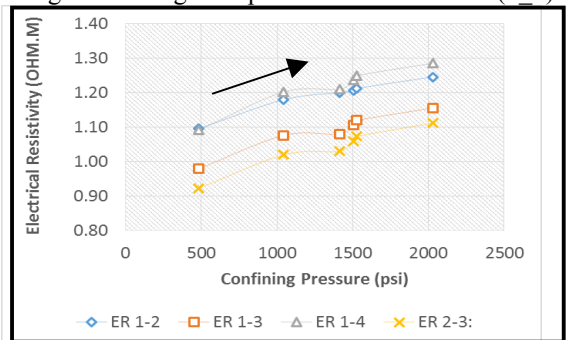


Figure 10. Plot of resistivity vs. pressure (1\_8).

## **A Lattice-Boltzmann Based Method Applied to Digital Rock Characterization of Perforation Tunnel Damage**

Bernd Crouse, David M Freed, Nils Koliha, Gana Balasubramanian EXA CORP  
Rajani Satti, Derek Bale, Stephen Zuklic BAKER-HUGHES INC

*This paper was prepared for presentation at the International Symposium of the Society of Core Analysts held in Snowmass, Colorado, USA, 21-26 August 2016*

### **ABSTRACT**

The lattice-Boltzmann method (LBM) for computational fluid dynamics has received considerable attention as a favorable approach for performing direct numerical simulation of pore-scale flow in porous media, especially for predicting permeability properties of reservoir rocks. The well recognized benefits of LBM as an approach for digital rock flow simulations include parallelizability, reliable convergence, and the opportunity to introduce multi-phase physics at the kinetic theory level. One of the challenges with LBM is to implement a surface boundary condition that avoids near-wall numerical issues, especially when portions of the relevant pore space are resolved with only a small number of grid cells. The present study examines LBM for digital rock using a boundary scheme based on explicit surface elements. A basic academic example of flow around packed spheres is presented, demonstrating the accuracy of the method even for coarse grid resolution. The method is then applied to the study of permeability alteration due to perforation tunnel damage. Using single-phase flow simulations based on micro-CT images of a small plug taken from a Berea sandstone test section, variations in porosity and absolute permeability of the damage zone around a typical perforation tunnel are characterized and visualized.

### **INTRODUCTION**

Conceived about 30 years ago, the lattice-Boltzmann method (LBM) for computational fluid dynamics has become well established for various fluid flow applications [1]. An alternative to traditional Navier-Stokes PDE-based methods, LBM is based on kinetic theory and solves a discrete form of the Boltzmann transport equation for the fluid particle distribution function [2-5]. The usual implementation yields a flow simulator which is inherently transient, viscous, and uses a cubic lattice as the computational grid.

In addition to successful application to turbulent flow problems [6], LBM has recently received considerable attention as a favorable approach for performing direct numerical simulation (DNS) of pore-scale flow within porous media. A particularly active application area is digital rocks [7], in which fluid flow in petroleum reservoir rock samples is simulated in order to predict important petrophysical properties such as absolute permeability, relative permeability curves, and capillary pressure curves. In digital rocks, high resolution scanning is performed to obtain a 3D image differentiating the rock grains and pore space. Various image processing techniques are applied to

generate a sufficiently accurate representation of the pore space geometry to be suitable as input for analyses such as computational flow simulation [8].

There are well recognized benefits of LBM as an approach for such pore-scale flow simulation. The localized nature of the algorithm supports parallelization and scalability. The mesoscopic approach of tracking particle distributions provides a deep connection to the underlying statistical mechanics of fluid flow, giving rise to favorable accuracy, reliable solution convergence, and the opportunity to include complex physics (e.g. multi-phase flow [9]) in a more robust way than traditional Navier-Stokes methods. However, there are also challenges to be addressed, even for single-phase flow. As in any method, near-wall behavior may be compromised if sufficient care is not taken in the surface boundary condition scheme. This is particularly important for digital rock, where the surface to volume ratio is large and near-wall flow behavior has a dominant impact on the results. Moreover, in order to simulate a sufficient volume of rock to be representative, the grid resolution must be chosen so as to keep the computational costs manageable. In practice, this means resolving much of the pore space, including critical pore throats, with only a small number of grid cells. Hence for digital rocks there is a high burden on the surface boundary condition scheme to perform adequately under coarse grid conditions.

This paper examines the use of LBM with a surfel-based boundary scheme [10,11] for application to digital rocks. This particular surface treatment has the potential to perform well even for complex geometry and relatively coarse resolution conditions. To demonstrate the efficacy of the present approach, a basic academic case (packed spheres) and a real rock study (perforation damage in Berea sandstone) are presented.

## **NUMERICAL METHOD**

Simulations are carried out using LBM with the wall boundary condition scheme given in [10,11], which employs a set of connected planar facets. These surface elements (“surfels”) provide a high fidelity geometric representation of the boundary and precise control of surface fluxes. To highlight the importance of the boundary scheme for digital rocks, Figure 1 shows a zoom-in of a tiny portion of a 2D slice of a real Berea sandstone image, comparing the stair-step boundary formed by the underlying cubic grid (1a) to the surfel-based boundary (1b), where a realistic (i.e. practical) grid resolution has been chosen. To alleviate stair-step boundaries, other LBM implementations commonly use point-wise interpolation schemes [12,13]; however, these methods face challenges in controlling the fluxes at the wall, such as ensuring exact mass conservation. In contrast, the volumetric-based scheme used here provides precisely defined boundary locations, precise control of surface fluxes, and robust handling of complex geometry.

## **PACKED SPHERES STUDY**

Flow around cubic-centered packed spheres (CCPS), which can be thought of as a simple porous medium, is simulated using the described LBM method. Figure 2 illustrates the configuration of spherical “grains” of diameter  $D$ , resulting in an inscribed radius

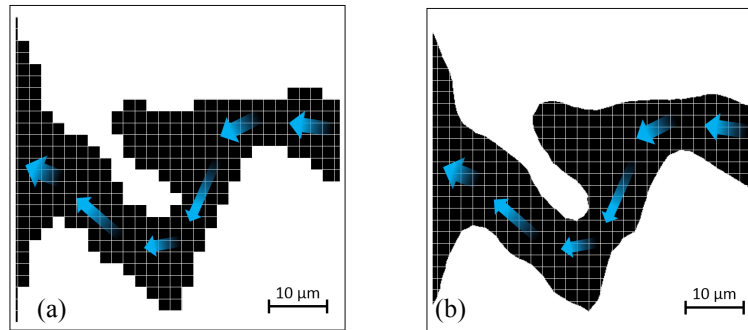


Figure 1: A small portion of a 2D slice of a Berea sandstone digital rock image for use in LBM flow simulation, comparing (a) stair-step surface representation and (b) surfel-based representation.

(effectively the pore radius)  $R_t = D(\sqrt{2} - 1)/2$ . The grains in this simulation are in contact with each other (no gap); hence even this simple case provides a challenging geometry condition at the contact points. The reference solution for absolute permeability  $k$  is given by the Kozeny-Carman equation  $k = \phi^3 D^3 / [72\tau(1 - \phi)^2]$  for porosity  $\phi$ , grain diameter  $D$ , and tortuosity  $\tau$ . This particular geometry is known to have  $\phi = 0.476$  and  $\tau = 2.08$ , resulting in absolute permeability  $k/D^2 = 0.00262$ . The simulation uses a body force to drive the flow and periodic boundaries, with Reynolds number kept well below unity to ensure Darcy flow conditions.

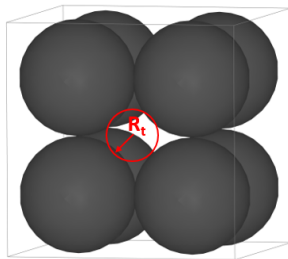


Figure 2: Cubic-centered packed spheres.

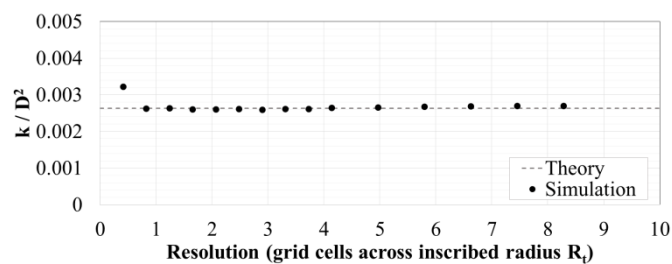


Figure 3: CCPS predicted  $k$  vs grid resolution.

Figure 3 plots the simulation results for permeability versus the number of grid cells across  $R_t$ . For  $R_t \geq 1$  (corresponding to  $D \geq 4.8$ ) the results are in excellent agreement with the reference solution, demonstrating accurate flow behavior even for very coarse grid resolution. Other LBM boundary schemes require higher resolution [14].

## PERFORATION DAMAGE STUDY

For well completions in the oil and gas industry, shaped charge jet perforation is the most widely used method of establishing hydraulic communication between the formation and the wellbore [15]. A primary objective of this method is to create tunnels that efficiently transport hydrocarbons. However, detonation of the explosive charge compresses the formation, resulting in a damage zone of compacted rock adjacent to the perforation tunnel which can have significantly reduced permeability. Characterization of the altered

permeability is an important factor in designing perforating jobs, but it is impractical to obtain the desired information from traditional laboratory methods.

In this work, an API RP19B-Section IV test is conducted using a Berea sandstone core. The perforated core is then sectioned and small core plugs drilled from various tunnel sections (Figure 4). For each plug, 3D images are obtained from a micro-CT scanner, and image processing is used to segment the images into grain vs pore regions to provide a geometric representation of the pore-space. Presented here is analysis of one plug (3 mm dia. by 12 mm length) taken from a section near the perforation tunnel opening. The entire plug is imaged by a series of 4 scans at resolution 2.4  $\mu\text{m}$ , with the scans partly overlapping to enable a continuous reconstruction (Figure 5). The domain is subdivided into 6 regions for analysis. Pore size distributions are determined using a maximum sphere method [16], and flow simulations using the present LBM approach [10,11] are performed for absolute permeability prediction. A one-to-one mapping of grid cells to scan voxels was chosen for the LBM flow simulations.



Figure 4: (a) Perforated core cut into sections; (b) section of tunnel with 3x12mm plug (c) drilled out.

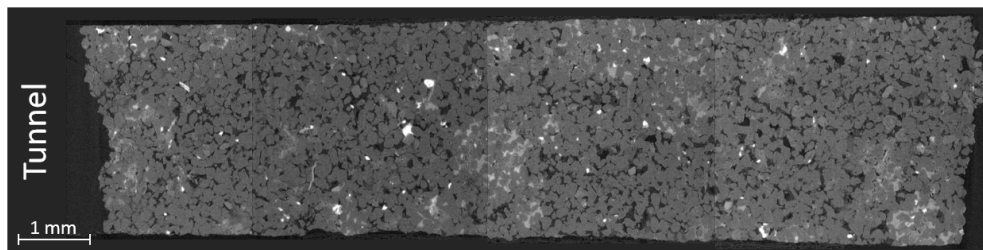


Figure 5: Center-plane of reconstructed micro-CT images of test section plug.

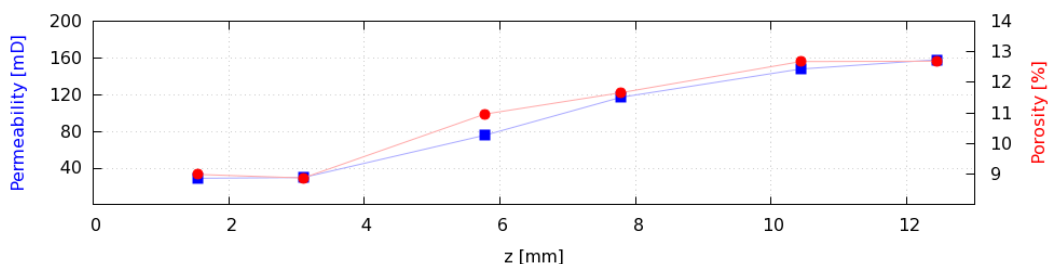


Figure 6: Porosity (right y-axis) and absolute permeability (left y-axis) of test section plug.

Figure 6 shows the resulting porosity and absolute permeability profiles through the plug, aligned to match Figure 5; the x-axis indicates distance from the tunnel surface (i.e. going

deeper into the rock). It is seen that the damage zone extends  $\sim 10$  mm for this tunnel location, and the permeability variation is well correlated with the porosity. In the transition from damaged to native regime, porosity changes from 9% to 12% ( $\sim 25\%$  variation), whereas permeability changes from 30 mD to 160 mD ( $\sim 530\%$  variation).

To highlight the shaped charge explosion impact on pore structure, a 2D plane from the damage zone is compared to one from the native rock region in Figure 7, where the pore space is colored by local pore size (min. blue, max. red). Fewer large pores and more small pores are seen in the damaged rock. Pore size distributions for native and damaged rock are quantitatively compared in Figure 8, which plots volume fraction of pore space occupied by pores of radius  $R$  versus  $R$ ; the shift to smaller pores in the damage zone is readily seen. Note that a significant volume fraction is associated with small pores, with the most frequent pore radius having 2-3 grid cells; this highlights the importance of achieving accurate simulated flow behavior for such coarse resolution conditions.

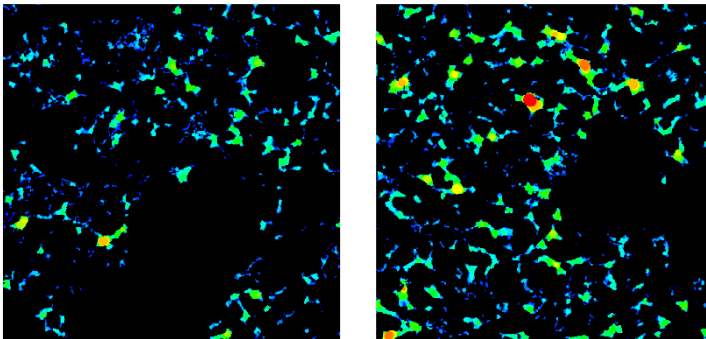


Figure 7: Pore space colored by local pore size for damaged rock (left) and native rock (right).

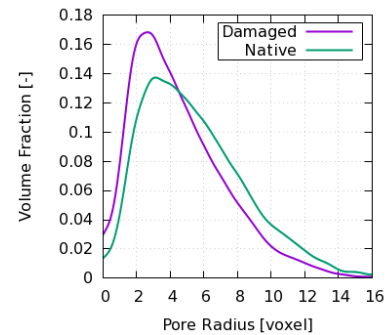


Figure 8: Pore size distributions.

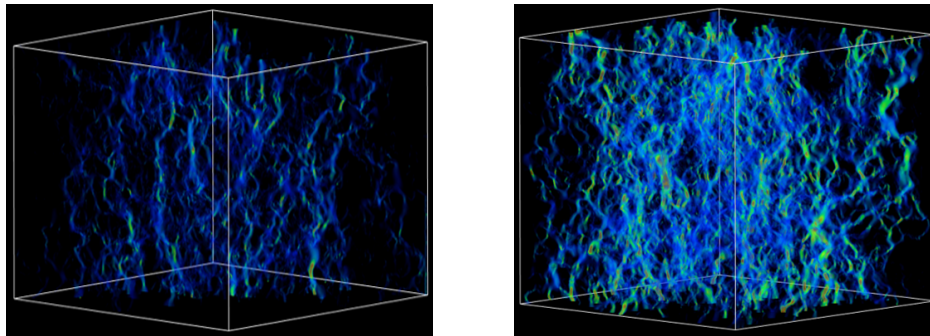


Figure 9: Visualization of local velocity field in damaged rock region (left) and native rock region (right).

In Figure 9, the local velocity field is visualized for damaged rock compared to native rock, using opacity to emphasize the high velocity locations. The overall flow in the damaged rock appears lower, with fewer connected paths involved in contributing significantly to the flow conduction.

## CONCLUSION

A lattice-Boltzmann based method incorporating the surfel-based boundary technique is examined for application to digital rock pore-scale flow simulation. A grid resolution study of flow past cubic centered packed spheres demonstrates accurate prediction of single-phase absolute permeability with resolution as low as one grid cell across the inscribed (effective pore) radius. The ability to remain accurate at such coarse resolution is highly advantageous for minimizing the computational cost of digital rock cases where it is important to have a large enough field of view to simulate a statistically representative region of pore space. Application to a real digital rock study characterizing the damage zone around a perforation tunnel is demonstrated using a micro-CT image of a sample plug from the tunnel. Profiles of porosity and absolute permeability through the damage zone out to native rock are determined. Visualization of pore size distribution and flow within the pore space of the rock are presented and highlight the observed trends. Most of the pore space is resolved with a small number of grid cells per effective pore radius, with the pore size distribution peaking at about 3 grid cells; therefore, the demonstrated accuracy of the numerical scheme at such coarse resolution is of critical importance to the reliability of the real rock simulation results.

## REFERENCES

1. S. Chen, G. Doolen, "Lattice Boltzmann method for fluid flows", *Annu. Rev. Fluid Mech.* 30:329 (1998)
2. S. Chen, H. Chen et al, "Lattice Boltzmann model for simulation of magnetohydrodynamics", *Phys. Rev. Lett.* 67, 3776 (1991)
3. H. Chen, S. Chen, W. Matthaeus, "Recovery of the Navier-Stokes equations using a lattice-gas Boltzmann method", *Phys. Rev. A* 45, 5339 (1992)
4. Y. Qian, D. d'Humieres, P. Lallemand, "Lattice BGK models for Navier-Stokes equation", *Europhys.Lett* 17, 479 (1992)
5. H. Chen, C. Teixeira, K. Molvig, "Digital physics approach to computational fluid dynamics: some basic theoretical features", *Intl. J. Mod. Phys. C* 9, No.8, 1281 (1998)
6. H. Chen, S. Kandasamy et al, "Extended-Boltzmann Kinetic Equation for Turbulent Flows", *Science*, Vol 301, Issue 5633, 633 (2003)
7. H. Andra, N. Combaret et al, "Digital rock physics benchmarks – part II: Computing effective properties", *Comp. Geosci.* 50, 33 (2013)
8. H. Andra, N. Combaret et al, "Digital rock physics benchmarks – part I: Imaging and segmentation", *Comp. Geosci.* 50, 33 (2013)
9. X. Shan, H. Chen, "Lattice Boltzmann model for simulating flows with multiple phases and components", *Phys Rev E* 47, 1815 (1993)
10. H. Chen, C. Teixeira, K. Molvig, "Realization of Fluid Boundary Conditions via Discrete Boltzmann Dynamics", *Int. J. Mod. Phys. C* 09, 1281 (1998)
11. H. Chen, "Volumetric formulation of the lattice Boltzmann method for fluid dynamics: Basic concept", *Phys. Rev. E* 58:033955 (1998)
12. X. He, and G. Doolen, "Lattice Boltzmann method on curvilinear coordinates system: vortex shedding behind a circular cylinder", *Phys. Rev. E* 56, 434 (1997).
13. I. Ginzburg, D. d'Humieres, "Multireflection boundary conditions for lattice Boltzmann models", *Phys. Rev. E* 68:066614 (2003)
14. C. Pan, L. Luo, C. Miller "An evaluation of lattice Boltzmann schemes for porous medium flow simulation", *Comp. & Fluids* 35, 898 (2006)
15. N. Osarumwense, R. Satti et al, "Shaped Charge Selection and Underbalance Optimization Using the Perforation Flow Laboratory for Deepwater Subsea Wells in Offshore Africa", 2014 SPE Deepwater Drilling & Completions Conf, SPE-170259-MS.
16. H. Dong and M. Blunt, "Pore-network extraction from micro-computerized-tomography images", *Phys. Rev. E* 80:036307 (2009)

## SURFACE RELAXIVITY ESTIMATION AND NMR-MICP MATCHING IN DIFFUSIONALLY COUPLED ROCKS

Pedro Mesquita, Andre Souza, Giovanna Carneiro, Austin Boyd, Flavio Ferreira, Patrick Machado, Schlumberger Brazil Research and Geoengineering Center, Vivek Anand, Schlumberger Houston Formation Evaluation, Lawrence Schwartz, Consultant

*This paper was prepared for presentation at the International Symposium of the Society of Core Analysts held in Snowmass, Colorado, USA, 21-26 August 2016*

### ABSTRACT

The surface relaxivity,  $\rho$ , is one of the most important parameters in NMR petrophysics, since it scales NMR relaxation time measurements of fluid saturated rocks to their pore size distributions. NMR-MICP matching techniques can be used to obtain an estimation of  $\rho$ , but in general they are very dependent on an optimal correlation between these two measurements, thus are not appropriate in cases where the NMR measurements are heavily affected by diffusional coupling between micro and macro pores. Simulations of the NMR  $T_2$  relaxation time phenomena were conducted using a coupled dual porosity model calibrated to match real  $T_2$  distributions of three carbonate samples. Once calibrated, the simulations were then repeated with the same parameters, but without allowing diffusional coupling between the micro and macro pores of the model. The results of the decoupled simulations showed better correlation with MICP data for these carbonates, and were used to improve the estimation of  $\rho$  using NMR-MICP matching techniques. Furthermore, a diffusional coupling parameter was calculated based on the model parameters, to evaluate the strength of diffusional coupling of these carbonates.

### INTRODUCTION

In Nuclear Magnetic Resonance (NMR) petrophysics, transversal relaxation time ( $T_2$ ) measurements of 100% brine saturated rocks are commonly used to estimate their pore size distribution, which then can provide reasonable estimations for the permeability ( $k$ ), irreducible water saturation ( $S_{wi}$ ) and other petrophysical properties. This approach is valid when four main assumptions are applicable: fluid's relaxation within pores occurs in the fast diffusion regime; diffusion and bulk relaxations are negligible; the diffusion coupling effect is negligible; and surface relaxivity is homogeneous throughout the pore walls [1]. By considering these assumptions, the pore size distribution of the pore system is related to  $T_2$  as follows:

$$\frac{1}{T_2} = \rho_2 \left( \frac{S}{V} \right)_{pore} \quad (1)$$

where  $\left( \frac{S}{V} \right)_{pore}$  is the surface-to-volume ratio of the pores and  $\rho_2$  is the transverse surface relaxivity. While  $(S/V)_{pore}$  is representative of the pore size, the surface relaxivity

parameter is related to the strength of the fluid's magnetic interaction with the pore walls, which causes the relaxation phenomena [2].

Equation 1 shows the importance of  $\rho_2$  for NMR petrophysics, since it scales  $T_2$  measurements with pore size. For simple lithologies,  $\rho_2$  is commonly considered to be homogeneous for each formation and several NMR predictions, such as the classical SDR permeability equation ( $k_{SDR}$ ) and Swi, can be reasonably estimated without knowing the actual value for  $\rho_2$ . However, in heterogeneous rocks with complex lithologies, like carbonates, variations of  $\rho_2$  may occur in small scales within a formation and the lack of information of this parameter may result in poor accuracy of the NMR predictions.

One of the first methods developed for estimating  $\rho_2$  from rock cores consists in correlating in a common dimension  $T_2$  distributions measurements with pore throat distributions obtained from the Mercury Injection Capillary Pressure technique (MICP). In this case, it is assumed that the pore geometry in the pore system is predominantly cylindrical, thus  $T_2$  and throat radius ( $R_t$ ) can be correlated through equation 1 by [3]:

$$\left(\frac{S}{V}\right)_{cylinder} = \frac{2\pi R_t l}{\pi R_t^2 l} = 2^*/R_t \rightarrow R_{t_{cylinder}} = 2\rho_s T_2 \quad (2)$$

where  $\rho_s$  is an effective surface relaxivity and  $l$  is the length of the cylinder. The value of  $2^*$  is the number that converts the  $(S/V)_{pore}$  term from equation 1 into the pore radius, called pore shape factor. The effective relaxivity  $\rho_s$  is then adjusted as the value that maximizes the cross-correlation (CC) between the  $T_2$  and  $R_t$  distributions, using:

$$CC(\rho_2) = \sum_i A_{Hg}(r_i) \cdot A_{NMR}(r_i = 2\rho_s T_2) \quad (3)$$

where  $A_{Hg}$  is the amplitude of the  $R_t$  distribution, and  $A_{NMR}$  is the amplitude of the  $T_2$  distribution scaled by  $2\rho_s$ . Although the NMR-MICP matching provides a reasonable estimation of  $\rho$ , it relies on the optimal correlation between these two techniques. So, it is dependent on the ability each technique has to reflect the actual pore size and pore throat distributions of the rock. Considering this, directly matching  $T_2$  and  $R_t$  may not be best approach in cases where the pore's saturating fluid dynamics is under a strong diffusional coupling between micro and macro pores, a situation that enhances the diffusional coupling effect. In these cases, diffusional coupling mixes the NMR magnetic response of coupled pores with different sizes, causing it to lose its correspondence to the actual pore size. Because of this, one must consider the strength of the diffusional coupling effect before applying the NMR-MICP matching and calculating  $\rho_s$ .

## NMR SIMULATIONS IN DUAL POROSITY SYSTEMS

In order to understand the diffusional coupling effect in complex porous systems, simulations of the NMR  $T_2$  relaxation time, developed by Ramakrishnan et al [6], were applied in porous media models with porosity mixed between interconnected micro- and macro-pores. These simulations use random walk techniques to mimic the saturating fluid's diffusion, in which each particle (called "walker") represents a group of fluid

molecules moving randomly inside pores. The simulation starts with the walkers being placed randomly in the model's porous space, with an initial energy that represents the magnetic moment. The random walking is then performed in a stepwise fashion, where the distance traveled by each step takes an amount of time related to the self-diffusion coefficient of the fluid. When a walker meets a pore wall, this energy can be decreased by a factor or annihilated by chance, where both approaches depend on the value of  $\rho$  [6,7].

The dual porosity model used in this work is the Micro-Grain Consolidation Model ( $\mu$ GC) [6,7], which is a cubic packing of overlapping spherical small grains with radius  $R_{small}$ , that composes bigger spherical grains centered at each corner of the cube, with radius  $R_{big}$ . This emulates the rock matrix as a network of bigger grains with intra-granular micro porosity, while the macro porosity consists in the inter-granular space of the bigger grains. Micro- and macro- porosity fractions are controlled by  $R_{small}$  and  $R_{big}$ , while the sizes of the micro- and macro- grids control the interconnectivity of the pores. An advantage of using this model is that we can introduce an artificial 'barrier' that prevents walkers from entering or exiting the micro or macro pores. This makes it possible to simulate the NMR experiment with or without diffusional coupling between the two domains. This approach is useful to infer how the MICP and NMR relaxation times correlate with each other when the diffusional coupling phenomenon is turned off.

## DIFFUSIONAL COUPLING STRENGTH

Diffusional coupling between micro and macro pores has been modeled by Anand et al [4], in which the fluid's molecules relaxes at the surface of flake-like micro-pores while diffusing between micro and macro pores. The model's coupled pore geometry is defined by its half-length and half-width, named  $L1$  and  $L2$  respectively, and the micro-porosity fraction  $\beta$ . In the work, the authors introduced a coupling parameter  $\alpha$ , described by:

$$\alpha = \beta\eta\mu \quad (4)$$

where  $\eta$  is  $L2/L1$  and  $\mu$  is the Brownstein Number [5].  $\mu$  can be estimated by calculating  $L2\rho/D$ , where  $D$  is the self-diffusion coefficient of the fluid ( $2.5 \times 10^{-9} \mu\text{m}^2/\text{s}$  for water at 25°C). The study also related this diffusional coupling model to the  $\mu$ GC by having  $L1 = R_{small}$  and  $L2 = R_{big}$ , in order to apply the model for carbonates. Furthermore,  $\alpha$  is described as being inversely proportional to diffusional coupling strength.

## RESULTS

To evaluate the described methodology, three carbonate rock cores were chosen, MICP measured, NMR  $T_2$  measured (as described in [2]) and simulated using the  $\mu$ GC model described above. The random walk simulations were written in Fortran™ language and the micro and macro grains radius  $R_{small}$  and  $R_{big}$  were determined by matching the micro- and macro-porosity fractions from the  $\mu$ GC model with the ones observed in the MICP distributions. These values are shown in Table 1. Other parameters of the simulation, such as micro- and macro-grid sizes, were adjusted so that the simulation results best match with the experimental  $T_2$  distributions. Figures 1, 2 and 3 show the distributions of

measured and simulated  $T_2$  and MICP from the selected carbonate samples, named respectively as H11, H23 and Silurian Dolomite. All samples showed (in the left side of the figures) excellent agreement between experimental (full blue curves) and simulated (called “coupled”, the green dashed curves) distributions. As described above, the random walk algorithm was executed again using the same parameters, but restricting the diffusive process of the walker: now, it is not allowed to leave the pore that they are randomly probing. The results of the decoupled simulations are shown on the figures as the black dashed curves called “uncoupled”. The difference between decoupled and real  $T_2$  distributions suggests that when coupled, the  $T_2$  distribution’s modes of micro- and macro-porosities (small and long  $T_2$ ’s, respectively) are averaged in a degree that indicates diffusional coupling. Through this approach and comparing it with the shape of the MICP distributions (right side of the figures), it is clear that samples H11 and H23 have higher diffusional coupling strength, while the Silurian Dolomite have lower effect.

In order to estimate  $\rho_e$ , both decoupled and real  $T_2$  distributions were matched with MICP distributions using the method described in equation 3. The matched distributions are shown together in the right side of the figures, while the values of  $\rho_e$  obtained from this matching are presented in Table 1. The results show that the decoupled distributions have much better correlation with MICP than the experimental  $T_2$  distributions, suggesting that matching decoupled  $T_2$  distributions with MICP  $R_t$  distributions provides a more robust and accurate  $\rho_e$  values. Both the H23 and Silurian Dolomite samples showed excellent correlations between decoupled  $T_2$  and  $R_t$ , while the micro- and macro-modes from the decoupled simulation of the sample H11 did not match exactly with the ones from MICP. This fact can be explained if both porosities did not match for a unique choice of  $\rho_e$  and pore shape factor, or the pore system have a variable pore body-to-throat ratio (BTR). On the other hand, the excellent correlations in the Silurian Dolomite and H23 samples suggest that  $\rho_e$  and the pore shape factor are constants throughout the cores (not being a function of pore size). These are interesting cases where the analysis of decoupled  $T_2$  distributions can provide significant insight about the properties of the porous system.

After matching the distributions, the  $\alpha$  parameter was calculated using the  $R_{small}$  and  $R_{big}$  from the simulations, the micro porosity fraction observed in the MICP distribution and the Brownstein number estimated with  $\rho_e$  from the matching of the decoupled distributions (with equation 3). The results showed that the initial supposition regarding the comparison between strengths of diffusional coupling on the samples were correct, as H11 and H13 shows more coupling effect ( $\alpha$  equals to 1.38 and 2.37 respectively), while the Silurian Dolomite shows much less effect ( $\alpha = 12.99$ ).

## CONCLUSION

The presented study showed that simulated decoupled  $T_2$  distributions produces better matching with  $R_t$  distributions obtained from MICP curves, thus providing a more reliable estimation for surface relaxivity for carbonates. In cases where this approach

does not generate an exact correlation between decoupled  $T_2$  and MICP, it was inferred that different pore size families on complex samples may present different pore shapes, BTR or surface relaxivities between them. This subject is important to the study of pore systems. The diffusional coupling parameter was calculated successfully using sample's parameters, showing indeed an inverse relation with the strength of the diffusional coupling effect on  $T_2$  distributions. This shows that the  $\alpha$  parameter can be used to estimate the coupling strength and that it helps to validate the  $T_2$  distribution as a reliable estimation of pore size.

## ACKNOWLEDGEMENTS

The authors would like to thank Fluminense Federal University and Schlumberger Ltd. for the support and permission to publish this work.

## REFERENCES

- 1- Lonnes, S., Guzman-Garcia, A., Holland, R., "NMR Petrophysical Predictions on Cores", *44th SPWLA Annual Logging Symposium*, (2003) paper DDD.
- 2- Souza, A., Carneiro, G., Zielinski, L., Polinski, R., Schwartz, L., Hurlimann, M., Boyd, A., Rios, E., Trevizan, W., Santos, B., Machado, V., Azeredo, R., "Permeability Prediction Improvement Using 2D Diffusion- $T_2$  Maps", *54th SPWLA Annual Logging Symposium*, (2013) paper U.
- 3- Marschall, D., Gardner, J. S., Mardon, D., Coates, G. R., "Method for Correlating NMR Relaxometry and Mercury Injection Data", *SCA Conference*, (1995) 9511.
- 4- Anand, V., Hirasaki, G. J., "Diffusional Coupling Between Micro and Macroporosity for NMR Relaxation in Sandstones and Grainstones", *Petrophysics*, (2007) v. 48, n. 4, 289-307.
- 5- Brownstein, K., Tarr, C., "Importance of Classical Diffusion in NMR Studies of Water in Biological Cells", *Physical Review A*, (1979) v. 19, n. 6, 2446-2453.
- 6- Ramakrishnan, T., Schwartz, L., Fordham, E., Kenyon, W., Wilkinson, D., "Forward Models for Nuclear Magnetic Resonance in Carbonate Rocks", *The Log Analyst*, (1999) v. 40, 260-270.
- 7- Carneiro, G., Souza, A., Boyd, A., Schwartz, L., Song, Y., Azeredo, R., Trevizan, W., Santos, B., Rios, E., Machado, V., "Evaluating Pore Space Connectivity by Diffusive Coupling", *55th SPWLA Annual Logging Symposium*, (2014) paper AA.

Table 1: Characteristic parameters used to, and extracted from, the experimental analysis and simulations performed.

Sample Name	H11	H23	Silurian Dolomite
Porosity (p.u.)	28.8	28.1	18.3
MICP micro-porosity fraction (%)	40.0	45.0	41.8
$R_{small}$ ( $\mu\text{m}$ )	1.29	1.27	1.34
$R_{big}$ ( $\mu\text{m}$ )	122.68	124.46	129.75
NMR-MICP matched $\rho_e$ (coupled) ( $\mu\text{m/s}$ )	1.72	1.76	9.78
NMR-MICP matched $\rho_e$ (decoupled) ( $\mu\text{m/s}$ )	0.74	1.08	6.17
Estimated Brownstein number	0.036	0.054	0.320
$\alpha$	1.38	2.37	12.99

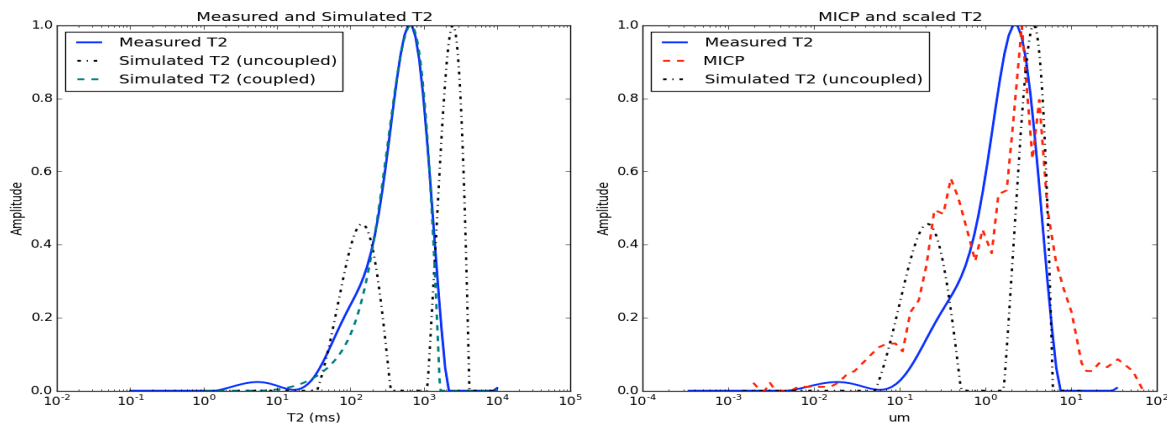


Figure 1: Data from the sample “H11”. Left: measured and simulated  $T_2$  distributions and right: MICP distribution with  $T_2$  measured and simulated, scaled by their optimal  $\rho_E$ .

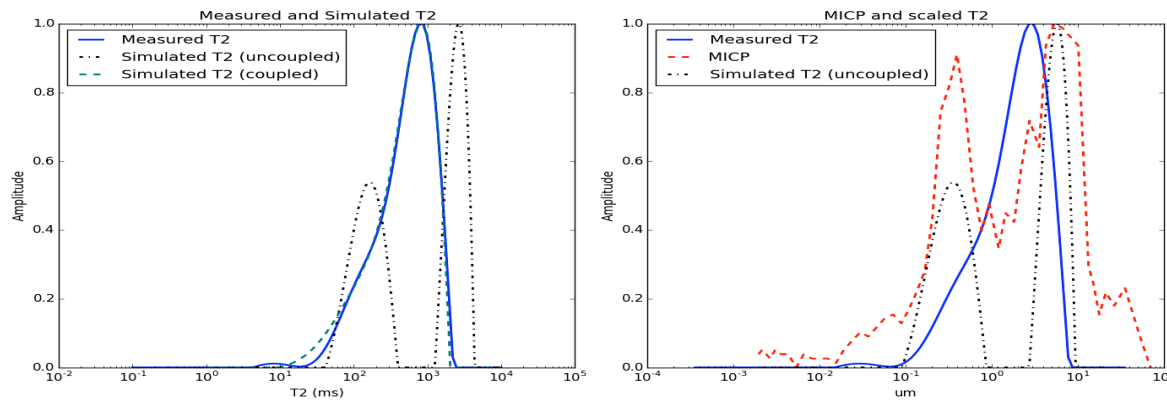


Figure 2: Data from the sample “H23”. Left: measured and simulated  $T_2$  distributions and right: MICP distribution with  $T_2$  measured and simulated, scaled by their optimal  $\rho_E$ .

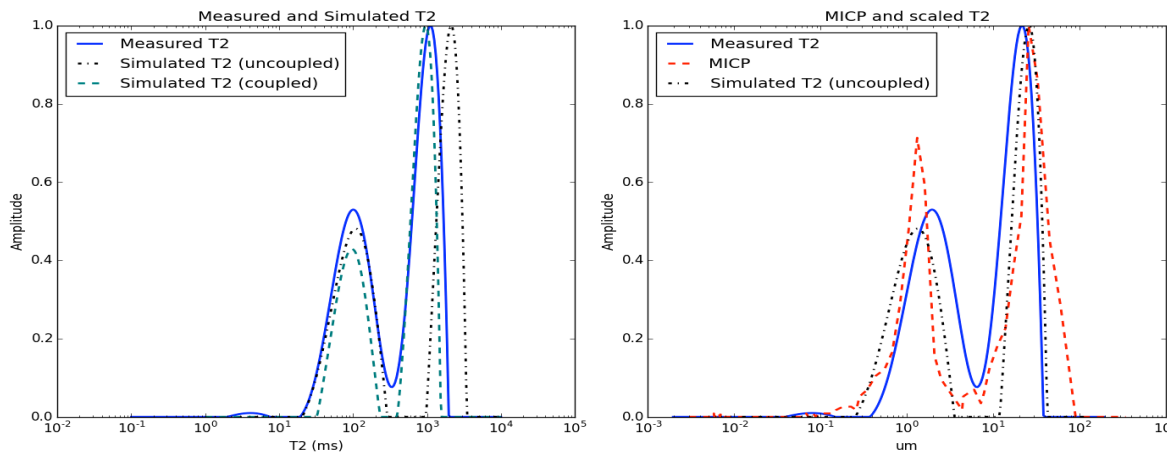


Figure 3: Data from the sample “Silurian Dolomite”. Left: measured and simulated  $T_2$  distributions and right: MICP distribution with  $T_2$  measured and simulated, scaled by their optimal  $\rho_E$ .

# A NOVEL RELATIVE PERMEABILITY MODEL - A TWO-FLUID APPROACH ACCOUNTING FOR SOLID-FLUID AND FLUID-FLUID INTERACTIONS

Dag C. Standnes<sup>1</sup>, Steinar Evje<sup>1,2</sup>, Pål Ø. Andersen<sup>1,2</sup>

<sup>1</sup>Department of Petroleum Engineering, University of Stavanger, Norway

<sup>2</sup>The National IOR Center of Norway, Norway

*This paper was prepared for presentation at the International Symposium of the Society of Core Analysts held in Snowmass, Colorado, USA, 21-26 August 2016*

## ABSTRACT

A novel model is presented for estimating relative permeabilities (RPs). It is derived based on a two-fluid Stokes formulation and friction terms due to phase interaction at the fluid-fluid and fluid-rock interfaces. The model gives consistent relationships between solid-fluid interaction terms, interstitial fluid velocities and corresponding RPs all vs. water saturation. Analysis of steady-state co-current flow predicts that fluid-fluid interaction gives a physical origin for RPs being dependent on viscosity ratio: A viscosity contrast can enhance the difference between the interstitial velocities and thus affect the drag exerted between the phases. The slower phase is accelerated as reflected in increased RP, and vice versa. Analysis of steady-state counter-current flow shows that counter-current RPs are lower than corresponding co-current curves for all intermediate water saturation values when fluid-fluid interaction is present. The model seems to capture essential features of two-phase flow in porous media. It looks like an attractive tool for analysis, understanding and interpretation of two-phase RP data in terms of the physical processes involved, i.e. solid-fluid and fluid-fluid interactions. Validation of the model should be pursued using high quality measurements where interaction terms and experimental artifacts, such as capillary end effects, are adequately quantified by simulation.

## INTRODUCTION

The simultaneous flow of two immiscible phases (in this work assumed to be oil (*o*) and water (*w*)) through a porous medium is commonly described by the Darcy velocity for each phase  $v_w, v_o$  [m/s] as:

$$v_o = -\lambda_o \frac{dP_o}{dx}, \quad v_w = -\lambda_w \frac{dP_w}{dx}, \quad \lambda_o = \frac{kk_{ro}}{\mu_o}, \quad \lambda_w = \frac{kk_{rw}}{\mu_w}, \quad (1)$$

where  $k_{ri}$ , [-],  $P_i$  [N/m<sup>2</sup>] and  $\lambda_i$  [N s/m<sup>4</sup>] ( $i=o,w$ ) are relative permeabilities (RPs), phase pressures and phase mobilities.  $k$  [m<sup>2</sup>] is the permeability. Hence, the flow of oil and water is assumed to take place in separate channels and no interaction between the two fluid phases is accounted for through fluid-fluid interaction terms. Experimental observations and theoretical analysis have, however, indicated that fluid-fluid interactions could be significant and important for the understanding of multi-phase flow in porous media [1, 2, 5, 7, 10]. We derive a novel RP formulation emphasizing this interaction.

## THEORY

In the following we assume the oil and water saturations,  $s_o$  and  $s_w$ , are normalized between their residual values, i.e. from 0 to 1. General momentum equations (ignoring acceleration and external body forces) for oil and water are given by [4, 9]:

$$0 = \nabla \cdot (s_o \sigma_o) + P_o \nabla s_o + F_{ow} + M_{om}, \quad (2)$$

$$0 = \nabla \cdot (s_w \sigma_w) + P_w \nabla s_w - F_{ow} + M_{wm}. \quad (3)$$

$F_{ow}$  [N/m<sup>3</sup>] denotes the drag that the water phase exerts on the oil. The oil exerts an equal and opposite drag  $-F_{ow}$  on the water phase. Similarly,  $M_{om}$  and  $M_{wm}$  [N/m<sup>3</sup>] represent interaction (drag) between fluid and pore walls (solid matrix), respectively, for oil and water. The terms  $P_o \nabla s_o$  and  $P_w \nabla s_w$  arise from an averaging process, see [3, 4] for details.

The stress term  $\sigma_i$  [N/m<sup>2</sup>] is conventionally given as the sum of the stationary isotropic stress associated with the hydrostatic pressure  $P_i$  [N/m<sup>2</sup>] and the viscous stress tensor  $\tau_i$  [N/m<sup>2</sup>] such that  $\sigma_i = -P_i \delta + \tau_i$  ( $\delta$  is the identity matrix). The viscous stress  $\tau_i$  is neglected in the following since our main purpose is to gain insight into the role of the interaction terms  $F_{ow}$ ,  $M_{om}$  and  $M_{wm}$ . They are modelled as follows (see also [5, 10]):

$$F_{ow} = \hat{k}(u_w - u_o), \quad M_{im} = -\hat{k}_i u_i, \quad (i = o, w) \quad (4)$$

where the terms  $\hat{k}$ ,  $\hat{k}_i$  [N s/m<sup>4</sup>] remain to be determined. Hence, the momentum equation for horizontal, collinear flow of two phases on the macroscopic scale restricted to a one-dimensional setting can be formulated as:

$$s_o P_{ox} = -\hat{k} u_o - \hat{k}(u_o - u_w), \quad (5)$$

$$s_w P_{wx} = -\hat{k} u_w + \hat{k}(u_o - u_w), \quad (6)$$

$P_{ox}$  and  $P_{wx}$  are partial derivatives of oil and water phase pressures with respect to space coordinate  $x$ . The effect of a  $\hat{k} > 0$  is that the faster moving fluid phase will be slowed down and vice versa for the slower moving phase due to transfer of momentum. Non-coupled flow equations are regained for  $\hat{k} = 0$ . The interstitial velocities  $u_o$ ,  $u_w$  are related to the Darcy phase velocities  $v_o$ ,  $v_w$  by:

$$v_o = s_o u_o \phi, \quad v_w = s_w u_w \phi, \quad (7)$$

where  $\phi$  is the fractional porosity. It is furthermore quite obvious that the solid-fluid friction terms  $\hat{k}_o$ ,  $\hat{k}_w$  should respect the relation  $\hat{k}_i \propto \mu_i / k$  ( $i = o, w$ ), to be consistent with standard porous media flow modeling. We assume the following form:

$$\hat{k}_o = I_o s_o^\beta \frac{\mu_o}{k} \phi, \quad \hat{k}_w = I_w s_w^\alpha \frac{\mu_w}{k} \phi, \quad \hat{k} = I s_w s_o \frac{\mu_w \mu_o}{k}. \quad (8)$$

$I_o$ ,  $I_w$  [-] and  $I$  [m<sup>2</sup>/N s] are interaction term coefficients. Note that the friction terms are related to the interfacial areas [6], which here are assumed to be related to the saturations, expressed implicitly through (8). For co-current flow, we assume equal phase pressure gradients and no capillary pressure effects and obtain effective  $k_{ri}$  from solving (1)+(5-8):

$$k_{rw} = \frac{I_o s_w s_o^{\beta-1} + (I/\phi) \mu_w [s_w^2 + s_w s_o]}{I_w I_o s_w^{\alpha-1} s_o^{\beta-1} + (I/\phi) [I_w s_w^\alpha \mu_w + I_o s_o^\beta \mu_o]}, \quad (9)$$

$$k_{ro} = \frac{I_w s_w^{\alpha-1} s_o + (I/\phi) \mu_o [s_o^2 + s_w s_o]}{I_w I_o s_w^{\alpha-1} s_o^{\beta-1} + (I/\phi) [I_w s_w^\alpha \mu_w + I_o s_o^\beta \mu_o]}.$$

For co-current flow, the Darcy velocities are related to the volumetric injection rate  $Q$ :

$$v_o + v_w = v_T = \text{constant} = \frac{Q}{A}, \quad (\text{co-current}) \quad (10)$$

where  $A$  is the cross-sectional area of the porous medium. The interstitial velocities can then be calculated by combining (1)+(7)+(9) to:

$$u_o = \frac{v_T}{\phi} \frac{\lambda_o}{s_w \lambda_w + \lambda_o}, \quad u_w = \frac{v_T}{\phi} \frac{\lambda_w}{s_w \lambda_w + \lambda_o}. \quad (11)$$

Table 1 Parameters for illustration of fluid-fluid interaction

VARIABLE	WITH FLUID-FLUID INTERACTION	NO FLUID-FLUID INTERACTION
$\mu_{\text{oil}}$	1.0	1.0
$\mu_{\text{water}}$	1.0	1.0
Oil-solid friction coefficient $I_o$	1.0	1.0
Water-solid friction coefficient $I_w$	4.0	4.0
Fluid-fluid interaction coefficient $I$	1.0	0.0
Water saturation exponent $\alpha$	0.3	0.3
Oil saturation exponent $\beta$	0.3	0.3

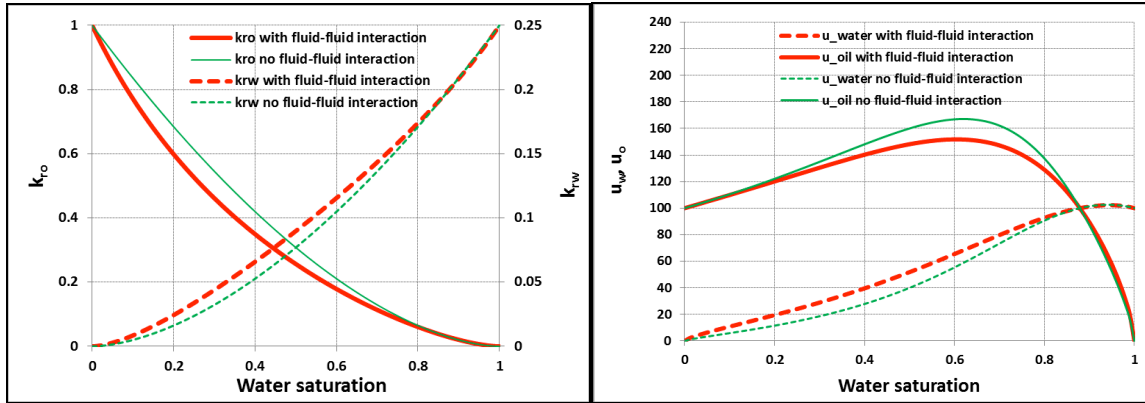


Fig. 1. Illustration of fluid-fluid interaction based on data in Table 1. Left: RP curves from (9) with (red) and without (green) fluid-fluid interaction ( $I=1$  or  $0$ ). Right: Corresponding fluid phase interstitial velocities from (11).

For counter-current flow, and now using equal, but *opposite* phase pressure gradients (assuming no capillary pressure effects) we obtain effective  $k_{ri}$  from solving (1)+(5-8):

$$k_{ro} = \frac{I_w s_w^{\alpha-1} s_o + (I/\phi) \mu_o [s_o^2 - s_w s_o]}{I_w I_o s_w^{\alpha-1} s_o^{\beta-1} + (I/\phi) [I_w s_w^\alpha \mu_w + I_o s_o^\beta \mu_o]}, \quad (12)$$

$$k_{rw} = \frac{I_o s_w s_o^{\beta-1} + (I/\phi) \mu_w [s_w^2 - s_w s_o]}{I_w I_o s_w^{\alpha-1} s_o^{\beta-1} + (I/\phi) [I_w s_w^\alpha \mu_w + I_o s_o^\beta \mu_o]}.$$

With no fluid-fluid interactions ( $I=0$ ) the expressions both in (9) and (12) simplify to the standard (ST) Corey formulation:

$$k_{roST} = \frac{s_o^{2-\beta}}{I_o}, \quad k_{rwST} = \frac{s_w^{2-\alpha}}{I_w}. \quad (13)$$

## NUMERICAL INVESTIGATIONS

Two sets of parameters are listed in Table 1, the only difference being that the fluid-fluid interaction is 0 in one case. Without fluid-fluid interaction ( $I=0$ ) the RPs (9) correspond to standard Corey formulation, see (13). Considering Fig. 1, for water saturations  $s_w < 0.88$  the interstitial velocity of oil  $u_o$  is greater than that of water  $u_w$  (calculated from (11)), while for larger saturations the water travels faster. Including fluid-fluid interaction induces a momentum transfer between the phases and for water saturations less than 0.88 the oil phase is slowed down, while the water velocity has increased. This is reflected in increased RP of water at low saturations and reduced oil RP. The opposite occurs at saturations larger than 0.88, where the water velocity is higher (although less visible).

Table 2 Parameters for illustration of viscosity effects

VARIABLE	OIL VISCOSITY = 1	OIL VISCOSITY = 10
$\mu$ oil	1.0	10.0
$\mu$ water	1.0	1.0
Oil-solid friction coefficient $l_o$	1.0	1.0
Water-solid friction coefficient $l_w$	4.0	4.0
Fluid-fluid interaction coefficient $I$	1.0	1.0
Water saturation exponent $\alpha$	0.3	0.3
Oil saturation exponent $\beta$	0.3	0.3

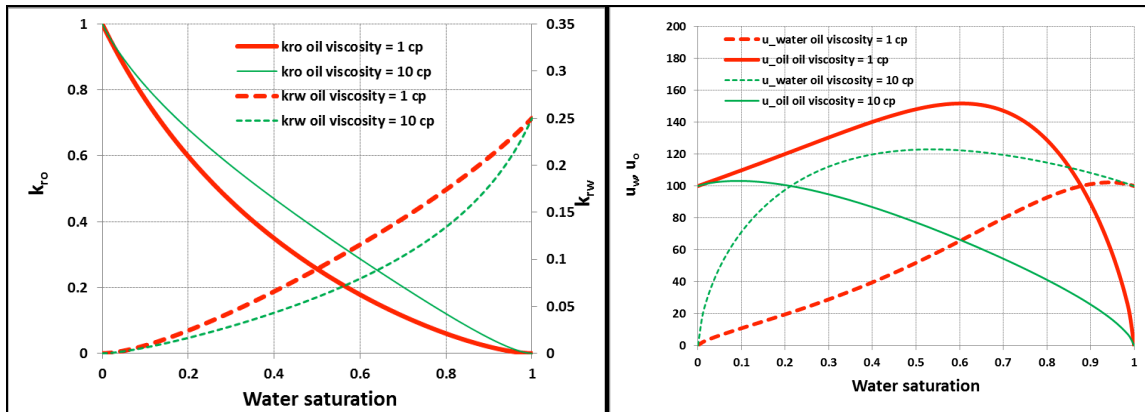


Fig. 2. Illustration of viscosity effects based on data in Table 2. Left: RP curves from (9) for oil viscosity of 1 cP (red curves) and 10 cP (green curves). Right: The corresponding interstitial velocities from (11).

Another set of input parameters to the RP model (9) is given in Table 2. The only difference is the oil viscosity (1 or 10 cP). Fluid-fluid interactions are included. Fig. 2 shows the RP curves and interstitial velocities. Both RP curves are affected by the viscosity change. The model predicts reduced oil and increased water interstitial velocities for the 10 cP case compared to the 1 cP case. This is expected since oil interstitial velocity is inversely proportional to oil viscosity for the same value of  $k_{ro}$ . Reduced oil velocity will at the same time increase the water interstitial velocity due to the condition of constant total Darcy velocity  $v_T$ . The more viscous fluid, which travels slower, is however, accelerated by the momentum transfer between the fluids and obtains a larger RP, while the opposite happens to the low viscous fluid. The expressions for  $k_{ro}$  and  $k_{rw}$

(9) show that an influence from fluid viscosities is possible only if there is fluid-fluid interaction ( $I > 0$ ). Such trends have been observed experimentally [10]. Further, it was seen in [8] that high oil viscosity increased the residual oil saturation,  $s_{orw}$ , and lowered the water RP in this point,  $k_{rw}(s_{orw})$ . Such end point effects are currently not included in the model. The extent at which RP curves in fact are viscosity dependent must be substantiated by simulation-evaluation accounting for artifacts such as capillary end effects.

Table 3 Parameters for illustration of flow direction effects

VARIABLE	COUNTER-CURRENT	CO-CURRENT
$\mu$ oil	3.0	3.0
$\mu$ water	1.0	1.0
Oil-solid friction coefficient $I_o$	1.0	1.0
Water-solid friction coefficient $I_w$	4.0	4.0
Fluid-fluid interaction coefficient $I$	1.0	1.0
Water saturation exponent $\alpha$	0.3	0.3
Oil saturation exponent $\beta$	0.3	0.3

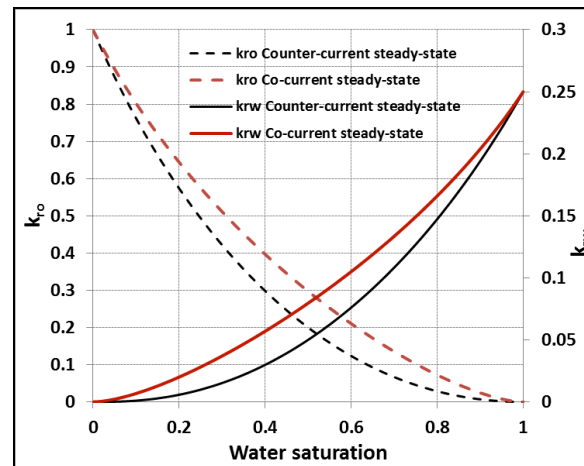


Fig. 3. Illustration of flow direction effects based on data in Table 3. Co- and counter-current steady-state RP functions predicted from (9) and (12), in red and black color, respectively.

Reported data in the literature [1, 2] indicate that counter-current RP curves are lower than the corresponding co-current curves. Table 3 contains equal parameter sets for simulation of co- and counter-current flow setups. It is seen in Fig. 3 that the predicted counter-current RPs are lower than the co-current permeabilities. By examining the expressions (9) and (12) it can be shown that this will always be the case, as long as fluid-fluid interaction is accounted for, i.e.  $I > 0$ . This observation naturally results from the increased drag obtained when the fluids flow counter-currently and decelerate each other.

## CONCLUSIONS

A model for flow in porous media was derived from momentum balance equations accounting fluid-fluid and fluid-rock interactions. Relative permeabilities were predicted.

- The momentum transfer between fluids increases the velocity of the slowly traveling fluid and slows down the fast traveling fluid. This is reflected in increased and reduced relative permeabilities of the respective phases.
- Viscosity changes can affect the relative permeabilities. The more viscous fluid slows down, but obtains higher relative permeability due to the drag from the faster traveling fluid, and vice versa.
- Counter-current relative permeabilities are lower than co-current relative permeabilities due to the greater flow resistance between the phases.
- The model should be validated further by comparison with high quality data and interpretation able to distinguish physical effects from experimental artifacts.

## ACKNOWLEDGEMENTS

The first author thanks Statoil ASA for supporting the adjunct prof. position at the University of Stavanger. The co-authors thank the Research Council of Norway and the industry partners of the National IOR Centre of Norway: ConocoPhillips Skandinavia AS, BP Norge AS, Det Norske Oljeselskap AS, Eni Norge AS, Maersk Oil Norway AS, DONG Energy A/S, Denmark, Statoil Petroleum AS, GDF SUEZ E&P NORGE AS, Lundin Norway AS, Halliburton AS, Schlumberger Norge AS, Wintershall Norge AS.

## REFERENCES

1. Bentsen, R.G. and A.A. Manai, "Measurement of concurrent and countercurrent relative permeability curves using the steady-state method", *AOSTRA J. Res.*, (1991) **7**, p. 169-181.
2. Bourbiaux, B.J. and F.J. Kalaydjian, "Experimental Study of Cocurrent and Countercurrent Flows in Natural Porous Media", *SPE RE*, (1990) **5**, p. 361-368.
3. Byrne, H.M. and M.R. Owen, "A new interpretation of the Keller-Segel model based on multiphase modeling", *J. Math. Biol.*, (2004) **49**, p. 604-626.
4. Drew, D.A. and L.A. Segel, "Averaged equations for two-phase flow", *Studies in Applied Mathematics*, (1971) **50** (3), p. 205-231.
5. Dullien, F.A.L. and M. Dong, "Experimental Determination of the Flow Transport Coefficients in the Coupled Equations of Two-Phase Flow in Porous Media", *Transport in Porous Media*, (1996) **25**, p. 97-120.
6. Hassanizadeh, S.M. and W.G. Gray, "Toward an improved description of the physics of two-phase flow", *Advances in Water Resources*, (1993) **16**, p. 53 – 67.
7. Liang, Q. and J. Lohrenz, "Dynamic Method of Measuring Coupling Coefficients of Transport Equations of Two-Phase Flow in Porous Media", *Transport in Porous Media*, (1994) **15**, p. 71-79.
8. Nejad, K.S., E.A. Berg and J.K. Ringen, "Effect of Oil Viscosity on Water / Oil Relative Permeability", (2011), SCA2011-12.
9. Rajagopal, K.R. and L. Tao, *Mechanics of mixtures*, World Science Publishing, Singapore, (1995).
10. Wang, J., M. Dong, K. Asghari, "Effect of Oil Viscosity on Heavy-Oil/Water Relative Permeability Curves", (2006), SPE 99763.

## **Study of the effect of heavy oil composition and temperature on wettability of reservoir rocks**

Shoulong Wang, Aifen Li, Ruigang Peng, Miao Yu, Shuaishi Fu  
School of Petroleum Engineering, China University of Petroleum (East China)

*This paper was prepared for presentation at the International Symposium of the Society of Core Analysts held in Snowmass, Colorado, USA, 21-26 August 2016*

### **ABSTRACT**

Wettability of reservoir rocks is a major factor that influences mobility and distribution of reservoir fluids (oil and water) within micro-pores. Also it has a significant impact on the determination of capillary pressure, relative permeability water flood behavior and simulated EOR. This paper presents a series of laboratory tests concerning the effects of heavy oil composition and temperature on rock wettability. Amott (imbibition and forced displacement) method was used to determine the wettability of reservoir rock in the presence of heavy oil (from Shengli Oilfield) and heavy oil + kerosene at temperatures of 40, 55, 70 and 80°C. The results show that the water-wet exponent of the rock tends to increase with the increase in kerosene composition. One possible explanation for this phenomenon may be that increase in the amount of kerosene results in a decrease in the fraction of polar compositions to be absorbed on the surface of rock. The experiments also showed that rock wettability in the presence of a fixed oil/kerosene ratio tends to shift to be water-wet as temperature increased from 40 to 80°C. This may be due to the aggravation of Brownian motion at higher temperatures, which results in less polar compositions to be adsorbed on rock surfaces. Besides, a sharp variation trend was demonstrated in rock wettability in the presence of different fractions of kerosene at a temperature of 40°C, whereas such variation at temperatures of 70 and 80°C exhibited a more subtle trend. It is suggested that a sensitive temperature may exist at which the amount of absorbed and desorbed polar components on the surface of reservoir rocks are balanced due to Brownian motion, making the change in wettability hardly to occur.

### **INTRODUCTION**

As is known to all, rock wettability has significant effect on the recovery properties including capillary pressure<sup>6</sup>, residual oil saturation<sup>5,10</sup>, and so on. An accurate understanding of rock wettability is crucial to determine the most efficient means of oil recovery, especially in the process of secondary and tertiary recovery. Generally speaking, both Amott and the USBM are the most widely used quantitative methods to measure the rock wettability, the results of which represent the average core wettability.

The Amott method<sup>4,6,9</sup> is widely applied to evaluate the rock wettability, which is a process of spontaneous imbibition depending on capillary pressure as a driving force. It is

remarkable that this method may arise some problems when the spontaneous imbibition is low, near neutral wettability. However, the USBM method has the advantage of quantifying wettability around intermediate wettability, while its disadvantage is that this method could only be used for a slug size core which is placed in centrifuge. Besides, the USBM method is also inaccurate for distinguishing intermediate wettability, such as mixed and fractional wettability.

Some studies indicate that wettability index is prominent reduced at lower initial water saturation. To eliminate the problem of saturation dependencies, the dynamic adsorption as an improved method is presented by Torske and Skauge<sup>2</sup>, Holbrook and Bernard<sup>1</sup>, et.al to measure rock wettability, which should preferably be performed with only one liquid phase present in the core. And n-heptanol and methylene blue are regarded relatively as the best choice to determine of the rock wettability for oil wet fraction and water wet fraction, respectively. Whereas the result by different methods ( Amott, USBM, Dynamic adsorption) is possibly different, which may be caused by the different conditions of core, such as physical properties, mineralogy.

The disadvantages for the Amott and the USBM method include time-consuming, high cost and not suitable for monitoring the change of rock wettability as a function of time or other experimental parameters. To overcome these disadvantages, the nuclear magnetic resonance (NMR) method<sup>12-17</sup> is more widely applied to provide information of rock wettability at arbitrary saturation (water or oil). Since NMR method was firstly presented by Brown and Fatt<sup>16</sup>, it has been gradually improved including data processing, computation formula and experimental reagents. And it is found that most of the previous studies were conducted by using refined or pure hydrocarbons on artificial unconsolidated formations, while it may neglect the effect of oil composition. This is not reasonable due to the fact that some polar components are well known to attach on the surface of rock and can change the rock wettability.

Investigations<sup>3,6,8, 10,11</sup> in recent years have been further and better conducted to research on the quantitative relationship between the rock wettability and various factors, such as the crude oil composition<sup>7</sup> and the rock type simultaneously, providing more accurate and convenient result among Amott, USBM and NMR method. However, few studies focus on the subtle change of rock wettability that performed with different oil composition under different temperature. One purpose of this paper is to discuss the effect of oil composition on rock wettability. In addition, the result of series of experiments is presented to indicate the influencing degree of different oil composition on rock wettability at different temperature.

## **Experiments**

If rock wettability is to be determined by core analysis, precautions should be taken to minimize the interference from experimental conditions, such as established routines, apparatus and reagents, and artificial error including volume measurement. This section mainly consists of sample preparation including the properties of rock and crude oil measurement, experimental procedure and the results of the data processing.

**Rock and Crude Oil Properties.** Solvent extraction procedures are observed to induce invariably changes of wettability when removes crude oil from the core. Therefore, it is not advised to use in core handling whose results are dependent on rock wettability.

Considering this factor and experimental conditions, many standard sintered cores (78mm long cylinders and 25mm diameters,  $K_g$  around  $1000 \times 10^{-3} \mu m^2$ ) with similar physical parameters, are used in this paper to eliminate the potential interference.

The heavy crude oil from Shengli Oilfield was used in this paper. The detailed analysis of crude oil including four components and the carbon distribution are shown in **Table 1** and **Fig 1**. Different mass fraction of kerosene was mixed with crude oil to obtain different oil compositions, whose viscosities were shown in **Table 2**.

**Table 1:** Four components of crude oil

Sample	Saturates, /%	Aromatics, /%	Resin, /%	Asphalt, /%
Cao 13-811 well	35.78	25.46	31.95	3.61

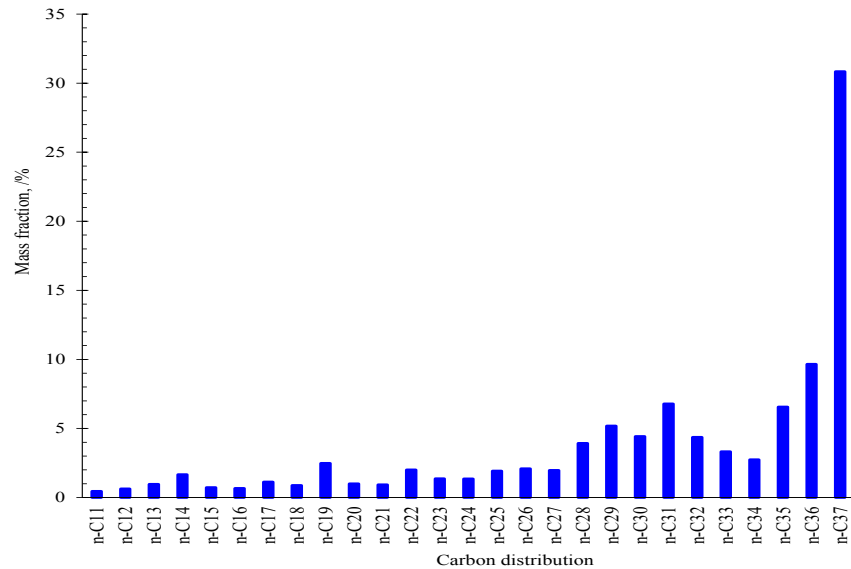


**Fig 1:** Carbon distribution of crude oil

**Table 2:** Measured viscosity of different oil composition

Temperature, °C \ Kerosene, w%	40	55	70	80
0	3622	1100	421	273
20	154.5	81.7	50.2	38.6
30	79.7	48	34	26.4
40	52.6	33.7	26	20
45	40.7	26.2	19	15.6

Note that the unit of above measured viscosity is mPa · s.

Evidence to date demonstrates that the components, especially the higher molecular weight ranges or polar in nature, absorbed on the surface of rock is the most plausible reason for wettability changes. And some studies indicate that the polar component in the light oil ranging from  $C_{10}$  to  $C_{12}$  may reduce the wettability of a water-wet rock. Therefore, as is shown in Fig 1, polar components that distributed from  $C_{26}$  to  $C_{37}$  in heavy oil are more crucial for the rock wettability. And different oil composition that primarily relatively different in the mass fraction of polar component in the crude oil were used to conduct this study.

**Measurement of rock wettability by Amott method.** All the core samples were water-saturated by vacuum first, and then oil flooding till the irreducible water saturation. The volume of drained oil by spontaneous imbibition should be recorded as  $V_{o1}$  after the core sample immersed 20h in water. Meanwhile, the volume of discharged oil by water driving to residual oil saturation should be recorded as  $V_{o2}$ . Then the rock wettability can be calculated by  $V_{o1}$  and  $V_{o2}$ . Besides, for the rubber containing some polar component in core holder may be affected at higher temperature, the experiment is performed at relative low temperatures, which is absolutely far below the maximum suitable temperature of rubber. The basic experimental parameters are shown in **Table 3** and the water-wet index under different conditions is shown in **Table 4**.

**Table 3:** Basic experimental parameters

T, °C Kerosene, w%	40			55			70			80		
	$S_{wc}$	$V_{o1}$	$V_{o2}$									
0	27.2	2.54	2.44	26.1	2.84	2.42	25.3	3.35	2.23	24.7	3.47	2.22
20	24.8	3.05	2.50	24.2	3.40	2.36	23.1	3.69	2.26	22.4	3.90	2.20
30	24	3.45	2.30	23.1	3.69	2.26	22.3	3.98	2.15	21.8	4.14	2.13
40	23.5	3.77	2.12	22.5	4.02	2.07	21.7	4.12	2.12	21.3	4.31	2.03
45	23	3.94	2.03	22.2	4.18	1.97	21.5	4.35	1.95	21	4.48	1.92

Note that the pore volume of all the experimental cores is around 10 ml (fluctuation range is 0.1ml) and the porosity is about 24%.  $S_{wc}$  represents of the initial water saturation.

**Table 4:** Water-wet index under different conditions

Temperature, °C Kerosene, w%	40	55	70	80	Standard deviation
0	0.51	0.54	0.6	0.61	0.041
20	0.55	0.59	0.62	0.64	0.034
30	0.6	0.62	0.65	0.66	0.024
40	0.64	0.66	0.66	0.68	0.014
45	0.66	0.68	0.69	0.7	0.014
Standard deviation	0.056	0.05	0.031	0.031	

Note that the rock wettability is calculated by  $V_{o1} / (V_{o1}+V_{o2})$ .

The results shown in **Table 4** indicate that the core wettability range from intermediate wettability to strong water-wet. When the mass fraction of kerosene keeps constant, the water-wet index increases with the increase of temperature. While the different of standard deviation under different kerosene concentrations states that the effect of temperature on wettability conducted at higher concentration is less than at low concentration, for the difference of oil properties at relative high concentration seems subtle. Another possible explanation for this phenomenon is that increasing the amount of kerosene results in a decrease in the fraction of polar compositions to be absorbed on the surface of rock.

When the temperature keeps constant, the water-wet index increases with the increase in mass fraction of kerosene. Besides, rock wettability in the presence of a fixed oil/kerosene ratio tends to shift to be water-wet as temperature increased from 40 to 80°C. This may be due to the aggravation of Brownian motion at higher temperatures, which results in less polar compositions to be adsorbed on rock surfaces. Besides, a sharp variation trend was demonstrated in rock wettability in the presence of different fractions

of kerosene at the temperature of 40°C, whereas such variation at temperatures of 70 and 80°C exhibited a more subtle trend.

## CONCLUSION

1 Various improved measurement and experimental details are conducted in this paper to obtain accurate rock wettability.

2 Temperature and oil composition are demonstrated to impact the rock wettability significantly. A sensitive temperature may exist at which the amount of absorbed and desorbed polar components on the surface of reservoir rocks is balanced due to Brownian motion, making the change in wettability hardly to occur.

## ACKNOWLEDGEMENTS

The authors would like to thank the fund by National Natural Science Foundation of China (51274226, 2013-2016) and Natural Science Foundation of Shandong Province (ZR2014EL017). Meanwhile, we would like to appreciate the help provided by research group for various experiments.

## REFERENCES

1. O. C. Holbrook, George G. Bernard, *Determination of Wettability by Dye Adsorption*. Society of Petroleum Engineers. 1958 213: p. 261-264.
2. Lisa Torske, Arne Skauge, *Core Wettability Measurement by Dynamic Adsorption*. Society of Petroleum Engineers. 1992: p. 105-118.
3. Gerald Hamon, *Field-Wide Variations of Wettability*. Society of Petroleum Engineers. 2000: p. 1-9.
4. G.J. Hirasaki, *Wettability: Fundamentals and Surface Forces*. Society of Petroleum Engineers. 1991 6(2): p. 217-226.
5. A.G. Mitchell, L.B. Hazell, K.J. Webb, *Wettability Determination: Pore Surface Analysis*. Society of Petroleum Engineers. 1990: p. 351-360.
6. J. E. Bobek, C. C. Mattax, M. O. Denekas, *Reservoir Rock Wettability-Its Significance and Evaluation*. 1958 213: p. 155-160.
7. J. Yan, H. Plancher, N.R. Morrow, *Wettability Changes Induced by Adsorption of Asphaltenes*. 1997 12(4): p. 259-266.
8. William Anderson, *Wettability Literature Survey- Part 2: Wettability Measurement*.
9. Society of Petroleum Engineers. 1986 38(11): p. 1246-1262.
10. J.M. Fleureau, *Wettability of Reservoir Core Samples*. Society of Petroleum Engineers. 1992 7(2): p.132-138.
11. Hussam Mohammed Goda, Peter Behrenbruch, *Wettability Quantification - Prediction of Wettability for Australian Formations*. International Petroleum Technology Conference. 2011: p. 1-20.

12. Elijah O. Odusina, Carl H. Sondergeld, Chandra Shekhar Rai, *NMR Study of Shale Wettability*. Society of Petroleum Engineers. 2011: p. 1-15.
13. W.J. Looyestijn, *Wettability Index Determination From NMR Logs*. Society of Petrophysicists & Well Log Analysts. 2008 49(2): p. 130-145.
14. Wim J. Looyestijn, Jan Hofman, *Wettability-Index Determination by Nuclear Magnetic Resonance*. Society of Petroleum Engineers. 2006 9(2): p. 146-153.
15. R. Freedman, N. Heaton, M. Flaum, G.J. Hirasaki, C. Flaum, M. Hürlimann, *Wettability, Saturation, and Viscosity From NMR Measurements*. Society of Petroleum Engineers. 2003 8(4): p. 317-327.
16. Robert J.S. Brown, Irving Fatt, *Measurements Of Fractional Wettability Of Oil Fields' Rocks By The Nuclear Magnetic Relaxation Method*. Society of Petroleum Engineers. 1956: p. 1-4.
17. George J. Hirasaki, Chein-Chung Huang, Gigi Qian Zhang, *Interpretation Of Wettability In Sandstones With Nmr Analysis*. Society of Petrophysicists & Well Log Analysts. 2000 41(3): p. 223-233.

# HOW WETTING CONDITIONS DICTATE CHALK MECHANICS AT UNI-AXIAL STRAIN CONDITIONS – INSIGHTS FROM EXPERIMENTS PERFORMED AT IN-SITU STRESS, TEMPERATURE AND PORE PRESSURE

Jaspreet S. Sachdeva<sup>1,2</sup>, Anders Nermoen<sup>1,2,3</sup>, Merete V. Madland<sup>1,2</sup>, Reidar I. Korsnes<sup>1,2</sup>

<sup>1</sup>University of Stavanger, Norway

<sup>2</sup>The National IOR Centre of Norway

<sup>3</sup>International Research Institute of Stavanger, Norway

*This paper was prepared for presentation at the International Symposium of the Society of Core Analysts held in Snowmass, Colorado, USA, 21-26 August 2016.*

## ABSTRACT

This paper documents how the mechanical strength of chalk depends on the chemistry of pore fluids. Three experiments with different pore fluid compositions were performed at uni-axial strain conditions maintaining constant overburden stress during pore pressure depletion and subsequent compaction phase. The pore fluids were: i) 100% NaCl-brine, ii) 10%-90% NaCl-brine and oil mixture and iii) 100% oil. Significant differences were observed during the depletion and time-dependent compaction phase. The oil-saturated core was stronger than core saturated by brine-oil mixture, while the brine-saturated core accumulated most strain. During compaction, seawater was injected that led to additional strain; most so in the oil-saturated core, intermediate additional strain in the brine-oil mixed core, and least additional strain was observed in the brine-saturated core. This is in line with earlier results on how the ion composition of seawater significantly impacted chalk mechanics. Other significant observations include the additional side stress required to maintain the zero radial strain requirement, and irrespective of the original fluid composition, it is found that after only 2.5 PVs of seawater injection the creep rate for all three cases attained the same value. This indicates that the seawater induced weakening is abrupt, and it is more prominent when there is less water in the core originally.

## INTRODUCTION

During primary phase oil production from a reservoir, the extraction of pressurized fluids reduce the pore fluid pressure leading to an increase in the effective stress, which in turn drives compaction. Reservoirs can be re-pressurized by injecting seawater to reduce the effective stress and mobilize oil. Even though the pressure is maintained, there is still considerable amount of compaction observed in the reservoirs. This compaction has been linked to the interaction of ions in the brines with the rock itself. Considerable research has been carried out concerning this water induced compaction in chalk reservoirs in the past few decades [1-4]. These studies have been carried out on water-wet chalk. This research has primarily shown that the pore fluid composition alters the mechanical

integrity of chalk, as seawater and other simplified brines affect the mechanical strength. Different ions in the water, e.g. sulphates and magnesium ions, change the macroscopic mechanical behaviour of chalk, thus altering the way in which the brines and oils move through the porous rock and hence affecting oil recovery [2-4]. In recent studies of isotropic (hydrostatic) loading tests [5,6], it was shown that values characterizing the mechanical properties of chalk decreased when the wetting state was changed towards more water-wet. However, how do the results in [5,6] apply to high fluid pressures at uniaxial strain condition? In addition, how does the initial water condition dictate the mechanical response after the core has been flooded by seawater? This paper deals with the cases where the cores are initially saturated by different fluids and then the wettability is altered by aging to more mixed-wet state.

## **MATERIAL, EQUIPMENT, AND EXPERIMENTAL PROGRAM**

### **Test Material and Saturation Fluids**

The experiments in this study are performed on an outcrop chalk from a quarry in west-central Kansas in the USA (~39% porosity). The Kansas chalk type is considered to be a pure chalk with a non-carbonate content in the range 1-3% [2,7] and a permeability in the range 1-2 mD. This chalk is from Late Cretaceous geological age. Tang and Firoozabadi [7] argue that it is a good analogue to some clean North Sea reservoir chalks in regards to porosity, capillary pressure, and absolute and relative permeability.

Three different initial fluid saturations were used: Core K01 was saturated and flooded by 1.1M NaCl-brine. NaCl-brine was used as a simplified formation brine to minimize rock-fluid interactions prior to seawater flooding. Core K02 was saturated by approx. 10% NaCl-brine and 90% of Heidrun and Heptane oil that were mixed in 60%-40% (by volume). This oil was filtered through a 6.5 $\mu$ m filter. Core K03 did not contain any brine and was saturated only by the same oil. Both cores K02 and K03 were flooded with two pore volumes of this oil in each direction at 50°C. After the cores, K02 and K03, were saturated, they were submerged into the same oil and aged for 3 weeks at 8 bar and 90°C. The aging was performed to alter the wettability properties of the chalk cores. Wettability was not measured after aging. The aging procedure followed here would yield a wettability along the same lines as the results of Zangiabadi et al. [6] where they aged the cores with the same oil together with 20% brine, which gave a wettability index of 0.65. The wettability index (WI) is a measure of the available sulphate adsorption sites, where a WI equal to 0 means completely oil-wet and 1 means completely water-wet [6]. Strand et al. [8] reported wettability indexes below 0.5 on Stevns Klint chalk that were aged after being completely saturated by 60%-40% Heidrun/heptane mixture without initial water. Zangiabadi et al. [6] also reported acid number 1.92 mg KOH/g oil for the same oil mixture that is used in this study as well. Zangiabadi et al. [6] and Strand et al. [8] conclusively report that by increasing the acid number in the oil, the cores become more oil-wet after aging.

### The Triaxial Cell Setup

The chalk cores were mounted into the triaxial cell that allows for continuous measurements of the axial and radial strains during flooding fluids at elevated stresses, pressures, and temperatures. The cell was equipped with a heating element and a regulating system with precise temperature control. Four pumps were connected to the triaxial cell to control the axial stress ( $\sigma_{ax}$ ), confining pressure ( $\sigma_{rad}$ ), flooding rate (Gilson pump) and pore pressure on the downstream side ( $P_p$ ). An external linear voltage differential transducer (LVDT) monitored the length of the plug (L). The circumferential diameter on the middle of the core was measured with an extensometer. All the tests were performed at uni-axial strain conditions, with varying radial stress to ensure zero lateral (radial) strain and constant overburden stress such that the stress-path is similar to those that are occurring in the real field scenarios. In these tests, the deformation only took place in the axial direction and a constant axial stress was maintained. The extensometer attached around the core plug measured the radial deformation in the core as a function of time. The signal from extensometer was sent to the computer (LabView software) and was used to change confining pressure for the purpose of avoiding any radial deformation and maintaining zero radial strain. Changes in the confining pressure also affected the axial stress, so the piston pressure was automatically regulated to ensure constant axial stress.

### Test Procedure

The experiments were performed at uni-axial strain conditions according to the following procedure: i) Mount the core in the triaxial cell; ii) Increase confining pressure ( $\sigma_{rad}$ ) to 1.2 MPa and pore pressure ( $P_p$ ) to 0.7 MPa simultaneously; iii) Increase temperature to 130°C; iv) Increase  $\sigma_{rad}$  to 40 MPa and  $P_p$  to 38 MPa simultaneously; v) Increase axial stress ( $\sigma_{ax}$ ) to 42.5 MPa; vi) Start uni-axial strain test. Pore pressure depletion from 38 MPa to 15 MPa; vii) Observe creep at constant overburden; viii) Inject seawater according to the recipe shown in Zangiabadi et al. [6] and observe the creep strain.

During pore pressure depletion in uni-axial strain experiments, Hooke's law is modified such that Young's Modulus is calculated using,

$$E\delta\varepsilon_{ax} = \frac{3\alpha\delta P_p\delta\sigma_{rad} - 2(\delta\sigma_{rad})^2}{\delta\sigma_{rad} - 2\alpha\delta P_p} \quad (1)$$

where  $E$  defines the Young's or elastic modulus,  $\delta P_p$  defines the change in the pore pressure from 38 MPa to the point where the core starts to yield,  $\delta\sigma_{rad}$  defines the change in the radial stress and  $\delta\varepsilon_{ax}$  defines the change in the axial strain corresponding to the same pore pressure values, and  $\alpha$  is the Biot coefficient taken equal to 1 for calculations.

## RESULTS

### Pore Pressure Depletion Phase

Pore pressure depletion is carried out from 38 MPa to 15 MPa at uni-axial strain conditions. The yield, total axial strain and Young's Modulus values for the three cores during the pore pressure depletion phase are given in

Table 1. For the K03 core (100% oil), the yield strength and elastic modulus is found to be 2 and 1.4 times larger, respectively, than the results for the K01 core (100% brine). The total axial strain after loading is 4 times larger for the K01 core compared to the K03 core. The axial stress vs axial strain curves for all cores are given in Figure 1(a).

### Uni-Axial Strain Compaction and Seawater Injection

The uni-axial compaction at constant overburden and pore pressures observed for the three cores is shown in Figure 1(b). The uni-axial compaction observed for K01 and K02 is 5.6% and 2.3%, before seawater injection, which goes up to 8.6% and 5.3%, respectively, after injecting seawater for 40 days. No compaction is observed for K03 prior to seawater injection, but shoots up to 7.5% after injecting the seawater for only 15 days. The strain rates before and after seawater injection for all tests are given in Figure 1(c). The strain rates for K01 and K02 prior to seawater injection are 0.05%/day and 0.07%/day, which increase to 0.17%/day and 0.19%/day, respectively, immediately after the start of injection. The strain rate shoots up to 0.77%/day from zero for K03 immediately after the start of seawater injection. After 2.5 PVs (5 days) of injection, all three cores attain the same value of around 0.17%/day strain rate. Please note that the starting time of seawater injection is taken as zero time (reference time) to make it easy to analyse the results.

## DISCUSSIONS

The uni-axial compaction experiments, similar to Omdal et al. [9], have been performed, where the radial stress is automatically adjusted to ensure zero radial strain. The experiments have been carried out by depleting pore pressure whilst keeping the overburden stress constant, before the pore pressure was kept constant at 15 MPa over time. This experimental setup opens up for a range of studies in addition to the mechanical consequences reported here. For example, we can simulate the actual reservoir history with respect to stress, temperature and pore fluid composition, how the pore pressure affects the mobility of oil and water at actual PVT-values, and, to which extent adsorption, dissolution and precipitation depend on pore pressure and stress.

As expected from simpler hydrostatic tests reported by e.g. Zangiabadi et al. [6], we observe that K03 (100% oil) obtains the highest elastic modulus and highest yield during pressure depletion and that these values decrease with increasing brine content.

Prior to seawater injection, the side stresses are automatically reduced as the core compacts (Figure 1(d)). This is interpreted as a signature of work hardening during time,

since less stress is required to keep the core at zero radial strain. However, when seawater is injected, the core weakens. Because of that, both the axial strain is increased, and similarly, the side stress required to maintain zero radial strain is increased. The side stress for the oil-saturated core increased by 6.3 MPa whilst the 10% and 100 % brine-saturated cores obtained approx. 3% additional axial strain, and correspondingly, the extra side stress required to sustain zero radial strain was 2.3 MPa and 1.7 MPa, respectively. We expect that a similar phenomenon could occur in reservoir systems when seawater is injected. In these cases, it is expected that the horizontal stresses would increase, since the uni-axial strain condition applies to reservoirs with large width to height ratios.

In Figure 1(c) before seawater injection, the compaction (strain) rate is different for all tests. However, irrespective of the original fluid composition, it is found that after only 2.5 PVs of seawater injection the creep rate for all three cases attained the same value. This shows that the wetting conditions have minor impact on the compaction rate after flooding 2.5 PVs of seawater through the core. In addition, it shows that the seawater induced weakening is abrupt and more prominent when there is almost zero initial water in the core. Thus in mixed wet cores, oil is not blocking seawater access to the intergranular contacts.

## CONCLUSIONS

1. Completely oil-saturated core is found to be stronger compared to partially or completely brine-saturated cores.
2. Uni-axial compaction rate accelerates when seawater is injected.
3. The initial accelerated compaction by seawater injection is affected by the initial fluid chemistry.
4. After injecting 2.5 PVs of seawater, initial saturation and wetting state have minor effects on compaction rate.

## ACKNOWLEDGEMENTS

The authors would like to thank the Research council of Norway and the industry partners; ConocoPhillips Skandinavia AS, BP Norge AS, Det Norske Oljeselskap AS, Eni Norge AS, Maersk Oil Norway AS, DONG Energy A/S, Denmark, Statoil Petroleum AS, ENGIE E&P NORGE AS, Lundin Norway AS, Halliburton AS, Schlumberger Norge AS, Wintershall Norge AS of the National IOR Centre of Norway for support.

## REFERENCES

1. Sylte, J.E., L.K. Thomas, D.W. Rhett, D.D. Bruning and N.B. Nagel, "Water Induced Compaction in the Ekofisk Field", Presented at the SPE Annual Technical Conference and Exhibition, Houston, Texas, SPE 56426 (1999).
2. Megawati, M., A. Hiorth, and M.V. Madland, "The impact of surface charge on the mechanical behaviour of high-porosity chalk", *Rock Mechanics and Rock Engineering*, (2012) 46(5), 1073-1090.

3. Madland, M.V., A. Hiorth, E. Omdal, M. Megawati, T. Hildebrand-Habel, R.I. Korsnes, S. Evje, and L.M. Cathles, “Chemical Alterations Induced by Rock-Fluid Interactions when Injecting Brines in High Porosity Chalks”, *Transport in Porous Media*, (2011) **87**, 679-702.
4. Korsnes, R.I., M.V. Madland, T. Austad, S. Haver, and G. Røsland, “The Effects of Temperature on the Water Weakening of Chalk by Seawater”, *Journal of Petroleum Science and Engineering*, (2008) **60**, 183-193.
5. Zangiabadi, B., T.A. Davidian, R.I. Korsnes, K.A.N. Vorland, T.G. Kristiansen and M.V. Madland, “The effect of wetting conditions on the mechanical strength of chalk”, *Proceedings of the 3<sup>rd</sup> International Conference on Coupled T-H-M-C Processes in Geo-systems, Lille, France*, (2008), 179-186.
6. Zangiabadi, B., R.I. Korsnes, M.V. Madland, T. Hildebrand-Habel, A. Hiorth and T.G. Kristiansen, “Mechanical Properties of High and Lower Porosity Outcrop Chalk at Various Wetting States”, Presented at the 43<sup>rd</sup> US Rock Mechanics Symposium and 4<sup>th</sup> U.S.-Canada Rock Mechanics Symposium, Asheville, NC, ARMA 09-139 (2009).
7. Tang, G. and A. Firoozabadi, “Effect of pressure gradient and initial water saturation on water injection in water-wet and mixed-wet fractured porous media”, *SPE Reservoir Evaluation & Engineering*, (2001) **4**(6), 516-524.
8. Strand, S., M.L. Hjuler, R. Torsvik, J.I. Pedersen, M.V. Madland and T. Austad, “Wettability of Chalk: Impact of Silica, Clay Content and Mechanical Properties”, *Petroleum Geoscience*, (2007) **13**, 69-80.
9. Omdal, E., M.V. Madland, T.G. Kristiansen, N.B. Nagel, R.I. Korsnes and A. Hiorth, “Deformation Behavior of Chalk Studied Close to In-Situ Reservoir Conditions”, *Rock Mechanics and Rock Engineering*, (2010) **43**, 557-580.

## FIGURES AND TABLES

Table 1: Mechanical properties of the chalk cores

Core		K01	K02	K03
Yield Stress	MPa	8.85	14.92	18.45
Total depletion strain	%	2.72	1.16	0.64
Young's Modulus	GPa	2.81	3.47	4.05

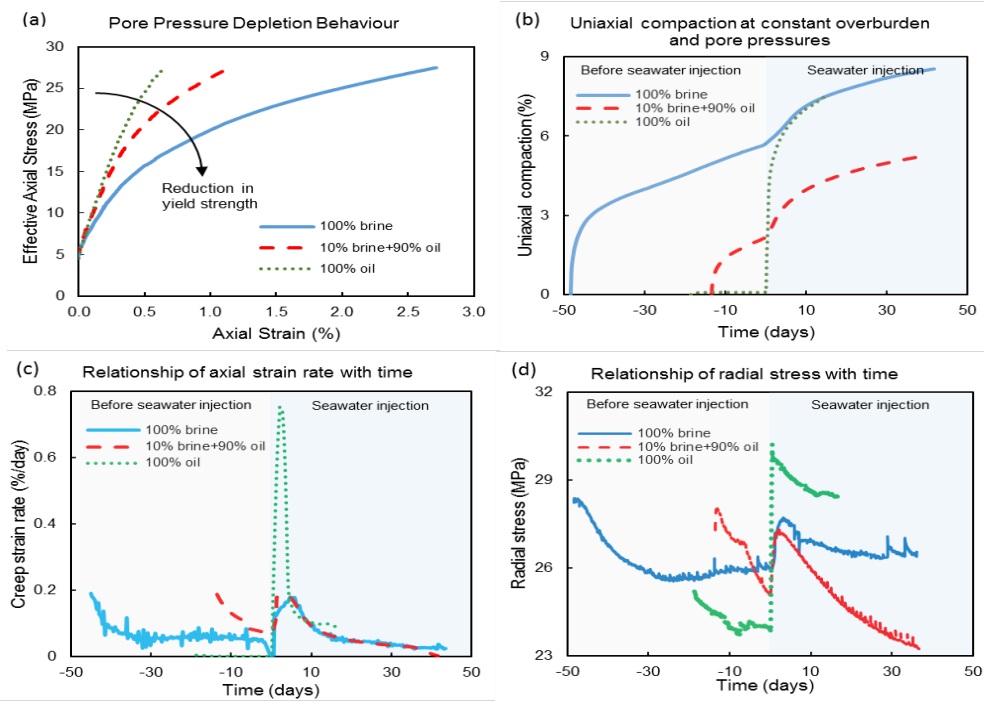


Figure 1: (a) Axial stress vs axial strain for all cores. (b) Compaction curves for all tests. (c) Compaction strain rate for all tests. (d) Radial stress curves for all tests. Please note that the starting time of seawater injection is taken as  $t=0$  days in (b), (c) and (d).

## Understanding Fractures and Pore Compressibility of Shales using NMR

M. Dick<sup>1</sup>, D. Green<sup>1</sup>, E.M. Braun<sup>2</sup>, and D. Veselinovic<sup>1</sup>

<sup>1</sup>*Green Imaging Technologies, Fredericton, NB, Canada*

<sup>2</sup>*Consultant, Houston, TX, USA*

*This paper was prepared for presentation at the International Symposium of the Society of Core Analysts held in Snowmass, Colorado, USA, 21-26 August 2016*

### Abstract

For the profitable development of shale reservoirs, it is critical to understand the natural fractures in the rock and how they may or may not interact with hydraulic fracturing. When performing core analysis, it is also important to assess whether the measured properties have been altered by fractures induced during coring. A key indication of the quantity of the fractures can be obtained by measuring the amount of porosity contained in the fracture network. Shale pores are typically very small and therefore have very short NMR T<sub>2</sub> relaxation times. The fractures are larger than the pores and therefore have longer T<sub>2</sub> relaxation times.

In this work, we describe and demonstrate techniques using NMR that can obtain not only the total porosity of shale samples but can also quantify the amount of porosity arising from the fractures. Simple NMR measurements of the T<sub>2</sub> relaxation time were performed at different confining pressures to quantify the porosity loss as confining stress increases.

In some cases, porosity loss occurred preferentially in large pores at low confining pressure, suggesting fracture closure. The micropores did not respond to confining pressure, indicating that they were not part of the mechanical fabric of the rock. In another example, the lowest-T<sub>2</sub> peak dominated the NMR signal, indicating negligible porosity in fractures or large pores.

### Introduction

NMR is widely used in the oil and gas sector to investigate both the types of fluids present and the size of the pores the fluids occupy [1]. Ignoring diffusion, the relationship between the NMR property T<sub>2</sub> and the pore size is governed by the following equation.

$$\frac{1}{T_2} = \frac{1}{T_{2-Bulk}} + \rho \frac{S}{V} \quad (1)$$

Where S/V is the surface to volume ratio of the pore, ρ is the relaxivity parameter and T<sub>2-bulk</sub> is the T<sub>2</sub> relaxation time of the fluid.

In shale formations there usually exists at least two distinct pore networks [2,3]. One associated with the intergranular pore network and one associated with the pores within the organic rich kerogen. The fracture network, either natural or induced, could be thought of as a third pore network which at ambient pressure would be the largest in size.

## Experiment

The total porosity and  $T_2$  distribution as a function of confining pressure of four shale core samples was investigated using NMR. All samples were from wells drilled into potentially hydrocarbon-bearing rock formations. Characteristic information on each shale sample can be found in Table 1. The table includes the He porosity measured for the shales tested. Typically, in shales the He porosity is lower than the NMR porosity. Figure 1 shows a contrast enhanced photo of each shale tested. The natural color of the shale samples was dark brown and much of the heterogeneity shown in the figures was not visible before the contrast enhancement. Each dry shale sample was first vacuum saturated with brine (2% KCl in water) for approximately an hour. Saturation of the tight shale pores was then achieved by applying 10000 PSI pressure with brine for approximately a week in a Phoenix Instruments pressure vessel. It is assumed that this saturation procedure fully saturates all the mineral lined pores. However, it is unlikely that the kerogen pores are fully saturated after this procedure. But, these pores are extremely small and will not make a significant contribution to the total porosity measured. Following this saturation procedure, each shale sample was confined hydrostatically by fluorinert in an Oxford Instruments P5 overburden NMR probe [4]. Once the confined sample in the probe was free of leaks, it was inserted into an Oxford Instruments GeoSpec 2-53 rock core analyzer [5]. The porosity of each shale core sample was then tested as a function of confining pressure at 0, 1000, 2000, 3000, 4000 and 5000 PSI. A  $T_2$  NMR acquisition scan of each sample at each pressure was used to measure the  $T_2$  pore distribution as a function of confining pressure. The  $T_2$  relaxation time is proportional to pore size. Data acquisition and data analysis of the  $T_2$  data was achieved via Green Imaging Technology software [6].

## Results

The pore-size distribution for each shale core sample tested at 5000 PSI of confining pressure can be seen in Figure 2. The data shown has not been background corrected. The total porosity of each shale could be determined by summing the area under its incremental porosity vs.  $T_2$  curve. Figure 3 shows the total porosity of each shale normalized to 0 PSI as a function of confining pressure. Each of these shales shows an approximate five percent compression of their total porosity as the confining pressure is increased from 0 to 5000 PSI.

What is not obvious from Figure 3 is that the total porosity in each of the shales occurs in different pore networks in each shale sample. Shales 1 and 3 have a single sized pore network while shales 2 and 4 have three pore networks of varying size. For shale samples 2 and 4, the cumulative porosity of each network was estimated by summing the incremental porosity in certain  $T_2$  ranges corresponding to the pore networks. The  $T_2$  ranges for each pore network were determined by finding the minimum or inflection points between adjacent  $T_2$  peaks. For example, in shale 2 the three pore networks were micro ( $T_2 < 1.7$  ms), meso ( $T_2 1.7-55$  ms) and macro ( $T_2 > 55$  ms).

The left panel of Figure 4 shows the porosity of each pore network of shale 2 plotted as a function of confining pressure. This plot shows that the micro pore network makes up

the majority of the total porosity of shale 2 (~3 p.u.) while the macro porosity (~0.5 p.u.) accounts for the least portion of the total porosity of shale 2. The shape of each data for each pore network also gives some indication that each of the pore networks is behaving differently as the pressure is increased. This difference in behavior is enhanced in the center panel of Figure 4 where the porosity has been normalized to 0 PSI and plotted as a function of pressure. From the plot it is now immediately obvious that each pore network behaves differently with confining pressure. The micro pore network (blue line) shows no compression with confining pressure. The meso pore network (green line) shows an approximately linear compression with confining pressure. The macro pore network shows a sharp decrease in porosity from 0 to 1000 PSI and then no further compression from 1000 to 5000 PSI. This is consistent with the observations of Chhatre et al. [7]. In their study, there was a significant decrease in permeability with increasing stress, suggesting that the largest pores compacted the most. Finally, the right panel of Figure 4 shows the cumulative porosity of shale 2 as a function of confining pressure. Again it is obvious that the micro pores contribute to the majority of the total porosity of shale 2 while the macro pores contribute the least. However, the pressure dependence of the cumulative porosity masks the unique behavior of the porosity of each pore network.

Figure 5 shows the porosity data for shale 4 analyzed in the same fashion as the data for shale 2. This plot shows that for shale 4, the meso pore network makes up the majority of the total porosity (~5 p.u.) while the macro porosity (~0.5 p.u.) accounts for the least portion of the total porosity. The center panel of Figure 5 shows the porosity normalized to 0 PSI and plotted as a function of pressure. This plot shows that there is consistency with shale 2 for the behavior of the micro, meso and macro pore networks as a function of pressure. Finally, the right panel of Figure 5 shows the cumulative porosity of shale 4 as a function of confining pressure. Again it is obvious that the meso pores contribute to the majority of the total porosity of shale 2 while the macro pores contribute the least. However, the pressure dependence of the cumulative porosity masks the unique behavior of the porosity of each pore network

### **Technique customization**

The measurements reported here were intended as a feasibility study, and followed identical protocols for all samples. For application to specific field development studies, it is expected that experimental protocols could be customized. Some options include:

- Changing net confining stress by reducing pore pressure, to more closely duplicate conditions during field development.
- Monitoring  $T_2$  relaxation times over time to study stress creep.
- Measuring permeability changes in conjunction with  $T_2$  relaxation times.
- Correlating compressibility behavior with other rock properties such as mineralogy, geologic facies, kerogen content, etc.

### **Conclusion**

A method has been presented for using NMR  $T_2$  relaxation times to identify pore networks in shales and their dependence on stress. Four samples were tested, all taken

from wells in potential hydrocarbon-bearing formations. Two samples had a complex (trimodal) pore size distribution, and two contained only very small pores.

Where a complex distribution was present, the stress-dependence varied by pore size. The largest (macro) pores compressed significantly at relatively low stress (1000 psi), and very little thereafter. We interpret this to indicate the closure of natural or induced fractures. The smallest (micro) pores show no significant change with stress. We interpret this to indicate that these pores are not part of the mechanical fabric of the rock. The intermediate size (meso) pores show a continuing compression across the range of stresses.

### References:

1. Coates, G.R., Xiao, L., and Prammer, M.G., *NMR Logging. Principles & Applications*, Halliburton Energy Services, Houston, 1999.
2. Kausik, R., Fellah, K., Rylander, E., Singer, P., Lewis, R., and Sinclair, S., NMR Relaxometry in Shale and Implications for Logging, SPWLA 56<sup>th</sup> Annual Logging Symposium, July 18-22, 2015.
3. Suarez-Rivera, R., Chertov, M., Willberg, D. M., Green, S. J., & Keller, J. (2012, January 1). Understanding Permeability Measurements in Tight Shales Promotes Enhanced Determination of Reservoir Quality. Society of Petroleum Engineers. doi:10.2118/162816-MS.
4. P5 Overburden Probe User Manual, Version 1, Oxford Instruments, Green Imaging Technologies.
5. Geo-Spec 2-53 User Manual, Version 1.8, Oxford Instruments.
6. GIT Systems and LithoMetrix User Manual, Revision 1.9, Green Imaging Technologies.
7. Chhatre, S.S., Braun, E.M., Sinha, S., Determan, M.D., Passey, M.D., Zirkle, T.E., Wood, A.C., Boros, J.A., Berry, D.W., Leonardi, S.A. and Kudva, R.A., Steady State Stress Dependent Permeability Measurements Of Tight Oil Bearing Rocks, 2014 Annual Symposium Of The Society Of Core Analysts (SCA2014- 012).

### Tables and Figures:

Table 1: Characteristic Information On Shale Samples Tested

Shale	1	2	3	4
Formation	Gates	Doig	Muskwa	Montney
Sample Depth (ft)	1392	5256	5422	6538
Core Diameter (cm)	2.5	2.5	2.5	2.5
Core Length (cm)	3.8	3.9	4.4	4.3
Bulk Volume (cm <sup>3</sup> )	18.7	19.1	21.6	21.1
Dry Core Mass (g)	51.68	51.2	55.0	54.8
Grain Density (g/cc)	2.74	2.68	2.61	2.72
Gas Permeability (mD)	4.28	1.3	0.301	5.18
He Porosity (p.u.)	5.9	5	7.4	8.9
Well Location	British Columbia	British Columbia	British Columbia	British Columbia

Figure 1: Contrast-enhanced photographs of the shale samples tested

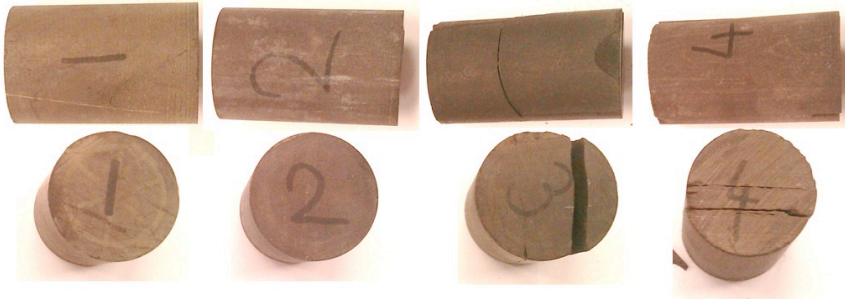


Figure 2: Pore Distribution For Shale Samples Tested At 5000 PSI Confining Pressure.

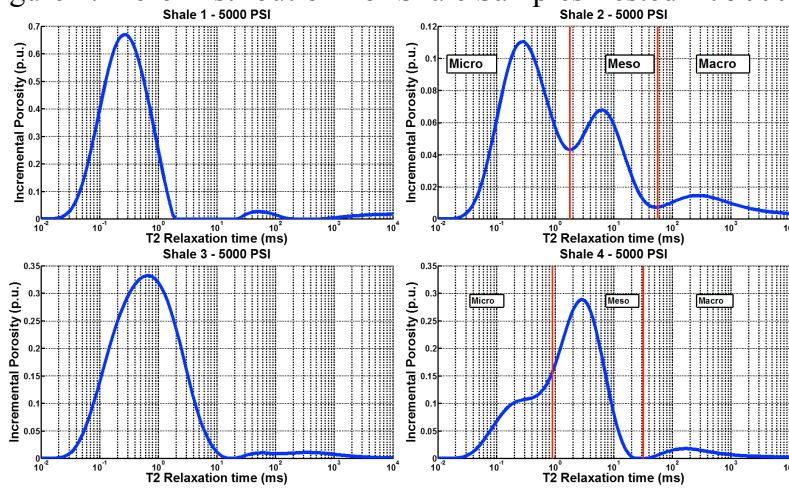


Figure 3: The Porosity (Normalized to 0 PSI) Of Shales 1-4 As A Function Of Confining Pressure

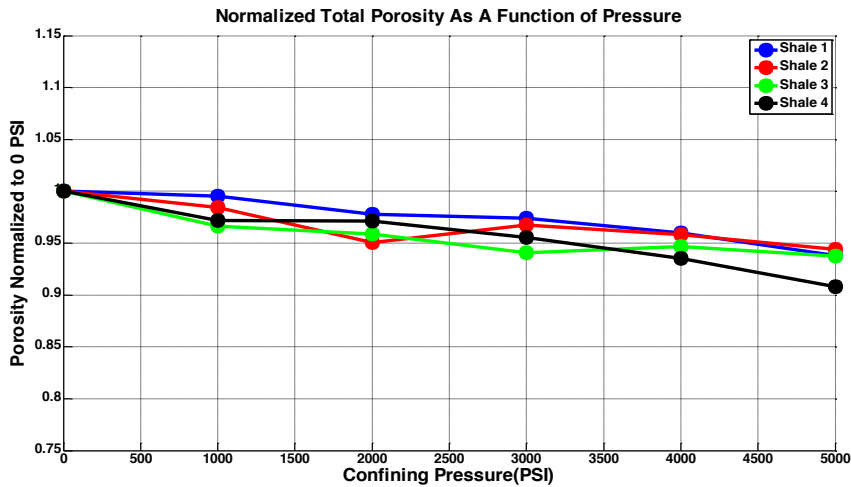


Figure 4: The Porosity Of The Pore Networks Of Shale 2 As A Function Of Pressure

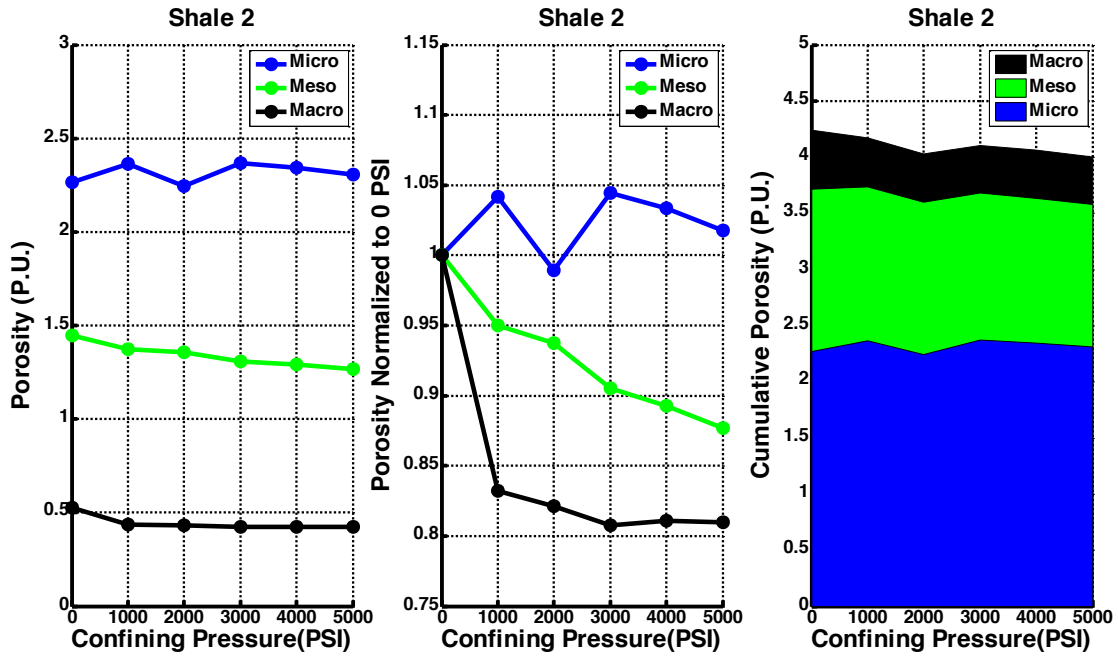
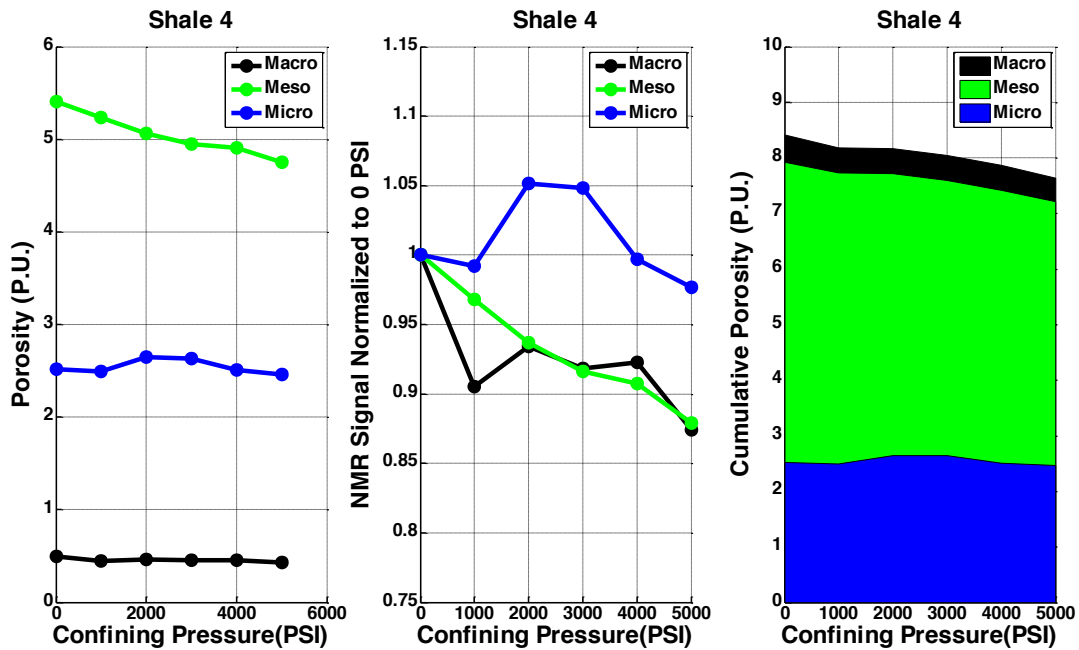


Figure 5: The Porosity Of The Pore Networks Of Shale 4 As A Function Of Pressure



# LONGITUDINAL DISPERSION COEFFICIENT CALCULATION DURING MISCIBLE FLOW IN HETEROGENEOUS POROUS MEDIA USING PORE SCALE SIMULATION

Saied Afshari<sup>1</sup>, Ali Heydari Beni<sup>1</sup>, Saeed Taheri<sup>1</sup>, Hossein Hejazi<sup>1</sup>, Apostolos Kantzas<sup>1,2</sup>

<sup>1</sup> Department of Chemical and Petroleum Engineering, University of Calgary, Calgary, Canada

<sup>2</sup> PERM Inc., TIPM Laboratory, Calgary, Canada

*This paper was prepared for presentation at the International Symposium of the Society of Core Analysts held in Snowmass, Colorado, USA, 21-26 August 2016*

## ABSTRACT

Miscible recovery techniques are among the most efficient and widely used enhanced oil recovery methods both in conventional and in heavy oil reservoirs (miscible gas flooding and solvent injection, respectively). The efficiency of a miscible flood is significantly dependent on the degree of mixing that occurs between the fluids. Mixing of the injected gas/solvent with oil leads to solvent dilution and thus reduces the effective strength of miscible displacement. The primary mechanisms of miscible mixing in pore space are molecular diffusion and convection (mechanical spreading) due to bulk flow velocity. The combined effect of these two mechanisms on the degree of mixing can be characterized by the dispersion coefficient. Laboratory measurement of this parameter is difficult due to the fact that it is strongly dependent on flow and porous media properties. An alternative approach is to numerically calculate dispersion coefficient using pore scale digital core analysis. In this study, pore level miscible displacements in heterogeneous porous media are computationally modeled through simultaneous solving of Navier-Stokes, Continuity, and Convection-Diffusion equations on virtual unconsolidated granular porous media. These virtual media are constructed by a pattern generator using the concept of random packing of grains. The heterogeneity level of these media is characterized by a coefficient of variations defined as the ratio of standard deviation in grain diameter to the mean grain diameter. Using the results of numerical simulations, longitudinal (along the flow direction) dispersion coefficient is calculated at different values of flow velocity, viscosity ratio, and pore scale medium heterogeneity. The input diffusion coefficients are either constant or functions of concentration. The results of the simulations show that when viscosity ratio is unity, at very low Peclet numbers the dominant transport mechanism is molecular diffusion. At high Peclet numbers, however, advection is dominant and the magnitude of longitudinal dispersion coefficient scales with  $N_p^{1.2}$ . Higher heterogeneity of media will result in higher values of longitudinal dispersion coefficient. Also, it is found that using an appropriate average diffusion coefficient over the range of concentration interval can adequately account for concentration dependency of diffusion coefficient. The effect of viscosity contrast on

longitudinal dispersion coefficient is shown to be significant. Viscous fingering due to an unfavorable viscosity ratio leads to higher values for longitudinal dispersion coefficient.

## INTRODUCTION

Miscible displacement and mixing of fluids in porous media is of fundamental importance in many natural processes and engineering applications, including but not limited to enhanced oil recovery [1,2], environmental remediation [3-6], and CO<sub>2</sub> sequestration [7]. Fluids mixing in porous media is the combined result of molecular diffusion due to Brownian motion of fluid particles, as well as mechanical dispersion caused by interstitial flow velocity and its variations (both in magnitude and direction) due to medium heterogeneity.

The level of mixing in porous media is generally quantified by dispersion coefficient. In the past, dispersion coefficient has been used extensively to quantify the degree of mixing during miscible flows in porous media, both theoretically and experimentally. Taylor [8] and later Aris [9,10] investigated the viscous flow of a soluble matter in a fluid flowing through a straight circular capillary tube and theoretically described the degree of mixing by an effective dispersion coefficient. Brigham et al. [11] used glass bead packs and natural cores to investigate the effect of various parameters on the dispersion coefficient and degree of mixing through miscible displacement experiments. Perkins and Johnston [12] discussed the effect of molecular diffusion and dispersion on miscible flows and summarized information and interpretations from previous literature on miscible fluids. Coelho et al. [13] numerically obtained the values of dispersion coefficient in random spherical packings and concluded that their results were in a good agreement with experiments in consolidated sandpacks and sands. Transient and asymptotic dispersion coefficients have been calculated in regular and random sphere packings by using random-walk particle tracking and Lattice-Boltzmann methods to model solute transport and fluid flow, respectively [14]. Bijeljic et al. [15] used pore scale network simulation to calculate dispersion coefficient in a diamond lattice of throats representing Berea sandstone. Beard and Wu [16] presented an analytical dispersion coefficient for the flow of solute inside a system of capillary tubes with randomly assigned velocities. Pore scale simulations also have been used to study dispersion phenomena in porous media. Garmeh et al. [17] explored different aspects of mixing in porous media by numerical simulations at the pore scale in series and layered heterogeneous porous media constructed by different arrangements of circular grains. Their numerical results were in agreement with classical relationship between dispersion coefficient and velocity reported by [12]. Mostaghimi et al. [18] used direct images of porous media obtained from microcomputed tomography scan of rock cores and simulated flow and transport on these images using a Stokes solver for flow modeling and a streamline-based algorithm for solute transport. They were able to accurately predict the available data for longitudinal dispersion coefficient in the literature. Taheri et al. [19] developed a sub pore scale modeling approach based on numerical methods and investigated the values of dispersion coefficient during miscible displacement in several images of micro-models with different properties.

The rate of mixing and magnitude of dispersion coefficient during miscible displacement in porous media is strongly dependent on medium heterogeneity and viscosity ratio of fluids. Presence of microscale/macroscale heterogeneities results in preferred paths for fluid particles to move and thus channeling of flow. An unfavorable viscosity ratio also gives rise to instabilities at the leading edge of concentration profile and subsequently results in viscous fingering. This heterogeneity induced channeling and viscous fingering will increase the size of miscible mixing zone and consequently the magnitude of dispersion coefficient. The experimental works of [20] and [21] on glass bead columns demonstrated that increasing the variance of bead size resulted in higher dispersion rates. Experimental study of dispersion tests by [11] on random bead packs showed that higher dispersion coefficients were encountered during flow and transport at higher viscosity ratios. Bretz et al. [22] used thin sections to analyze porous medium heterogeneity and experimentally measured higher dispersion coefficient for wider pore size distributions. Numerical simulations of [23] and [24] on heterogeneous permeability fields demonstrated that increasing macroscale heterogeneity of medium in terms of Dykstra-Parson's (DP) coefficient will lead to higher dispersion coefficients. Garmeh and Johns [25] conducted numerical simulations of miscible displacement on correlated permeability fields to predict the values of dispersivities (dispersion coefficient normalized by flow velocity) at different levels of macroscale medium heterogeneity and viscosity ratio. They concluded that an increase in medium's heterogeneity (in terms of DP coefficient) and viscosity ratio results in higher values of dispersivity.

In this study, miscible displacements in two dimensional heterogeneous porous media are simulated through simultaneous solving of Navier-Stokes, continuity, and convection-diffusion equations in pore scale. Two dimensional packings of grains with different levels of microscale (local) heterogeneity are reconstructed using a pattern generator package developed by [1]. These media are constructed by random packing of circular grains with different diameters randomly taken from a particle size distribution (PSD). The heterogeneity level of these media is characterized by a coefficient of variations defined as the ratio of standard deviation in grain diameter to the mean grain diameter. Through this study, the effects of viscosity ratio and pore scale heterogeneity of porous media on the values of dispersion coefficient during miscible displacement at different Peclet numbers (flow velocities) are investigated. Both constant and concentration-dependent molecular diffusion coefficients are considered here to investigate how it affects the results.

## **METHODOLOGY**

### **Governing Equations**

We model miscible displacement in pore scale by solving flow and transport equations together. In order to achieve that, three equations of continuity, Navier-Stokes, and convection-diffusion (Eqs.1-3, respectively) are solved numerically using commercially available code COMSOL multi-physics:

$$\nabla \cdot (\rho \mathbf{u}) = 0 \quad (1)$$

$$\rho \frac{\partial \mathbf{u}}{\partial t} + \rho (\mathbf{u} \cdot \nabla) \mathbf{u} = \nabla \cdot [-p \mathbf{I} + \mu \nabla \mathbf{u}] \quad (2)$$

$$\frac{\partial c}{\partial t} + \nabla \cdot (-D \nabla c) + \mathbf{u} \cdot \nabla c = 0 \quad (3)$$

In the above equations,  $\rho$  is mixture density,  $\mathbf{u}$  is pore velocity vector,  $p$  is pressure,  $\mu$  is mixture viscosity,  $c$  denotes the concentration of solute in displacing fluid, and  $D$  is the mutual diffusion coefficient of the fluids. In simulations of this study, both constant and concentration dependent diffusion coefficients are employed. To account for concentration dependent diffusion coefficient, Vignes' equation (Eq. 4) is used [26]:

$$D(x) = ((D_{BA}^0)^x (D_{AB}^0)^{1-x}) \frac{\partial \ln a_A}{\partial \ln x}$$

(4)

In this equation,  $x$  is mole fraction of solute (component  $A$ ),  $D_{BA}^0$  is diffusivity of component  $B$  in essentially pure component  $A$ , and  $D_{AB}^0$  is diffusivity of component  $A$  in essentially pure component  $B$ . The last term in Eq.5 is the activity correction factor which assumed to be equal to 1 following the results of [27] at intermediate times of diffusion. A quarter power mixing rule for viscosity (Eq.5) is adopted from [28] and implemented in the simulations to estimate the mixture viscosity-concentration behavior:

$$\mu(x) = \left( \mu_1^{-0.25} + \frac{x}{x_{inj}} (\mu_2^{-0.25} - \mu_1^{-0.25}) \right)^{-4} \quad (5)$$

The subscripts 1 and 2 denote displaced (in-place) and displacing (injected) fluids, respectively.  $x_{inj}$  is the mole fraction of solute (component  $A$ ) in the injecting fluid (fluid 2). Table 1 shows the values of parameters used in the simulations. For constant diffusion coefficient a value of  $1 \times 10^{-10}$  m<sup>2</sup>/s is assumed for  $D$ . The values of  $D_{BA}^0$  and  $D_{AB}^0$  are assumed to be  $2 \times 10^{-9}$  and  $5 \times 10^{-11}$  m<sup>2</sup>/s, respectively. Note that the value for constant diffusion coefficient ( $1 \times 10^{-10}$  m<sup>2</sup>/s) is equal to the average value of  $D(x)$  over the range of  $x = 0$  to mole fraction of solute in the injecting fluid ( $x = x_{inj}$ ).

### Porous Media Model

The pore scale representation of heterogeneous porous media is achieved by two dimensional packings of circular grains. These media are constructed by random packing of circular grains with different diameters randomly taken from a particle size distribution (PSD). The heterogeneity level of these media can be characterized by a coefficient of variations defined as:

$$CV = \frac{S_{d_p}}{\bar{d}_p} \quad (6)$$

In this definition,  $\bar{d}_p$  is the average particle (grain) diameter and  $S_{d_p}$  is the standard deviation in diameter (mean and standard deviation of PSD, respectively). Figure 1 shows four media with the same average grain diameter and different coefficients of variation along with their corresponding PSDs. As it is shown in this figure, a higher value of  $CV$  results in a more heterogeneous medium with more irregular pore space. The properties of these media are shown in Table 2.

The solid-fluid boundary at the grain surface is considered to be no flow/no slip (zero velocity) for flow and no flux for transport equations. The boundary conditions at the top and bottom boundaries are considered to be symmetrical (zero gradient for velocity and concentration). The inlet condition for flow is constant injection velocity while the outlet is constant atmospheric pressure. For transport equation, constant concentration inflow is imposed on the inlet and outlet boundary condition is assumed to be zero gradient.

### Theory of Dispersion

As stated before, dispersion is the combined effect of molecular diffusion and convective spreading in porous media due to variations of velocity field arising from complex structure of pore and throats. This phenomenon in porous media at macro-scale and along the direction of flow can be described by a convection-dispersion equation as:

$$\frac{\partial c}{\partial t} + \nabla \cdot (-K_L \nabla c) + \mathbf{u} \cdot \nabla c = 0 \quad (7)$$

In this equation  $K_L$  is the longitudinal dispersion coefficient. Depending on the values of flow velocity, molecular diffusion coefficient, and characteristic length of porous medium, different transport regimes may be encountered during miscible flow. These transport regimes can be correlated to a dimensionless Peclet number defined as:

$$N_P = \frac{uL_c}{D} \quad (8)$$

In this definition,  $u$  is the characteristic velocity and  $L_c$  is the characteristic length. For random packing of grains, the characteristic length is the average grain diameter and the characteristic velocity is considered to be the injection velocity divided by porosity. Therefore, a pore-Peclet number can be defined as:

$$N_P = \frac{v_{inj} \bar{d}_P}{\phi D} \quad (9)$$

Following [29], the longitudinal dispersion coefficient normalized by molecular diffusion coefficient can be correlated to Peclet number as:

$$\frac{K_L}{D} = \frac{1}{F\phi} + \alpha N_P + \beta N_P^\delta + \gamma N_P^2 \quad (10)$$

In this equation,  $F$  is formation factor and  $\alpha$ ,  $\beta$ ,  $\delta$ , and  $\gamma$  are correlation parameters. At very low Peclet numbers (usually  $N_P < 0.1$ , [15]) the dominant transport mechanism is pure molecular diffusion. However, because of the presence of solid grains in the path of fluid particles, diffusion is restricted compared to the diffusion in a bulk fluid and therefore the normalized dispersion coefficient is smaller than unity and is equal to  $1/F\phi$ . At higher Peclet numbers, advection is the dominant transport mechanism. If advection is the sole mechanism of transport (mechanical dispersion), normalized dispersion coefficient scale with  $N_P$  (second term on the right hand side of Eq.10). If advection is dominant, but still diffusion from the boundary layer near the surface of solids is contributing to the transport, normalized diffusion coefficient scales with  $N_P^\delta$  (third term on the right hand side of Eq.10), where the power law coefficient  $\delta$  is usually between 1.1 to 1.3 [15] with a value of 1.2 for unconsolidated bead packs [30]. The last term in Eq.10 accounts for hold-up dispersion which occurs due to both diffusion from

dead end pores and recirculation. Since in our porous media models usually there is no dead end pore, we can assume that there is no hold-up dispersion, so the last term of Eq. 10 is ignored. The magnitude of dispersion coefficient in a simulated miscible displacement can be calculated by matching the numerically obtained effluent concentration profile at the outlet with the analytical semi-infinite solution of convection-dispersion equation [17,19].

## RESULTS AND DISCUSSIONS

We performed several numerical simulations to investigate the effect of injection velocity (in terms of  $N_p$ ), medium pore scale heterogeneity (in terms of  $CV$ ), and viscosity ratio of displacing and displaced fluids (in terms of log-viscosity ratio,  $R = \ln(\mu_1/\mu_2)$ ) on the magnitude of dispersion coefficient. Two values of 0 and 3 for log-viscosity ratio are considered and simulations are run on the four media of Figure 1 at different pore-Peclet numbers.

### Case 1: $R = 0$ , Constant $D$

The values of longitudinal dispersion coefficient normalized by molecular diffusion coefficient are plotted against pore-Peclet number in Figure 2 for the four porous media of Figure 1. A power law equation has been fit on the data at high Peclet numbers to obtain the value of  $\delta$ . The results show that  $\delta \approx 1.2$  which is in agreement with the value of 1.2 for unconsolidated bead packs [30]. Also, it seems that  $\beta$  is increasing as the heterogeneity of medium ( $CV$ ) is increasing. All of the graphs of Figure 2 are plotted on a single graph in Figure 3. It is evident that the magnitude of longitudinal dispersion coefficient is higher for more heterogeneous media and this effect of heterogeneity is more significant at larger Peclet numbers.

### Case 2: $R = 0$ , Concentration-Dependent $D$

To explore how the concentration dependency of mutual diffusion coefficient affects the performance of miscible displacement, several simulations at unit viscosity ratio are run on the four media considered here. Note that the average value of  $D(x)$  in Eq.5 over the concentration range of  $x = 0$  to mole fraction of solute in the injecting fluid ( $x = x_{inj}$ ) is equal to the constant diffusion coefficient ( $1 \times 10^{-10}$  m<sup>2</sup>/s) assumed in previous case. The reason is to make the results of case 1 and 2 comparable to each other. Also this value of average diffusion coefficient is used in definition of pore-Peclet number in Figure 4. This figure shows how dispersion coefficient is changing with  $N_p$ . The results show that the values of dispersion coefficient and the power low trend line are comparable to that of case 1 (Figure 2). It implies that using an appropriate average value for diffusion coefficient can sufficiently account for the concentration dependency of diffusion coefficient.

### Case 3: $R = 3$

Because the results of previous section showed that using an average value of  $1 \times 10^{-10}$  m<sup>2</sup>/s for diffusion coefficient can predict the same results as using Eq.5 and

corresponding values of  $D_{BA}^0$  and  $D_{AB}^0$  from Table 1, the simulations of miscible displacement at log-mobility ratio of 3 are just performed for the case of constant diffusion coefficient. Figure 5 shows the results of the simulations. The development of vicious fingering due to unfavorable viscosity contrast enhances the mixing and therefore leads to higher values of longitudinal dispersion coefficient compared to results of Figure 3. Also, at this unfavorable viscosity ratio, the normalized longitudinal dispersion coefficient scales with  $N_p$  on a log-log plot at all values of  $N_p > 0.1$  (Figure 5).

## CONCLUSIONS

In this study, pore scale simulations of miscible displacement in heterogeneous two dimensional packings of grains are conducted to estimate the magnitude of longitudinal dispersion coefficient at different values of flow velocity, medium heterogeneity, and viscosity ratio. The results of simulations at a unit viscosity ratio show that at very low Peclet numbers, diffusion is the dominant mechanism of transport, while at high Peclet numbers, transport is advection dominated and dispersion coefficient scales with Peclet number by a power law equation. The heterogeneity of packings described as the ratio of standard deviation in grain diameter to the mean grain diameter is shown to have an impact on dispersion coefficient: more heterogeneous media have higher dispersion coefficients. Also, as long as we use an appropriate average value for diffusion coefficient, it seems that there is no need to consider the concentration dependency of diffusion coefficient. The results of simulations at a higher viscosity ratio demonstrated that the occurrence of viscous fingering gives rise to enhanced mixing and therefore higher values of dispersion coefficient.

## ACKNOWLEDGMENT

The authors gratefully acknowledge the financial support of the FUR program from NSERC, AITF/i-CORE, and the sponsoring companies: Laricina Energy, Athabasca Oil Corporation, Devon Canada, Foundation CMG, Husky Energy, Brion Energy, Canadian Natural, Maersk Oil, Suncor Energy, and the Schulich School of Engineering, University of Calgary.

## REFERENCES

1. Taheri, S., Ghomeshi, S., Bryan, J. L., Kryuchkov, S., and Kantzas, A. (2014). Sub-Pore Scale Modelling of Viscous Fingering During Heavy Oil Miscible Flood. Paper SPE 170090-MS presented at the *SPE Heavy Oil Conference-Canada* held in Calgary, Alberta, Canada, 10-12 June 2014.
2. Kamali, F., Hussain, F., and Cinar, Y. (2015). A Laboratory and Numerical-Simulation Study of Co-Optimizing CO<sub>2</sub> Storage and CO<sub>2</sub> Enhanced Oil Recovery. *Society of Petroleum Engineers Journal*, 20(06), 1227-1237.
3. Rolle, M., and Kitanidis, P. K. (2014). Effects of compound-specific dilution on transient transport and solute breakthrough: A pore-scale analysis. *Advances in Water Resources*, 71, 186-199.

4. Cirpka, O. A., Chiogna, G., Rolle, M., and Bellin, A. (2015). Transverse mixing in three-dimensional nonstationary anisotropic heterogeneous porous media. *Water Resources Research*, 51(1), 241-260.
5. Ye, Y., Chiogna, G., Cirpka, O., Grathwohl, P., and Rolle, M. (2015). Experimental investigation of compound-specific dilution of solute plumes in saturated porous media: 2-D vs. 3-D flow-through systems. *Journal of contaminant hydrology*, 172, 33-47.
6. Nicolaides, C., Jha, B., Cueto-Felgueroso, L., and Juanes, R. (2015). Impact of viscous fingering and permeability heterogeneity on fluid mixing in porous media. *Water Resources Research*, 51(4), 2634-2647.
7. Haajizadeh, M., Fayers, F. J., and Cockin, A. P. (2000). Effects of Phase Behavior, Dispersion and Gridding on Sweep Patterns for Nearly Miscible Gas Displacement. Paper SPE 62995-MS presented at the *SPE Annual Technical Conference and Exhibition* held in Dallas, Texas, U.S.A., 1-4 October 2000.
8. Taylor, G. (1953). Dispersion of soluble matter in solvent flowing slowly through a tube. In *Proceedings of the Royal Society of London A: Mathematical, Physical and Engineering Sciences*, 219(1137), 186-203.
9. Aris, R. (1956). On the dispersion of a solute in a fluid flowing through a tube. In *Proceedings of the Royal Society of London A: Mathematical, Physical and Engineering Sciences*, 235(1200), 67-77.
10. Aris, R. (1959). On the dispersion of a solute by diffusion, convection and exchange between phases. In *Proceedings of the Royal Society of London A: Mathematical, Physical and Engineering Sciences*, 252(1271), 538-550.
11. Brigham, W.E., Reed, P.W., & Dew, J.N. (1961). Experiments on mixing during miscible displacement in porous media. *Society of Petroleum Engineers Journal*, 1(1), 1-8.
12. Perkins, T. K., and Johnston, O. C. (1963). A review of diffusion and dispersion in porous media. *Society of Petroleum Engineers Journal*, 3(01), 70-84.
13. Coelho, D., Thovert, J. F., and Adler, P. M. (1997). Geometrical and transport properties of random packings of spheres and aspherical particles. *Physical Review E*, 55(2), 1959.
14. Maier, R. S., Kroll, D. M., Bernard, R. S., Howington, S. E., Peters, J. F., and Davis, H. T. (2000). Pore-scale simulation of dispersion. *Physics of Fluids (1994-present)*, 12(8), 2065-2079.
15. Bijeljic, B., Muggeridge, A. H., and Blunt, M. J. (2004). Pore-scale modeling of longitudinal dispersion. *Water Resources Research*, 40(11).
16. Beard, D. A., and Wu, F. (2009). Apparent diffusivity and Taylor dispersion of water and solutes in capillary beds. *Bulletin of mathematical biology*, 71(6), 1366-1377.
17. Garmeh, G., Johns, R. T., and Lake, L. W. (2009). Pore-scale simulation of dispersion in porous media. *Society of Petroleum Engineers Journal*, 14(04), 559-567.
18. Mostaghimi, P., Bijeljic, B., and Blunt, M. (2012). Simulation of flow and dispersion on pore-space images. *Society of Petroleum Engineers Journal*, 17(04), 1131-1141.
19. Taheri, S., Abedi, J., and Kantzas, A. (2013). Prediction of Effective Diffusion and Dispersion Coefficients, Considering Different Flow and Heterogeneity Properties of Porous Media. Paper SPE 165520-MS presented at the *SPE Heavy Oil Conference-Canada* held in Calgary, Alberta, Canada, 11-13 June 2013.

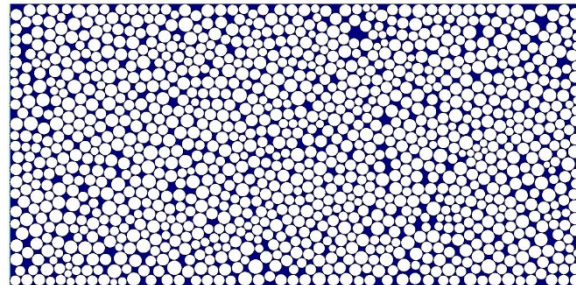
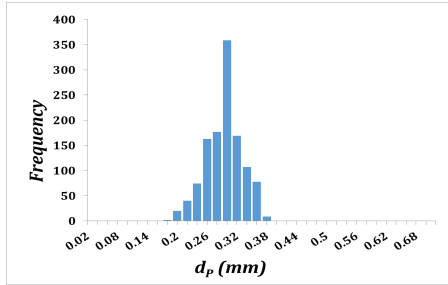
20. Raimondi, P., Gardner, G. H. F., and Petrick, C. B. (1959, December). Effect of pore structure and molecular diffusion on the mixing of miscible liquids flowing in porous media. In *AIChE-SPE Joint Symposium, San Francisco*.
21. Orlob, G. T., and Radhakrishna, G. N. (1958). The effects of entrapped gases on the hydraulic characteristics of porous media. *Eos, Transactions American Geophysical Union*, 39(4), 648-659.
22. Bretz, R. E., Specter, R. M., and Orr Jr, F. M. (1988). Effect of pore structure on miscible displacement in laboratory cores. *SPE Reservoir Engineering*, 3(03), 857-866.
23. Kelkar, B. G., and Gupta, S. P. (1988, January). The Effects of Small-Scale Heterogeneities on the Effective Dispersivity of Porous Medium. In *SPE Enhanced Oil Recovery Symposium*. Society of Petroleum Engineers.
24. Arya, A., Hewett, T. A., Larson, R. G., and Lake, L. W. (1988). Dispersion and reservoir heterogeneity. *SPE Reservoir Engineering*, 3(01), 139-148.
25. Garmeh, G., and Johns, R. T. (2010). Upscaling of miscible floods in heterogeneous reservoirs considering reservoir mixing. *SPE Reservoir Evaluation and Engineering*, 13(05), 747-763.
26. Vignes, A. (1966). Diffusion in binary solutions. Variation of diffusion coefficient with composition. *Industrial and Engineering Chemistry Fundamentals*, 5(2), 189-199
27. Guerrero-Aconcha, U. E., Salama, D., and Kantzas, A. (2008, January). Diffusion Coefficient of n alkanes in Heavy Oil. In *SPE Annual Technical Conference and Exhibition*. Society of Petroleum Engineers.
28. Koval, E. J. (1963). A method for predicting the performance of unstable miscible displacement in heterogeneous media. *Society of Petroleum Engineers Journal*, 3(02), 145-154.
29. Sahimi, M. (1995). Effect of long-range correlations on transport phenomena in disordered media. *AIChE Journal*, 41(2), 229-240.
30. Pfannkuch, H. O. (1963). Contribution à l'étude des déplacements de fluides miscibles dans un milieu poreux. *Revue de l'Institut français du pétrole et Annales des combustibles liquides*.

Table 1. Parameters used in the simulations

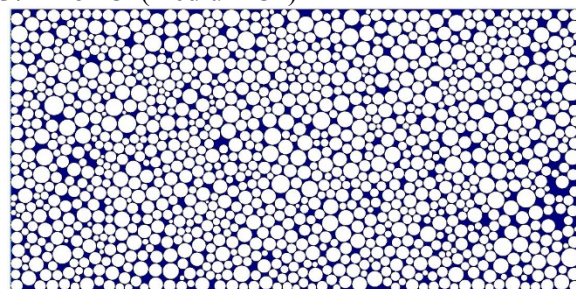
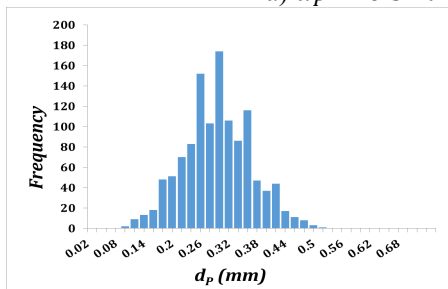
Parameter name	Value
$\rho_A = \rho_B = \rho$	1000 kg/m <sup>3</sup>
$c_{inj}$	1 k-mole/m <sup>3</sup>
$M_A$	100 kg/k-mole
$M_B$	500 kg/k-mole
$x_{inj}$	0.357
$\mu_1$	1 and 20 cp
$\mu_2$	1 cp
$D$ (when assumed to be constant)	$1 \times 10^{-10}$ m <sup>2</sup> /s
$D_{BA}^0$	$2 \times 10^{-9}$ m <sup>2</sup> /s
$D_{AB}^0$	$5 \times 10^{-11}$ m <sup>2</sup> /s

Table 2. Patterns used in the simulations of this study and their properties

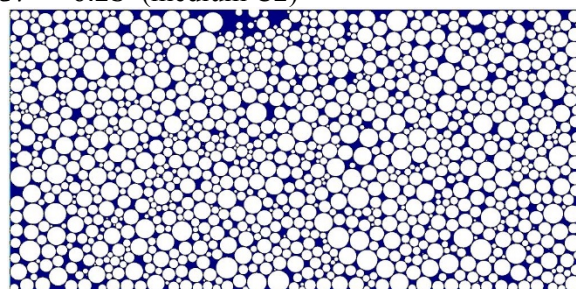
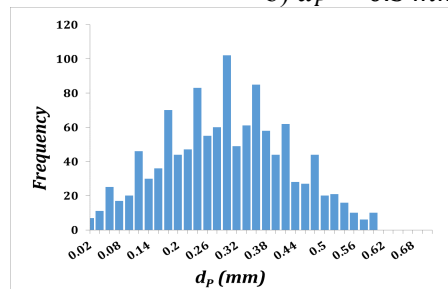
Name	$\overline{d_p}$ (mm)	CV	Number of Particles	Length ( $L$ ) (mm)	Width ( $W$ ) (mm)	Porosity	Permeability (Darcy)
<b>C1</b>	0.3	0.13	1200	13.87	6.93	0.240	1.729
<b>C2</b>	0.3	0.25	1200	14.22	7.11	0.235	2.039
<b>C3</b>	0.3	0.44	1200	15.13	7.56	0.227	2.650
<b>C4</b>	0.3	0.53	1200	15.85	7.92	0.253	3.342



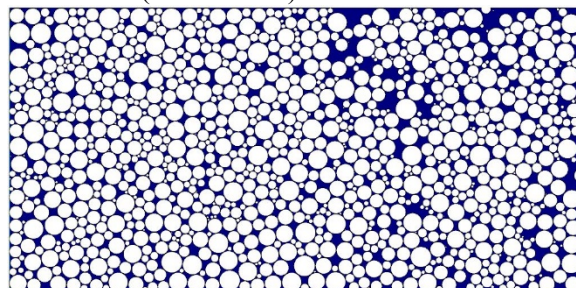
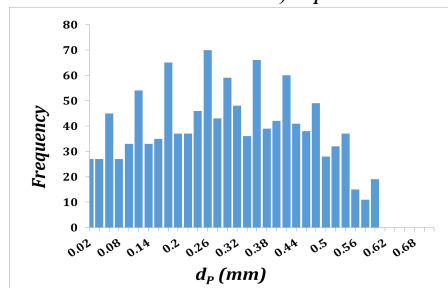
a)  $\overline{d_p} = 0.3$  mm , CV = 0.13 (medium C1)



b)  $\overline{d_p} = 0.3$  mm , CV = 0.25 (medium C2)



c)  $\overline{d_p} = 0.3$  mm , CV = 0.44 (medium C3)



d)  $\overline{d_p} = 0.3 \text{ mm}$  ,  $CV = 0.53$  (medium C4)

Figure 1. Sample media with the same  $\overline{d_p}$  and different  $CV$  along with their corresponding PSDs

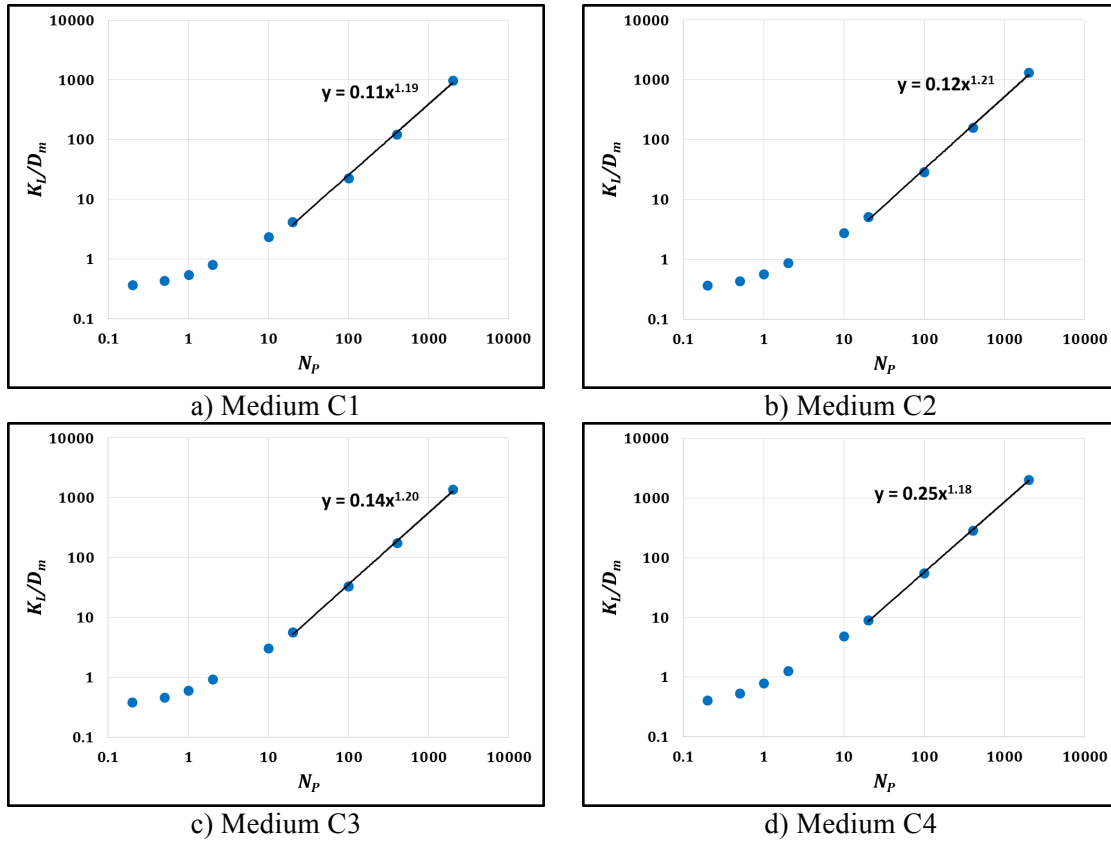


Figure 2. Variation of normalized longitudinal dispersion coefficient with pore-Peclet number at unit viscosity ratio ( $R = 0$ ) and constant diffusion coefficient of  $1 \times 10^{-10} \text{ m}^2/\text{s}$

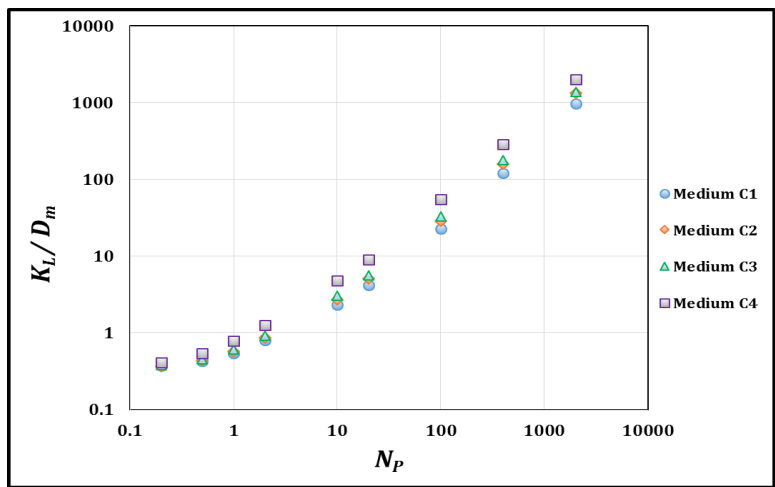


Figure 3. Effect of medium heterogeneity on longitudinal dispersion coefficient at unit viscosity ratio ( $R = 0$ ) and constant diffusion coefficient of  $1 \times 10^{-10} \text{ m}^2/\text{s}$

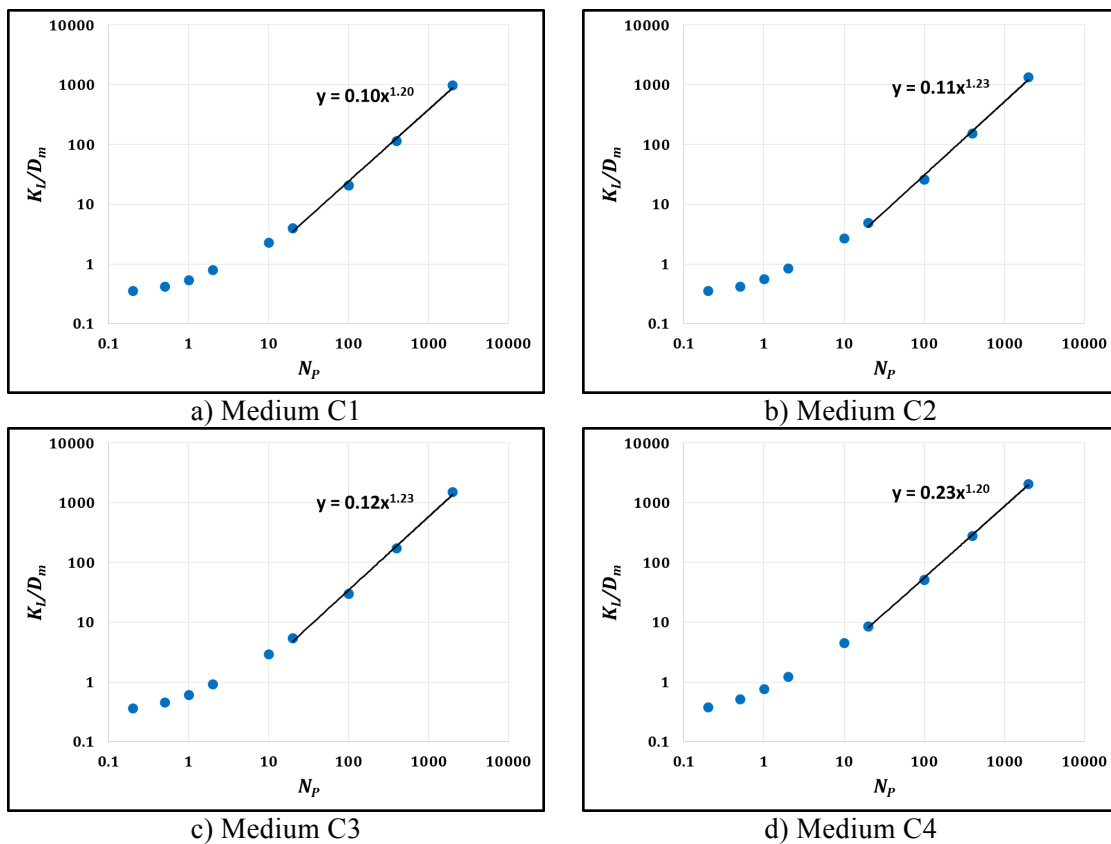


Figure 4. Variation of normalized longitudinal dispersion coefficient with pore-Peclet number at unit viscosity ratio ( $R = 0$ ) and concentration-dependent diffusion coefficient

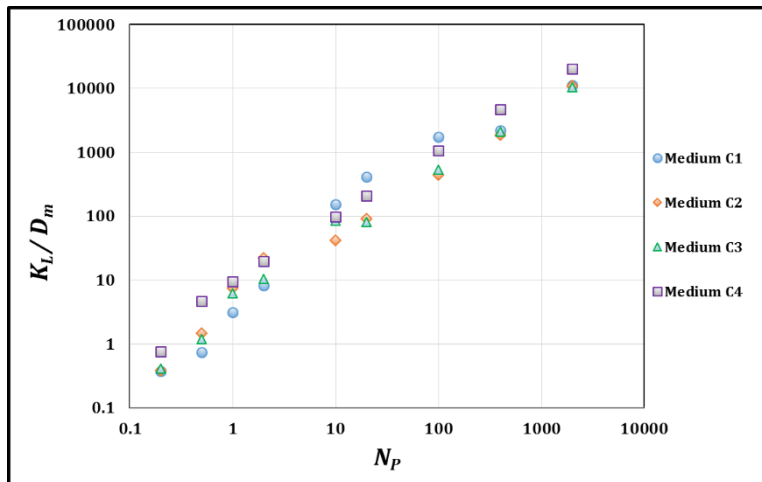


Figure 5. Variation of normalized longitudinal dispersion coefficient with pore-Peclet number at unfavorable viscosity ratio ( $R = 3$ ) and constant diffusion coefficient of  $1 \times 10^{-10} \text{ m}^2/\text{s}$

## DETERMINING THE SATURATION EXPONENT BASED ON NMR PORE STRUCTURE INFORMATION

Xu Hongjun<sup>1,2</sup>, Fan Yiren<sup>1</sup>, Zhou Cancan<sup>2</sup>, Hu Falong<sup>2</sup>, Li Chaoliu<sup>2</sup>, Yu Jun<sup>2</sup> and Li Changxi<sup>2</sup>

<sup>1</sup>School of Geosciences, China University of Petroleum, Qingdao, China

<sup>2</sup>PetroChina RIPED, Beijing, China

*This paper was prepared for presentation at the International Symposium of the Society of Core Analysts held in Snowmass, Colorado, USA, 21-26 August 2016*

### ABSTRACT

In the tight sandstone reservoir, the saturation exponent with Archie's relation varies greatly from the usual value  $n=2$ . This is usually attributed to complex porous structure. In this work, we involved a series of NMR T2 measurements and experimental RI measurements on core plugs in different brine saturations. Based on NMR, MICP porous structure characterizations and RI results, we found a close relationship between NMR porous structure information and the saturation exponent. The new approach enables deeper understand of the rock porous structure and how the porous structure controls the flow path of the core plug by NMR.

### INTRODUCTION

In petroleum industry, the brine saturation is important in reservoir evaluation and production, and the electrical property is used to estimate the saturation exponent and the brine saturation. In experimental RI measurements, the fluid in core plugs of the tight sandstone reservoir is very hard to be drained, so the RI results cannot show the real transport property of core plugs, and saturation exponents vary greatly from the usual value  $n=2$ . In this paper, we attempt to present an experimental method to estimate the saturation exponent from NMR measurements. As a transport property, the electrical conductivity depends not only on porosity but is also strongly sensitive to the connectivity of the pore space and their micro-geometry (Cerepi et al., 2002). In a T2 measurement, the NMR signal, when extrapolated back to zero time, is proportional to the population of the hydrogen nuclei in the probed zone. When properly calibrated, the NMR measurement is an excellent way to measure lithology-independent total porosity. And NMR has matured over into a powerful petrophysical tool for permeability estimation, which is a transport property of the reservoir (Kenyon, 1997). So the NMR technology has potential as a new tool for describing transport properties and determining the saturation exponent. Coates, G.R. (1994) comprehensively dealt with the MRIL data and deep resistivity data, and built the MRIAN model for brine saturation evaluation. Emmanuel Toumelin (2006) introduced a geometrical framework to simulate electrical conductivity and NMR rock responses with diffusion random walks. Luo Shaocheng

(2014) used NMR T2 distribution to deliver porous structure parameters, and built the empirical formula by several important parameters. The results from these studies show that NMR is capable of delivering both porous structure parameters and saturation evaluation parameters.

In the present work, fully brine saturated core plugs were centrifuged in air with different capillary pressures in sequence. We did NMR T2 measurements and RI measurements on core plugs in fully brine saturated state and partially saturated state, and studied the relationship between the electrical property and the NMR information. In this way, we analyzed the connectivity of the pore space and their micro-geometry. We calculated ratios of the logarithmic mean T2 between the fully saturation and partially saturations, and these ratios were able to reveal effects on the flow path of core plugs. The saturation exponent can be found by analyzing the functional relationship between ratios and the corresponding saturations. During these experiments, partially saturated core plugs were always in high saturation range. In order to study their micro-geometry at low saturation range, we found a relationship between the logarithmic mean T2 and the T2 mean value. Based on this relationship, the logarithmic mean T2 in any saturation can be obtained, which laid a foundation for up-scaling to reservoir level. When core plugs were in low saturation, the saturation exponent can show the real connectivity of the pore space and their micro-geometry and would be helpful for reservoir evaluation and production.

## **EXPERIMENTAL**

### **Core Samples and Measurements**

For Chang7 reservoir characteristics, representative core plugs were used in this study. The porosity ranged from 6.2% to 12.2%, and the permeability ranged from 0.012mD to 0.262mD. Core plugs had length and diameter of about 3 cm and 2.5 cm, respectively (cf. Table1). They were dried and then evacuated for 12 hours before brine was introduced into the vacuum chamber. A method combined the NMR measurement, the electrical measurement and the centrifuge technique was carried out to measure these core plugs in fully brine saturation and partially brine saturation. NMR T2 measurements were performed by using a 2 MHz MARAN DRX spectrometer from Oxford Instruments. A CPMG pulse sequence was used to generate the T2 decay. Parameters used for NMR measurements were: 512 scans, 4096 echoes and an inter-echo time of 200  $\mu$ s. The de-saturation experiments were carried by the URC-628 URLTRA-ROCK centrifuge and centrifugal forces were designed as 150 psi, 600 psi, 940 psi. Figure1 shows experimental procedures.

## **RESULTS AND DISCUSSIONS**

### **Relation between Porous Structure and Saturation Exponent**

Table 1 indicates petrophysical parameters and porous structure parameters. N94 and N19 were selected for detailed studies. Figure 2 shows the mercury injection capillary pressure curves of the previous cores. Figure 3 presents the incremental saturation plots of the same mercury injection tests showed in Figure 2. As can be seen in the two figures, the main pore throat radius range of N94 is in MESO size, while N19 is dominated by MICRO and NANO pore throats. A better understanding of the behavior of MICP is

achieved when it is integrated with the information provided by NMR. The main part of N94's T2 distribution is over 10ms and its peak value is about 70ms, while the T2 distribution of N19 is concentrated below 10ms, and the peak value is about 3ms. In order to find the relationship between the porous structure and the saturation exponent, porous structure parameters from MICP, NMR and the saturation exponent were analyzed. It was found that a good fit was achieved between the mean value of throat radius and the logarithmic mean T2 (cf. Figure 4). Figure 5 is the crossplot between the saturation exponent and the mean value of throat radius. This points out that the saturation exponent of tight sandstones reservoir is to a large extent controlled by porous structure. The saturation exponent of the core plug with good pore structure quality, such as N94, ranges from 1.5 to 2. When the main pore throat radius that contributes to the flow property is the MICRO or NANO size, the saturation exponent is over 2 (cf. Figure 5). Basically, the worse of the porous structure, the larger of the saturation exponent.

### Relation between Logarithmic Mean T2 and Electrical Property

As can be seen, the logarithmic mean T2 and the mean value of throat radius play an equally important role in describing the porous structure (cf. Figure 4). The logarithmic mean T2 is calculated by Equation 1, which is a comprehensive parameter on the pore radius and the porosity in theory. Where, T2 is the relaxation time and Sa is the signal amplitude.

$$\langle T_{2LM} \rangle = \exp\left(\frac{\sum_i Sa_i * \log T_{2i}}{\sum_i Sa_i}\right) \quad (1)$$

In order to validate that NMR technology could be a tool for describing the transport property, we need to analyze the evolution data of the core plug in drainage mode, and find the relationship between the logarithmic mean T2 and the electrical resistivity. During the centrifugation process (cf. Figure 6, 7), the meso-pores are drained progressively at low speed. At high speed, the partial brine in the micro-pores is drained out of the core plug. The brine in nano-pores is very hard to drain ( $S_w=75\%$  of N19). In the process of de-saturation, micro-pores and nano-pores have a growing influence on the transport property. Specifically, with decreasing the brine saturation, the logarithmic mean T2 decreases and the electrical resistivity increases. Although their changes are different, they show the change of the transport property from different aspects. Figure 8 shows that there is a power function relationship between the logarithmic mean T2 and the electrical resistivity. There are differences in the porous structure of N94 and N19. So the power function varies with the porous structure in a way, which lays a foundation for calculating saturation exponent with NMR method.

### New NMR Method for Saturation Exponent

New NMR method is concentrated on the logarithmic mean T2 and the corresponding brine saturation. At each saturation, we calculated the ratio of the logarithmic mean T2 between the fully saturation and the corresponding saturation. These ratios revealed the effect of porous structure on the flow path of the core plug. The new saturation exponent was calculated by Equation 2. New results and saturation exponents from traditional RI measurements are showed in Table 1.

$$\frac{T_{2LM(S_w=100\%)}}{T_{2LM(S_w)}} = \frac{B}{S_w^N} \quad (2)$$

Where,  $T_{2LM(S_w=100\%)}$  is the logarithmic mean T2 in fully brine saturated condition,  $T_{2LM(S_w)}$  is the logarithmic mean T2 in different partially brine saturated condition, N is the new saturation exponent, B is the coefficient.

In the new experimental procedure, on the one hand, we need to do several NMR measurements and centrifuge measurements, which were inconvenient for us to up-scale to the reservoir level. On the other hand, the irreducible brine saturation was in the high saturation range. In Figure 9, we found that there was a good fit between the logarithmic mean T2 and the T2 mean value (Equation 3). The T2 mean value in any saturation is easily to calculate from the T2 distribution in fully brine saturation, so the logarithmic mean T2 in any saturation can be obtained from Equation 3. Where, X is the T2 mean value.

$$\langle T_{2LM} \rangle = 1.0943X - 0.1237 \quad (3)$$

At low saturation range, the flow path is limited, and depends on the connectivity of the micro-porosity and the water film. In order to reduce the influence of the disconnection of the pore space, the minimal water saturation was selected as 30%, and the water saturation step was 10%. We recalculated the logarithmic mean T2 in different water saturations, and recalculated the saturation exponent using Equation 2. The results are also showed in Table 1. As more micro-porosity is included, results are slightly different from centrifuge ones.

## CONCLUSION

We introduced a new method to calculate the saturation exponent in the tight sandstone reservoir. This method was focused on the porous structure, and solved some difficulties in calculating the saturation exponent with the traditional method. It was more helpful for the oil saturation determination and reservoir evaluation in the tight sandstone reservoir.

## ACKNOWLEDGEMENTS

The authors wish to thank Petrochina for allowing us to publish the study. We would like to thank Shi Yujiang and Zhang Haitao at Changqing Oilfield for providing us core plugs.

## REFERENCES

1. Kenyon, W.E., Petrophysical Principles of Application of NMR Logging, *The Log Analyst*, (1997) 38, No.2, 21-43
2. Emmanuel Toumelin,, An Integrated Pore-Scale Approach for The Simulation of Grain Morphology, Wettability, and Saturation-History Effects on Electrical Resistivity and NMR Measurements of Saturated Rocks, *International Symposium of the Society of Core Analysts held in Trondheim*, Norway 12-16 September, 2006, SCA2006-20

3. M. Han, V. Tariel, S. Youssef, the Effect of the Porous Structure on Resistivity Index Curves. An Experimental and Numerical Study, *SPWLA 49<sup>th</sup> Annual Logging Symposium*, May 25-28,2008, BBB
4. Luo Shangcheng, Research on Saturation Index n of Tight Sandstone Reservoir, *Journal of Southwest Petroleum University(Science&Technology Edition)*, (2014) 36,No.4, 116-121
5. Libny Leal, Roberto Barbato, Alfonso Quaglia, Bimodal Behavior of Mercure-Injection Capillary Pressure Curve and its Relationship to Pore Geometry, Rock-Quality and Production Performance in a Laminated and Heterogeneous Reservoir, *SPE Latin American and Caribbean Petroleum Engineering Conference held in Buenos Aires, Argentina, 25-28 March 2001*, SPE 69457

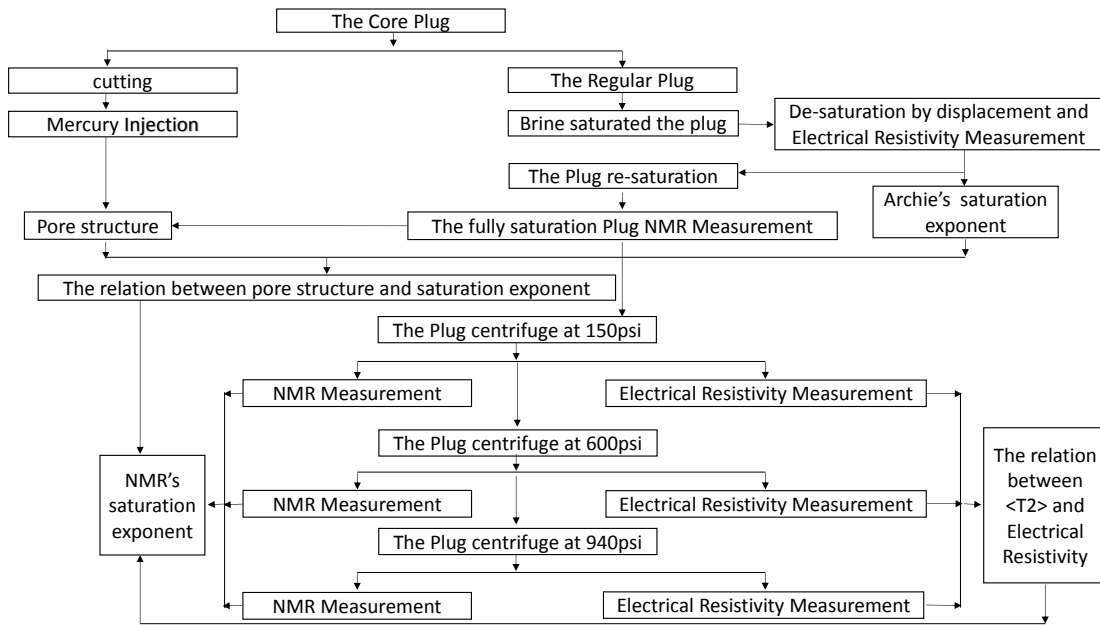


Figure1. Experimental Procedures

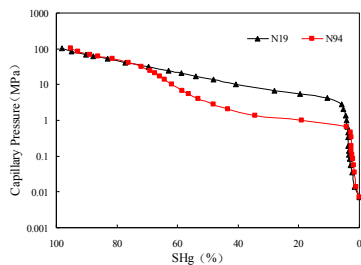


Figure 2. MICP profile

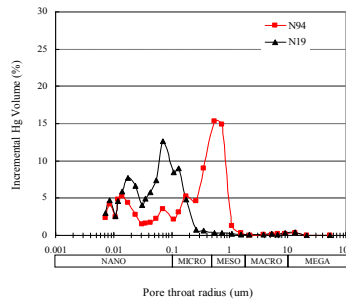


Figure 3 Incremental saturation plots

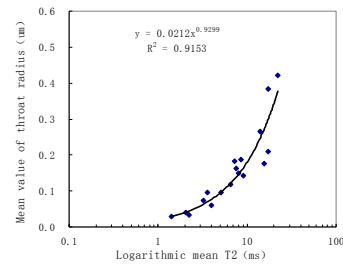


Figure 4 Corssplot of the logarithmic mean T2 and the mean value of throat radius

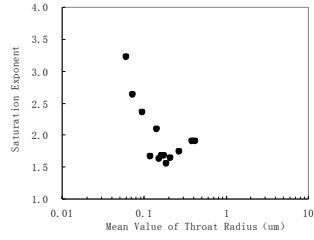


Figure 5. Crossplot of the saturation exponent and the mean value of throat radius

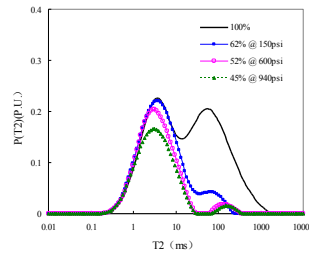


Figure 6 The T2 distribution evolution of N94 in drainage

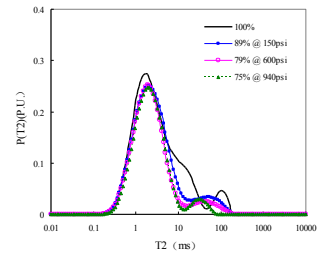


Figure 7 The T2 distribution evolution of N19 in drainage

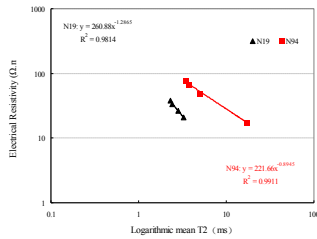


Figure 8. Crossplot of the logarithmic mean T2 and the electrical resistivity

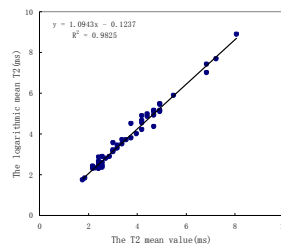


Figure 9. Crossplot of the logarithmic mean T2 and the T2 mean value

Table1.Petrophysical Parameters and Saturation Exponents

Sample ID	Helium Porosity(%)	Permeability (mD)	Mean Value of Throat Radius(um)	logarithmic mean T2(ms)	Saturation Exponent(Electrical Resistivity)	Saturation Exponent(NMR & centrifuge)	Saturation Exponent(NMR @ any saturation)
N15	11.2	0.105	0.151	8.0	1.624	1.642	1.352
N17	8.1	0.037	0.095	5.1	2.354	2.069	1.225
N19	7.1	0.028	0.073	3.2	2.635	1.651	1.127
N24	8.5	0.062	0.142	9.1	2.097	1.834	1.286
N45	11.5	0.217	0.187	8.5	1.548	1.756	1.376
N51	7.3	0.098	0.176	12.6	1.682	1.971	1.507
N53	11.0	0.115	0.163	7.8	1.684	1.659	1.347
N58	7.7	0.099	0.209	13.9	1.643	1.676	1.482
N64	9.7	0.012	0.061	4.0	3.221	2.138	1.225
N75	12.2	0.075	0.118	6.6	1.664	1.622	1.351
N90	6.2	0.103	0.266	13.9	1.736	1.577	1.398
N91	9.4	0.214	0.422	22.3	1.908	1.920	1.616
N94	10.0	0.262	0.384	17.6	1.910	2.158	1.709

# **EXPERIMENTAL ASSESSMENT OF THE HYDROCARBONS YIELDS FROM BAZHENOV SHALE FORMATION BY KEROGEN CONVERSION IN THE PRESENCE OF SUPERCRITICAL WATER**

Tatiana Bondarenko, Evgeny Popov, Alexey Cheremisin,  
Skoltech Center for Hydrocarbon Recovery  
Skolkovo Institute of Science and Technology, Moscow, Russia  
Igor Karpov, Nikita Morozov  
LLC Gazpromneft STC, St.-Petersburg, Russia

*This paper was prepared for presentation at the International Symposium of the Society of Core Analysts held in Snowmass, Colorado, USA, 21-26 August 2016*

## **ABSTRACT**

The study presents experimental results on the use of supercritical water (SCW) as an Enhanced Oil Recovery (EOR) agent for Bazhenov formation. Bazhenov formation is the biggest potential shale reserves in Russia. Therefore, as the world's oil supply decreases, the need to find EOR techniques in order to develop Bazhenov formation becomes evident. The experimental studies on oil shale performed in the work will help to advance the move to large scale oil production from the hydrous pyrolysis of shale. The main purpose of the study was to estimate experimentally a potential of hydrocarbon recovery from oil shales and to evaluate technique of kerogen conversion in the presence of supercritical water. In order to investigate a temperature influence on hydrocarbon recovery during kerogen conversion in the presence of supercritical water, a series of experiments were conducted on non-extracted crushed samples at 300, 350, 400 and 480°C and at pressure of 27 MPa in a pressure vessel. In result, only gaseous products were received at temperature below 400°C, whereas liquid hydrocarbons in state of films on the rock sample and the vessel's walls were detected only starting from temperature of 400°C. For the sake of evaluating amount of converted kerogen, open-system pyrolysis on rock samples before and after experiments with SCW were carried out. Results indicate almost total recovery of free hydrocarbons (S1) and 82% decrease in the amount of hydrocarbons generated through thermal cracking of non-volatile organic matter (S2) after SCW injection at 480°C. Gaseous products were analyzed by gas-chromatography. Significant amount of methane was detected in the gas products at 480°C. It suggests that secondary oil cracking and coke production may starts at temperatures around 480°C. The samples' matrix porosity and matrix permeability before and after SCW injection were measured by GRI method [8]. Analysis revealed negligible porosity increase and sufficient growth in permeability when temperature is raised. We attribute this to the start of core destruction process with formation of multiple microfractures. The investigation

determined the “hydrocarbon generation window” within temperature range of 400°C and 480°C for the general Bazhenov formation rocks with low kerogen maturity at western part of West Siberian Petroleum Basin. Preliminary results show that supercritical water is a promising EOR agent for Bazhenov formation rocks.

## **INTRODUCTION**

As recovery from conventional reservoirs decreases, the need to find a new EOR technique to develop unconventional resources becomes necessary. Bazhenov formation (BF) is the biggest oil-shale reserve in Russia. The Upper Jurassic organic-rich clay-siliceous shale occurs in the West Siberian Basin. Geochemical analyses of its core samples showed total organic carbon (TOC) values of 2 to 18 wt. %, consisting mainly of amorphous kerogen, and where the level of maturity varies within the range of 429° - 446°C. The main rock section of BF is characterized by low open porosity (up to 2 %) and absolute gas permeability ranging from a microdarcy to a nanodarcy, and even less than 1 nanodarcy. [1, 2].

Despite of the huge amount of reserves, oil shales in Russia have not been developed extensively due to the absence of suitable recovery technique [3, 4]. There has been extensive research and field pilots in the Bazhenov shale using different methods by different research groups and companies [5, 6, 7]. Nevertheless, none of them has been establish as a development method. The potential of supercritical water as an EOR agent is not fully investigated for Bazhenov formation. Therefore, the experimental studies on oil shale performed in this work will help to advance the move to large-scale oil production from the hydrous pyrolysis of shale. The main purpose of the study was to estimate the potential of hydrocarbon recovery from oil shales and to evaluate the mechanism of kerogen conversion in the presence of supercritical water.

Open-system pyrolysis and closed system hydrous pyrolysis were used to evaluate the effectiveness of SCW method. Since measurements of reservoir parameters cannot be done with standard conventional techniques because of the extremely low permeability and porosity of Bazhenov shale, GRI Analysis methods were used [8]. To analyze products, gas and liquid compositional analysis was performed using gas chromatography.

## **MATERIALS AND METHODS**

Four rock samples from a well drilled in Krasnoleninsky vault in South-West Siberian Petroleum Basin were chosen to represent the Bazhenov Shale (Fig.1), the samples depth range is 2558-2561 m. The samples were crushed and homogenized to 0.5-2 mm.

The following instruments were used: monel alloy pressure vessel with pressure and temperature control, volume of the experimental cell is 200 cc (Fig. 2); HAWK Pyrolysis

Instrument; gas chromatograph “Kristall – 2000”; CoreLab SMP-200 matrix permeameter.

The GRI method for measuring permeability uses sized crushed rock samples and detects the pressure pulse response in the sample cell. Permeability is then calculated through the analysis of the pressure decay over time.



Figure 1. Disintegrated sample of Bazhenov shale.

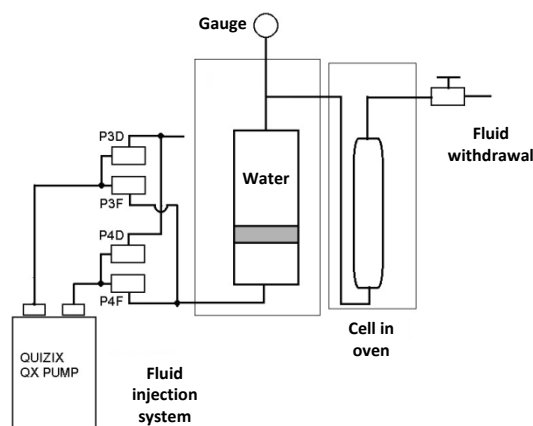


Figure 2. Hydraulic Scheme of the experimental setup.

## PROCEDURES

The experiments were designed to investigate the influence of temperature on hydrocarbon recovery during kerogen conversion in the presence of supercritical water. A series of experiments was conducted on non-extracted crushed samples at pressure of 27 MPa in Monel alloy pressure vessel fully filled with deionized water and 55 g of crushed rock sample. The reactor was sealed and the chamber then evacuated for one hour. The hydrous pyrolysis experiments were performed at temperatures 300, 350, 400 and 480°C with heating rate of 20°C/h. Time of treatment was 30 hours for all samples at the test temperature. After that, the pressure vessel was cooled down to room temperature and depressurized to atmospheric pressure.

Cumulative volume of produced gas was measured using a wet test meter and was collected for further evaluation using gas chromatography. Liquid samples were collected into graduated cylinders and were submitted to a compositional analysis. Organic solvent dichloromethane was used to extract oil from the oil-in-water emulsion and remove adsorbed hydrocarbons from the vessel's walls and the core crushed sample surface. The extracted oil was separated from the solvent using rotary evaporation and compositional analysis was performed. Then the rock chips were removed from the vessel and dried in an oven at 105°C to constant weight. GRI Analysis was used to evaluate the changes in shale samples' permeability and porosity after extraction with supercritical water.

In order to get percentage of kerogen converted to hydrocarbons after SCW extraction, open-system pyrolysis was performed. Two main parameters S1 and S2 were measured using HAWK pyrolysis instrument. S1 is the amount of thermally freed hydrocarbons in the sample in milligrams hydrocarbons per gram of rock by temperature of 300 °C. S2 is the amount of hydrocarbons generated through thermal cracking of non-volatile organic matter. S2 is an indication of the quantity of hydrocarbons that the rock has the potential of producing under increased burial and maturation, namely it is the kerogen yield. Samples were analyzed before and after SCW extraction to investigate the change.

## RESULTS

Only gaseous products were collected in the tests under 400°C, whereas very small volumes of liquid hydrocarbons were released from the organic matter during SCW extraction and were detected in the form of films on the rock sample and on the vessel's walls in the test at 400°C. The hydrous pyrolysis test on 55g of sample at 480°C generated 1350 scm<sup>3</sup> of gas. According to the gas chromatography results (Fig. 3), methane production increased at higher temperature. Significant amount of methane was determined in the gas products at 480°C. This suggests that secondary oil cracking and coke production started near 480°C. Oil extract was 0.308 g. The content of the polar resin-asphaltene compounds was 21.0%. Content of saturated and unsaturated hydrocarbons, aromatic and other compounds was 77.5%, 3.9% of them were n-alkanes (C10-C35).

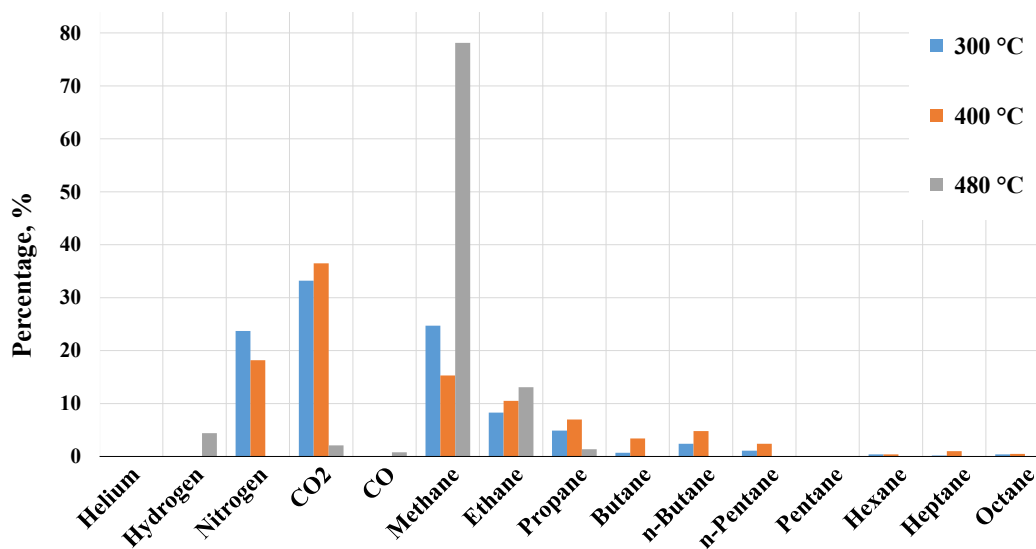


Figure 3. Produced gas compositional analysis.

GRI analysis of the rock chips revealed negligible porosity increase when temperature is raised and sufficient growth in permeability in the test #4 (Table 1). Open-system pyrolysis analysis results indicate almost total recovery of free hydrocarbons (S1) and 82% decrease in the amount of hydrocarbons generated through thermal cracking of non-volatile organic matter (S2) after SCW injection at 480°C (Table 2). Porosity of the core

after extraction is unknown and therefore original oil in place and recovery factor cannot be calculated accurately. Nevertheless, we can estimate recovery factor according to the open-system pyrolysis analysis, namely by change in S1 and S2 parameters after SCW extraction. At temperature of 480°C recovery factor is around 83%, which confirms that SCW might be a suitable EOR agent for Bazhenov formation shales.

Table 1. GRI (Crushed Shale) Analysis results.

Sample ID	Temperature, °C	Before the SCW extraction		After the SCW extraction		Percentage change, %	
		Porosity, %	K, nD	Porosity, %	K, nD	Porosity	K
1	300	1.07	20	1.14	23.3	7	17
2	350	0.75	14.4	0.97	17.8	29	24
3	400	1.40	37	1.56	45.2	11	22
4	480	1.04	28	1.55	244	49	771

Table 2. S1 and S2 parameters before and after the SCW extraction

Sample ID	Temperature, °C	Before the SCW extraction		After the SCW extraction		Percentage change, %	
		S1, mg HC/g rock	S2, mg HC/g rock	S1, mg HC/g rock	S2, mg HC/g rock	S1, mg HC/g rock	S2, mg HC/g rock
1	300	8.40	78.30	4.70	75.50	-44.0	-3.6
2	350	5.20	66.80	2.93	64.13	-43.7	-4.0
3	400	6.30	107.60	2.52	97.50	-60.0	-9.4
4	480	9.03	77.07	0.29	13.83	-96.8	-82.1

## CONCLUSION

In this study, we evaluated a technique of kerogen conversion in the presence of supercritical water. The investigation determined the “hydrocarbon generation window” within temperature range of 400°C and 480°C for the general BF rocks with low kerogen maturity of South-West Siberian Petroleum Basin. The compositional analysis of evolved products indicated that secondary oil cracking and coke production starts at 480°C. Open-system pyrolysis results indicate almost total recovery of free hydrocarbons and 82% decrease in the amount of hydrocarbons generated through thermal cracking of kerogen after SCW extraction at 480°C. GRI analysis on crushed rocks revealed negligible porosity increase and sufficient growth in permeability when temperature is raised above 400°C, which can be attributed to the start of core destruction with formation of

microfractures. Preliminary results show that supercritical water could be a promising EOR agent for Bazhenov formation shales. Obtained data might be a very useful in numerical simulation of supercritical water injection in BF. Due to the small number of hydrous pyrolysis experiments conducted, future work therefore should include different temperatures experiments to determine an accurate temperature of kerogen conversion in Bazhenov formation. In addition, effects of heating rate and minerals on hydrous pyrolysis of kerogen should be investigated.

## ACKNOWLEDGEMENTS

The research work was done with financial support of the Russian Ministry of Education and Science (unique identification number RFMEFI58114X0008).

## REFERENCES

1. Zumberge John E., Curtis John B. (2014) Petroleum Geochemistry of the UJ Bazhenov Shale and Corresponding Crude Oils, West Siberia, Russia. *Unconventional Resources Technology Conference, Denver, Colorado, USA, 25-27 August 2014*. URTeC: 1922785.
2. Khamidulin R.A. et al. (2012) Reservoir properties of the Bazhenov formation. *SPE Russian Oil&Gas Exploration&Production Technical Conference and Exhibition, Moscow, Russia, 16-18 October 2012*. SPE 162094.
3. Khalimov E.M., Melik-Pashaev V.S. (1980) About the search for commercial oil accumulations in the Bazhenov Formation. *Geologiya nefi i gaza*, 6.
4. Braduchan Y.V. et al.(1986) The Bazhenov formation of Western Siberia. *Nauka, Novosibirsk*– 216p.
5. Kokorev V.I. et al. (2013) The Impact of Thermogas Technologies on the Bazhenov Formation Studies Results. *SPE Arctic and Extreme Environments Conference & Exhibition held in Moscow, Russia, 15–17 October 2013*. SPE 166890.
6. Kokorev V.I. et al. (2014) The results of the Field Tests and Prospects of Thermogas Development of Bazhenov Formation in OJSC RITEK. *SPE Russian Oil&Gas Exploration&Production Technical Conference and Exhibition, Moscow, Russia, 14-16 October 2014*. SPE-171172-MS.
7. Vashkevich A. et al. (2014) Gazprom Neft Experience of Bazhenov Suite Development *SPE Russian Oil&Gas Exploration&Production Technical Conference and Exhibition, Moscow, Russia, 14-16 October 2014*. SPE-171165-MS.
8. Development of laboratory and petrophysical techniques for evaluating shale reservoirs (1996). *GRI-95/0496, Final technical report. Gas Research Institute, Chicago, Illinois*.

# TESTING OF THE CIRCLE AND LINE ALGORITHM IN THE SETTING OF MICRO-CT

Alexander Katsevich<sup>1,2</sup> and Michael Frenkel<sup>1</sup>  
<sup>1</sup> iTomography Corp., <sup>2</sup> University of Central Florida (UCF)

*This paper was prepared for presentation at the International Symposium of  
the Society of Core Analysts held in Snow Mass, Colorado, USA, 21-26 August 2016*

## ABSTRACT

Computed Tomography (CT) image artifacts and long scan times are common problems faced by many micro-CT users. To avoid artifacts, pure circular scanning requires small cone angles leading to longer core scan times. We describe the implementation and present the results of testing on synthetic phantoms and a real core sample of the exact 3D Filtered Backprojection (FBP) algorithm for CT image reconstruction from cone-beam data acquired with the Circle-and-Line (C&L) X-ray source trajectory. The C&L algorithm is fast and eliminates cone-beam artifacts for any cone angle. We show that adding a relatively sparse line scan allows one to both decrease the scan time (by placing circular scans farther apart) and improve image quality. A core example illustrates that a circular scan protocol utilized by a micro-CT scanner can be modified without hardware upgrades to enable the same scanner to collect data sufficient for performing C&L reconstruction.

## INTRODUCTION

Core imaging using cone-beam micro-CT is required to produce images of high quality. The most common source trajectory consists of a sequence of circular scans. Such a trajectory is incomplete, which leads to cone-beam artifacts [1]. To reduce artifacts, micro-CT systems use small cone angle scanning by placing circular scans close to each other, which leads to long scan times. Instead, one can use a helical or Circle-and-Line (C&L) trajectory (both techniques were originally developed for medical CT applications [2-7]). These trajectories are complete and, when coupled with an exact reconstruction algorithm, eliminate constraints on the cone angle. Hence they allow for faster scanning and elimination of cone-beam artifacts. These considerations motivate the use of novel source trajectories and exact reconstruction algorithms for micro-CT imaging of cores.

The case when the source trajectory is a helix is already understood well [8-9]. Less is known about 3D exact reconstruction algorithms and their practical advantages for the C&L trajectories. In this paper, we evaluate the application of the Katsevich FBP image reconstruction algorithm to the C&L trajectory [5-7]. We show that, when compared with circular scanning, C&L allows to improve both the scanner throughput and image quality.

## BRIEF DESCRIPTION OF THE C&L ALGORITHM

Consider a source trajectory consisting of a circle in the plane  $x_3 = 0$  and a line. The circle is of radius  $R$  and centered at the origin. The line is perpendicular to the plane of the circle and intersects the circle at the point  $(R, 0, 0)$ . The exact FBP algorithm for reconstruction from the cone beam data corresponding to the C&L trajectory was reported in a number of publications [5-7, 10], so here we will describe only its general high-level outline and discuss some of its practical aspects. We will assume that the detector is flat. Let  $s$  be the parameter along the source trajectory,  $y(s)$  represent the points on the trajectory,  $(u, w)$  be the coordinates on the detector (along the row and along the column, respectively), and let  $g(s, u, w)$  denote the cone beam data. We assume that the (virtual) detector contains the axis of rotation. The main steps of the algorithm are as follows (cf. [11-12]):

1. Derivative at constant direction:  $g_1(s, u, w) = \frac{d}{ds} g(s, u(s, \Theta), w(s, \Theta))$ .

Here  $u(s, \Theta), w(s, \Theta)$  are the detector coordinates of the point where the ray  $y(s) + t\Theta$ ,  $t > 0$ , hits the detector. See [13] for a simple, yet high-resolution algorithm for computing this derivative.

2. Length correction weighting:  $g_2(s, u, w) = (1 + (u^2 + w^2) / R^2)^{-1/2} g_1(s, u, w)$ .
3. Forward height rebinning:  $g_3(s, u, \rho) = g_2(s, u, w(u, \rho))$ . Here  $\rho$  is a variable that parametrizes filtering lines.
4. Filtering:  $g_4(s, u, \rho) = H g_3(s, u, \rho)$ , where  $H$  is the Hilbert transform along  $u$ .
5. Backprojection.

Suppose the region of interest inside the object being scanned fits inside the cylinder

$$x_1^2 + x_2^2 < R_0^2, |x_3| < H, \quad (2.1)$$

for some  $R_0$ ,  $0 < R_0 < R$ , and  $H > 0$ . The object itself can extend outside  $|x_3| < H$ .

Let us describe the steps (3), (4), and (5) in more detail. The data on the circle and the line are processed slightly differently. Consider the circle first. In this case filtering is performed along detector rows, so the parameter  $\rho$  mentioned in steps (3) and (4) above coincides with the variable  $w$ . Hence, forward height rebinning is not needed and  $g_3 \equiv g_2$ . Suppose that the circle is parametrized by  $(R \cos s, R \sin s, 0)$ ,  $0 \leq s < 2\pi$ . Denote

$$\begin{aligned} v^*(s, x) &:= R - (x_1 \cos s + x_2 \sin s), \\ u^*(s, x) &:= \frac{R}{v^*(s, x)} (-x_1 \sin s + x_2 \cos s), \quad w^*(s, x) := \frac{R}{v^*(s, x)} x_3. \end{aligned} \quad (2.2)$$

Here  $u^*(s, x), w^*(s, x)$  are the detector coordinates of the point  $x$  projected onto the detector. The backprojection step is given by the integral

$$f_c(x) = \frac{1}{4\pi^2} \int_0^{2\pi} \frac{g_4(s, u^*(s, x), w^*(s, x))}{v^*(s, x)} ds, \quad (2.3)$$

where we have used that  $\rho = w$ .

Next consider the line scan. Now  $s$  represents the  $x_3$ -coordinate of the source on the line. If the source is above (resp., below) the plane of the circle, then  $s > 0$  (resp.,  $s < 0$ ). The extent of the line required for reconstruction is given by

$$|s| \leq h_{\max} := 2H / (1 - (R_0 / R)). \quad (2.4)$$

Pick some  $q \in [0, 2\pi)$ , and consider the plane through the point  $(R, 0, s)$  (which represents the source on the line) tangent to the circle at  $(R \cos q, R \sin q, 0)$ . Intersection of the plane with the detector gives a filtering line. Thus, for each source position, we obtain a family of filtering lines parametrized by the point of tangency on the circle. Parametrizing filtering lines by the point of tangency leads to singularities as  $q \rightarrow 0, 2\pi$ . So, instead, we define  $\rho := \cot(q/2) \sqrt{|s| / (2H)}$ . In terms of  $\rho$  the family of filtering lines on the detector is given by

$$w = m(\rho)u + w_0(\rho), \quad m(\rho) := \frac{\sqrt{2H|s|}}{R} \rho, \quad w_0(\rho) := \operatorname{sgn}(s)H\rho^2 - \frac{s}{2}, \quad (2.5)$$

$$|\rho| \leq \rho_{\max}, \quad \rho_{\max} := \sqrt{(h_{\max} - |s|) / (2H)}.$$

For a reconstruction point  $x$ , compute

$$c_1 = 2(1 - x_1 / R), \quad c_2 = |s|(1 - (x_1^2 + x_2^2) / R^2), \quad d := c_1 |x_3| - c_2. \quad (2.6)$$

If  $d > 0$ , the image at  $x$  is affected by the cone beam data corresponding to the current source position, so backprojection at  $x$  is performed. If  $d < 0$ , the image at  $x$  is not affected by the cone beam data corresponding to the current source position, so backprojection at  $x$  is not performed. Denote

$$\rho_{\pm}^* := -\frac{\operatorname{sgn}(s) \sqrt{|s|} (x_2 / R) \pm \sqrt{d}}{\sqrt{2H} (1 - (x_1 / R))}. \quad (2.7)$$

The values  $\rho = \rho_{\pm}^*$  determine two planes that pass through the current source position and contain the reconstruction point  $x$ . The existence of two planes implies that there are two filtering lines that pass through the projection of  $x$  onto the detector. The backprojection step is then given by the integral

$$f_l(x) = -\frac{1}{4\pi^2} \int \operatorname{sgn}(x_3) \frac{g_4(s, u^*(s, x), \rho_+^*(s, x)) - g_4(s, u^*(s, x), \rho_-^*(s, x))}{v^*(s, x)} ds. \quad (2.8)$$

If  $x_3 > 0$ , the integral in (2.8) is only over the top portion of the line  $s > 0$ . If  $x_3 < 0$ , the integral in (2.8) is only over the bottom portion of the line  $s < 0$ . For each  $x$  the integral is over a finite segment of the line, since  $d$  in (2.6) becomes negative if  $|s|$  is large enough. As before,  $u^*(s, x)$  is the coordinate along the row of the projection of  $x$  onto the detector. Finally, the complete reconstruction is given by:

$$f = f_c + f_l \quad (2)$$

From the above description it is clear that the per view reconstruction times of our exact C&L algorithm and the well-known FDK algorithm are very similar.

## NUMERICAL EXPERIMENTS

In this section, we present the results of C&L testing with simulated and real core data.

**Phantom 1.** Addition of a line scan coupled with an exact reconstruction algorithm eliminates cone-beam artifacts [5-7]. On the other hand, adding a line increases the overall scan time. Hence, it is of interest to determine the maximal stepsize along the line such that cone-beam artifacts are still under control. To investigate this question we conduct experiments on a synthetic data set with parameters typical of those that occur in micro-CT. Our phantom is a collection of identical uniform balls with the attenuation coefficient 1 and radius 0.8 mm. Their centers are at  $(5i_x, 5i_y, 2i_z)$ , where  $i_x, i_y = -1, 0, 1$ ; and  $i_z = -8, -7, \dots, 8$ . We select  $R_\theta = 12.5$  mm,  $H = 9.56$  mm (cf. (2.1)). Radius of the circle  $R = 50$  mm, there are 720 views on the circle. The detector is of size 975x975 pixels, with pixels  $27 \times 27 \mu\text{m}$ .

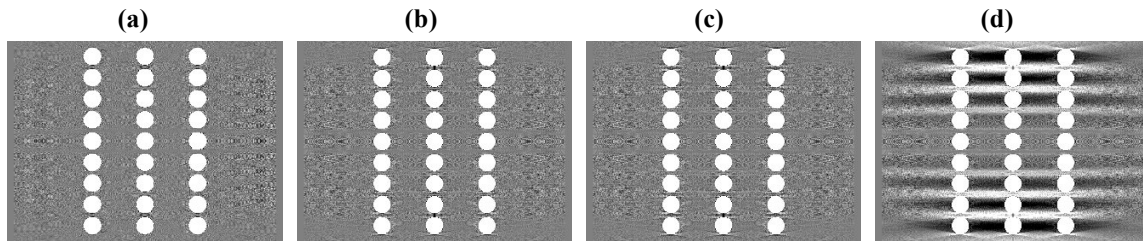


**Figure 1:** Comparisons of C&L (a-c) and Circular (d) reconstructions for cross-section  $x_1=0$  mm through the reconstructed Phantom 1. (a), (b), and (c) – 720, 360, and 180 exposures on the line scan, respectively. (d) Circular reconstruction only. Window level: WL=0; window width: WW=0.1; the balls' radii: 0.8 mm.

We conduct three experiments with 720, 360, and 180 sources on the line distributed uniformly over the length of 51 mm. The corresponding reconstruction results for the C&L scan and from only the circular scan are shown in Fig. 1. The images show the region  $|x_2| < 12.5$ ,  $|x_3| < 9.56$  mm in the plane  $x_1 = 0$  mm. Cone-beam artifacts (dark shadows between and outside the balls) are rather prominent in Fig. 1d, and are practically eliminated in Figs. 1a – 1c. In (d), the artifacts become stronger away from the plane of the circle. Hence, to keep them in check, circular scans need to be close to each other.

Comparing the images in Fig. 1, we see that as the step size on the line gets larger, some discretization artifacts (streaks coming off the tops and bottoms of the balls) get more prominent. Our results suggest that going below 180 source positions (i.e., above the stepsize 0.28 mm) results in noticeable artifacts. However, even with as few as 180 sources on the line, image quality with the line scan is far superior to that with only a circular scan.

**Phantom 2.** Here we choose a collection of small uniform balls. Their radii and centers are selected randomly in the range 0.1-0.3 mm and in the plane  $x_3 = 8.14$  mm, respectively. We perform four reconstructions: with 720, 360, and 180 sources on the line and without a line scan. All other parameters remain the same. The results are shown in Fig. 2.

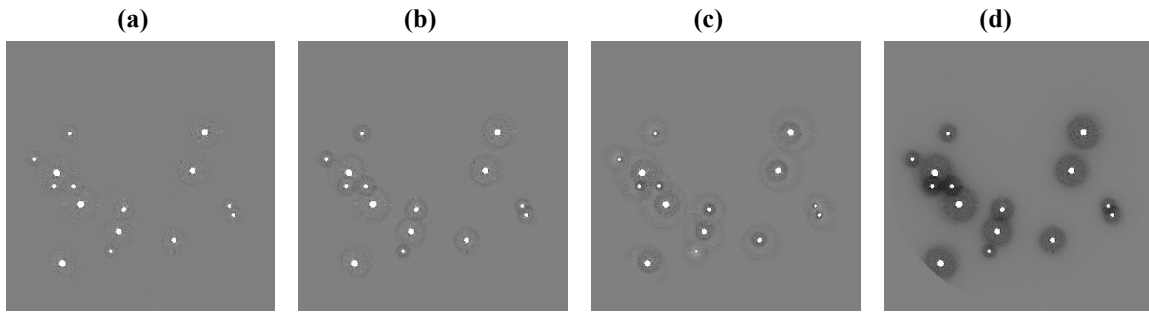


**Figure 2:** Reconstruction results for Phantom 2. (a), (b), and (c) are the C&L images generated for 720, 360, and 180 exposures on the line, respectively; (d) is the Circular reconstruction performed without a line scan. Cross-sections  $x_3 = 8.14$  mm for the region:  $|x_1| < 12.5$ ;  $|x_2| < 12.5$  mm are shown.  $WL = 0$ ,  $WW = 0.1$ .

As with Phantom 1, cone-beam artifacts (dark halos around white balls) are quite prominent in Fig. 2d. Cone-beam artifacts and discretization artifacts (ripples around the balls) are practically eliminated in Fig. 2a, and become progressively more prominent as sampling of the line scan is reduced. As before, adding even a fairly sparse line scan results in significant image quality improvement.

**Micro-CT imaging of a core sample.** A real core sample (about 8.1 mm in diameter and 7.1 mm tall) was scanned by a micro-CT scanner using a C&L X-ray source trajectory without any hardware changes but by adding a line scan to the circular scan. The source-to-isocenter distance is 25.3 mm, the detector pixel size (at isocenter) is  $14 \times 14 \mu\text{m}$ , and the results of reconstructions are computed on  $972 \times 972 \times 550$  grid.

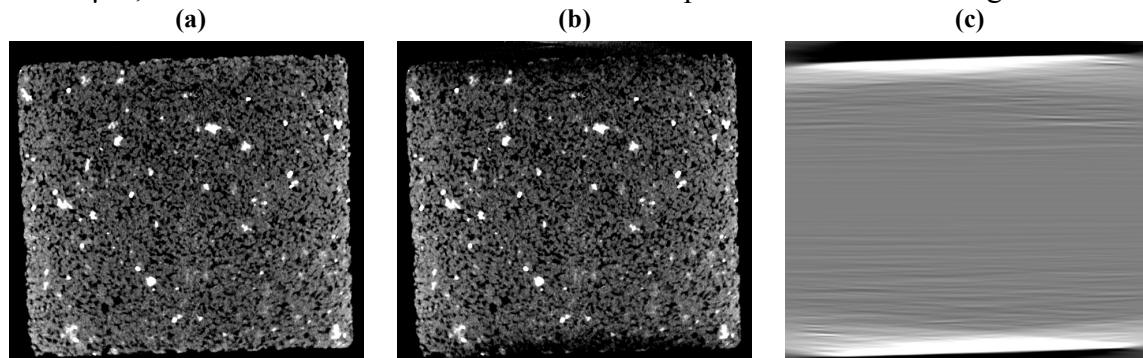


**Figure 3:** Core micro-CT imaging results. (a) C&L and (b) Circular reconstructions ( $WL = 0.12$ ,  $WW = 0.1$ ), (c) line contribution ( $WL = 0$ ,  $WW = 0.05$ ). Image (a) is the sum of images (b) and (c), see eq. (2.9).

In Figs. 3a and 3b, we present the results of C&L and circular reconstructions for a vertical slice through the core, respectively; the images are of size  $972 \times 550$ . Due to a large cone angle used during the scans (half-cone angle =  $12^\circ$ ), the top and the bottom parts of the core in Fig. 3b generate strong artifacts masking the image. These parts will have to be cropped out during the subsequent digital micro-CT core analysis. At the same time, the C&L image in Fig. 3a displays perfect image quality for the entire core slice. To better illustrate the artifacts in the circle-only image, in Fig. 3c, we show the reconstruction from the line data. In other words, the image in Fig. 3a is the sum of images in Figs. 3b and 3c.

**Throughput improvement.** Standard circular scan trajectories have to utilize 5-6 degrees half-cone angles to keep cone-beam artifacts below detectable limits [8-9]. In the above experiments with simulated phantom data, we used an 11 degree half-cone angle. This allows for a significant throughput increase, since wider spacing between circular scans makes up for the time used to collect line data. Indeed, our results show that a volume of twice the axial extent can be reconstructed when adding a line scan: 9.5 mm vs. 19 mm. With 720 sources on the circle and one circular scan per every 9.5 mm of axial extent gives for the conventional approach  $720/9.5 = 75.8$  views/mm. With 720 sources on the circle and one circular scan per every 19 mm of axial extent and with 0.28 mm step size on the line, we get for the C&L approach  $720/19 + 1/28 = 41.4$  views/mm. This is approximately a factor 1.83 improvement of the throughput (or decrease the scan time by 1.83 times). Similar comparisons of throughput for circular and C&L trajectories can be performed for any micro-CT scanner. It should be noted that 11 degrees half-cone angle was used in this study as a starting point, and C&L works equally well with any higher cone angle [5-7].

## CONCLUSIONS

Noticeable cone-beam artifacts can appear when the source trajectory is a circle or a collection of circles. We show that even with as few as 180 sources on the line, image quality with the C&L scan is far superior to that with only one circular scan. The results presented in the paper indicate that for a given micro-CT scanner it is possible to obtain nearly artifact-free high image quality of cores by utilizing the C&L scan trajectory and application of the Katsevich theoretically exact FBP reconstruction algorithm. Using a real core micro-CT data example, we also illustrate that a conventional circular scan protocol utilized by an existing micro-CT scanner can be modified without hardware upgrades to enable the same scanner to collect C&L data sufficient to perform image reconstruction using the algorithm presented in this paper. C&L allows to use much wider cone angles than those in pure circular scans, which also allows for a significant throughput increase.

## ACKNOWLEDGEMENTS

We would like to thank Igor Frenkel for fruitful discussions regarding the C&L technology.

## REFERENCES

1. Hsieh, J., "Computed Tomography: Principles, Design, Artifacts, and Recent Advances", Wiley, (2009), 510 pp.
2. Katsevich, A., "Analysis of an exact inversion algorithm for spiral cone-beam CT", *Physics in Medicine and Biology*, **47**, (2002), 2583–2597.
3. Katsevich, A., "Exact filtered back projection (FBP) algorithm for spiral computer tomography", (2003), US patent **6,574,299**.
4. Katsevich, A., "Improved exact filtered back-projection algorithm for spiral CT", *Advances in Applied Mathematics*, **32**, (2004), 681-697.

5. Katsevich, A., “Image reconstruction for the circle and line trajectory”, *Physics in Medicine and Biology*, **49**, (2004), 5059–5072.
6. Katsevich, A., “Image reconstruction for a general circle-plus trajectory”, *Inverse Problems*, **23**, (2007), 2223–2230.
7. Katsevich, A., “Efficient image reconstruction algorithm for the circle and line cone beam computed tomography”, (2007), US patent **7,197,105**.
8. Sheppard A., S. Latham, J. Middleton, A. Kingston, G. Myers, T. Varslot, A. Fogden, T. Sawkins, R. Cruikshank, M. Saadatfar, N. Francois, C. Arns, and T. Senden, “Techniques in helical scanning, dynamic imaging and image segmentation for improved quantitative analysis with X-ray micro-CT”, *Nuclear Inst. Methods in Physics Res.*, **324**, (2014), 49-56.
9. Katsevich, A., M. Frenkel, M. Feser, Z. Huang, M. Andrew, T. Case, A. Gu, and W. Thompson, “New Fast and Accurate 3D Micro Computed Tomography Technology for Digital Core Analysis”, (2015), *SPE ATCE*, Houston, Texas, 13pp.
10. Zamyatin, A., A. Katsevich, and B. S. Chiang, “Exact image reconstruction for a circle and line trajectory with a gantry tilt”, *Physics in Medicine and Biology*, **53**, (2008), N423–35.
11. Katsevich, A., K. Taguchi, and A. Zamyatin, “Formulation of four Katsevich algorithms in native geometry”, *IEEE Trans. Medical Imaging*, **25**, (2006), 855–868.
12. Noo, F., J. Pack, and D. Heuscher, “Exact helical reconstruction using native cone-beam geometries”, *Physics in Medicine and Biology*, **48**, (2003), 3787–3818.
13. Katsevich, A., “A note on computing the derivative at a constant direction”, *Physics in Medicine and Biology*, **56**, (2011), N53–N61.

# On the Influence of Mixed Wettability on the Simulation of Multi-Phase Transport Properties of Core Samples

J.-O. Schwarz<sup>1</sup>, S. Linden<sup>1,2</sup>, J. Becker<sup>1</sup>, C. Wagner<sup>1</sup>, A. Wiegmann<sup>1</sup>

<sup>1</sup>Math2Market GmbH, 67657 Kaiserslautern, Germany

<sup>2</sup>Fraunhofer ITWM, 67663 Kaiserslautern, Germany

*This paper was prepared for presentation at the International Symposium of the Society of Core Analysts held in Snowmass, Colorado, USA, 21-26 August 2016*

## ABSTRACT

The determination of transport properties of reservoir rocks in laboratories is difficult and time-consuming. Therefore there interest is increasing in predicting relative permeability by pore-scale simulations. The wettability of the rock forming minerals is a well-known phenomenon of natural samples that represents a challenge for numerical simulations of rock properties. Through recent innovations, this challenge can be met by our digital rock physics software GeoDict. Comparison of simulations of the relative permeability with and without mixed wettability for a Berea sandstone exhibit clear differences. The most striking difference is the different crossover points between  $k_{r,w}$  and  $k_{r,o}$ . Because this point is a good first indicator for the amount of recoverable oil, the incorporation of mixed wettability in relative permeability simulations is crucial for getting realistic multiphase transport properties from numerical simulations.

## INTRODUCTION

In reservoir engineering multiphase flow in porous media is mainly described by parameters such as porosity  $\phi$ , (absolute) permeability  $K$ , fluid viscosities  $\mu_i$ , the capillary pressure  $p_c$  vs saturation  $S_w$  function and the relative permeability  $k_r$  [1]. The relative permeability vs. saturation function together with absolute permeability has a large influence on the flux of fluid phases. Relative permeability can largely vary depending on rock type, wettability and other parameters. At the same time, experimental determination of relative permeability is difficult and time-consuming. Therefore over the last decade interest has been increasing in predicting relative permeability by pore-scale simulation [2]. GeoDict, the digital rock physics software produced by the Math2Market GmbH, computes relative permeability directly on the pore space as identified by X-ray computed tomography (XCT) by a quasi-static approach that employs the pore morphology method [3,4,5].

Pore morphology (PM) methods determine the capillary pressure – saturation curve of a porous media [3,5]. They are based on modelling the three-dimensional geometric distribution of the fluid phases in the pore space. PM methods are in wide use but were originally limited to a single contact angle ( $\theta$ ). This restriction does not allow for the

complexity of core samples, because the different  $\theta$  of the mineral phases (mixed wettability) influence the distribution of the fluid phases and their potential path ways through the pore space. Recently, this limitation was overcome and demonstrated in 2d for highly porous materials [6]. Our consideration of multiple  $\theta$  (i.e. mineral specific  $\theta$ ) in 3d allows for a realistic modelling of core samples. The multiple  $\theta$  PM method was implemented in GeoDict recently. In this study it is applied to a core sample of a Berea sandstone and the results of these PM calculations are compared to constant  $\theta$  PM calculations for primary drainage.

## **METHODS**

Digital rock physics (DRP) are employed to simulate the multi-phase transport properties of a core sample. The general DRP workflow of scanning the sample by XCT, image-processing of the scan and simulation of the physical rock properties is followed.

### **XCT scanning and sample**

The sample and raw data for this study derive from one of our former studies [7]. Here we use the Berea sandstone sample and its synchrotron-based XCT raw data obtained at the TOMCAT beamline at the Swiss Light Source (Paul Scherrer Institute, Villigen, Switzerland) provided along with that study.

### **Image processing**

The XCT raw data from the benchmark study is further processed with GeoDict to prepare the data for the numerical simulations. The XCT scan is filtered by a Non-local means filter and artifacts are removed by dilation and erosion operations. The different mineral phases in the sample are subsequently segmented by a threshold segmentation. Quartz and feldspar expose an identical range of grey values and could not be separated in that way. However, both minerals exhibit different structures due to the decay of feldspar to clay minerals. This structural difference can be detected by a combination of erosion and dilation algorithms. This feature is used for the differentiation between quartz and feldspar in the final segmentation. See figure 1.

### **Relative permeability**

The relative permeability for the Berea sandstone is simulated in a three step workflow explained in the following. In GeoDict this workflow is fully automated.

### **Absolute permeability**

In a first step the absolute permeability of the Berea sample is computed on the segmented pore space assuming that it is completely saturated with one fluid phase. Absolute permeability ( $K_{\text{abs}}$ ) is obtained by simulation of Stokes flow with GeoDict.

### Capillary pressure vs. saturation relationship

In a second step, capillary pressure vs. saturation relationships are approximated with the PM method. The PM method [4], predicts the distribution of a wetting phase (WP) and a non-wetting phase (NWP) inside a porous medium. The method approximates drainage or imbibition by finding Young–Laplace equilibrium states through a series of morphological erosion and dilation operations using a spherical structuring element.

Here, primary drainage of the sample is computed. The drainage algorithm starts with a completely water-saturated porous medium and begins with a maximal pore radius  $R$ , which is then decreased step by step. In each step, a pore is drained if (i) the pore radius is larger than  $R$ , (ii) the entering non-wetting phase is connected by pores larger than  $R$  to the non-wetting phase reservoir, and (iii) the replaced wetting phase is connected to the wetting phase reservoir. Conditions (i) and (ii) describe the original algorithm as defined by [4] and used in [8]. Condition (iii) introduces a residual wetting phase and was added by [3].

The output of the algorithm is a finite sequence of quasi-stationary states. Each state is a 3D image again that encodes the solid phase(s), WP and NWP. In this study, the WP is a brine and the NWP an oil. In a post-processing step the Young-Laplace equation based on the radii of the inscribed spheres and the interfacial tension is used to predict the capillary pressure curve. The sequence of 3D images is then the input data to predict relative properties.

Most crucial for the calculations of the capillary pressure curve are the  $\theta$  of the fluid interfaces on the minerals present in the sample. Table 1 provides the  $\theta$  for the wetting phase used in the simulations. Realistic  $\theta$  for the present phases were not available in the literature and hence generic values are used that should illustrate the effect of different wettability on the transport properties. Generally, realistic  $\theta$  for individual minerals can be determined by experiments as described by [9, 10].

### Relative permeability

In a third step, the permeability for each fluid phase ( $K_w$ ,  $K_o$ ) in the Young–Laplace equilibrium states is computed by simulations of Stokes flow. These permeabilities are normalized with the corresponding  $K_{abs}$  yielding the relative permeabilities  $k_{r,w} = K_w / K_{abs}$  and  $k_{r,o} = K_o / K_{abs}$ .

## RESULTS

### Capillary pressure curves

The general shape of the capillary pressure curves exhibit differences in the capillary pressure required to maintain a certain water saturation ( $S_w$ ). In general, the simulation with multiple contact angles exhibits lower capillary pressures for a certain  $S_w$  in the sample especially for low  $S_w$  (Figure 2). The curves for primary drainage show further differences in the irreducible wetting phase saturation and displacement pressure. The irreducible wetting phase saturation is  $\sim 16\%$  for the run with constant  $\theta$  and  $\sim 10\%$  for the

run with multiple  $\theta$ . The displacement pressure is about 14 kPa for the constant  $\theta$  run and about 12 kPa for the multiple  $\theta$  run.

The capillary pressure curves exhibit an  $S_w$ -range ( $\sim 50\%$  -  $95\%$  for constant  $\theta$  and  $\sim 40\%$  -  $\sim 90\%$  for multiple  $\theta$ ) in which the PM method does not provide quasi-stationary states of the fluid distribution due to the structure of the pore space. In consequence, no  $k_r$  values could be computed in that range.

### Relative permeability

The  $k_r$  curves in Figure 3 are a combination of computed  $k_r$  values and  $k_r$  values derived from a Corey fit (see e.g. [1]). The Corey fits cover the above described  $S_w$ -range and are based on the computed  $k_r$  values.

The  $k_r$  curves for simulations with a constant  $\theta$  and multiple  $\theta$  show clear differences. The  $k_{r,w}$  curve for multiple  $\theta$  shows higher  $k_{r,w}$  values than the curve for constant  $\theta$  for similar  $S_w$ . Percolation of the WP stops for the Corey fits at  $S_w = 0.28$  (constant  $\theta$ ) and  $S_w = 0.09$  (multiple  $\theta$ ). The  $k_{r,o}$  curve for the multiple  $\theta$  displays lower  $k_{r,o}$  values for similar  $S_w$  in comparison with the constant  $\theta$  curve. Percolation of the NWP starts for the Corey fits at  $S_w = 0.79$  (constant  $\theta$ ) and  $S_w = 0.72$  (multiple  $\theta$ ).

However, the most striking feature is the difference in the crossover points between  $k_{r,w}$  and  $k_{r,o}$  which lie at  $S_w = 0.65$  for the constant  $\theta$  case and  $S_w = 0.57$  for the multiple  $\theta$  case. The crossover point between  $k_{r,w}$  and  $k_{r,o}$  is a good first indicator for the amount of recoverable oil [1]. The difference between the two crossover points is significant and non-consideration of multiple  $\theta$  may shift this point to artificially high  $S_w$  values. In order to avoid such effects, multiple  $\theta$  should be considered in digital rock physics workflows.

### REFERENCES

- [1] Berg, S, Rücker, M, Ott, H, Georgiadis, A, van der Linder, H, Enzmann, F, Kersten, M, Armstrong, R, de With, S, Becker, J, Wiegmann, A, "Connected pathway relative permeability from pore-scale imaging of imbibition", *Adv Water Resour*, (2016) 90, 24–35 .
- [2] Blunt, MJ, Jackson, MD, Piri, M, Valvatne, PH, "Detailed physics, predictive capabilities and macroscopic consequences for pore-network models of multiphase flow", *Adv Water Resour*, (2002) 25, 1069–89.
- [3] Ahrenholz, B, Tölke, J, Lehmann, P, Peters, A, Kaestner, A, Krafczyk, M, Durner, W, "Prediction of capillary hysteresis in a porous material using lattice-Boltzmann methods and comparison to experimental data and a morphological pore network model", *Adv Water Resour*, (2008) 31, 1151–73.
- [4] Hilpert, M, Miller, TC, "Pore-morphology-based simulation of drainage in totally wetting porous media", *Adv Water Resour*, (2001) 24, 243–55.

- [5] Silin, D, Tomutsa, L, Benson, S, Patzek, TW, “Microtomography and pore-scale modeling of two-phase fluid distribution”, *Transp Porous Media*, (2010) 86, 495–515.
- [6] Schulz, V, Wargo, E, Kumbur, E, “Pore-Morphology-Based Simulation of Drainage in Porous Media Featuring a Locally Variable Contact Angle”, *Transp Porous Media*, (2015) 107, 13-25.
- [7] Andrä, H, Combaret, N, Dvorkin, J, Glatt, E, Junehee, H, Kabel, M, Keehm, Y, Krzikalla, F, Lee, M, Madonna, C, Marsh, M, Mukerji, T, Saenger, E, Sain, R, Saxena, N, Ricker, S, Wiegmann, A, Zhan, A, “Digital rock physics benchmarks Part I: Imaging and segmentation”, *Computers & Geosciences*, (2013) 43, 25-32.
- [8] Becker, J, Schulz, V, Wiegmann, A, “Numerical determination of two-phase material parameters of a gas diffusion layer using tomography images”, *J Fuel Cell Sci Technol*, (2008) 5, 2, 21006-21014.
- [9] Brown, K, Schlüter, S, Sheppard, A, Wildenschild, D, “On the challenges of measuring interfacial characteristics of three-phase fluid flow with x-ray microtomography”, *J Microsc*, (2014) 253, 3, 171-182.
- [10] Andrew, M, Bijeljic, B, Blunt M, “Pore-scale contact angle measurements at reservoir conditions using X-ray microtomography” *Adv Water Resour*, (2014) 68, 24–31.

**Table 1.** Mineral phases and their associated contact angles to the wetting phase

Mineral phase	Constant contact angle [°]	Multiple contact angles [°]	Volume percentage [%]
Quartz	10	10	70.64
Feldspar	10	70	8.05
Ankerite	10	40	1.58
Zircon	10	60	0.14

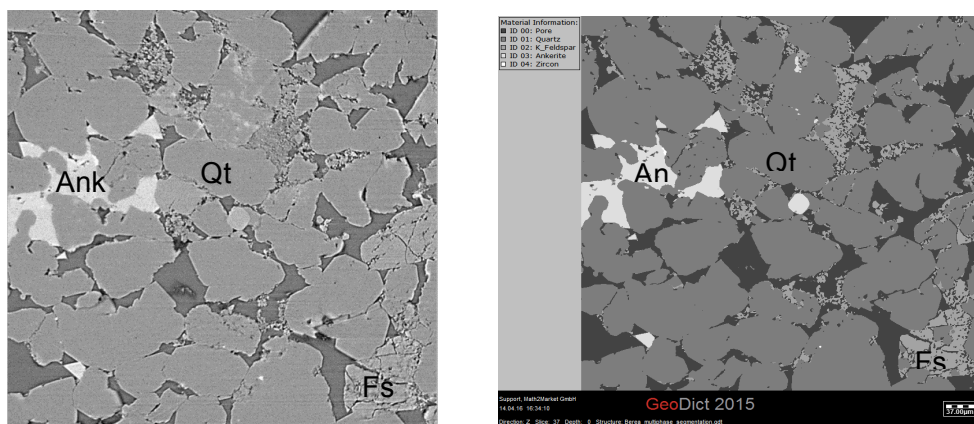


**Figure 1.** 2D illustration of the Berea sandstone. Qtz: quartz, Fsp: feldspar, Ank: ankerite. Left: XCT raw data. Mineral identification according to [7] and references therein. Right: Segmented data set.

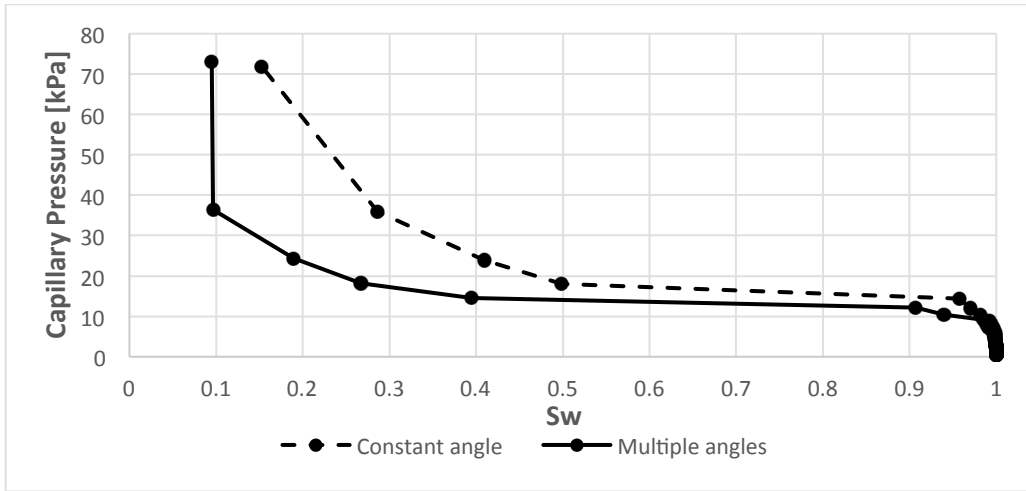


**Figure 2.** Capillary pressure curves for primary drainage in the Berea sandstone. Dashed line: simulation with a constant contact angle for all minerals. Continuous line: simulation with multiple contact angles.

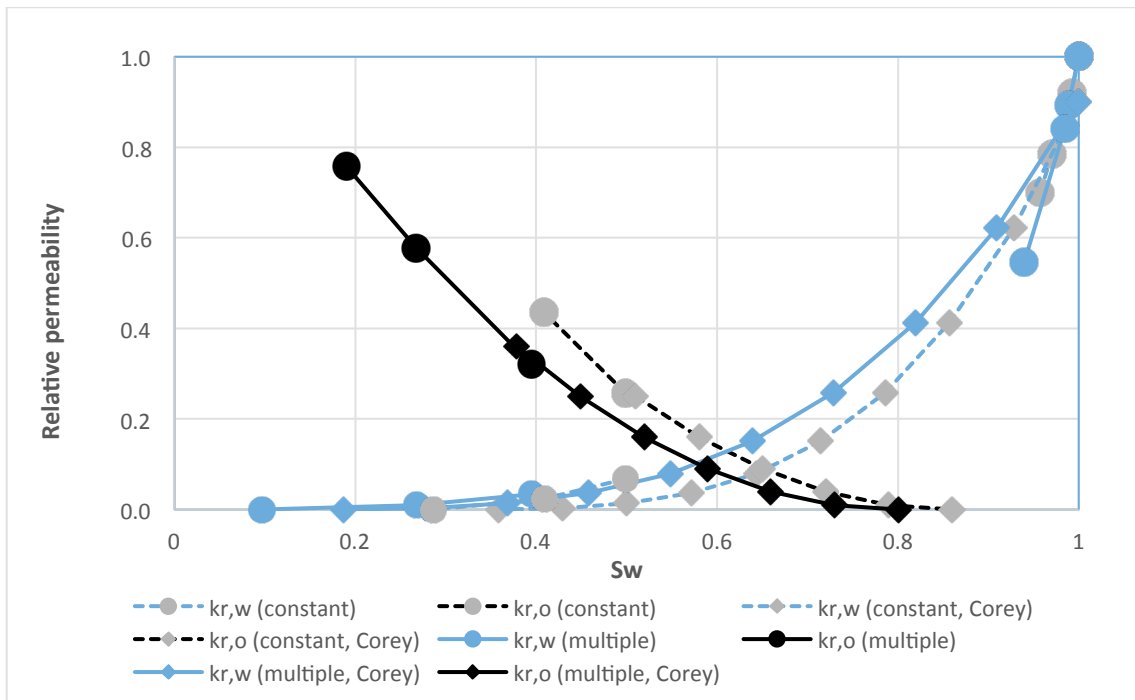


**Figure 3.** Relative permeability curves for primary drainage in the Berea sandstone. Simulations with a constant contact angle (dashed line) and with multiple contact angles (continuous line).

# **PERMEABILITY MEASUREMENTS ON HYDRATE-BEARING SANDSTONE CORES WITH EXCESS WATER**

Stian Almenningen, Håkon Juliussen and Geir Ersland  
Department of Physics and Technology, University of Bergen

*This paper was prepared for presentation at the International Symposium of the Society of Core Analysts held in Snowmass, Colorado, USA, 21-26 August 2016*

## **ABSTRACT**

Methane hydrates exist in large quantities in natural sediments and methane gas can be produced from them by either dissociating the hydrate structure or by injecting a more stable hydrate former, which leads to spontaneous exchange of guest molecules. In either way, it is important with sufficient permeability to allow for injection and extraction of fluids. The effect of hydrate saturation on effective gas permeability is reported in this paper. Bentheim sandstone cores with high intrinsic permeability hosted the gas hydrate formed with both excess gas and excess water. Effective methane gas permeability was measured in cores with different initial water saturations. The flowrate of the injected methane gas was low and the water was immobile. After complete hydrate formation, the effective gas permeability was measured and evaluated with respect to different hydrate and water saturations. The results showed that the presence of hydrate in the pores highly influenced the effective gas permeability even at constant gas saturations; the effective gas permeability in hydrate-water-gas systems was in some cases reduced with as much as five orders of magnitude compared to the water-gas system. Cores with similar saturations of gas, water and hydrate displayed large variations in effective gas permeability (ranging from  $\mu\text{D}$  to  $\text{mD}$ ). The effect of hydrate growth pattern and phase distribution on permeability is discussed, and interpretation of experimental results showed pore-filling hydrate growth in these experiments.

## **INTRODUCTION**

Production of methane gas from natural gas hydrates has experienced growing interest during the last couple of decades due to its vast energy potential [1]. A key factor in all production scenarios is the permeability of the hydrate-filled sediments. Pressure depletion requires sufficient permeability to allow for pressure perturbations to reach within the reservoir and allow for flow of liberated methane gas to production wells. Injection of  $\text{CO}_2$  fluid is similarly dependent on adequate permeability in order to maintain flow through the reservoir from injector to producer well. Reservoir simulation models need reliable permeability data to assess the potential of sedimentary hydrate reservoirs as commercial production sites [2]. The goal of permeability studies on hydrate-filled sediments is to

determine whether there is a relationship between hydrate saturation and gas-phase permeability. However, the permeability-saturation correlation is affected by other parameters, most notably the distribution of hydrate in the pore space [3]. The pore-level location of hydrates affects the permeability severely as does also the amount and distribution of free gas and immobile water in addition to hydrates. Immobile water is the water that is left behind after hydrate formation due to capillary trapping or salinity inhibition. Free water is additional water that is left behind because of local unavailability of methane gas. All the free water was immobile during the flow experiments in this study (because of low flowrates of gas), but local formation of additional hydrates may have taken place if injected methane gas came in contact with free water.

Johnson *et al* [4] performed relative permeability tests on unconsolidated sediments retrieved from the Mount Elbert gas hydrate stratigraphic test well in Alaska. Nitrogen gas was used to avoid secondary hydrate formation during injection, and the end-point relative permeability of the gas was measured to be below 0.01 for a core with a hydrate saturation of 0.13 ( $S_g \approx 0.25$  and  $S_w \approx 0.65$ ). In fact, the hydrate saturation could not exceed approximately 0.36 in order to provide measurable permeability values, despite the fact that the hydrate interval in Mount Elbert contains twice the amount of hydrates. In comparison, Ahn *et al* [5] found the end-point relative permeability of methane gas to be around 0.1 with a hydrate saturation of 0.15 ( $S_g \approx 0.3$  and  $S_w \approx 0.55$ ). The end-point relative permeability in these studies varies with one order of magnitude although the saturations are of comparable size. These results point to the importance of hydrate and fluid distribution, which was not investigated in these experiments. The methodology for creating hydrate was different in the two studies. Ahn *et al* [5] used the excess gas method that is based on pressurizing a water saturated core with gas whereas Johnson *et al* [4] used water to pressurize a core already saturated with gas and water. The excess gas method was previously believed to produce grain-cementing hydrate [6], but other research showed that the method results in pore-filling hydrate growth [3, 7]. Kumar *et al* [8] found the reduction in permeability with increased hydrate saturation to agree with a model based on hydrates coating the mineral surfaces for hydrate saturations below 0.35. For hydrate saturations above 0.35, the agreement was better with a model based on hydrates filling the pore centers. Pore-filling behavior was also observed by Liang *et al* [9] and end-point relative permeability decreased from 0.36 to 0.0036 as hydrate saturations increased from 0.12 to 0.43. One common feature of these previous permeability studies, was that the hydrate saturation was limited to low values. This study investigated the effective gas permeability for intermediate hydrate saturations up to values as high as 0.61. *In situ* hydrate saturations have been quantified to exceed 0.80 in the Mallik gas hydrate field in Canada [10] and tend towards 0.80 in the Daini Atsumi Knoll area of the Eastern Nankai Trough offshore Japan [11]. It is therefore natural to expand hydrate permeability measurements towards higher saturations.

## EXPERIMENTAL PROCEDURE

Cylindrical Bentheim sandstone cores (length  $\approx 15$  cm and diameter  $\approx 5$  cm) were used as porous medium. They have a fairly constant porosity of 0.22 and an absolute permeability measured before every experiment that ranges between 1.3 and 1.9 D. Every core was saturated to a predefined value with brine containing 3.5 wt% NaCl and then mounted into the rubber sleeve inside the core holder (Figure 1). All pump lines and tubings were purged under vacuum before filling the pumps with methane gas ( $>99.5\%$ ). The core was pressurized to 8.3 MPa from both ends and the overburden pressure was applied by pressurized oil (3 MPa above pore pressure) surrounding the rubber sleeve. Permeability measurements prior to hydrate formation were achieved by injecting methane gas with one pump at the inlet side of the core and producing methane gas with another pump at the outlet side. The volume rate of injection and production was identical and held below 16 mL/min to avoid extraction of water from the core. Differential pressure along the core was recorded with a differential pressure transducer, along with measurements of inlet pressure and core surface temperature. Hydrate formation was initiated by circulation of antifreeze into a cooling jacket that surrounds the core holder and that reduced the temperature to a constant  $4^{\circ}\text{C}$  for all tests. Permeability measurements were repeated when hydrate formation was completed, but at this point the outlet pump was set to hold a constant pressure rather than constant production rate. This was done to avoid artificial under-pressure at the outlet side of the core that could be an issue if the core was completely clogged by hydrates. Flow rates were varied for all permeability measurements and the permeability was calculated for each flow rate by Darcy's law. The reported permeability values are arithmetic averages of the permeability of each flowrate.

## RESULTS AND DISCUSSION

Measured permeability values for the range of hydrate saturations in these tests show considerable variability (Table 1). Subscript  $i$  refers to initial values, i.e. prior to hydrate formation, and subscript  $f$  refers to final values obtained after hydrate formation. Calculation of final saturations are based on PVT-data. The final gas relative permeability shows a strong dependence on the final gas saturation, and a permeability transition zone occurs at a saturation of 0.34-0.38 for these experiments (Figure 2). The effective gas permeability was in the order of  $\mu\text{D}$  below this saturation and in the order of mD above this saturation. Experiments 1 and 2 displayed final permeability values in the mD range, but had nearly similar hydrate saturations as experiment 3 and 4 which had final permeability values in the  $\mu\text{D}$  range. This demonstrates the importance of all phases found in the pore space and that it is impossible to correlate permeability to hydrate saturation when both excess water and gas reside in the pores. In order to generate basic permeability relationships, it is desirable to remove one of the fluid phases from the experiment, but this is not easy to implement in practice. Complete removal of fluids is impossible due to capillary trapping and even reducing one of the phases to residual saturation may affect the hydrate stability severely and thereby induce melting. Actual attempts to reduce the gas

saturation to residual value by injection of precooled water have shown to induce hydrate dissociation [12]. Water production was not monitored continuously during the permeability measurements in this study but visual inspection of the outlet pump cylinder after each experiment showed no sign of water. However, there was a small increase in permeability with increased flowrate for the cores with low final gas saturation ( $<0.34$ ). Some of these cores did also experience a small decline in differential pressure at constant flowrate. Limited water production may thus have taken place in these experiments and the final permeability will then be an average over a slightly varying gas saturation.

Pore-space distribution of phases was not explicitly investigated in these experiments. The location of fluids within the porous media affects the permeability significantly and utilization of any kind of imaging device would improve the understanding of flow behavior. Some comments can nevertheless be given regarding hydrate growth. As previously mentioned, permeability values dropped to  $\mu\text{D}$ -scale when the gas saturation was lower than 0.34-0.38 after hydrate formation. In experiment 8, the permeability prior to hydrate formation was measured to be 57 mD for a gas saturation of only 0.27. The final permeability was not just limited by the low gas saturation for experiment 3-8, but the presence of hydrates in the pores seemed to decrease the permeability further. The observation that the permeability was lower for a gas-water-hydrate system compared with a gas-water system for approximately equal gas saturations, indicates that the hydrate growth occurred in the pore bodies. The configuration of fluids prior to hydrate formation is believed to consist of gas occupying the interior of the biggest pores due to the strong water-wet nature of Bentheim sandstone. Initial hydrate growth in the pore throats would have notably reduced the connectivity of the gas phase from pore to pore and is not likely because of relatively high permeability for hydrate saturations of almost 0.50 (experiment 1 and 2). Pore-coating hydrate growth in the large pores would have had little effect on the permeability-reduction even for intermediate hydrate saturations as the gas could flow in the middle of the pores, and is also unlikely (e.g. experiment 6 and 7). The observed permeability can best be explained by pore-filling hydrate growth. Hydrate occupying the center of large pores obstructed the flow significantly when the hydrate saturation reached intermediate/high values, and the gas permeability was lower when hydrates were present for similar gas saturations. However, a situation described by Kumar *et al* [8], where the hydrate growth was pore-coating for low saturations and pore-filling for high saturations, is possible.

## CONCLUSIONS

Effective gas permeability for hydrate-filled sandstone cores was measured in a series of experiments. The methane hydrate saturation varied between 0.37-0.61 and immobile excess water was present during permeability measurements. The effective gas permeability decreased from mD-scale to  $\mu\text{D}$ -scale when the gas saturation dropped below 0.34-0.38 independent of the hydrate saturation. However, comparison of different experiments showed that the presence of hydrate decreased the permeability even though

the gas saturation was constant. This indicated pore-filling hydrate growth for the experiments conducted in this study.

## REFERENCES

1. Kvenvolden, K.A., "Origins of Methane in the Earth Methane hydrate — A major reservoir of carbon in the shallow geosphere?", *Chemical Geology*, (1988) **71**, 1, p. 41-51.
2. Moridis, G.J., T.S. Collett, R. Boswell, M. Kurihara, M.T. Reagan, C. Koh and E.D. Sloan, "Toward Production From Gas Hydrates: Current Status, Assessment of Resources, and Simulation-Based Evaluation of Technology and Potential", *SPE Reservoir Evaluation & Engineering*, (2009) **12**, 5, p. 745-771.
3. Kleinberg, R.L., C. Flaum, D.D. Griffin, P.G. Brewer, G.E. Malby, E.T. Peltzer and J.P. Yesinowski, "Deep sea NMR: Methane hydrate growth habit in porous media and its relationship to hydraulic permeability, deposit accumulation, and submarine slope stability", *JOURNAL OF GEOPHYSICAL RESEARCH*, (2003) **108**, B10, p. 1-17.
4. Johnson, A., S. Patil and A. Dandekar, "Experimental investigation of gas-water relative permeability for gas-hydrate-bearing sediments from the Mount Elbert Gas Hydrate Stratigraphic Test Well, Alaska North Slope", *Marine and Petroleum Geology*, (2011) **28**, 2, p. 419-426.
5. Ahn, T., J. Lee, D.G. Huh and J.M. Kang, "Experimental Study on Two-phase Flow in Artificial Hydrate-bearing Sediments", *Geosystem Engineering*, (2005) **8**, 4, p. 101-104.
6. Waite, W.F., W.J. Winters and D.H. Mason, "Methane hydrate formation in partially water-saturated Ottawa sand", *American Mineralogist*, (2004) **89**, 8-9, p. 1202-1207.
7. Kneafsey, T.J., Y. Seol, A. Gupta and L. Tomutsa, "Permeability of Laboratory-Formed Methane-Hydrate-Bearing Sand: Measurements and Observations Using X-Ray Computed Tomography", *SPE Journal*, (2011) **16**, 1, p. 78-94.
8. Kumar, A., B. Maini, P.R. Bishnoi, M. Clarke, O. Zatsepina and S. Srinivasan, "Experimental determination of permeability in the presence of hydrates and its effect on the dissociation characteristics of gas hydrates in porous media", *Journal of Petroleum Science and Engineering*, (2010) **70**, 1-2, p. 114-122.
9. Liang, H., Y. Song, Y. Chen and Y. Liu, "The Measurement of Permeability of Porous Media with Methane Hydrate", *Petroleum Science and Technology*, (2011) **29**, 1, p. 79-87.
10. Dallimore, S.R., T.S. Collett, T. Uchida, M. Weber, H. Takahashi and T. Mroz, "Overview of Gas Hydrate Research at the Mallik Field in the Mackenzie Delta, Northwest Territories, Canada". Presentation, (2004).
11. Yamamoto, K., Y. Terao, T. Fujii, T. Ikawa, M. Seki, M. Matsuzawa and T. Kanno, "Operational overview of the first offshore production test of methane hydrates in the Eastern Nankai Trough", in *Offshore Technology Conference*, (2014), Houston, Texas, USA.

12. Li, B., X.S. Li, G. Li, J.L. Jia and J.C. Feng, “Measurements of Water Permeability in Unconsolidated Porous Media with Methane Hydrate Formation”, *Energies*, (2013) **6**, 7, p. 3622-3636.
13. Hågenvik, C., “CO<sub>2</sub> Injection in Hydrate Bearing Sandstone with Excess Water”. MSc., Department of Physics and Technology, University of Bergen, Norway, (2013).
14. Ersland, G., J. Husebø, A. Graue, B. Kvamme, B. Baldwin, J.J. Howard and J. Stevens, “Measurements of Gas Permeability and Non-Darcy Flow in Gas-Water Hydrate Systems”, in *Proceedings of the 6th International Conference on Gas Hydrates*, (2008), Vancouver, Canada.

**Table 1.** List of all experiments with related saturations and permeability values. Margins of error reflect equipment uncertainties.

Experiment ID	$K_{abs}$ [D]	$S_{wi}$ ±0.01	$S_{gi}$ ±0.01	$K_i$ [D]	$S_{wf}$ ±0.02	$S_{hydrate}$ ±0.02	$S_{gf}$ ±0.02	$K_f$ [μD]	$K_f$ [mD]	$k_r$
1	1.7 ±0.2	0.46	0.54	0.20 ±0.02	0.10	0.46	0.44		32 ±3	0.019 ±0.003
2	1.9 ±0.6	0.53	0.47	0.4 ±0.1	0.17	0.47	0.37		2.3 ±0.4	0.0012 ±0.0004
3	1.6*	0.54	0.46	0.14 ±0.02	0.19	0.45	0.37	2.52 ±0.02		1.6E-06 ±0.2E-06
4	1.6*	0.54	0.46	0.09 ±0.02	0.17	0.47	0.36	6.1 ±0.1		3.8E-06 ±0.5E-06
5	1.6*	0.54	0.46	0.088 ±0.008	0.14	0.51	0.35		0.20 ±0.02	0.00013 ±0.00002
6	1.9 ±0.6	0.64	0.36	0.15 ±0.02	0.16	0.61	0.23	0.851 ±0.005		4E-07 ±1E-07
7	1.3 ±0.1	0.64	0.36	0.18 ±0.02	0.23	0.53	0.24	1.277 ±0.005		9.9E-07 ±0.8E-07
8	1.8 ±0.2	0.73	0.27	0.057 ±0.008	0.45	0.37	0.19	1.25 ±0.01		7.1E-07 ±0.8E-07

\*Absolute permeability was not measured. The given value is the midpoint of the other permeability values.

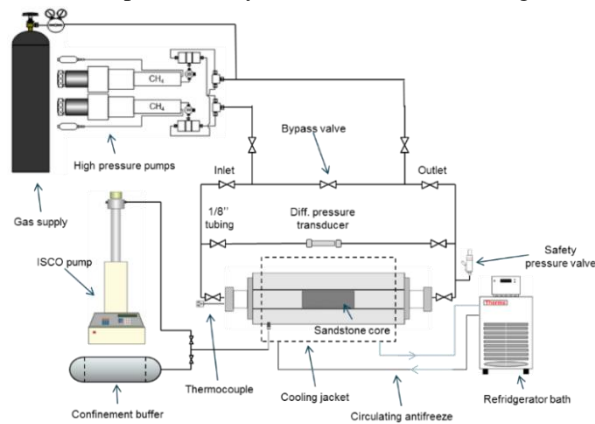


**Figure 1.** Experimental setup. Modified from Hågenvik [13].

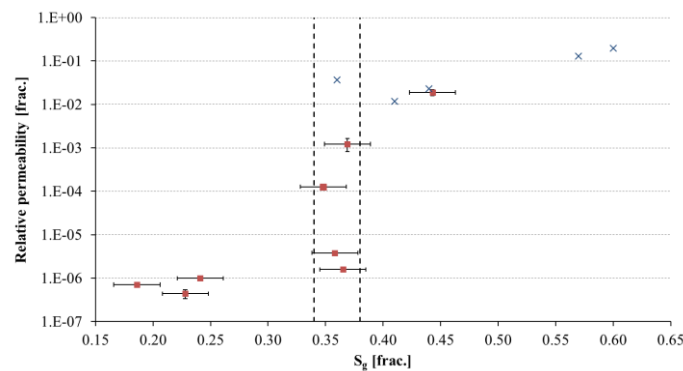


**Figure 2.** Gas relative permeability after hydrate formation. The data points denoted as crosses (blue) are permeability values obtained by Ersland *et al* [14]. A transition zone between  $S_g = 0.34-0.38$  is indicated by vertical dotted lines. Margins of error reflect equipment uncertainties.

# **AFFECTING WETTABILITY ON RELATIVE PERMEABILITY PARAMETERS FOR QUARTZ SANDSTONES**

Such P. Leśniak G.

Oil & Gas Institute – National Research Institute Kraków, Poland

*This paper was prepared for presentation at the International Symposium of the Society of Core Analysts held in Snowmass, Colorado, USA, 21-26 August 2016*

## **ABSTRACT**

Full lithological profiles of the Cambrian sandstones were investigated. Alteration of wettability upon contact with oil were observed (predominantly oil wetting). The following parameters were recorded: porosity, permeability, relative permeability, wettability and MICP. Subsequent Correlation between wettability and relative permeability were investigated. The investigation demonstrated that the relative permeability to water increases when oil wetting tendency increases. For single samples a great variability of results was observed. No correlation between Amott Wettability Index and pore space parameters (porosity, permeability, threshold diameter, fractal dimension [8], specific surface) was obtained.

## **INTRODUCTION**

The Cambrian quartz sandstones are the base reservoir rocks in the Baltic Syncline. Reservoir sandstones belong generally to Pardoixides paradoxissimus bed. There are silicified quartz sandstones, fine and mid grained, classified as quartz arenites. Quartz is a dominating mineral which content comes up to 98%. Quartz also dominates in cements (quartz overgrowths). Reservoir bed is formed as sandstone layers mixed with clay – mud layers. Long series of laboratory investigations were performed over the course of a few years. It was found that the oil wetting is a dominating phenomenon for majority of reservoir samples. Amott Wettability Index investigations were performed using Donaldson et al. [2] method. The scale of this phenomenon is shown in a Figure 1 (frequency diagram of Amott Wettability Index). The authors have investigated influence of wettability on oil – water relative permeability.

Figures 2 and 3 presented results of relative permeability measurements and investigations of Amott Wettability Index. The relative permeabilities [9] were measured using the original reservoir fluids in simulated reservoir conditions. Steady state measurement regime was applied. Permeability covers the range from 0.52 to 465 mD, porosity values from 5 to 21%. Our database could be classified as a typical Cambrian sandstones from the North of Poland [4,10].

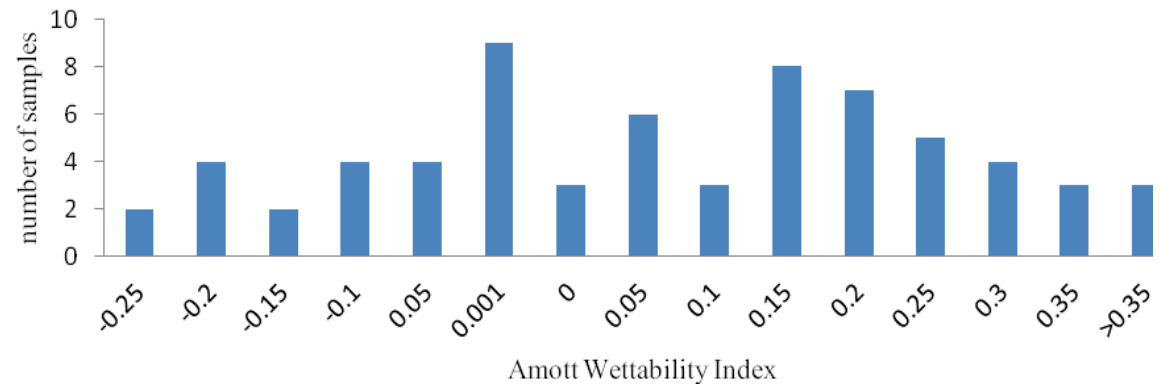


Figure1. Frequency diagram of Amott Wettability Index (AWI) for investigated samples.

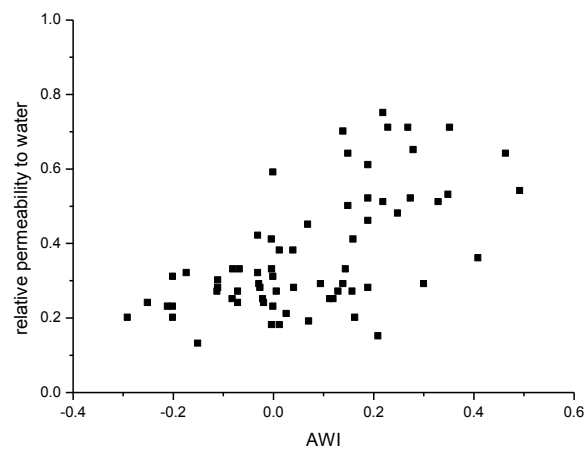


Figure 2. Relative permeability to water as a function of AWI

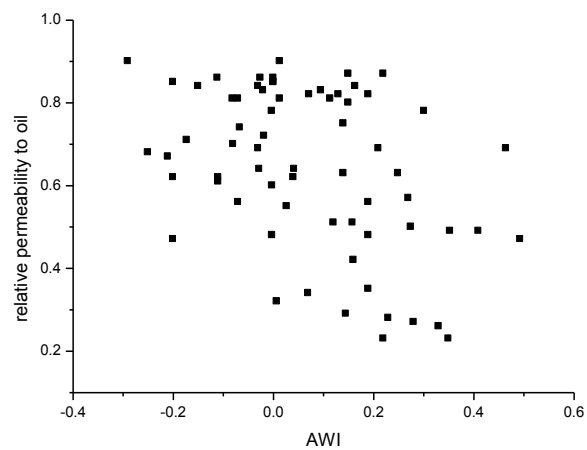


Figure 3. Relative permeability to oil as a function of AWI

Figure 4 presents relative permeability (to water and to oil) as a function of absolute permeability. Authors especially wanted to connect wettability and relative permeability with specific surface and fractal dimension but the results of our attempts were not satisfactory. Such trends were obtained only using values of spontaneously displaced water (during Amott wettability tests) and values of relative permeability to water and oil. Figure 5 and 6 present these results.

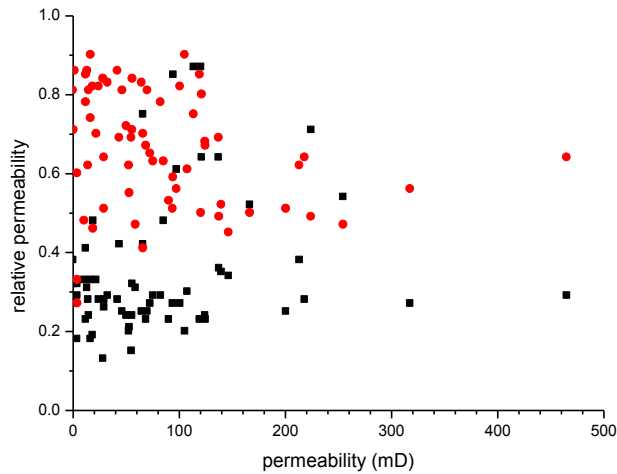


Figure 4. Relative permeability as a function of permeability to gas (red – relative permeability to oil, black – to water)

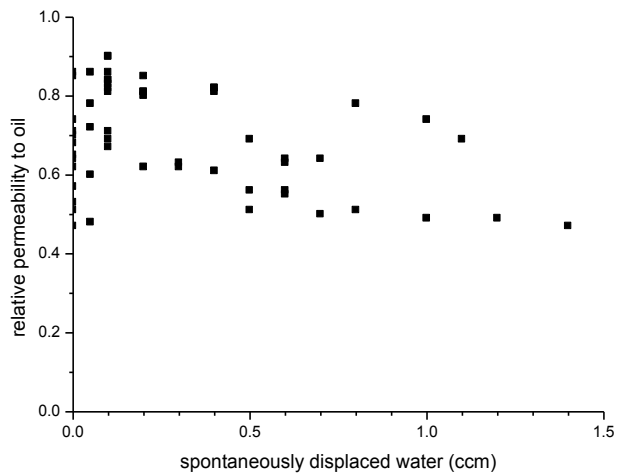


Figure 5. Relative permeability to oil versus spontaneously displaced water during Amott Wettability Tests

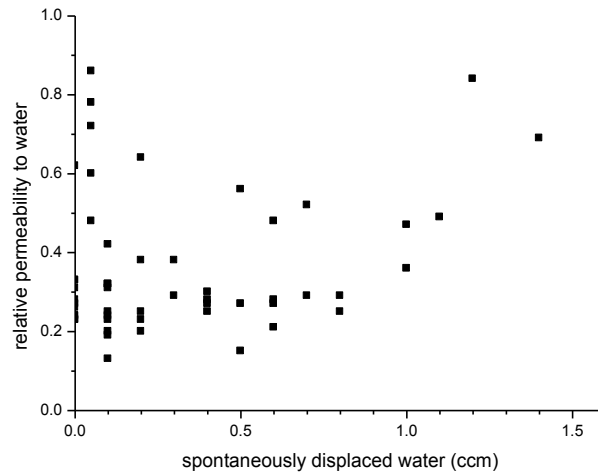


Figure 6. Relative permeability to water versus spontaneously displaced water during Amott Wettability Tests

## DISCUSSION

It was demonstrated that wettability of the Cambrian reservoir sandstones was altered when contacted with oil [1, 3]. In this work the full profiles were investigated, so we can compare the original and altered sandstones. Temperatures and pressure fluctuations during geological history of these reservoirs [5] are factors which played the main role in altering wettability. The authors applied correlation procedures to demonstrate processes which are connected with wettability alteration values of relative permeability [6]. Values of AWI for investigated data amounted to 0.49 (strongly oil wet samples). Two obvious trends are observed in fig 2 and 3. i.e. increase of relative permeability to water and decrease of relative permeability to oil associated with shifting AWI towards greater values. Relative permeability to water is more sensitive than permeability to oil for AWI variability. Figure 4 shows relative permeability versus permeability to gas. The greatest values of permeability to water (connected with greater values of AWI) are observed for the range of permeability from 50 to 220 mD. For greater values of permeability the relative permeability to water decreases. All investigated parameters were gathered in figure 7. Only samples with positive value of AWI were taken into account. Such set of data allows us to investigate main trends. Average values of relative permeability to water increased and became comparable with relative permeability to oil in the range 100 – 200 mD. For this range of permeability the AWI reaches the greatest average value. For greater permeabilities a decrease of all investigated parameters is observed. Finally it can be concluded that the investigated parameters show regularity in the range from 10 to 200 mD. For greater permeabilities the phenomenon connected with velocity of flowing fluids became important. For permeability smaller than 10 mD the considerable reduction of relative permeability to oil is observed (connected with resistance of pore space). Figure 8 presents frequency diagram of residual water saturation for the whole database. Process of

altering wettability didn't change this parameter. It is connected with the fact that micropores were filled with water all the time.

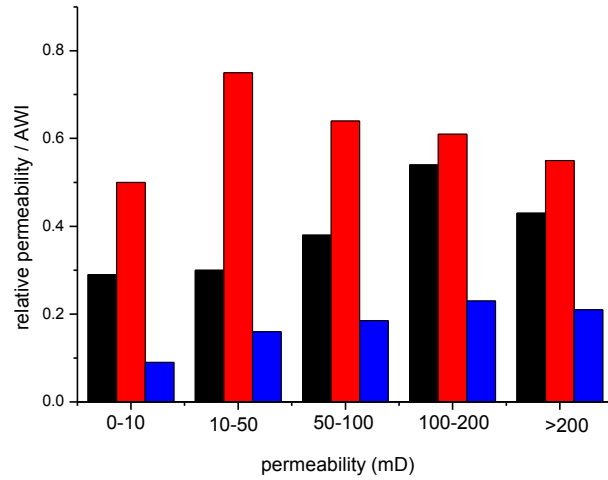


Figure 7. Average values of relative permeability and AWI in given partition of permeability (black – relative permeability to water, red relative permeability to oil, blue – AWI).

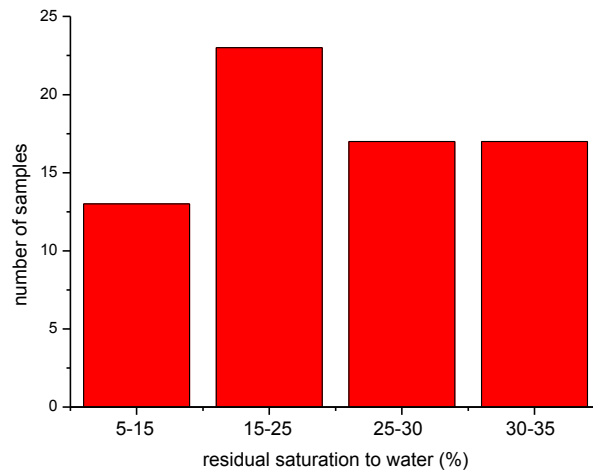


Figure 8. Residual saturation to water (full database)

Table 1. Variability of relative permeability for the same value of AWI

AWI	Relative permeability to water	Relative permeability to oil	Permeability to gas (mD)
0.19	0.46	0.48	19.21
0.19	0.32	0.52	140.0
0.19	0.56	0.64	131.0
0.19	0.28	0.82	24.2

Statistically some regularities are observed but for the single samples the variability of parameters could be huge. In table 1 all samples characterized by AWI equal to 0.19 are shown. Relative permeability to water changes from 0.28 to 0.56, relative permeability to oil changes from 0.48 to 0.82. One can conclude from the above that the process of altering wettability affects only a part of pore space and that this process is rather of statistical nature and does not depend only on pore space parameters.

## CONCLUSION

1. Contact with oil is altering wettability of the Cambrian sandstones.
2. Two main trends are observed: relative permeability to water increases and relative permeability to oil decreases while AWI grows. Relative permeability to water is the more sensitive parameter. Statistic trend is coupled with great variability of investigated parameter for single samples.
3. No correlations were found for parameters of pore space.
4. For AWI equal to 0.34 or greater the values of both relative permeabilities are comparable.
5. The greatest values of AWI are observed for the range of permeability 100 - 200 mD.

## REFERENCES

1. Buckley J.S., Liu Y., Minsterleet S., "Mechanism of Wetting Alteration by Crude Oil" SPE Journal, (1998) 3, 1, p. 54-61
2. Donaldson E.C., Tiabb D.: Petrophysics, Gulf Publishing Comp. Houston, Texas, 1996
3. Flovik V., Sinha S., Hanses A.: "Dynamic Wettability Alteration in Immiscible Two-phase Flow in Porous Media: Effect on Transport Properties and Critical Slowing Down", Frontiers in Physics. November (2015), vol.3.article 86
4. Karczewska A., Leśniak G., Such P., Żurawski E.: "A pore space development of the Cambrian sandstones and their transport system of reservoir fluids", The International Conference "Baltic Petrol' 2010"
5. Roosta A., Escrochi M., Varsandech F., Khatibi J., Sh., Schafiee M.: "Investigating the Mechanism of Thermally Induced Wettability Alteration" (2010) SPE Paper 120354
6. Skauge A., Ottesen B." A Summary of Experimentally Derived Relative Permeability and Residual Saturation on North Sea Reservoir Cores" SCA Papers (2002)
7. Such P.: The pore space investigations for geological and field engineering purposes. Prace IGNiG, Kraków, Nr 104 (2000),95
8. Such P. Investigations of a pore space of reservoir rock with the use of the fractal approach. Prace IGNiG Nr 115, Kraków (2002), 28
9. Such P., Lesniak G.: "Factors Affecting Relative Permeability Measurements for the Miocene and the Rotliegend Poorly Consolidated Sandstones" SCA Paper, (2003)
10. Such P., Leśniak G., Budak P.: Complex methodic of investigations of petrophysical properties of rocks. Prace INiG, Nr.142, Kraków (2007), 69

# **COUPLING LATTICE BOLTZMANN AND FINITE VOLUME METHODS FOR SIMULATION OF REACTIVE TRANSPORT**

Min Liu, Peyman Mostaghimi

School of Petroleum Engineering, The University of New South Wales, NSW 2052,  
Sydney, Australia

*This paper was prepared for presentation at the International Symposium of the Society of Core Analysts held in Snowmass, Colorado, USA, 21-26 August 2016*

## **ABSTRACT**

A numerical model is developed to study reactive transport at pore scale. It couples lattice Boltzmann and finite volume methods to compute fluid flow and reaction processes. The model is validated by comparing numerically simulated reactive flow against the published results of dynamic imaging of carbonate dissolution. The porosity profiles and permeability-porosity relationship are compared with the experimental results. The variation of the porous structure is quantitatively analysed and compared with those obtained from dynamic imaging experiments. The findings show that the numerical framework provides robust and accurate prediction of porous media alteration due to flow of reactive fluids and can be used as a predictive tool for resolving reaction mechanisms in porous media with applications in reservoir engineering, carbon dioxide sequestration, hydrological and environmental studies.

## **INTRODUCTION**

Reactive transport in porous media is of great importance in a wide range of science and engineering applications including reservoir engineering, carbon dioxide sequestration, hydrogeological and environmental studies. Chemical reactions at the pore scale can dramatically alter the pore structure and change the petrophysical properties of reservoir rocks [1]. Pore scale modelling methods for reactive transport studies include network modelling and direct modelling [2]. Pore network modelling has been used to study the permeability and porosity variation due to reaction [3,4], but it cannot accurately predict the alteration of local microstructure in very heterogeneous porous media [5]. Direct modelling addresses this issue by simulating fluid flow directly in voxels of micro-computed tomography (micro-CT) images. As the most popular method of direct simulation, the lattice Boltzmann (LB) method has been widely used to investigate the dissolution and precipitation in two-dimensional porous media [6,7]. Apart from the LB approach in direct simulation, finite difference, volume and element methods [8-11] and

particle-tracking methods [12,13] have been applied to simulate flow and predict reaction rates in porous media. However, numerical model with the lattice Boltzmann method have mainly focused on 2D geometries. Although 3D investigations of reactive flow have been performed by other direct modelling methods [13], the maximum size of the micro-CT image is limited due to computational limitations.

In this paper, an efficient pore scale model is developed for simulating the reactive transport directly on 3D micro-CT images. We simulate reactive transport directly on the micro-CT image and compare our results with published dynamic micro-CT imaging performed at Imperial College London [14].

## MATHEMATICAL FORMULATIONS

The Lattice Boltzmann method and Finite Volume method are coupled in Fortran codes to calculate fluid flow and chemical reaction directly on micro-CT images.

### Lattice Boltzmann Simulation of Flow

We use the lattice Boltzmann method based on D3Q19 to solve the incompressible fluid flow [9] by applying the discrete Boltzmann equation,

$$f_i(\mathbf{x} + \mathbf{e}_i \Delta t, t + \Delta t) - f_i(\mathbf{x}, t) = -\frac{1}{\tau} \left( f_i(\mathbf{x}, t) - f_i^{eq}(\mathbf{x}, t) \right), \quad (1)$$

where  $f_i$  is the distribution function along the  $i$ -direction,  $\mathbf{e}_i$  is the discrete lattice velocity,  $\Delta t$  is the time step,  $\tau$  is the relaxation time parameter and  $f_i^{eq}$  is the equilibrium distribution function. The fluid flow density and velocity can be calculated by  $\rho = \sum_i f_i$  and  $\underline{\mathbf{v}} = \frac{1}{\rho} \sum_i \mathbf{e}_i f_i$ , respectively. The no-slip boundary condition is enforced at the solid surface by applying the bounce-back scheme [15]. The solution obtained based on the lattice Boltzmann simulations reproduces the incompressible Newtonian Navier-Stokes equations with constant kinematic viscosity of  $\frac{1}{3}(\tau - \frac{1}{2})$  [16].

### Finite Volume Simulation of Reaction

The solute concentration can be updated by solving the advection-diffusion equation,

$$\frac{\partial C}{\partial t} + (\underline{\mathbf{v}} \cdot \nabla) C = \nabla \cdot (D \nabla C), \quad (3)$$

in which  $C$  [ $mol\ m^{-3}$ ] is concentration and  $D$  [ $m^2 s^{-1}$ ] is the diffusion coefficient. A finite volume scheme is applied to discretize the concentration equation on micro-CT images. The first order kinetic is enforced at solid surface via

$$D \frac{C(t + \Delta t) - C(t)}{\Delta x} = -\kappa(C(t) - C_s), \quad (4)$$

where  $\kappa$  [ $ms^{-1}$ ] is the reaction rate constant,  $\Delta x$  [ $m$ ] is the image resolution,  $\Delta t$  [ $s$ ] is time step, and  $C_s$  [ $mol\ m^{-3}$ ] is the saturated concentration.

The solid volume fraction update is related with the reaction flux by

$$\frac{p(t + \Delta t) - p(t)}{\Delta t} = -V_m S \kappa (C(t) - C_s), \quad (5)$$

where  $p$  is the solid volume fraction,  $V_m [m^3 mol^{-1}]$  is the molar volume, and  $S [m^{-1}]$  is the specific surface area. The concentration is initially set to  $C = 0.79 mol m^{-3}$  and a Dirichlet boundary condition is applied at the inlet. Table 1 provides the constant values used in the simulations to reproduce the experimental reactive and transport regimes. For more details regarding the mathematical formulation and the numerical method, refer to [9].

Table 1. Reaction and transport parameters used for simulations

Pe	Da	Reaction rate constant [ $ms^{-1}$ ]	Diffusion coefficient [ $m^2 s^{-1}$ ]	Characteristic length [ $m$ ]
2100	0.05	$1.08 \times 10^{-7}$	$7.5 \times 10^{-10}$	$4.07 \times 10^{-4}$

## RESULTS

The numerical results for reactive transport are compared with dynamic imaging experiment of a Ketton carbonate dissolution performed at Imperial College London [14]. The Peclet and Damkohler numbers are set to be identical to the experimental conditions;  $Pe=2100$  and  $Da=0.05$ . The developed numerical method with no tuning parameter and only setting the Peclet and Damkohler numbers can reproduce the experimental observations. Note that the Peclet and Damkohler numbers are the dimensionless number characterising the regimes of transport and reaction, respectively. The dissolved core sample and orthogonal slices are presented in Figure 1, which demonstrate a uniform dissolution. Our numerical results show very similar uniform dissolution pattern as observed in the experiment observations using identical reaction parameters.

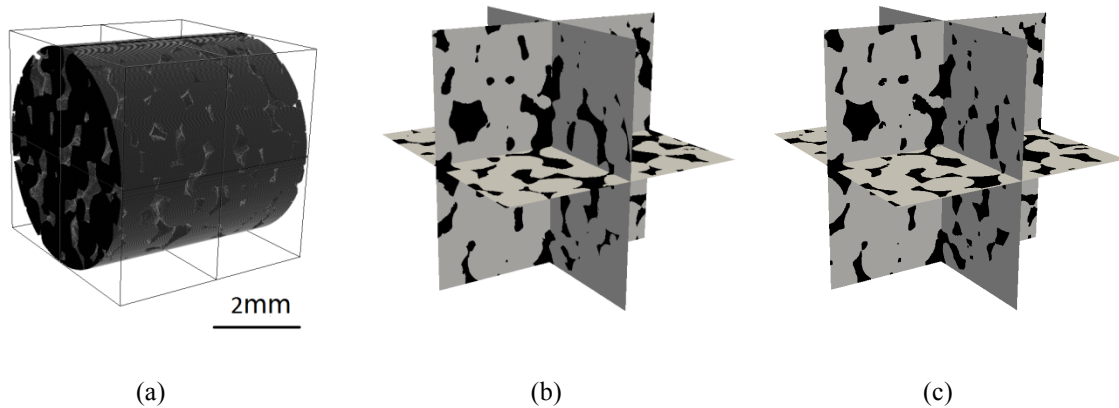


Figure 1 The 3D carbonate geometry after dissolution; (a) the full sample after 50 min, and orthogonal slices of (b) experiments, (c) simulation after 50 min of reaction.

The comparison of porosity variations between the numerical results and experimental measurements is demonstrated in Figure 2(a). There is minor difference between the predicted porosity and the experimental observations and on average our results show 3.8% difference to the experimental measurements.

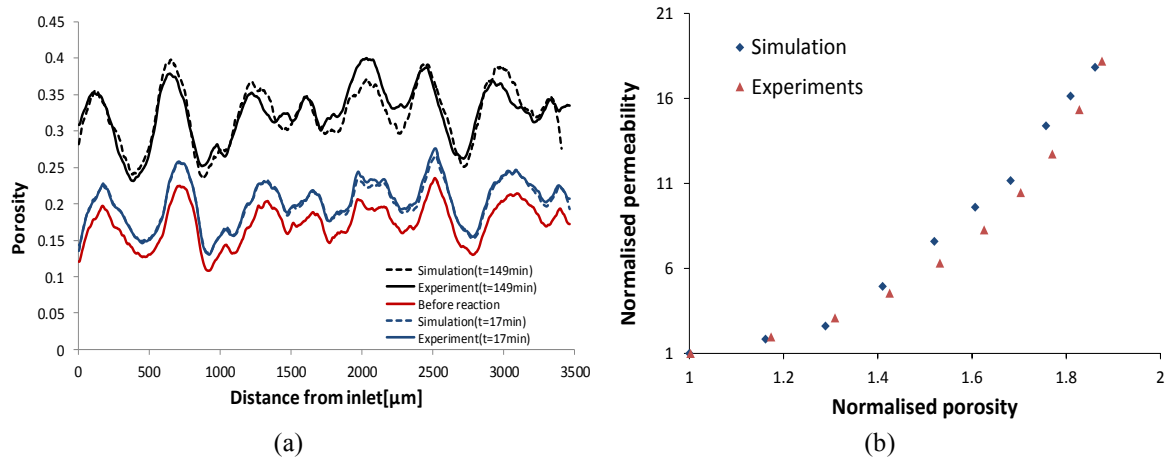


Figure 2 (a) Porosity profiles across layers normal to the main direction of flow before reactions (red); after 17 min (blue); and 149 min (black) of reaction. Solid lines are experimental measurements and dash lines are simulation results. (b) Permeability-porosity relationships of experiment and numerical results (Normalised porosity and permeability are calculated as the ratio of the porosity and permeability of the sample divided by the initial values).

The permeability-porosity relationship of both experimental and simulation results are shown in Figure 2(b). The value of  $n$  in the power-law correlation ( $K=\phi^n$ ) is calculated as 4.58 for the experiment and for the simulation, the exponent is 4.83 (5.4% difference). The simulation results match very well with those calculated from experimental data.

In our recent published work [9], we have applied the numerical method to analyse the sensitivity of rock permeability, porosity and their relationships to the Peclet and Damkohler regimes. It was shown that the values and scaling of rock permeability and porosity is strongly dependent upon the reaction and transport regimes as well as the rock heterogeneity.

During the process of reaction, the microstructure of the pore space changes. The chord length distribution can be used to discriminate the pore structure of porous media by presenting the probability of forming a random chord length in the pore space. Chord length is described as the length of any line-segment lying in one specific phase with its endpoints at the phase interface [17]. The chord length distribution is measured directly on the images of experiments and simulation results to reflect the pore structure alteration during the dissolution. The chord length distributions of simulation and experiments in solid phase are presented in Figure 3(a). The distribution of the predicted chord lengths is identical to that of experimental measurements after 149 min of reaction.

Critical radius is defined as the radius of the largest sphere percolating through a porous medium from one side to the opposite one. A larger critical radius indicates a better connectivity of the porous media. We calculate the critical radius from images of experiments and results from simulations after different time of dissolution as shown in Figure 3(b). All the values are normalised by the critical radius of the original image prior to reaction. As can be seen in the figure, the critical radius of simulation shows a very

similar trend to the one in experiments. This justifies the good match between numerical simulations of permeability and experimentally measured permeability since permeability is strongly correlated with the critical radius. The average difference of the numerical prediction and experimental results is less than 6% during the reaction process.

In brief, critical radius and chord length are applied as two quantities expressing the morphological changes of the porous structure due to dissolution. The observed variations justify the permeability increase due to reaction; the critical radius increases with time which means larger throats are available for fluid flow and the probability of short chord lengths in the solid phase increases indicating occurrence of dissolution.

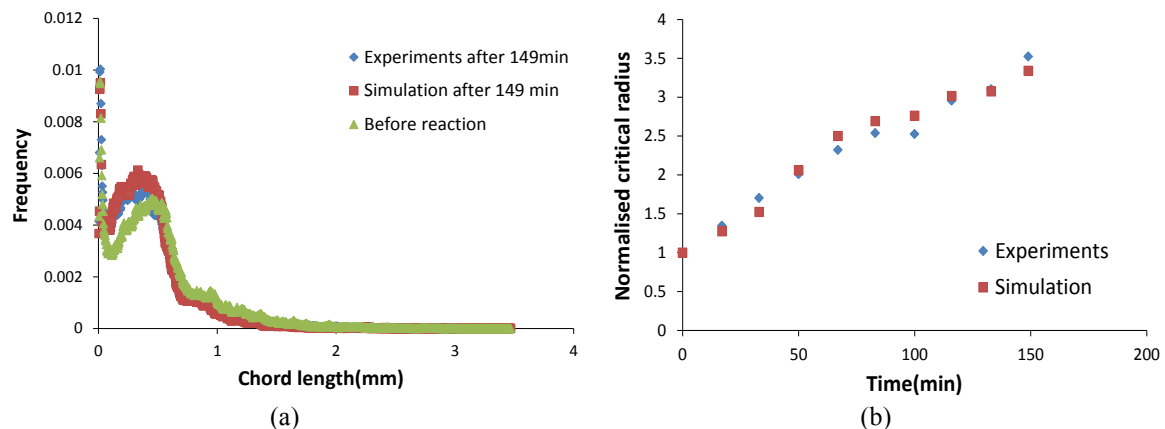


Figure 3 (a) Distribution of chord length in the solid phase for experiments and simulations; (b) Variation of critical radius of experiments and simulation with time.

## CONCLUSION

We have developed a numerical model to simulate the reactive flow on micro-CT images of carbonate. We compare the numerical results with dynamic imaging observations to validate the model. The permeability-porosity relationship of simulations and experiments are measured. The predicted permeability in the simulations presents very good agreement with the experimental measurements. The local porosities and chord length distribution as well as critical radius in simulation match very well with experimental measurements. The numerical framework coupling lattice Boltzmann method and finite volume formulations can accurately predict the reactive flow and provide important understanding in pore scale reactive transport.

## REFERENCES

- Noiriel, C., Gouze, P. and Bernard, D., "Investigation of porosity and permeability effects from microstructure changes during limestone dissolution." *Geophysical Research Letters*, (2004) **31**, 24.
- Blunt, M.J., Bijeljic, B., Dong, H., Gharbi, O., Iglauer, S., Mostaghimi, P., Paluszny, A. and Pentland, C., "Pore-scale imaging and modelling." *Advances in Water Resources*, (2013) **51**, 97-216.

3. Algive, L., Bekri, S. and Vizika, O., "Pore-network modeling dedicated to the determination of the petrophysical-property changes in the presence of reactive fluid." *SPE Journal*, (2010) **15**, 03, 618-633.
4. Varloteaux, C., Békri, S. and Adler, P.M., "Pore network modelling to determine the transport properties in presence of a reactive fluid: From pore to reservoir scale." *Advances in Water Resources*, (2013) **53**, 87-100.
5. Dong, H. and Blunt, M.J., "Pore-network extraction from micro-computerized-tomography images." *Physical Review E*, (2009) **80**, 3, 036307.
6. Kang, Q., Chen, L., Valocchi, A.J. and Viswanathan, H.S., "Pore-scale study of dissolution-induced changes in permeability and porosity of porous media." *Journal of Hydrology*, (2014) **517**, 1049-1055.
7. Chen, L., Kang, Q., Tang, Q., Robinson, B.A., He, Y.L. and Tao, W.Q., "Pore-scale simulation of multicomponent multiphase reactive transport with dissolution and precipitation." *International Journal of Heat and Mass Transfer*, (2015) **85**, 935-949.
8. Maheshwari, P., Ratnakar, R.R., Kalia, N. and Balakotaiah, V., "3-D simulation and analysis of reactive dissolution and wormhole formation in carbonate rocks." *Chemical Engineering Science*, (2013) **90**, 258-274.
9. Mostaghimi, P., Liu, M, Arns, C.H., "Numerical simulation of reactive transport on micro-CT images." *Mathematical Geosciences*, (2016), [doi:10.1007/s11004-016-9640-3](https://doi.org/10.1007/s11004-016-9640-3).
10. Molins, S., Trebotich, D., Steefel, C.I. and Shen, C., "An investigation of the effect of pore scale flow on average geochemical reaction rates using direct numerical simulation." *Water Resources Research*, (2012) **48**, W03527.
11. Mostaghimi, P., Percival, J. R., Pavlidis, D., Ferrier, R. J., Gomes, J. L., Gorman, G. J., Jackson, M. D., Neethling, S.J. and Pain, C. C., "Anisotropic mesh adaptivity and control volume finite element methods for numerical simulation of multiphase flow in porous media." *Mathematical Geosciences*, (2015), **47**(4), 417-440.
12. Paster, A., Bolster, D. and Benson, D.A., "Particle tracking and the diffusion-reaction equation." *Water Resources Research*, (2013) **49**, 1, 1-6.
13. Pereira Nunes, J.P., Blunt, M.J. and Bijeljic, B., "Pore-scale simulation of carbonate dissolution in micro-CT images." *Journal of Geophysical Research: Solid Earth*, (2016) **121**, 558–576.
14. Menke, H.P., Bijeljic, B., Andrew, M.G. and Blunt, M.J., "Dynamic three-dimensional pore-scale imaging of reaction in a carbonate at reservoir conditions." *Environmental Science & Technology*, (2015) **49**. 7, 4407-4414.
16. Martys, N.S. and Chen, H., "Simulation of multicomponent fluids in complex three-dimensional geometries by the lattice Boltzmann method." *Physical Review E*, (1996) **53**, 1, 743.
17. Chen, S., Wang, Z., Shan, X. and Doolen, G.D., "Lattice Boltzmann computational fluid dynamics in three dimensions." *Journal of Statistical Physics*, (1992) **68**, 3-4, 379-400.
18. Arns, C.H., Bauguet, F., Limaye, A., Sakellariou, A., Senden, T., Sheppard, A., Sok, R.M., Pinczewski, V., Bakke, S., Berge, L.I. and Oren, P.E., "Pore scale characterization of carbonates using X-ray microtomography." *SPE Journal*, (2005) **10**, 04, 475-484.

## TO WHAT DEGREE THERMAL CYCLES AFFECT CHALK STRENGTH

Tijana Livada<sup>1,3</sup>, Anders Neramoen<sup>1,3</sup>, Reidar Inger Korsnes<sup>1</sup>, Ida Lykke Fabricius<sup>1,2</sup>

<sup>1</sup> University of Stavanger, <sup>2</sup> Technical University of Denmark

<sup>3</sup> The National IOR Center of Norway

*This paper was prepared for presentation at the International Symposium of the Society of Core Analysts held in Snowmass, Colorado, USA, 21-26 August 2016*

### ABSTRACT

Chalk reservoirs could potentially undergo destabilization as the result of repeated cold water injection into a hot reservoir during water flooding. Preliminary results of an ongoing study are presented in this paper, which compare the impact of temperature cycling on mechanical behavior on dry and water saturated chalk. Sixty disks of dry Kansas chalk exposed to different number of temperature cycles were tested for tensile strength using a Brazilian test. Changes in elastic properties as function of number of temperature cycles of the same chalk, but now saturated in water, were studied using triaxial cell experiments. For dry rock, no significant effects of temperature cycling was found on average tensile strength, however the range of the tensile failure stress is doubled for the samples exposed to 50 temperature cycles, as opposed to those to none. For water saturated cores, the temperature cycling had a significant effect and a significant accumulative irreversible deformation was seen for the core exposed to cyclical temperature variations, so that the elastic bulk modulus consequently increased more than for a core that had been tested at constant temperature. The inconsistency of the results from the two tests suggests the importance of the pore fluid.

### INTRODUCTION

Thermal cycling effects are observed on (calcitic) marble cladding, which after being exposed to repeated seasonal change, experience considerable deformation. A famous example is the degradation of marble cladding on the Finlandia Hall in Helsinki [1]. Similar to marble, chalk is mostly composed of calcite. The thermal expansion of calcite is temperature dependent, and very anisotropic [2], so when temperature is increased the grain expands parallel to the c-axis, but also contracts in the perpendicular direction. The deformation observed in marble probably arises due to the combined effect of the expansion of single calcite crystals, the difference in the thermal expansion coefficient and the angle between neighboring crystals. Decoupling of reversible and irreversible processes is another important factor to consider when rock is exposed to stress. The total strain is defined as the sum of the irreversible  $\epsilon_{irr}$  and reversible  $\epsilon_{rev}$  strain,

$$\epsilon_{tot} = \epsilon_{irr} + \epsilon_{rev} \quad (1)$$

As plastic deformation accumulates the rock becomes stiffer and harder to further deform, such that the rock is hardened by plastic deformation. This phenomenon is called work hardening.

## PROCEDURE

### Material

Chalk is a carbonate rock mostly composed of calcitic coccoliths originating from skeletons of algae. The grains in chalk are held together by contact cement and attractive van der Waals forces at short distances between the particles, counteracted by electrostatic repulsion at intermediate distance. These forces are dependent on temperature and brine composition [3-5].

Chalk from Kansas (USA) was used in this study. It is an indurated chalk with wackestone texture. Petrophysical properties of selected samples are listed in Table 1. The average porosity  $\phi$  was calculated to be 34%, permeability was measured to be 0.3 and 0.9 mD, and elastic wave velocity,  $V_p$ , around 3000 m/s. The samples thus resemble North Sea reservoir chalk with respect to porosity, permeability, and

Table 1. Petrophysical properties of selected samples for the Brazilian test.

Sample number	# of cycles	$\phi$ -sat. (%)	Diameter (mm)	Length (mm)	$V_p$ (m/s)	He-gas (g/cm <sup>3</sup> )	$\phi$ -He gas (%)
<b>K1-3</b>	0	35.1	38.09	26.28	2857	2.71	35.7
<b>K1-4</b>	30	33.9	38.10	27.51	3057	2.72	34.9
<b>K2-1</b>	50	34.7	38.09	26.95	2929	2.70	34.7
<b>K2-5</b>	15	30.9	38.09	23.21	3179	2.70	31.2
<b>K4-2</b>	0	34.9	38.10	26.04	2504	2.69	35.0
<b>K5-3</b>	30	34.6	38.10	22.83	2890	2.69	34.6
<b>K6-3</b>	15	33.8	38.08	30.09	2812	2.71	34.4
<b>K7-1</b>	8	34.8	38.08	25.26	2476	2.71	36.0
<b>K8-5</b>	8	32.6	38.10	19.59	3160	2.69	32.5
<b>K10-6</b>	50	33.4	38.13	22.63	2487	2.69	34.4

induration.

### Brazilian test

Precautions were taken to keep track of the spatial directions in the block to remove any anisotropy effects that would affect direct comparison. Long cores were shaped and cut into disks with diameters double the length. 60 samples were prepared. After drying at 120°C overnight, each sample was weighed and saturated in a vacuum chamber with distilled water to estimate porosity and solid density. He-gas pycnometry was used to confirm measures of the solid density and porosity. The dried samples were then repeatedly heated and cooled and the effect on the tensile strength in Brazilian tests were investigated. Dry samples were used to single out the effects of temperature fluctuations, without the influence that pore fluids might have.

In Brazilian tests, the tensile strength ( $T_0$ ) at failure is estimated from the critical force ( $F$ ) applied by two parallel plates,  $T_0 = 2F/\pi DL$ , where  $D$  and  $L$  are diameter and length of the sample. 10 samples were tested directly before any temperature cycling was performed. The other 50 specimens were put in an oven at 135°C for 8h, and then switched off for 16h, allowing the samples to cool. After eight temperature cycles 10

samples were tested, and the rest of the samples were tested after 15, 30 and 50 cycles (see Table 2).

### Hydrostatic test

Two cores from the same chalk block were prepared for testing in a triaxial cell, and saturated with calcite equilibrated brine that was prepared by placing chalk pieces in distilled water. The average pH of the brines were 8.7 and the salinity were approx. 300 ppm (ion chromatography). The triaxial cell has two pumps to control the confining pressure ( $P_c$ ) and fluid pressure ( $P_f$ ). The cell is additionally equipped with a heating jacket which allows temperature control, as well as with extensimeter and internal LVDT to measure radial and axial deformation of the core. The elastic bulk modulus ( $K_b$ ) is measured using Equation 3. For both cores, the modulus is calculated for both the loading phase and unloading phase.

$$K_b = \frac{P_c}{\varepsilon_{vol}}, \quad (2)$$

Each core was mounted into the triaxial cell, followed by increasing the  $P_c$  to 0.5 MPa. Next,  $P_f$  and  $P_c$  were increased to 0.7 and 1.2 MPa respectively. Then each core was tested: one was subjected to confining pressure cycling alone, where the temperature was kept constant at 30°C throughout the test. The second experiment included a temperature cycle for each stress cycle that could be compared to the constant temperature experiment. Each morning, at 30°C, a confining stress cycle was performed to measure stress-strain behavior and to quantify the elastic bulk modulus. The stress cycle is characterized by a loading phase (1.2→5.2 MPa) and unloading (5.2→1.2 MPa), 30 minutes each way. The bulk modulus was measured as an average during both loading and unloading phase of each cycle, along with the reversible and irreversible strain components. Directly after each stress cycle, the cell-temperature was increased to 130°C, and six hours later the temperature was reduced back to 30°C. This procedure was repeated daily to explore the evolution in the strain and bulk modulus for 10 days. An additional 11<sup>th</sup> cycle was performed on the core, however this cycle did not include the temperature variation. This was done in order to confirm if the effects observed were temperature and not sample dependent.

## RESULTS

The results of the Brazilian tests for tensile strength  $T_0$  and the dynamic evolution of the stress-strain behavior during hydrostatic loading are shown here.

### Brazilian Test

Average tensile strength for each temperature cycling procedure is presented in Table 2. The average tensile strength does not show any significant response to temperature cycling, however the distribution of the data is significantly broader when the samples have been exposed to temperature cycling. The standard deviation is doubled for samples

Table 2. Average tensile strength failure for the Brazilian tests and their std. dev.

# of cycles	# of tests	$T_0$ (MPa)	Std. dev (MPa)
0	10	3.10	0.40
8	10	3.07	0.62
15	15	3.30	0.50
30	10	3.32	0.58
50	15	3.08	0.82

exposed to 50 temperature cycles as opposed to those unaged. Figure 1 (a) illustrates the distribution of tensile strengths at which chalk fails. Figure 1 (b) shows that there is no obvious trend between porosity and the failure strength, indicating that the results obtained are not porosity dependent.

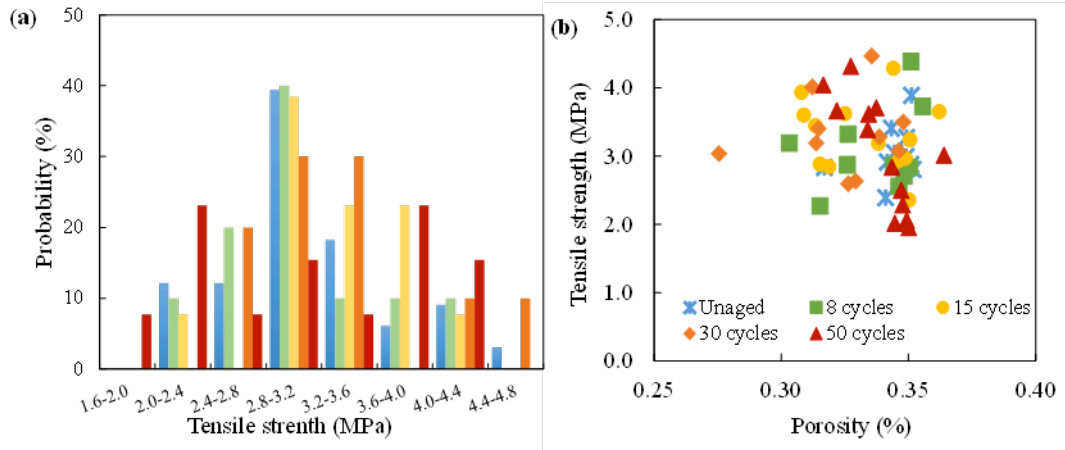


Figure 1. Results from the Brazilian test: (a) probability of the sample to fail within a tensile strength range; (c) Tensile strength shows no dependency on porosity.

### Hydrostatic test

The results of the two experiments are presented in Table 3 and Figure 2 (for all values in the figures, but every second in the table). The irreversible fraction of the total strain during each stress cycle  $\varepsilon_{irr} / \varepsilon_{tot}$  was calculated by modifying Equation 1, and is shown in Table 3. To ensure the comparability of the results, the first cycle for both experiments was completed without any temperature variation.  $K_b$  and the strain fraction for both experiments during loading and unloading phase have similar values. But once the temperature cycling was applied to one of the cores, the fraction is much higher for cycles in the experiment where temperature is varied (Figure 3). The additional 11th cycle proves this effect does not depend on the strain but on the temperature cycling. The  $K_b$  of the core with constant temperature increases slightly during loading and decreases slightly during unloading. However, for the core treated with heating/cooling cycles,  $K_b$  increases more significantly during loading and unloading as irreversible strain increase.

Table 3.  $K_b$  and irreversible fraction of strain (\*additional cycle with const. temp.)

# of cycles	Constant temperature			Temperature cycling		
	$K_b$ load (GPa)	$K_b$ unload (GPa)	$\varepsilon_{irr} / \varepsilon_{tot}$ (%)	$K_b$ load (GPa)	$K_b$ unload (GPa)	$\varepsilon_{irr} / \varepsilon_{tot}$ (%)
1	1.60	3.07	48.2	1.64	2.91	44.1
2	2.44	2.77	14.7	2.26	2.95	28.3
4	2.48	2.71	7.2	2.67	3.40	21.6
6	2.47	2.64	7.0	2.74	3.37	18.0
8	2.50	2.66	5.5	2.79	3.28	17.5
10	2.52	2.55	4.0	2.79	3.58	17.8
11	/	/	/	3.23*	3.43*	2.55*

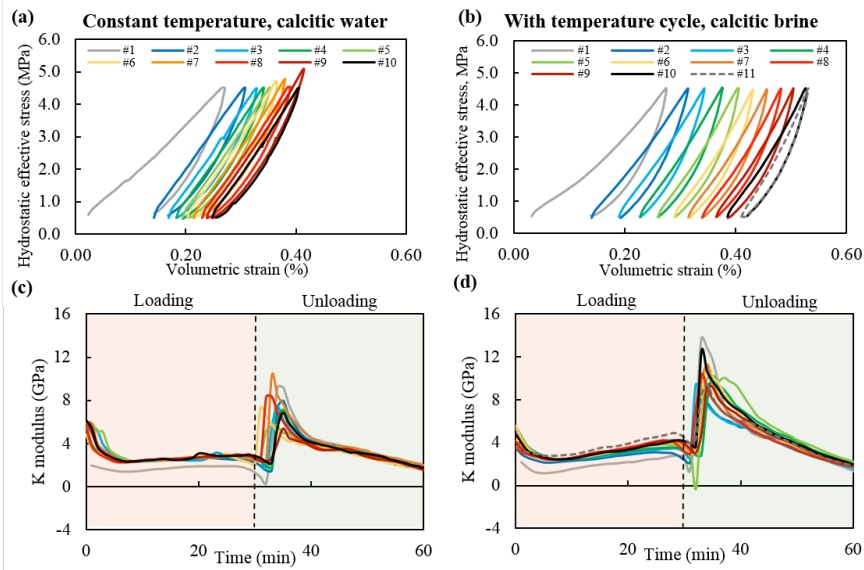


Figure 2. Hydrostatic test results for constant temperature in the left column (a and c) and with temperature cycling in the right column (b and d). Stress versus volume strain in (a) and (b). Slopes during loading and unloading in (c) and (d).

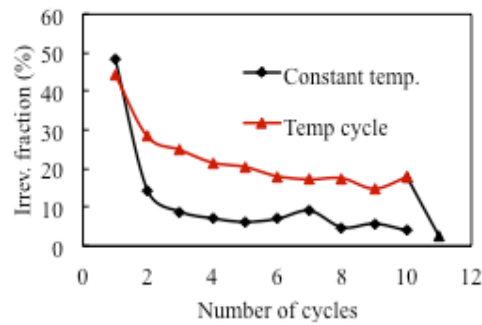


Figure 3. Irreversible strain fraction,  $\varepsilon_{irr}/\varepsilon_{tot}$ , for individual hydrostatic cycles.

## DISCUSSION

Brazilian tensile failure of dry chalk displays no weakening of tensile strength for increasing numbers of temperature cycles, except an increased spread in the tensile strength after 50 cycles (Table 2). For the saturated cores in the hydrostatic tests, the fraction of irreversible strain,  $\varepsilon_{irr}/\varepsilon_{tot}$ , is significantly higher when temperature has been cycled between each stress cycle (Figure 3). After 10 stress cycles the temperature exposed core accumulates 0.40% total volumetric strain as opposed to the constant temperature core that only accumulated 0.25% (Figure 2 a and b). In fact, the core exposed to the temperature cycling reaches 0.25% irreversible deformation after only 4 cycles. The 11th cycle that was performed with constant temperature, shows that the irreversible fraction drops down to 2.5%, which is comparable to the constant temperature experiment (Figure 3). This shows that the magnitude of the irreversible component is due to the temperature cycling. The evolution of the elastic stiffness during loading and unloading ( $K_b$ ) with respect to number of cycles is different between the constant temperature and temperature cycle tests (Table 3).  $K_b$  during unloading is reduced for the constant temperature while increases for the temperature

exposed cores, while  $K_b$  during loading increases independent of temperature exposure. In reservoirs, the accumulation of irreversible deformation alters the pore volume and thus the reservoir permeability. Variations in temperature and effective stresses are expected since injection rates may vary, thus impacting the irreversible strain component. The results from the Brazilian tests and hydrostatic test seem not to show a clear relation between temperature variations and mechanical strength. This may indicate the importance of either the pore fluid, or inconsistencies of mechanical properties tested (tensile vs compaction).

## CONCLUSION

Two different tests procedures were performed on Kansas chalk to determine if temperature cycling has an effect on chalk mechanical strength. The Brazilian test on dry samples reveals no significant weakening observed with temperature cycling. Hydrostatic tests show that temperature cycling on water saturated samples has an effect on the reversible and irreversible strain partitioning, and the bulk modulus during loading and unloading. At this point, presented evidence does not univocally show if thermal expansion coefficients play a role in dictating the mechanical strength of chalk.

## NOMENCLATURE

$\phi$	Porosity	$L$	Length	$K_b$	El. bulk modulus
$V_p$	P wave velocity	$D$	Diameter	$\varepsilon_{vol}$	Vol. strain
$F$	Force	$P_c$	Confining pres.	$\varepsilon_{irr}$	Irr. strain comp.
$T_o$	Tensile strength	$P_f$	Pore fluid pressure	$\varepsilon_{tot}$	Total strain

## ACKNOWLEDGEMENTS

The authors would like to thank the Research council of Norway and the industry partners; ConocoPhillips Skandinavia AS, BP Norge AS, Det Norske Oljeselskap AS, Eni Norge AS, Maersk Oil Norway AS, DONG Energy A/S, Denmark, Statoil Petroleum AS, ENGIE E&P NORGE AS, Lundin Norway AS, Halliburton AS, Schlumberger Norge AS, Wintershall Norge AS of the National IOR Centre of Norway for support. In addition, COREC is acknowledged for financial support.

## REFERENCES

- [1] Royer-Carfagni, G., "Some considerations on the wrapping of marble façades: the example of Alvar Aalto's Finlandia Hall in Helsinki," *Construction and Building Materials*, (1999), **13**, 449-457.
- [2] Rosenholtz, J. L. and D. T. Smith, "Linear thermal expansion of calcite, var. Iceland Spar, and Yule marble," *Am. Mineralogist*, (1949) **34**, 846-854.
- [3] Neramoen, A., R. I. Korsnes, I. L. Fabricius, and M. V Madland, "Extending the effective stress relation to incorporate electrostatic effects," *Society of Exploration Geophysicists*, (2015), 5891149.
- [4] Megawati, M., A. Hiorth, M. V. Madland, "The impact of Surface Charge on the Mechanical Behavior of High-Porosity Chalk", *Rock Mech. and Rock Eng.* (2013), **46**, 5, 1073-1090.
- [5] Røyne, A., K. N. Dalby, T. Hassenkam, "Repulsive hydration forces between calcite surfaces and their effect on the brittle strength of calcite-bearing rocks", *Geophys. Res. Lett.*, (2015), **42**, 4786-4794.

## **NMR Fluid Typing Using Independent Component Analysis Applied to Water-Oil-displacement Laboratory Data**

Pedro A. Romero, Geoneurale, and Manuel M. Rincón, Central University of Venezuela

*This paper was prepared for presentation at the International Symposium of the Society of Core Analysts held in Snowmass, Colorado, USA, 21-26 August 2016*

### **ABSTRACT**

In low field NMR relaxometry for hydrogen, the  $T_1$  or  $T_2$  spectra of core samples are mixtures of the individual contributions of the saturating phases filling the pore space, either water or hydrocarbon. Fluid typing (identification and quantification of each phase) becomes challenging, however, when individual spectra overlap within a certain relaxation time window.

A traditional fluid typing approach, based on the diffusion effect, is complex and expensive. It requires magnetic field gradient, multiple radio frequencies, and a special fit-for-purpose inversion software. This approach applies to  $T_2$  only;  $T_1$  is not affected by diffusion relaxation mechanisms.

Independent component analysis (ICA) has been tested as a means of solving this problem. ICA is a blind source separation (BSS) technique that yields statistical independent  $T_2$  spectral source components of the present fluids, without previous knowledge of either relaxation mechanisms or fluid properties. The technique can also be applied to  $T_1$ .

In a water-oil drainage experiment, beginning with 100% oil saturation, we measured the  $T_2$  spectra of the samples at five water saturation stages, to nearly 97%, and used these spectra as input for the BSS-ICA processing. As output, we obtained the statistical independent  $T_2$  spectra for oil and water and a mixing matrix containing the individual weights that define the measured  $T_2$  spectra at any acquisition step. The results show close correlation between the oil- $T_2$  ICA-component and the  $T_2$  spectrum of the 100% oil saturated sample. The ICA-derived water saturations show a good match with reported experimental values. The water- $T_2$  ICA-component shows a bimodal behavior, reflecting the pore size distributions for  $T_2$  shorter than 400ms and the bulk water for  $T_2$  values greater than 1000ms. The bulk relaxation is caused by the presence of remaining oil layers that prevent a magnetic interaction between water molecules and the pore surface.

### **INTRODUCTION**

In reservoir characterization fluid identification is a key element, as it provides very valuable information to determine the strategy for enhanced recovery processes. Specifically, in the Santa Bárbara Field, Eastern Venezuela's, where water injection has been proposed as recovery mechanism, there has been a great interest in improving fluid typing techniques. In this regard understanding the applicability of NMR is considered of high importance [1].

Fluid identification by NMR is a very challenging task, especially when relaxation spectra  $T_1$  or  $T_2$  of the different fluids overlap. Classic examples are extra heavy oil and clay-bound water, heavy oil and capillary-bound water, light oil (including oil-based mud filtrate) and free water at higher  $T_2$  times. In principle, the spectral overlap on  $T_2$  can be solved using Diffusion- $T_2$  intrinsic ( $DT_2$ ) maps, where the diffusion as a second dimension can provide a spectral separation of fluids [2]. Unfortunately, many times due to technical limitations of NMR equipment in failing to provide enough frequencies and long enough data sets (echo trains), the applicability of  $DT_2$  maps is limited and unprecise. Given these circumstances and the fact that in the most common scenario only  $T_2$  distributions data are available, the spectral separation using a data-driven method from Machine Learning can become a very important solution.

The BSS-ICA [2] is a Machine Learning approach based on statistical assumptions made on the probability distribution functions of the spectral components -the unknown sources that setup a composed signal. In this work, a BSS-ICA algorithm, *fastica*, is applied to retrieve individual water and oil  $T_2$  spectra from their mixtures in  $T_2$  distributions from core plug samples during a water-oil displacement experiment. The BSS-ICA-derived water saturation at the different water-oil displacement steps is quantified and compared against the reported experimental values.

## BLIND SOURCE SEPARATION BASED ON INDEPENDENT COMPONENT ANALYSIS

The BSS-ICA model is based on the assumption that a set of mixtures  $[x_1, x_2, \dots, x_n]$  are generated from the linear mixture of  $n$  independent source components  $[s_1, s_2, \dots, s_n]$ , where

$$x_j = a_{j1}s_1 + a_{j2}s_2 + \dots + a_{jn}s_n = \sum_{k=1}^n a_{jk}s_k \quad (1)$$

and  $[x_1, x_2, \dots, x_n]$  and  $[s_1, s_2, s_n]$  are considered random. The values of the signals are considered samples (instantiations) of the random variables, not functions of time. In vector matrix notation, the observable variable vector  $x$  is expressed as

$$x = [x_1, x_2, \dots, x_n]^T = \begin{bmatrix} x_1 \\ x_2 \\ \vdots \\ x_n \end{bmatrix} \quad (2)$$

and the source variable vector  $s$  is expressed as

$$s = [s_1, s_2, \dots, s_n]^T = \begin{bmatrix} s_1 \\ s_2 \\ \vdots \\ s_n \end{bmatrix} \quad (3)$$

The mixing matrix  $A$ , which encodes the estimation of the fluid saturation, is

$$\begin{aligned}
 A &= (a_{ij} | i = 1, n; j = 1, n) = (a_j | j = 1, n) \\
 &= \begin{bmatrix} a_{11} & \cdots & a_{1j} & \cdots & a_{1n} \\ \vdots & & \vdots & & \vdots \\ a_{i1} & \cdots & a_{ij} & \cdots & a_{in} \\ \vdots & & \vdots & & \vdots \\ a_{n1} & \cdots & a_{nj} & \cdots & a_{nn} \end{bmatrix} \quad (4)
 \end{aligned}$$

The linear mixing equation, i.e. the independent component analysis model, the ICA-model, is reduced to:

$$x = A * s \quad (5)$$

Denoting by  $a_j$ , the  $j$ th column of matrix  $A$ , the model thus becomes:

$$x = \sum_{i=1}^n a_i s_i \quad (6)$$

The measured data  $x$  may be reconstructed by performing the above calculation individually for each source  $s_i$ . The fluid saturation at any depth level may be obtained by integrating the area of each spectrum  $x_i = a_i \cdot s_i$  at its corresponding displacement steps (or sequence). The ICA model is a generative model in that it describes how the observed data are generated by mixing the components  $s_i$ . The independent components are latent variables; they are not directly observable. The term “blind” in BSS reflects the fact that very little, if anything, is known in the mixing matrix  $A$ , and few assumptions are made with respect to the source signals. Specifically, the basic assumption is that the source components are statistically independent, and hence have unknown distributions as non-Gaussian as possible, to optimize a certain contrast function. The best  $W$  is found, where  $W$  is the unmixing matrix that yields

$$y = Wx \quad (7)$$

which is the best estimate of the independent source vector.

If the unknown mixing matrix  $A$  is square and non-singular, then

$$W = A^{-1} \text{ and } s = y \quad (8)$$

Otherwise, the best unmixing matrix that separates the sources is given by the generalized inverse Penrose-Moore matrix

$$W = A^+ \text{ and } \|s - y\|_s = \min \quad (9)$$

The BSS-ICA algorithm used in this work is *fastica* [3].

## THE EXPERIMENT

To test the hypothesis whether it is possible to calculate the water saturation ( $S_w$ ) from BSS-ICA applied on  $T_2$  distributions, data from an oil-water displacement experiment on core plugs has been used. Two core plugs of 1x1.5 inches' size were selected from the mega porosity facies, considered the best in terms of storage and drainage capacity.

Table 1. below shows some petrophysical characteristic parameters of these core samples.

**Table 1. Petrophysical characteristics of samples A and B**

Sample	Porosity [%]	Permeability [mD]	Swi [%]	BVI [%]	FFI/BVI	T2cutoff [ms]
A	15.3	1038.3	9.5	6.4	14.6	47.4
B	13.7	635.1	12.3	11.7	7.5	68.6

Starting with 100%  $S_o$ , the oil was gradually displaced by water in a centrifuge experiment. For the NMR measurements the sample was taken from the centrifuge at 4 different water saturation levels. For reference, the oil  $T_2$  distribution was also measured inside the core samples (100%  $S_o$ ). Table 2. shows the characteristics of the oil samples used in each displacement experiment for core plug A and core plug B.

**Table 2. Displacement Parameters**

Displacement Parameters	Sample A	Sample B
Oil viscosity	Lower	Higher
$T_2$ oilpeak inside sample/outside (bulk) [ms]	350/610	235/415

Figures 1.a and 1.b show the  $T_2$  distributions for sample A and B respectively. The water saturation is shown as a parameter calculated from the centrifuge experiment data. The first  $T_2$  distributions at the top of each figure correspond for the 100% water saturated sample (blue) and for 100% oil saturation (red). These spectra are considered only for reference purposes, but not used as input for the ICA approach. For each core sample A and B the  $T_2$  distributions at different levels of water saturation, were used as block input for the BSS-ICA model.

The *fastica* algorithm takes as input the 4 individual  $T_2$  spectra of each core sample data set and estimates 2 IC's as output, which are interpreted as the oil and water spectral sources. The estimated oil saturation at any of the 4 stages of the experiment is calculated as the area under the IC-oil spectrum times its corresponding weight in the mixing matrix A. The complement value to it yields the water saturation, which is later compared against the assumed true value calculated from the displacement experiment.

## RESULTS AND DISCUSSIONS

The results of applying BSS-ICA with 4  $T_2$  distributions as input and 2 IC's as output reflecting the oil and water sources, can be seen in Figures 2a. and 2b. for each core plug sample. It is worth noticing that the water distributions show two peaks corresponding one to the S/V relaxation and the other to bulk relaxation. In the oil spectra, the secondary peak at higher  $T_2$  times is due to lack of separation power of the algorithm given the relatively poor statistics of the input data.

The numerical results of the BSS-ICA for sample A and sample B are shown in Table 3. and Table 4. respectively.

Table 3. BSS-ICA results for sample A

Measure. No.	NMR-Porosity	Sw Displacem.	Sw BSS-ICA
1	14.2	16.7	X
2	16.3	41.9	38.4
3	17.2	58.7	56.6
4	16.5	71.3	81.4

Table 4. BSS-ICA results for sample B

Measure. No.	NMR-Porosity	Sw Displacem.	Sw BSS-ICA
1	12.6	39	40.8
2	14.1	56.2	62.5
3	13.6	77.9	72.2
4	14.0	86.7	72.3

Despite of experimental errors due to the non-uniform fluid distribution along the core plug longitudinal axis and missing hydrogen index correction, the results show that *fastica* can be used to obtain a good estimate for the water saturations of the samples.

Figure 3. shows the comparison between the water saturation as calculated from the displacement experiment and the values derived from BSS-ICA, using only the non-negative part of the spectra.

Theoretically, an improvement of results can be achieved by increasing the statistics of the input data with more NMR measurements at different water saturation levels, but with detrimental effect on the experimental time. Performing the displacement experiment inside the NMR resonator could be an interesting option to pursue as it would also mimic the wellbore scenario in the invading zone.

## CONCLUSIONS

The BSS-ICA is a powerful tool for fluid typing from NMR  $T_2$  distributions. The retrieved independent components match well with the expected oil and water  $T_2$  spectra, validating the undelaying ICA-model.

The BSS-ICA water saturation shows a good agreement with the values from the displacement experiment, specially in the range between 20% – 80%. At lower or higher water saturation values, a non homogeneous fluid distributions along the longitudinal axis may cause greater errors in the BSS-ICA estimated water saturation.

## ACKNOWLEDGEMENTS

The authors thank the Central University of Venezuela and PDVSA for supporting the BSc. thesis of Manuel Rincón.

## REFERENCES

1. Rincón, M., “Identificación de petrofacies y fluidos de formación a partir de resonancia magnética en tapones de núcleos de pozos del miembro Naricual Inferior, Campo Santa Bárbara, Norte de Monagas”, BSc. Thesis, Central University of Venezuela, Caracas, Venezuela, May, 2004.
2. Romero, P., Q. Zhang, “Fluid Typing with a Gradient Magnetic Field”, 2010 Rio Oil & Gas Expo and Conference, Rio de Janeiro, Brazil, 13-16 September, 2010.
3. Romero, P., “Nuclear Magnetic Resonance Evaluation Using Independent Component Analysis (ICA)-Based Blind Source Separation”, Pub. No.: WO / 2009 / 038744, Pub. Date: March, 26<sup>th</sup>, 2009, Int. Appl. No.: PCT / US2008 / 010867 2009.
4. Hyvärinen, A., J. Karhunen and E. Oja. “Independent Component Analysis”, John Wiley & Sons, Inc, New York Inc. (2001).

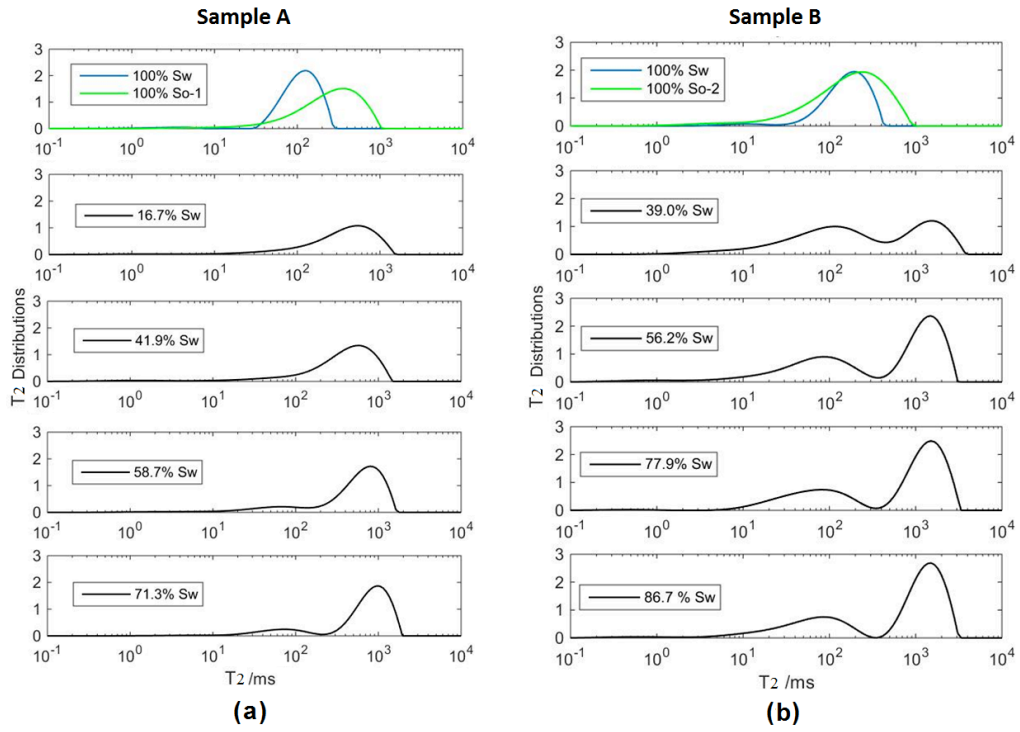


Figure 1.  $T_2$  distributions of samples A and B.

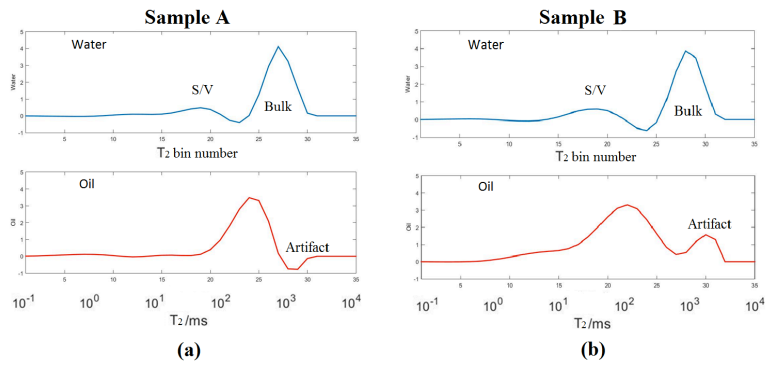


Figure 2 Water and oil IC- $T_2$  of samples A and B.

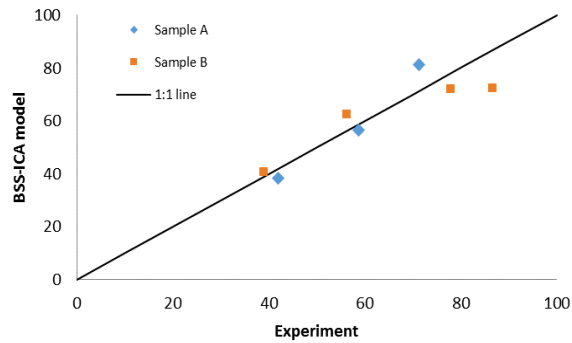


Figure 3. Water saturations from BSS-ICA vs. displacement experiment.

## **Micro-Scale Modeling of Matrix-Fracture Interactions in Fractured Porous Media**

Samuel Kazmouz<sup>a</sup>, Maziar Arshadi<sup>a</sup>, Arash Aghaei<sup>b</sup>, Mohammad Piri<sup>a</sup>,

- a) Department of Chemical and Petroleum Engineering, University of Wyoming, Laramie, WY 82071-2000, USA.  
b) Americas Oil and Gas, FEI Company, Houston, TX 77084

*This paper was prepared for presentation at the International Symposium of the Society of Core Analysts held in Snowmass, Colorado, USA, 21-26 August 2016*

### **ABSTRACT**

In this study, we utilize a fully dynamic pore-scale network model to upscale two-phase flow from pore to core in fractured porous media. The key features of the model used include incorporation of viscous, capillary, and gravity pressure drops, accounting for wetting-phase corner flow in elements with angular cross sections, the ability to adjust the corner interfaces between wetting and non-wetting phases based on changes in local capillary pressures, and heavy parallelization. We utilize a miniature fractured Berea sandstone core with the fracture extending from the inlet to the middle of the core. The core is scanned using X-ray microtomography (micro-CT) imaging techniques at pore-scale resolutions. Two networks are generated from the processed micro-CT images; one for the matrix and another for the fracture. The two networks are then merged statistically based on actual matrix-fracture connections in the sample core, acquired after segmenting the matrix pores and fracture opening in the CT images. Oil-displacing-brine (drainage) and brine-displacing-oil (imbibition) processes are simulated through the fractured core. Primary results of the model, including fluid saturation and configuration at different locations within the fracture and the matrix, are then discussed. The model results are then used to draw a better understanding of multi-phase flow through matrix pores and fracture aperture.

### **INTRODUCTION**

Multi-phase flow in porous media, in a petroleum engineering context, is the basis to predict fluid-rock properties (such as relative permeability curves) which are crucial for accurate predictions of reservoir performance. Pore network models, a form of pore scale modelling, transform the pore space into a representative pore-throat network which preserves its properties. Displacements are carried throughout the network in order to predict multi-phase flow [1]. Pore network models were introduced in the 1950s and have improved immensely since then [2]. The knowledge of pore scale physics has also

improved and while the majority of previous models were quasi-static, models now are fully dynamic and better represent the flow in the vicinity of the well bore [1].

While previous work has explored two-phase fully dynamic models in a porous rock [1] as well as isolated single fractures [3], we will take advantage of this study to explore fracture-matrix interactions. Fractures exist naturally in porous media and affect both its conductivity and continuity. Natural fractures were typically modeled using the dual-porosity approach and assigned straight line relative permeabilities. This approach is not sufficient and induces significant errors when predicting the performance of the fractured porous media [4]. Hence, in this work we use an accurate fracture aperture map as well as Berea Sandstone pore network, both constructed from real micro-CT images of a fractured core. The matrix and the fracture are then joined to create a single pore network which is representative of the fractured core. Two phase immiscible flow is then simulated using a fully dynamic model presented previously in [1]. The simulation results are then used to draw conclusions about the fracture, the matrix, and their interaction.

## MODEL

In this paper, we use a fully parallelized model previously presented in [1] as a two-phase fully dynamic pore network model. It is a pore-to-core up scaling model which assumes Newtonian, incompressible, and immiscible fluids, where there is no diffusion between phases. In addition, network elements can be both, angular and non-angular. The model accounts for piston-like, snap-off, and pore-body filling displacements. It also includes wetting phase corner flow, simultaneous injection of the wetting and non-wetting phases, and a constant outlet pressure. The simulations start with fully saturated pores and throats. All possible displacements, based on accessibility are listed. Then, the displacements proceed from the highest to the lowest potential. After each displacement, the list is updated because new pores are now accessible. Displacement potential includes viscous, capillary, and gravitational effects and is described in Eq. 1 [1]. For a displacement to occur, displacement potential should be greater than zero. This means that the pressure of the invading phase needs to overcome the pressure of the defending phase and the pressure drop that would be incurred by the displacement.

$$\Phi_{\text{disp}} = P^{\text{invd, inlet}} - P^{\text{def, outlet}} - \Delta P^{\text{disp}}$$

In order to evaluate the displacement potential, the pressure field needs to be known. The pressure field is calculated by solving a system of linear equations (by using the MUMPS package), which is created by writing a volume balance for each pore-throat-pore configuration [1].

The model utilized accounts for a wetting phase in the corner, which in turn allows for snap-off displacement. Throughout the simulation, capillary pressure in the pore changes and this might move the location of the AM [1]. It is also important to add that the contact angles input into this model were measured in-situ, after experiments (refer to Fig. 1).

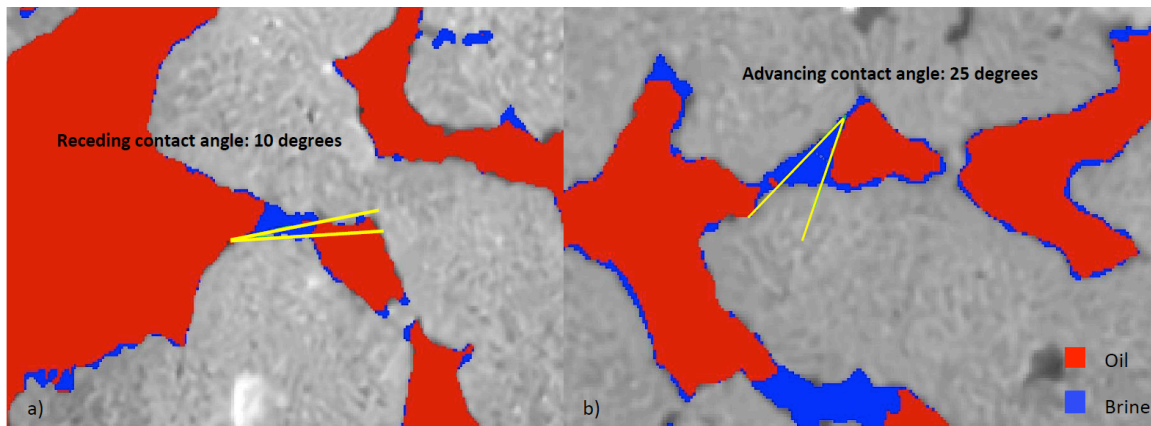


Figure 1: In-situ measurements of brine-oil contact angle in pore space in the Berea sandstone core sample.

## NETWORK REPRESENTATION OF THE FRACTURED POROUS MEDIA

In order to construct the network for this work, a fractured Berea sandstone core was scanned with a  $2.5 \mu\text{m}$  resolution using high resolution X-ray CT scanner. The fractured core has a length of 53.9 mm and a diameter of 10 mm, while a fracture of width 10 mm, extends from the inlet to the middle of the core (Fig. 2-a). In order to study matrix-fracture interactions, in this work we select the region of the core where the fracture ends. As a result, a cylindrical subdomain (6 mm diameter, 6 mm long), which includes part of the fracture, was then extracted from the original scans (Fig. 2-b). These images were then segmented using histogram thresholding method. Histogram thresholding is a widely-used method for image analysis [5]. Maximum ball algorithm [6] was then used to generate the matrix pore network (Fig. 2-c), while the fracture pore network was generated using the aperture map of the real fracture, by converting the voxels of the CT images into a representative pore-throat network which preserves the properties of the fracture, such as connectivity. (Fig. 2-d). The two networks (matrix and fracture), were then connected statistically based on real number of connections between the fracture and matrix obtained from the fractured core scans to create the final network which includes both the matrix and the fracture as one pore network (Fig. 2-e). The final network has a diameter of 6 mm and a length of 6 mm, while the fracture has a width of 6 mm and extends 2 mm from the inlet into the core. The total number of elements in the final network is 511406 with 167707 being pores and 343699 being throats. In addition, Table. 1 lists the properties of the pore network.

Table 1: Properties of the pore network

Property	Fracture	Matrix	Total(with connections)
Pores	91405	49396	167707
Throats	178657	106587	343699
Total elements	270062	155983	511406
Pore space volume (m <sup>3</sup> )	$7.15 \times 10^{-10}$	$2.66 \times 10^{-8}$	$2.7315 \times 10^{-8}$
Percent pore space volume (%)	2.618 %	97.382 %	100 %

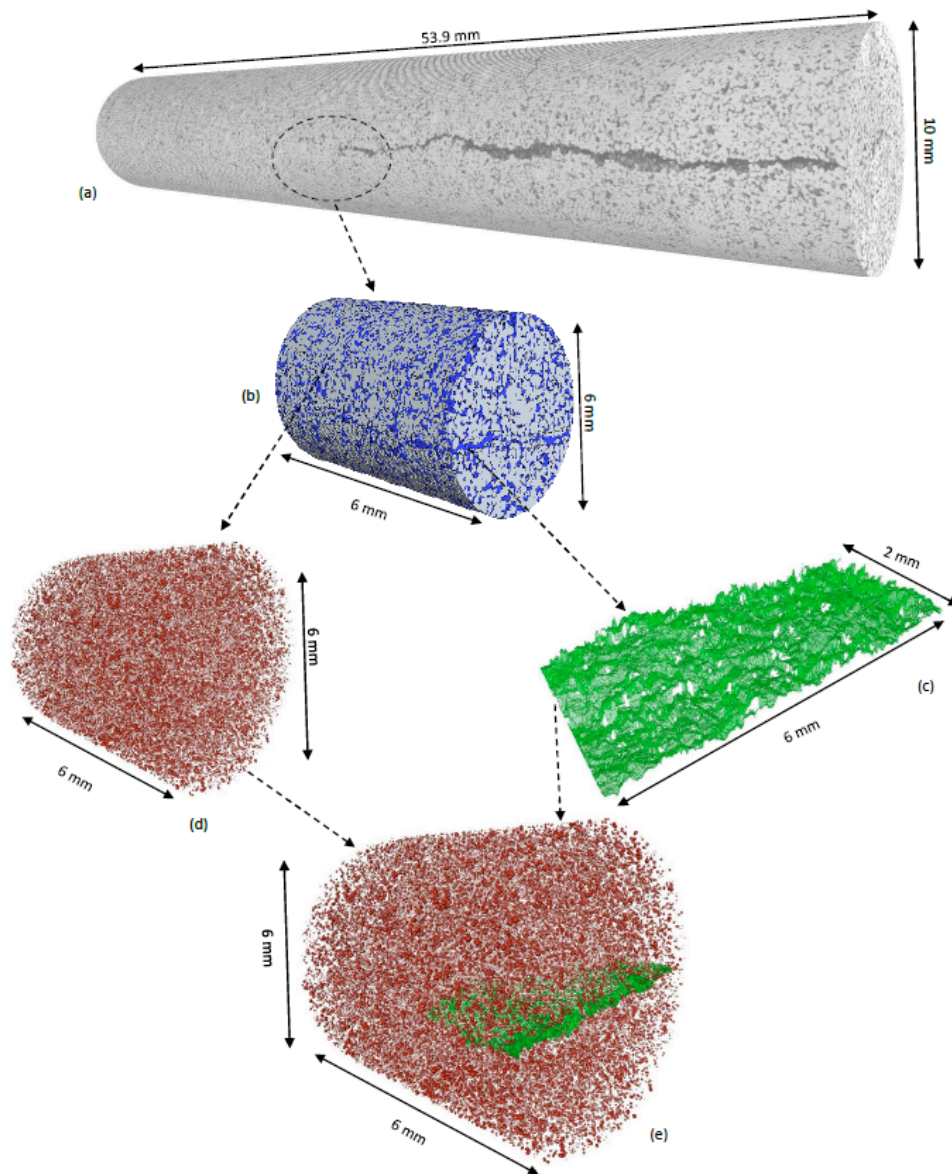


Figure2: Pore network construction stages

## RESULTS AND DISCUSSION

Flow through the core sample described in section 3 was simulated using the model explained in section 2. Every simulation consisted of eighteen flow steps where brine and oil were injected simultaneously into the core. The medium was water wet and initially saturated with brine. At every step, the flow rates of brine and oil were increased or decreased depending on the type of flow process being simulated. Increasing oil flow rate while decreasing brine flow rate simulated drainage. On the other hand, increasing brine flow rate and decreasing oil flow rate simulated imbibition. In this work, two simulations were performed. Both simulations had the exact first nine steps, where drainage was maintained. However, for the final nine steps, the flow rate of brine was increased hundred times in the second simulation, compared to that of the first simulation. The first and second simulations are referred to as Sim.1 and Sim.2. The flow rates and the capillary numbers of each simulation can be seen in Table 2.

Table 2: Flow rates and capillary numbers of Sim.1 and Sim.2

Flow step	Oil flow rate (Sim.1, Sim.2) (m <sup>3</sup> /s)	Brine flow rate (Sim.1) (m <sup>3</sup> /s)	Brine flow rate (Sim.2) (m <sup>3</sup> /s)	Oil capillary number (Sim.1, Sim.2)	Brine capillary number (Sim.1)	Brine capillary number (Sim.2)
1	1.667E-11	1.667E-09	1.667E-09	2.78E-06	3.65E-04	3.65E-04
2	8.333E-11	8.333E-10	8.333E-10	1.39E-05	1.82E-04	1.82E-04
3	1.667E-10	3.333E-10	3.333E-10	2.78E-05	7.29E-05	7.29E-05
4	3.333E-10	1.667E-10	1.667E-10	5.55E-05	3.65E-05	3.65E-05
5	6.667E-10	8.333E-11	8.333E-11	1.11E-4	1.82E-05	1.82E-05
6	1.333E-09	3.333E-11	3.333E-11	2.22E-04	7.29E-06	7.29E-06
7	1.667E-09	1.667E-11	1.667E-11	2.78E-04	3.65E-06	3.65E-06
8	3.333E-09	1.667E-11	1.667E-11	5.55E-04	3.65E-06	3.65E-06
9	6.667E-09	1.667E-11	1.667E-11	1.11E-03	3.65E-06	3.65E-06
10	3.333E-09	3.333E-13	3.333E-11	5.55E-4	7.29E-08	7.29E-06
11	1.667E-09	6.667E-13	6.667E-11	2.78E-04	1.46E-07	1.46E-05
12	8.333E-10	1.333E-12	1.333E-10	1.39E-04	2.92E-07	2.92E-05
13	3.333E-10	1.667E-12	1.667E-10	5.55E-5	3.65E-07	3.65E-05
14	1.667E-10	3.333E-12	3.333E-10	2.78E-05	7.29E-07	7.29E-05
15	8.333E-11	6.667E-12	6.667E-10	1.39E-05	1.46E-06	1.46E-04
16	3.333E-11	1.333E-11	1.333E-09	5.55E-06	2.92E-06	2.92E-04
17	1.667E-11	1.667E-11	1.667E-09	2.78E-06	3.65E-06	3.65E-04
18	0.000E0	3.333E-11	3.333E-09	0.000E0	7.29E-06	7.29E-04

## FIRST SIMULATION - LOW FLOW RATE IMBIBITION

The first simulation is performed sequentially starting with the first step. Displacements are carried out until a steady state is achieved and no more changes are possible to the network fluid occupancy map. The capillary pressure ( $P_c$ ), relative permeability ( $K_r$ ), brine saturation ( $S_w$ ), and occupancy per element of both oil and brine are written in output files, and then the solver proceeds to the second step. This algorithm is executed until all 18 flow steps are successfully simulated. The relative permeability curves of Sim.1 are presented in Fig. 3. Each point on Fig. 3 represents one flow step.  $S_w$  starts at around 82%, and drops to around 32% (initial brine saturation) at the end of drainage, then increases to 58% at the end of imbibition (residual oil saturation of 42%). The maximum  $K_{rw}$  exists at the first computed point of drainage (around 0.5), while the maximum  $K_{ro}$  occurs at the end of drainage (around 0.85). Fig. 3 shows that for a given saturation,  $K_{rw}$  and  $K_{ro}$  are, as expected, larger during drainage than during imbibition.

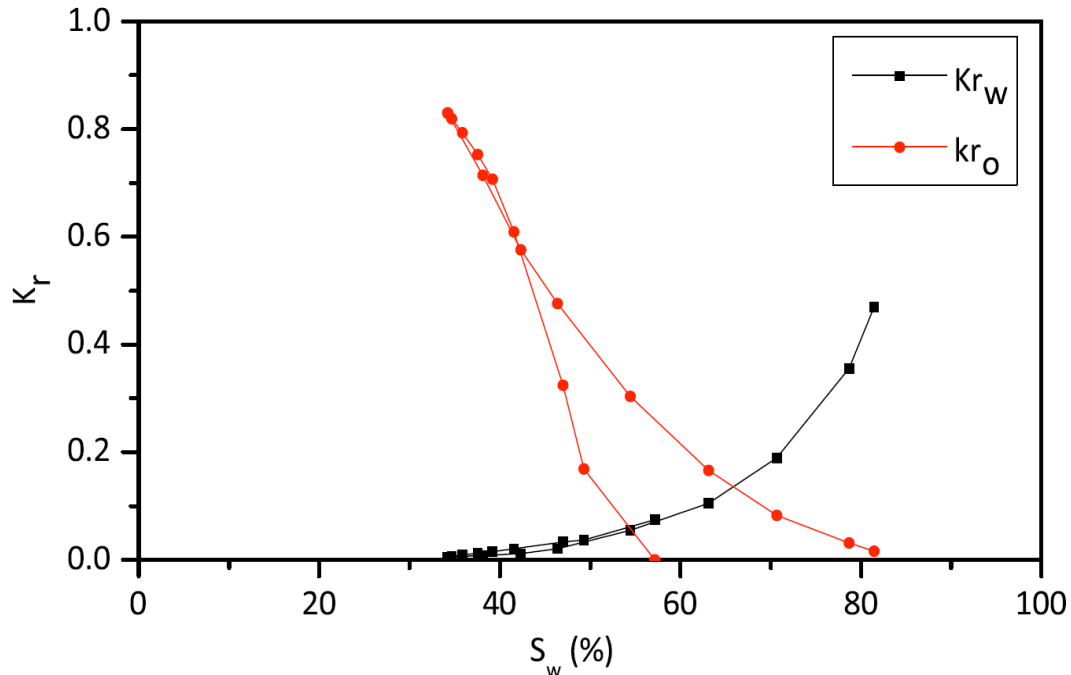


Figure 3: Relative permeability curves (Sim.1)

As stated earlier, the model writes out results files that hold the occupancy of each element (pore and throat) at the end of each flow step. The core sample is sectioned into 100 slices, and for each slice  $S_w$  and  $S_o$  are calculated for the matrix alone and the fracture alone portions (The saturation values were derived only using the center phase in the elements, and hence the results differ from those portrayed in Fig. 3. Since this is our first work in this field, the saturation profiles are used to compare trends, rather than actual values. Accurate saturation profiles which consider corner wetting phases, are in progress, and would be included in future work). Fig. 4 displays variations of  $S_w$  versus

the distance from the inlet for the matrix and the fracture, at the end of drainage and imbibition processes. As it is seen in this figure, the data of the fracture ends at a distance of 2 mm, which is the total length of the fracture network.

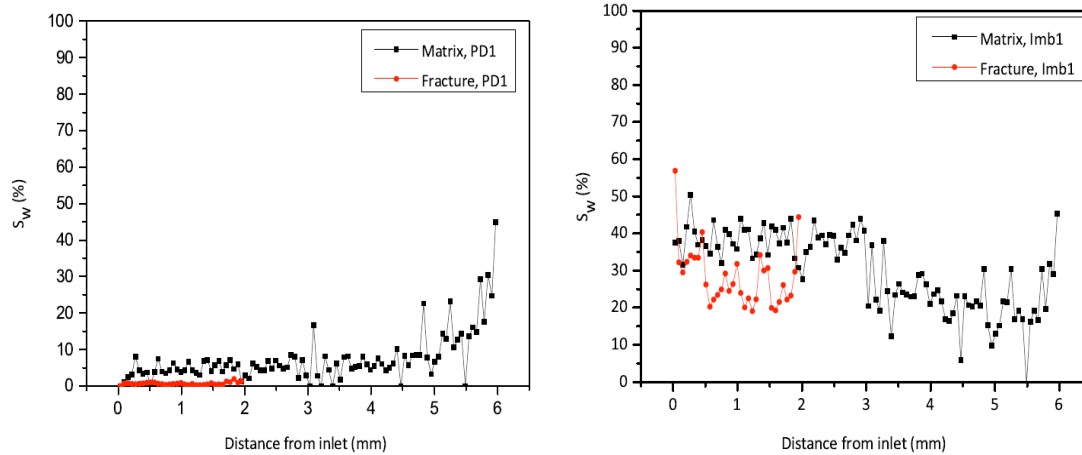


Figure 4: Water saturation ( $S_w$ ) versus distance from the inlet for Sim.1

When considering drainage, it is expected that  $S_w$  will decrease in the network, since oil is displacing brine. Fig. 4-a shows that  $S_w$  drops to around 0% within the fracture, after drainage is complete, while  $S_w$  drops to around 5% in the region of the matrix closer to the inlet, but reaches values as high as 45% in the regions farther away from the inlet. This saturation profile is dependent on the aperture and pore size distributions in the fracture and matrix, respectively. During drainage, the largest elements are invaded first, due to their low threshold capillary pressure. The fracture includes large apertures (larger than the matrix pores), and hence it is favored for invasion by the oil. The final  $S_w$  in the fracture will be very close to 0% as the fracture is invaded completely by oil and brine only maintains wetting layers on the walls of the fracture, while brine remains in some pores and throats of the matrix depending on the oil flow rate, pore size distribution, and rock and fluid properties. In addition, as the oil flows through the network, it loses its viscous potential and hence the region of the matrix farthest away from the inlet will experience fewer displacements than those located closer, leading to a  $S_w$  being as large as 45% in regions close to the outlet.

Similarly, when considering imbibition, it is expected that  $S_w$  will increase in the network, since brine is displacing oil. Fig. 4-b shows that  $S_w$  increases to only 30% in the fracture due to swelling of brine layers and snap-off mechanism that occurs in areas with small apertures.  $S_w$  in the matrix increases to around 40% in the sections closer to the inlet, and it drops to 20% in the regions farther away from the inlet. For imbibition, smaller pores are invaded first and hence the matrix is favored over the fracture when brine is displacing oil, and this leads to the matrix having higher  $S_w$  than the fracture. For the regions farther away from the inlet, the same reasoning for the lower  $S_w$  applies; the flow loses its viscous potential to invade the pores away from the injection site.

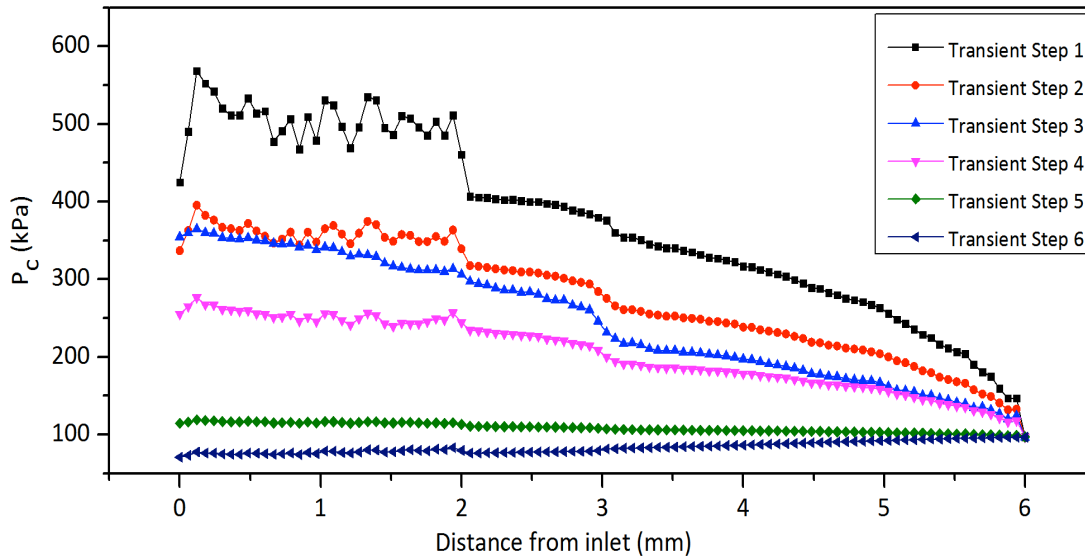


Figure 5: Capillary pressure ( $P_c$ ) versus distance from the inlet (Sim.1)

As mentioned earlier, the difference between matrix pore sizes and the fracture apertures is the main factor affecting the differences in  $S_w$ . This becomes evident when the variation of capillary pressure with time is visualized. Fig. 5 shows the drainage capillary pressure  $P_c$  values versus the distance from the inlet, plotted for several time steps during the transient stage when displacements are still being carried out. The presence of the fracture within the matrix, and its subsequent effect on  $P_c$  is evident in the sharp drop of  $P_c$  in Fig. 5 "Transient Step 1", at a distance of 2 mm, which is exactly the length of the fracture. This happens because oil pressure is high at the inlet which causes a high capillary pressure.  $P_c$  experiences minimal drop within the fracture due to the large aperture, which does not reduce viscous pressure significantly. However, throughout the matrix, viscous pressure of oil drops, which leads to a drop in  $P_c$ . As displacements are carried out, the system approaches steady state and  $P_c$  decreases, until it eventually becomes uniform throughout the core at around 50 Pa.

## SECOND SIMULATION - HIGH FLOW RATE IMBIBITION

The second simulation proceeds in a similar manner as that of Sim.1, with the first nine flow steps being identical. Hence, at the end of drainage, the  $S_w$  profile was exactly the same as that seen in Fig. 4-a. However the flow rate for steps 10 through 18 for Sim.2 were 100 times larger than those of Sim.1. This meant that the results of this imbibition test were going to be different, and this can be seen in Fig. 6 that is a plot of  $S_w$  versus the distance from the inlet for the matrix and the fracture at the end of imbibition.

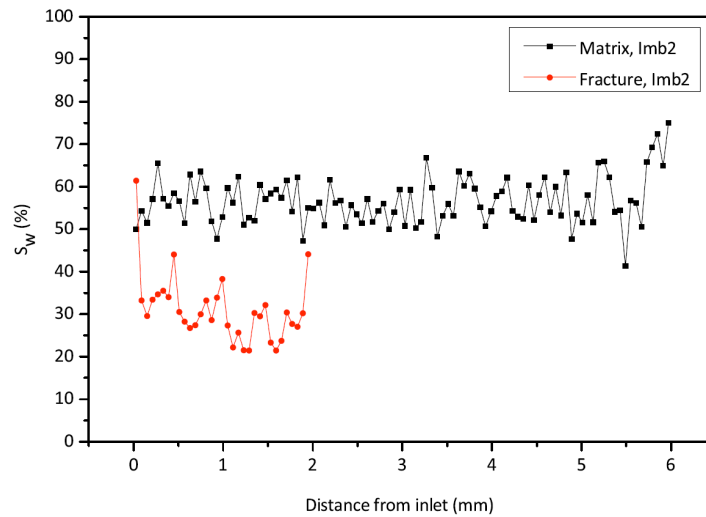


Figure 6: Water saturation ( $S_w$ ) versus distance from the inlet, for imbibition (Sim.2)

Fig. 6 shows that  $S_w$  of the fracture is around 30% while that of the matrix is around 60% throughout the length of the core. The increase of flow rate in Sim.2 did not lead to a significant increase in  $S_w$  of the fracture, but caused  $S_w$  in the matrix to increase from 40% to 60% in the regions close to the inlet, and from 20% to 60% in the regions away from the injection site. This means that  $S_w$  in the matrix is not just greater, but more uniform across the length of the medium, when comparing the results of Sim.1 and Sim.2. The increased flow rate had enough viscous potential to uniformly displace the oil from the matrix. However, for the fracture, the increase in flow rate was not able to increase  $S_w$ , because the flow rate is still not large enough to overcome the threshold capillary pressure of the large aperture of the fracture. The increased flow rate might have caused the wetting brine layers in the fracture to swell, but not significantly enough to increase  $S_w$  appreciably.

## CONCLUSION

In this study we utilized a fully dynamic pore network model to simulate drainage and imbibition processes in a fractured core, represented by a single pore network. The model utilized accounted for viscous, gravitational, and capillary effects. The pore network was constructed using micro-CT images of matrix and fracture in an actual fractured core sample. It was generated by connecting separate matrix and fracture pore networks. We performed two flow simulations each including drainage and imbibition steps. We used identical drainage steps in simulations to establish the same initial brine saturation distributions before inset of imbibition tests. The imbibition flow rates were significantly different. It was shown that at the end of drainage, the fracture was almost fully saturated with oil, while the matrix had some brine left in the corners and small pores ( $S_w$  of 5%). However after imbibition, the fracture  $S_w$  was resistant to changes in flow rate. For both simulations,  $S_w$  in the fracture was approximately 30%. On the other hand, water saturation in matrix showed significant sensitivity to changes in imbibition flow rate,

increasing from 20-40% to 60% from Sim.1 to Sim.2. Furthermore, water was distributed more uniformly throughout the length of the core at the end of imbibition in Sim.2. This was thought to be due to the increased flow providing sufficient pressure to establish efficient oil displacements in the entire core. It was shown that the presence of the fracture within the matrix increases  $P_c$ . A distinct change in  $P_c$  was observed along the medium where the fracture was present.

## ACKNOWLEDGEMENTS

We gratefully acknowledge financial support of FEI, Saudi Aramco, Hess Corporation, and the School of Energy Resources at the University of Wyoming.

## REFERENCES

- [1] Aghaei, A. and Piri, M., “Direct pore-to-core up-scaling of displacement processes: Dynamic pore network modeling and experimentation”, *Journal of Hydrology*, 2015.
- [2] Karpyn, Z. T. and Piri, M., “Prediction of fluid occupancy in fractures using network modeling and x-ray microtomography. I: Data conditioning and model description”, *Physical Review E*, 2007.
- [3] Arshadi, M. and Khishvand, M. and Aghaei, A. and Al-Muntasheri, G. A. and Piri, M., “Micro-Scale Investigation of Matrix-Fracture Interactions in Fractured Porous Media”, *Physical Review E*, 2016.
- [4] Blunt M, “Flow in porous media--- pore-network models and multiphase flow”, *Current Opinion in Colloid & Interface Science*, 2001.
- [5] D. Wildenschild and AP. Sheppard, “X-ray imaging and analysis techniques for quantifying pore-scale structure and processes in subsurface porous medium systems.”, *Advances in Water Resources*, 2014.
- [6] Dong H, “Micro-CT Imagin and Pore Network Extraction”, *Imperial College London*, 2007.

# EFFECTIVE THERMAL CONDUCTIVITY ASSESSMENTS OF AN OIL SAND RESERVOIR

James Arthur<sup>1</sup>, Evgeny Skripkin<sup>2</sup>, Sergey Kryuchkov<sup>1,2</sup> and Apostolos Kantzas<sup>1,2</sup>

1. PERM Inc. / TIPM Laboratory, Calgary, AB, Canada.

2. Department of Chemical and Petroleum Engineering, University of Calgary, Calgary, AB, Canada.

*This paper was prepared for presentation at the International Symposium of the Society of Core Analysts held in Snow Mass, Colorado, USA, 21-26 August 2016*

## ABSTRACT

In order to properly assess the effective thermal conductivity of an oil sand reservoir undergoing thermal production, adequate mixing rules that incorporate grain statistics, porosity, and relative contributions of the saturations and thermal conductivities of the constituent fluids and solids, are required. However, such a requirement is often not adequately met because it can result in a considerable volume of costly physical tests with limited application. In this work, a method consisting of a combination of physical experimental tests and numerical computations is used to provide a resolution to the problem. The proposed method shows how adequate mixing models may be generated in a timely and cost-effective manner and used for specific oil sand reservoir applications. To achieve this goal, using a recently developed thermal conductivity measurement approach, a limited number of thermal conductivity tests are also conducted on oil sand samples to provide effective thermal conductivities of multi-fluid phase combinations. Additionally, porous pattern generation algorithms together with geometry-based meshing and heat transfer computational physics, are used to develop a model that includes particle size distribution as a parameter. The evaluations of both physical and numerical tests are then used to develop and demonstrate robust effective thermal conductivity models. The results show that using a combination of selected tests and computations, adequate mixing rules can be developed that predict effective thermal conductivity for an oil sand thermal reservoir. In the particular example demonstrated, a combination of a numerical sigmoid model and empirical models are generated to sufficiently account for grain distribution, porosity, and relative contributions of the saturations and thermal conductivities of the constituent fluids and solids.

## INTRODUCTION

A proper assessment of effective thermal conductivity is a requirement for an adequate assessment of the heat transfer effects of oil sand reservoirs undergoing thermal production. However, such a determination is often complicated by the multiple factors associated with porous media. While some mixing models have been proposed in the literature (Evgeny 2015), they typically have serious limitations, making it necessary for the conduct of an array of physical tests to cover a wide range of parameters such as grain

distribution, porosity, and relative contributions of the saturations and thermal conductivities of the reservoir materials. Physical testing on the other hand, can also be a challenging task, giving the very intricate nature of porous media materials. In this work, a solution to the above mentioned problems is presented for which adequate mixing models may be generated in a timely and cost-effective manner and yet applicable for specific and varied oil sand reservoirs.

### Analytical Justification

Assuming conduction as the main means of heat transfer in a multicomponent porous media system, its effective thermal conductivity  $k_{eff}$  at a given sample temperature can be defined in multi-dependent terms such as the following

$$k_{eff} = f(k_s, k_{fi}, \varepsilon, \text{parameter for particle size distribution (PSD)}, S_i, \text{wettability factors}) \quad (1)$$

where,  $k_s$ ,  $k_{fi}$ ,  $\varepsilon$  and  $S_{fi}$ , are respectively the thermal conductivity (in W/m/K) of the solid phase, the thermal conductivity (in W/m/K) of a fluid component  $i$ , the total porosity of the porous medium and the saturation of a fluid component  $i$ . The symbol  $f$  represents the functional relationships between the parameters. The sheer number of factors in equation (1) does not only suggest the complexity of the heat transfer phenomena in view, but also the volumes of experimental tests required to adequately characterize the system.

However, if such a system is limited to a porous medium saturated with a single fluid component and a given PSD, equation (1) may be streamlined to

$$\frac{k_{eff}}{k_f} = f\left(\frac{k_s}{k_f}, \varepsilon\right) \quad (2)$$

With such a simplification, estimates of effective thermal conductivity are possible through analytical derivations. The result of such have been some effective thermal conductivity models (*e.g.* Kunii and Smith 1960, Krupiczka 1967). The limitation of such models however, is that they may not be applicable for the reservoir's PSD. However, with computational physics modelling, it is possible to obtain an equation such that

$$\frac{k_{eff}}{k_f} = f\left(\frac{k_s}{k_f}, PSD\right) \quad (3)$$

Furthermore, while it may be computationally expensive to consider wettability and saturation effects, it is possible to use experiments to discern these effects in multi-fluid considerations. Previous measurements (Somerton 1990) show that a polynomial relation exists and may be defined for a limited range of tests of appropriate spread. From this, it is reasonable to hypothesize the following form of mixing rule for the thermal conductivity of a multi-fluid porous medium

$$k_{eff} = k_{eg}S_g^\alpha + k_{eo}S_o^\beta + k_{ew}S_w^\gamma \quad (4)$$

In equation (4) subscripts  $S_g$ ,  $S_o$  and  $S_w$  are saturations of gas, oil and water respectively; and  $k_{eg}$ ,  $k_{eo}$ ,  $k_{ew}$  are the effective thermal conductivities (in W/m/K) of porous medium of the same solids component when fully saturated with single fluid components gas, oil and

water respectively. The parameters  $\alpha$ ,  $\beta$ , and  $\gamma$  are saturation exponential constants which may be tuned to fit a given set of empirical data to give a measure of wettability.

The above analysis infers then that it is possible to contrive adequate models of effective thermal conductivity considering PSD by: (a) Sampling portions of the reservoir and determine the PSDs of representative zones; (b) Conducting thermal conductivity tests of constituent fluids of the reservoir if it is established that there are multiple PSDs identified in the reservoir; (c) Testing sand packs of similar PSD and porosity to determine the effective thermal conductivity  $k_{ei}$  when respectively fully saturated with each constituent fluid (if the sand grain mineralogy is unknown); (d) Testing for effective thermal conductivities for at least 3 varying but known saturations; (e) Undertaking a parametric numerical study to determine porosity effects; and (f) Repeating steps (c) to (e) for any additional PSD consideration. Utilizing such a method can reduce test experiments (and its related time and money costs) by more than half when a pair of PSDs are at play in a reservoir, and by far more when more PSDs are considered. In the following sections the method is briefly described, followed by a sample demonstration.

## MEASUREMENT AND NUMERICAL APPROACH

An important aspect of the assessment of effective thermal conductivity is the conduct of tests that provide reliably accurate data. To this end, the present approach was to use two different apparati that conduct heat radially or axially respectively through a standard material, and then through the test medium, under steady state conditions. The power input and temperature distribution across multiple collinear locations in the test section are measured. The thermal conductivity is then determined through numerical analyses. The distinctive feature of this approach is that it accommodates various forms and shapes of samples, and at more realistic reservoir conditions. Furthermore, this approach uniquely allows for the accurate assessment of the physics of the set-up by using a detailed real-size dimensioned numerical analyses that solves the thermal-fluid flow field. Schematic arrangements of the radial and axial systems are shown in Figure 1. A more comprehensive description of the test systems is described in Arthur *et al.* (2015). In that work, the accuracy and reliability of data are demonstrated.

Current computational resources have opened up the possibility of modelling detailed fluid flow and heat transfer assessments on a porous medium at pore scale level. To do this however involves the generation of an adequate virtual geometry. In this study, a pattern generation approach was used in generating that virtual porous media. The pattern generation method is executed by an algorithm that fills a box of a given size with rigid spheres of radii from a specific particle size distribution. The spheres are added on by a simultaneous generation procedure (called particle swelling). Starting points are randomly distributed along with designations of growth (swelling) rate at each point. The sphere radii are increased iteratively from point to final value according to the assigned growth rate until the target porosity is reached without any conflict. The result of this algorithm is a porous medium pattern, as shown in Figure 2. This is then meshed using an appropriate meshing software that is preferably geometry-based. In this work, all meshing and computational solutions were obtained using COMSOL Multiphysics considering only single fluid and single solid phases. Each phase is taken to be isotropic

in heat transfer, and the heat equation is then numerically solved under requisite assumptions. The effective thermal conductivity is then calculated through Fourier's law. In a thorough review and assessment, Skripkin (2015) has shown that using the right configuration, this method is capable of generating accurate and valid results.

## **SAMPLE TEST PROGRAM**

The aims of the current study are met in a sample test program. The tests were conducted using one synthetic and one reservoir oil sand from three different sources obtained from in-house inventory. The constituent fluids were that of water, air and light oil for the synthetic oil sand, and formation water, air and dewatered bitumen of 7.29°API for the reservoir sample. The sand grain sizes were measured using an AS 200 vibratory sieve shaker. In the present tests, preliminary review showed no evidence of PSD variability in sample source, implying no need to conduct studies to determine the effect of PSD. However, the utility of the method described in this work shows that the necessary tests identified in the analyses conducted earlier for the constituent reservoir materials, and for selected saturations of the porous media. Thermal conductivities of the constituent fluids and porous media were determined at 25°C sample temperature using the integrated measurement approach. Where required, saturations were determined using nuclear magnetic resonance or Dean-Stark extraction analyses. The utility of the porous pattern generation numerical approach was tested using input of PSD to show how this can be used to determine the effects of PSD and porosity.

## **RESULTS AND DISCUSSION**

Results indicate that at 25°C, the thermal conductivities of light oil and bitumen are 0.13 and 0.17 W/m/K respectively. The results of de-ionized water and 0.33M NaCl solution. All of these data are comparable with published results (Arthur *et al.* 2015). Having determined the thermal conductivities of the constituent fluids, oil sands at selected fluid saturations of the oil sand were tested for effective thermal conductivity. The results are plotted against the saturation of water  $S_w$  and oil  $S_o$  in Figure 3. In Figure 3(a) in particular, plots indicate a non-linear relationship between the effective thermal conductivities and the wetting saturation for values obtained at a porosity value of 46%. Testing the hypothesized equation (4), the parameters  $\alpha$ ,  $\beta$ , and  $\gamma$  were set at 0.1, 0.01 and 0.85 respectively. While the physical meaning of these empirical values are not totally clear, it is possible that these are related to the contact between the fluid and solid grains. The values fit the data plots optimally with a maximum deviation of 10% between data points and the model.

In an earlier analytical justification, the need to obtain measurements at the same porosity was emphasized. However, the result of mixing model in equation (4) is demonstrably not a factor of porosity. This is proven in Figure 3(b) where despite the variation of porosity of the tests (38% to 48%), the results depicted a functional relationship described by equation (4). This means that equation (4) is an incomplete model when it comes to predicting effective thermal conductivity in response to porosity changes. Regardless, for this specific case shown in Figure 3(a), it was determined that

equation (4) curve fit was best suited when parameters  $\alpha$ ,  $\beta$ , and  $\gamma$  were set at 0.1, 0.90 and 0.75 respectively. While such a result suggests that parameters  $\alpha$ ,  $\beta$ , and  $\gamma$  may be saturation / wettability indicators, this is something to be explored in a future study.

To complete the effective thermal conductivity model, numerical experiments may be carried out with the aid of a porous pattern generation method using a typical PSD as an input parameter. The results (Figure 4a) show that the effective thermal conductivity for a single fluid component oil sand  $k_{ei}$  is related to constituent fluid and solid components thermal conductivity (*i.e.*  $k_i$ ,  $k_s$  respectively) through the following sigmoid function

$$k_{ei} = \frac{g}{h + e^{-\left(c \ln(k_s/k_i)\right)}} \quad (5)$$

Where  $c$ ,  $g$  and  $h$  are constants that can be determined through analyses. Of note, the result of equation (5) follows the form expressed in equation (3). Additionally, the implication then is that if constants  $c$ ,  $g$  and  $h$  are known as well as input measurement results of  $k_{ei}$ ,  $k_i$ , and  $k_s$ , then  $k_{ei}$  (for every related fluid component  $i$ ) can be determined using equation (5) without measurement, reducing cost of time and money. Furthermore, results showed that for a given PSD, there is a linear relationship between effective thermal conductivity and porosity at the porosity of interest ( $0.38 \leq \varepsilon \leq 0.48$ ) so that

$$k_{eff} = A + B\varepsilon \quad (6)$$

where  $A$  and  $B$  are respectively constants in W/m/K units. It is pointed out that this result is reasonable as models in the literature of the form of equation (2) typically show that the relationship between effective thermal conductivity and porosity at that porosity of interest can be estimated to be linear with a good level of accuracy (coefficient of determination  $R^2 \geq 0.90$ ). Thus with equations (4) to (6), a complete set of mixing models is realized to predict the effective thermal conductivity of an oil sand, as desired in equation (1). This was done with a limited array of tests and numerical assessments.

## CONCLUSIONS

The study demonstrates a cost and time-effective method for determining effective thermal conductivity of an oil sand reservoir. This is achieved through a combination of a numerical sigmoid model and empirical models to sufficiently account for grain distribution, porosity, saturations and the thermal conductivities of reservoir materials.

## ACKNOWLEDGEMENTS

The financial contributions of Laricina Energy Ltd., Cenovus Energy, Alberta Innovates, Athabasca Oil Corporation, Devon, Barrick, Husky Energy, Foundation CMG, Dover Operation Corp., Schulich School of Engineering, NSERC-CRSNG, Maersk Oil and Suncor Energy through the FUR Chair held by Prof. A. Kantzas, are gratefully acknowledged.

## REFERENCES

1. Arthur, J., Akinbobola, O., Kryuchkov, S., and Kantzas, A. 2015. "Thermal Conductivity Measurements of Bitumen Bearing Reservoir Rocks" *SPE Canada Heavy Oil Technical Conference*, 09-11 June, Calgary, Alberta, Canada, SPE-174434-MS.

2. Krupiczka, R. 1967. "Analysis of thermal conductivity in granular materials." *International Chemical Engineering* 7 (1): 122-144.
3. Kunii, D., and Smith, J. M. 1960. "Heat Transfer Characteristics of Porous Rocks." *AIChE Journal* 6 (1): 71-78.
4. Skripkin, E. "Effective Thermal Conductivity of Porous Media: An Integrated Approach" (2015) *Master of Science Thesis*, University of Calgary.
5. Somerton, W. H. "Thermal Properties and Temperature-related Behavior of Rock/Fluid Systems" (1992) Amsterdam: Elsevier.

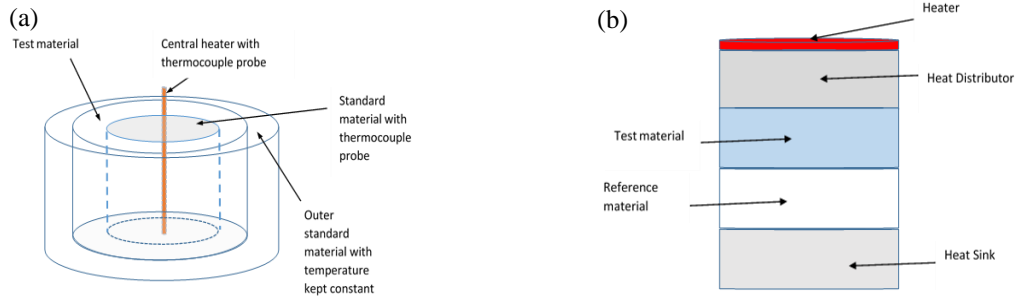


Figure 1: Typical arrangements of (a) radial and (b) axial testing apparatus.



Figure 2: Porous patterns generated in (a) two and (b) three dimensions.

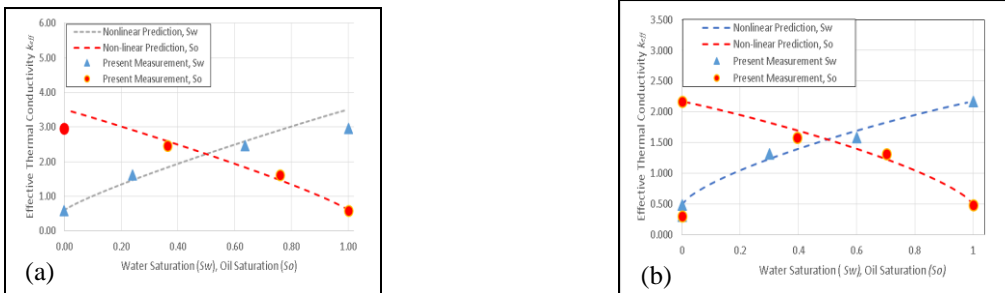


Figure 3: Results of tests for (a) synthetic oil sand and (b) real oil sand system

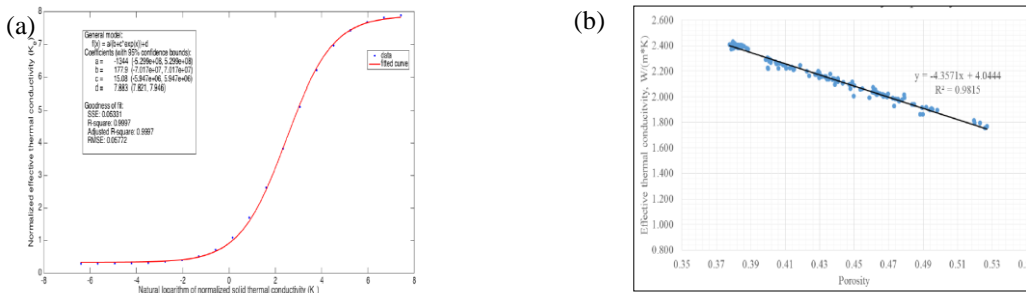


Figure 4 (a) Custom mixing rule generated for an oil sand (b) Porosity effects demonstrated.

## **Pore Shapes and Pore Geometry of Reservoir Rocks from $\mu$ -CT Imaging and Digital Image Analysis**

Matthias Halisch<sup>1</sup>, Mayka Schmitt<sup>1,2</sup>, Celso Peres Fernandes<sup>2</sup>

<sup>1</sup> Leibniz Institute for Applied Geophysics (LIAG), Dept. 5 Petrophysics & Borehole Geophysics, Stilleweg 2, D-30655 Hannover, Germany

<sup>2</sup> Federal University of Santa Catarina, Porous Media and Thermophysical Properties Laboratory (LMPT), Mechanical Engineering Department, 88040-900 Florianópolis, SC, Brazil

*This paper was prepared for presentation at the International Symposium of the Society of Core Analysts held in Snowmass, Colorado, USA, 21-26 August 2016*

### **ABSTRACT**

Recent years have seen a growing interest in the characterization of the pore morphologies of reservoir rocks and how the spatial organization of pore geometry affects the macroscopic behaviour of rock-fluid systems. With the availability of high-resolution 3D imaging, such as X-ray micro-computed tomography ( $\mu$ -CT), the detailed quantification of particle shapes has been facilitated by progress in computer science. Here, we show how the shapes of irregular rock structures (pores) can be classified and quantified based on binary 3D images. The methodology requires the measurement of basic 3D particle descriptors (length, width and thickness) and a shape classification that involves the similarity of artificial objects, which is based on main pore network detachment and 3D sample size. A watershed algorithm was applied to preserve the pore morphology after separating the main pore networks, which is essential for the pore shape characterization. The results were validated for a variety of sandstones, either from distinct reservoirs or used as reference material for laboratory research. Furthermore, this study generalizes a practical way to correlate specific particle shapes, such as rods, blades, cuboids, plates and cubes, to characterize asymmetric particles of any material type with 3D image analysis. In this manuscript we would like to showcase results for a small variety of reservoir sandstones from the North German Basin area.

### **INTRODUCTION**

Natural and artificial materials are often characterized by their pore/grain shape or size distributions as determined by distinct analytical instruments. Several investigations have been conducted to classify pore types/shapes, and most of them are associated with 2D quantification. However, a 3D pore with irregular shapes cannot be appropriately characterized from 2D image sections in pore-typing procedures, nor can the number of pores (Buller et al., 1990). Knowledge of pore morphology is essential and is one of the main parameter that controls fluid flow at the pore scale.

Petrophysical properties such as permeability, electrical conductivity and drainage capillary pressure are strongly influenced by throat sizes, which are constrictions of minimal cross-sectional area between pores. Moreover, to the best of our knowledge, the systematic 3D pore shape quantification of sedimentary rocks based on sample size, pore network detachment and distinct geometrical descriptor measurements has not been comprehensively reported in the literature.

Though 3D imaging has become a reliable method for qualitative and quantitative pore scale characterization, many investigations that analyse irregular particle shapes are still performed with 2D approaches (Petruk et al., 2015; Zhang et al., 2016). So far,  $\mu$ -CT studies of 3D features have mostly been related to the characterization of volcanic rocks (Eiríksson et al., 1994; Riley et al., 2003) or spheroid objects (Robin & Charles, 2015), and these features are usually described by means of equivalent size or shape parameters, such as roundness or aspect ratio (Little et al., 2015). All of these authors concluded that these measurements cannot adequately describe the diverse forms of irregularly shaped particles. Available high-resolution techniques might provide qualitative and quantitative pore structure information. However, many materials, including sedimentary rocks, lack information regarding the deep comprehension of irregular particle (pore or grain) shape analysis and a systematic way of classifying it, e.g., describing it to be similar to artificial object forms. A detailed pore shape characterization is necessary for many applications and can be used to infer the dominant mechanisms that act in a heterogeneous rock in response to its macro properties.

## **SAMPLES & METHODOLOGY**

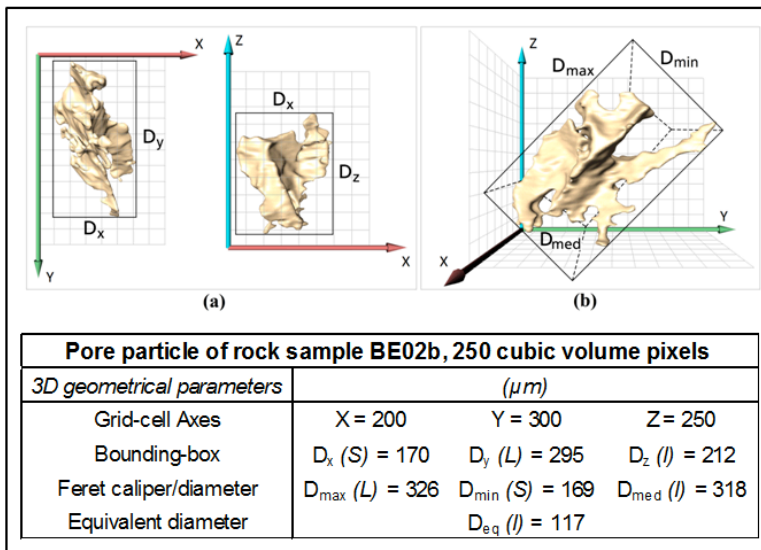
In this study, the pore shapes of three sandstone rocks from distinct fields in Germany were analysed and classified based on X-Ray  $\mu$ -CT and digital image analysis. The sandstone samples (Bentheimer, Obernkirchen and Flechtingen sandstone) have been used and characterized in previous studies in detail (Halisch et al., 2013, 2015). The 3D images of the analysed rocks were acquired at similar scanning resolutions (1.5  $\mu$ m voxel size). A watershed algorithm was applied to separate the main pore networks into individual pores and to preserve the essential pore morphology. Next, the most suitable marker extent parameter was defined. Three subsamples with volumes of 1000<sup>3</sup>, 500<sup>3</sup> and 250<sup>3</sup> voxels were extracted from each rock to investigate the effect of sample sizes (representativeness) on the pore shape classification. The advantage of using the proposed approach is that shape parameters can be calculated directly from the preserved pore textures with no need for an equivalent volume (sphere or resistor) conversion, which creates absolutely mismatched results for the shape classification. Additionally, the image visualization and analysis are completely automated and performed with the Avizo Fire (Ver. 9.01) software suite for a large number of particles, which are geometrically described to facilitate the quantification analysis.

To describe and quantify a particle form (in this case: pores) in three-dimensions, morphological parameters such as length, width and thickness are required. These 3D parameters must be perpendicular (orthogonal) to each other but do not need to intersect

at a common point (Blott & Pye, 2008). To perform the pore shape classification approach that is proposed and described in this work, we conventionally assigned the following practice for the geometrical descriptor of individual particles: ( $L$ ) is the longest pore dimension, ( $l$ ) is the longest pore dimension that is perpendicular to  $L$ , and ( $S$ ) is the smaller pore dimension and perpendicular to both  $L$  and  $l$ . In practice, two methods were applied to measure  $L$ ,  $l$  and  $S$  from the 3D irregular shaped objects, such as the pores that were found in the analysed sedimentary rocks: (i) the bounding-box (BB) and (ii) the Feret caliper (FC) geometries. With this geometrical information, it is possible to perform pore shape classification for equancy based upon the different aspect ratios as described by Schmitt et al. (2016). Another common dimensional feature that is used to characterize the “thickness” of 3D particles is the equivalent diameter (EqD), also known as the maximum inscribed sphere method (Dong, 2007), which gives the analysed object a corresponding spherical diameter size with equal voxel volumes.

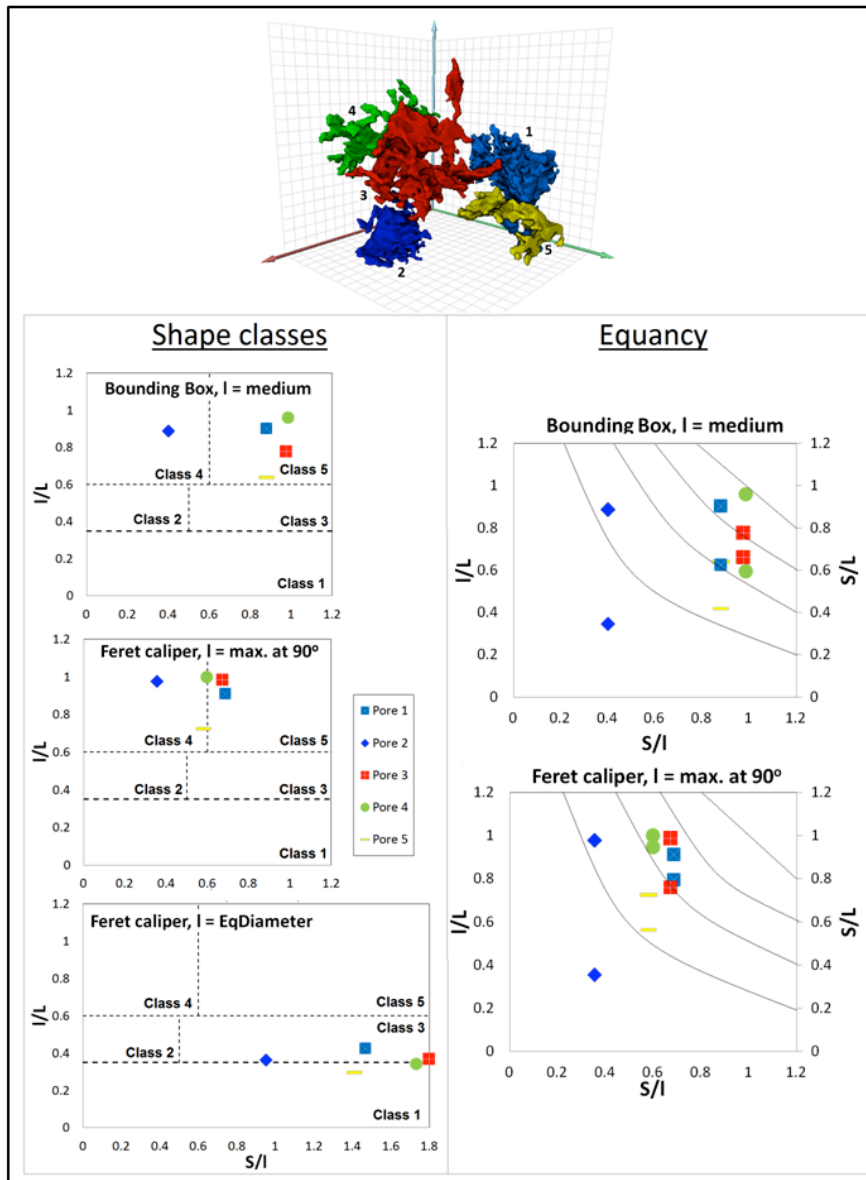
### RESULTS

Figure 1 shows the differences in the geometrical parameters  $L$ ,  $l$  and  $M$  for bounding-box (a) and Feret caliper (b) methods, which are drawn in a three-dimensional pore particle. The showcased pore was detached from the main pore network of the Bentheimer sample after applying the watershed algorithm and choosing the third highest 3D lengths from the 25 highest 3D volume particles. The attached table depicts the values of the grid-cell axes and 3D geometrical parameters of the analysed pore particle. For BB methods, a box is assigned to each pore, with the box orientated parallel to the coordinate system of the 3D data set. FC methods assign an individual surrounding box to each separated pore, directly related to the true main elongation of the structure. The classical BB and EqD methods under estimate the pore geometry and the pore volume significantly in comparison to the FC methods. This result has been observed for any of the investigated reservoir rocks, since the true pore / particle orientation is only taken into account for the advanced FC methods.



**Figure 1:** Comparison of different results of the geometrical pore extent estimation for the classical bounding box methods (upper left, a) and Feret caliper methods (upper right, b) for a single pore of a Bentheimer sandstone.

Accordingly, the pore shape classification is also severely affected by using different pore geometry descriptors. Results of the pore shape classification of the five largest pores within a  $250^3$  voxel volume of the Obernkirchen sandstone sample are shown in figure 2. The right column of figure 2 shows the results of the equancy plots, determined by BB (upper plot) and FC (lower plot) methods. Whereas BB methods lead to mostly slightly non-equant and moderately non-equant shapes (upper right and right corner of the plot), FC methods shift towards moderately non-equant and very non-equant shapes (right corner and middle of the plot). More importantly, the aspect ratios change significantly.



**Figure 2:** Pore shape results of equancy (right column) and shape classes (left column) based on different descriptors for five selected pores in a  $250^3$  voxel volume of Obernkirchen sandstone.

Furthermore, the left column of figure 2 shows the results for the shapes classes, determined by BB, FC and EqD methods. BB descriptors lead to mostly cubic/spherical-like pore shapes (upper right corner of the shape plot), FC descriptors shift towards more plate-like shapes which estimate the true pore shapes much better, related to the 3D pore scale image on top of figure 2. EqD descriptors completely mismatch the true shape and lead to cuboid/ellipsoid/rod-like pores (lower right corner of the shape plot).

Very similar results have been observed for all of the investigated sandstone samples within this study. The classical BB and EqD descriptors always tend to underestimate the pore geometry. The study has shown that the mismatch for “well defined pore networks”, i.e. Bentheimer or Berea type rocks, is about 10 % - 18 % off the true axial geometry. The more “complex”, i.e. the more irregular shaped the individual pore gets, which is mostly the case for (e.g.) more compacted or layered rocks, the higher the geometrical mismatch will be for these methods. In case of the Flechtingen sandstone, a mismatch of up to 200 % has been measured. The FC methods still have a slightly mismatch against the true geometry, but within this study, it never exceeded  $\pm 20$  %. Accordingly, the resulting aspect ratios and shape classes are influenced in the same way for most of the investigated 3D volumes as described in the section above, which might lead to significantly falsified geometrical pore network characterizations.

## **SUMMARY & CONCLUSIONS**

Within this study we have investigated different methods to determine pore geometrical descriptors from binarized 3D pore scale imaging data sets. Additionally, we have created a pattern of shape classes that might be used for the enhanced classification of pore shapes. We have showcased the differences for the existing methods, as well as the significant impact upon the results. It can be concluded that BB and EqD methods are not the appropriate choice to characterize both, pore shape and geometry reliably. Accordingly, Feret caliper methods have shown the smallest deviation against the “true” pore characteristic of the investigated sandstones.

## **OUTLOOK**

As part of an ongoing research project, more and more types of sandstones from conventional and unconventional reservoirs are investigated. Consequently, other rock types like carbonates and claystones are included within the near future. The two main goals of this project are to “connect” topological pore features, such as surface area or fractal dimension, to corresponding pore classes. In a second step, these relationships will be used to calculate and characterize pore class dependent petrophysical properties, e.g. like pore class dependent  $T_2$ -diffusion mapping. First results are already promising.

## **ACKNOWLEDGEMENTS**

The authors would like to thank Mrs. Cornelia Müller and Mrs. Juliane Herrmann for support with the CT imaging and figure creation. Furthermore we would like to thank Conselho Nacional de Desenvolvimento Científico e Tecnológico (CNPq) of the Ministry of Science, Technology and Innovation of Brazil for granting a two year research stipend, grant no. 207204/2014-4.

## REFERENCES

1. Buller, A.T., Berg, E., Hjelmeland, O., Kleppe, L., Torsaeter, O., and Aasen, J.O. (1990): *North sea oil & gas reservoirs – II*. Graham and Trotman Publishing, London, 234-237, 1990.
2. Blott, S.J., and Pye, K. (2008): *Particle shape: a review and new methods of characterization and classification*. *Sedimentology*, 55, 31-63
3. Dong, Hu (2007): *Micro-CT Imaging and Pore Network Extraction*. PhD Thesis, Imperial College London, 2007.
4. Eiríksson, J., Sigurgeirsson, M., and Hoelstad, T. (1994): *Image analysis and morphometry of hydromagmatic and magmatic tephra grains, Reykjanes volcanic system, Iceland*. *Jökull*, 44, 41-65.
5. Halisch, M., Vogt, E., Müller, C., Cano-Odena, A., Pattyn, D., Hellebaut, P., and van der Kamp, K. (2013): *Capillary Flow Porometry - Assessment of an alternative method for the determination of flow relevant parameter of porous rocks*. Proceedings, Annual Meeting of the Society of Core Analysts 2013, Napa Valley, USA, SCA2013-007.
6. Halisch, M., Linden, S., Schwarz, J.O., Hupfer, S., and Wiegmann, A. (2015): *Systematic parameter study for formation factor modeling at the pore scale*. Proceedings, Annual Meeting of the Society of Core Analysts 2015, St. John's, Canada, SCA2015-A018.
7. Little, L., Becker, M., Wiese, J., and Mainza, A.N. (2015): *Auto-SEM particle shape characterization: Investigating fine grinding of UG2 ore*. *Miner. Eng.*, <http://dx.doi.org/10.1016/j.mineng.2015.03.02>
8. Petrak, D., Dietrich, S., Eckardt, G., and Köhler, M. (2015): *Two-dimensional particle shape analysis from chord measurements to increase accuracy of particle shape determination*. *Power Technology*, 284, 25-31.
9. Riley, C.M., Rose, W.I., and Bluth, G.J.S. (2003): *Quantitative shape measurements of distal volcanic ash*. *J. Geophys. Res.* 108, 2504 ff.
10. Robin, P.Y.F., and Charles, C.R.J. (2015): *Quantifying the three-dimensional shapes of spheroidal objects in rocks imaged by tomography*. *Journal of Structural Geology*, 77, 1-10.
11. Schmitt, M., Halisch, M., Müller, C., and Fernandes, C.P. (2016): *Classification and quantification of pore shapes in sandstone reservoir rocks with 3D X-ray micro-computed tomography*. *Solid Earth*, 7, 285-300, 2016, doi:10.5194/se-7-285-2016
12. Zhang, Y., Liu, J.J., Zhang, L., De Anda, J.C., and Wang, X.Z. (2015). *Particle shape characterization and classification using automated microscopy and shape descriptors in batch manufacture of particules solids*. *Particuology*, <http://dx.doi.org/10.1016/j.partic.2014.12.012>

# EXPERIMENTAL STUDY ON DYNAMIC FRACTURES INDUCED BY WATER FLOODING IN LOW PERMEABILITY RESERVOIRS

Gao Jian<sup>1,2</sup>, Zhang Zubo<sup>1</sup>, Liu Qingjie<sup>1</sup>, Chenxu<sup>1</sup>, Qian Yuchen<sup>1</sup>, Jia Ninghong<sup>1</sup>, Tan Xiqun<sup>3</sup>

1. State Key Laboratory of Enhanced Oil Recovery, Research Institute of Petroleum Exploration and Development, Beijing, China; 2. National Engineering Laboratory for Exploration and Development of Low Permeability Oil and Gas fields, 3. RIED, PetroChina Changqing Oilfield Company, China

*This paper was prepared for presentation at the International Symposium of the Society of Core Analysts held in Snowmass, Colorado, USA, 21-26 August 2016*

## ABSTRACT

The behavior of water flooding in low permeability reservoirs is directly influenced by various fracture systems in the reservoirs including natural fractures, hydraulic fractures and dynamic fractures induced by water flooding. These impacts can lead to some unexpected consequences that highly reduce the oil recovery rate such as higher water cutting rate, low sweep efficiency and off-trend with the orientation of natural fractures.

With lots of intensive work having been done in the past about the impact of natural fractures and hydraulic fractures on oil recovery rate, little work has been done to reveal the mechanism of the dynamic fractures being induced and there exists too few experimental data to support the correlation between the behavior of dynamic induced fractures and the production rate.

In this work, an experimental method is established to simulate dynamic fracture induced by injecting water into core samples. It can be observed that fractures start being induced when water injection pressure is 0.7-3.2MPa higher than the overburden pressure and becomes stable at 1.0-5.0Mpa higher than the overburden pressure. Experimental measurements show that the induced fractures, with length scale mainly within micrometer, tend to grow in a plane pattern, with both fracture width and fracture pressure increase with water injection rate, which can also explain the reason that absolute permeability of core samples under water flooding is significantly enhanced by 5-30 times. On the other hand, the displacement efficiency of the induced fractures is about 9.8-25.5%, which is lower than that of matrix controlled flow ability, which is about 56-63%.

**Key words:** low permeability reservoirs; water flooding; dynamic fractures; core experiment

## INTRODUCTION

The behavior of water flooding in low permeability reservoirs is directly influenced by various fracture systems in the reservoirs including natural fractures, hydraulic fractures and dynamic fractures induced by water flooding. These impacts can lead to some unexpected consequences that highly reduce the oil recovery rate such as higher water cutting rate and low sweep efficiency.

Fan Tianyi in 2015 conceptualized dynamic fractures and based on abundant data of low permeability oilfields, studied their evolution, including cracking, extension and closure. With the gradual extension of dynamic fractures, the injection water forms a narrow range of displacement, which leads to the severe imbalance of water flooding, aggravates the heterogeneity of low permeability reservoirs, and possibility of sudden water influx in the reservoirs.

Guo Farong in 2015 believes that the dynamic fractures in low permeability reservoir and hydraulic fractures of oil well all distribute along the high main stress, while water injection pushes the dynamic fracture to propagate continuously, flooding the main oil wells, and forming a regular pattern of cracks in the plane line.

Wang Youjing in 2015 believes that dynamic fractures refer to the new-generated fracture channels when bottom hole pressure exceeds rock breakdown pressure and propagation pressure. His study shows that the dynamic fractures changed the seepage characteristics of water displacing oil in the low permeability reservoir, aggravated the reservoir heterogeneity, which led to the reduction of profile producing degree and the distribution of remaining oil on both sides of the fractures in continuous or discontinuous belts.

According to site research carried out by Xie Jingbin in 2015 on Chang6 reservoir, Ansai oilfield, the opening pressures of dynamic fractures are 20-23 MPa. The dynamic fractures aggravate the reservoir heterogeneity and cause the quick water flooding along the current maximum horizontal major stress direction, which reduces the producing degree horizontally and vertically and influences the reservoir development effects.

Up to now, multiple researches have been carried out on the definition, genetic mechanism, parameter characterization and distribution prediction of natural fractures and hydraulic fractures through various ways. However, past studies on dynamic fractures induced by water flooding tend to focus on analyzing the communication between the production rate and the water injection rate.

## RESULTS

### **1. The establishment of water injection hydraulic fracture laboratory method**

Due to poor water absorption ability of low permeability reservoir, relatively high pressure at water injection well; during the actual injection process, the pressure at the bottom of the well is usually higher than the overburden pressure of the rock. The

conventional core holder, constrained by the design, can only simulate the situation when the overburden pressure is higher than the porosity pressure, but cannot simulate the situation when the bottom well pressure is higher than the overburden pressure. This laboratory approach constrains the simulation of low permeability oil well high pressure water injection process, leading to a gap in understanding seepage and displacement. The new approach introduced here installed sealing system on both sides of the conventional core holder, which helped to simulate the process when the injection pressure is higher than the overburden pressure. Below in Figure 1 is a diagram of the experimental apparatus. As is shown in Figure 2, the absolute permeability of core samples under water flooding is significantly enhanced by 5-30 times:

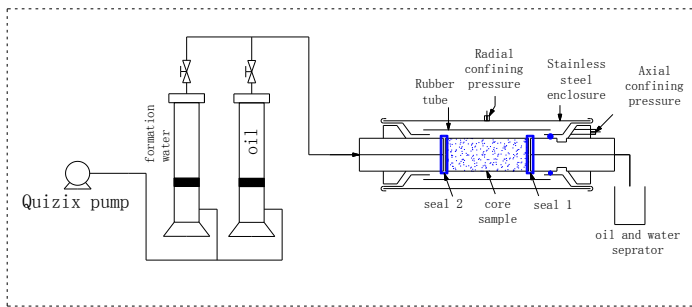


Figure 1: diagram of the experimental apparatus

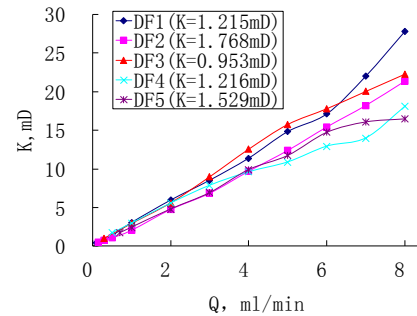


Figure 2: Dynamic fracture permeability vs flow

During the process, both injection pressure and overburden pressure data are collected, as in Figure 3. Meanwhile, the correlation between injection pressure and overburden pressure is shown along the time line, as in Figure 4. The curve mutation point  $\Delta P_A$  is breakthrough pressure of injection induced dynamic fracture;  $\Delta P_B$  is steady opening pressure of the dynamic fracture. After the fracture is open steadily, it remains stable.

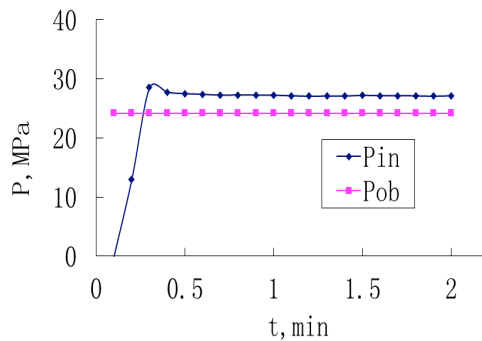


Figure 3: Injection pressure and overburden pressure curve

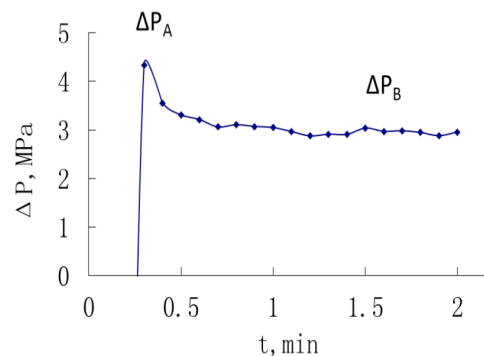


Figure 4: Injection pressure and overburden pressure difference curve along the time line

## 2. Pressure features of water injection dynamic fractures

Water flooding dynamic fracture stress analysis was carried out in two oilfields in Changqing. For Oil Field A, the oil field breakthrough pressure is 3.5-5MPa, and dynamic fracture open pressure is 2.8-3.4 MPa, as is shown in Figure 3. For Oil field B, the oil field breakthrough pressure is 3-4.5MPa, and dynamic fracture open pressure is 2-3MPa, see Figure 5-6.

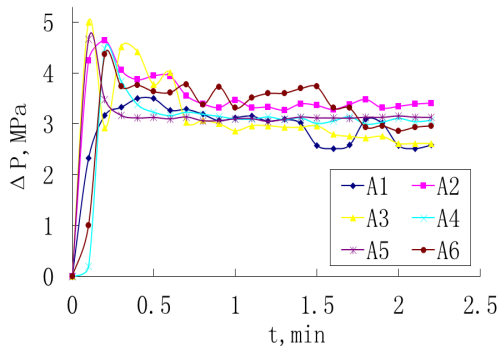


Figure 5: Oil field A-injection pressure and overburden pressure difference curve along the time line

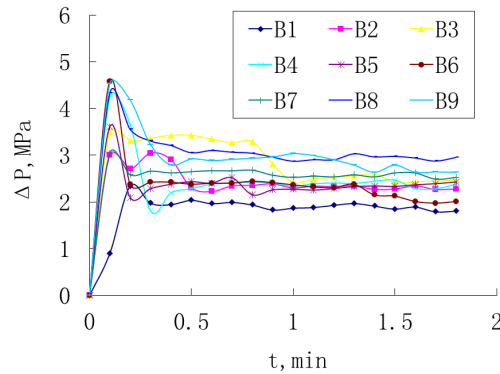
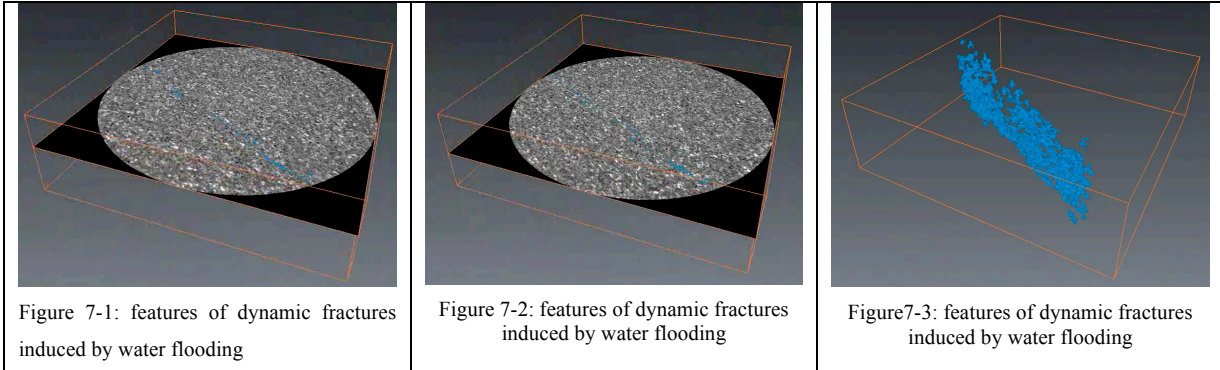


Figure 6: Oil field B-injection pressure and overburden pressure difference curve along the time line

**3. Distribution features of dynamic fractures induced by water flooding**

Dynamic fractures induced by water flooding cannot be seen by eyes, and can only be observed by microscopic amplification tools. This study conducted CT scanning for fractures, and selected different spots of the scanning plane, as show in figure 5-1 to 5-2, the blue area indicates fracture open surface, and figure 5-3 provided a three-dimensional reconstruction of the characteristics of the fracture surface. The fracture opening surface basically presents the plane distribution characteristics, and the average fracture width is 10-65 microns.



**4. Features of dynamic fractures induced by water flooding displacement**

Research was carried out on the dynamic fracture recovery degree and water ratio of rocks in an oilfield. After dynamic fractures induced by water flooding was open, the crude oil recovery degree was significantly lower than that of the matrix: the degree of matrix production was 56%, and the degree of dynamic fracture induced by water flooding was 8%-40%, with a wide distribution range, as shown in Figure 8. Comparison of the Daqing Oilfield, Jilin Oilfield, and Changqing oil field on dynamic fractures induced by water flooding is shown in Figure 9, and the core samples parameters are listed in table 1. We can see that matrix recovery rate is between 40%-68%, and dynamic fractures induced by water flooding recovery rate is significantly reduced.

Table 1: core sample parameters

NO.	$\phi$ %	Ka $10^{-3}\mu\text{m}^2$									
1	12.5	0.524	7	14.6	2.58	13	18	1.91	19	13.5	2.66
2	11.6	0.317	8	12	4.3	14	14	1.58	20	16.1	1.69
3	11.4	0.409	9	11.6	0.66	15	9.7	0.266	21	14.3	2.09
4	10.8	0.618	10	12.8	2.65	16	8.4	0.232	22	13.2	1.38
5	11.1	0.559	11	15.3	3.06	17	12.3	0.184	23	13.1	1.63
6	13.3	3.9	12	18.7	5.49	18	15.3	1.14	24	12.6	1.02

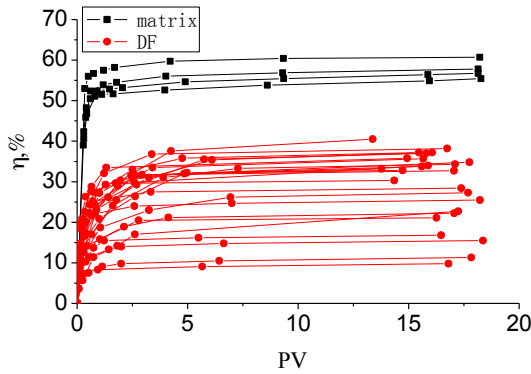


Figure 8: Matrix displacement and dynamic fracture injection multiple fractures and recovery efficiency curve

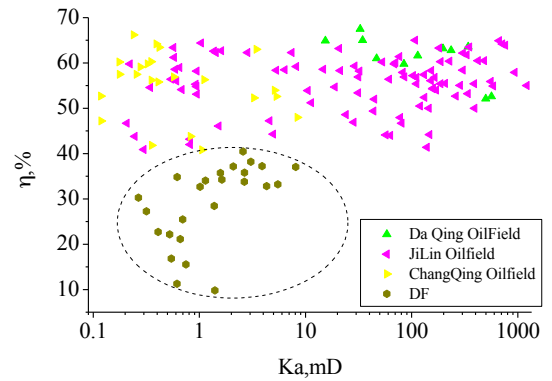


Figure9: Original Matrix displacement and dynamic fracture displacement recovery curve

After high pressure water injection in low permeability reservoir, the injected water flows along the fracture, and the water ratio is increased quickly: the rate of no water recovery rate is 0-15%, and the degree of matrix water recovery rate is between 37%-52%. Figure 10 and Figure 11 demonstrates a comparison between core samples result and oil field result. Figure 11 shows the characteristics of matrix displacement and fracture displacement in the oil field, and also shows the fast rising of water flooding in fractured reservoirs.

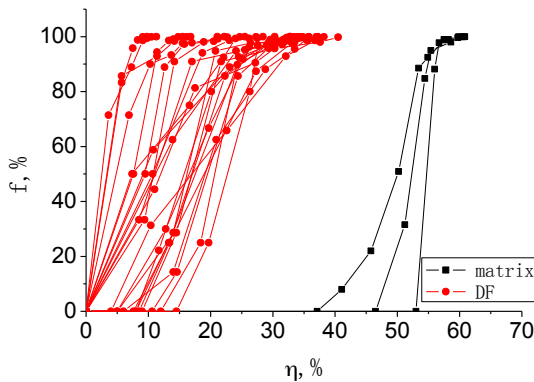


Figure 10: Core samples result- Matrix and dynamic fractures oil recovery( $\eta$ ) and water cut ratio( $f$ )

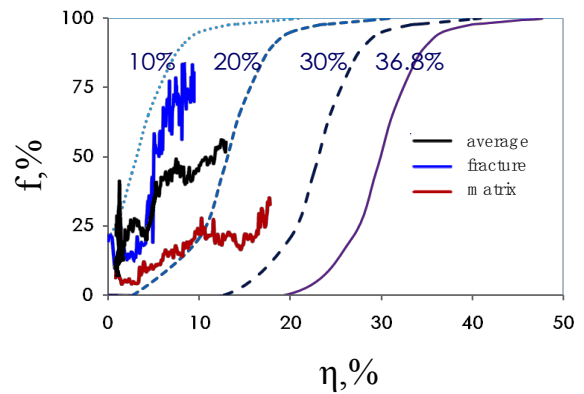


Figure 11: Oil field result-Relation between oil recovery ( $\eta$ ) and water cut ratio ( $f$ )

## CONCLUSION

This study provides data to support the correlation between the behavior of dynamic induced fractures and the production rate, by simulating dynamic fracture induced by injecting water into core samples. The process of water flooding is tracked by recording the variation of the overburden pressure with the water injection pressure and the characteristic of the induced fracture system and the flowing pattern are investigated as well.

Fractures start being induced when water injection pressure is 0.7-3.2MPa higher than the overburden pressure and becomes stable at 1.0-5.0Mpa higher than the overburden pressure. Experimental measurements show that the induced fractures, tend to grow in a plane pattern, while both fracture width and fracture pressure increase with water injection rate, which can also explain the reason that absolute permeability of core samples under water flooding is significantly enhanced by 5-30 times. On the other hand, the displacement efficiency of the induced fractures is about 9.8-25.5%, which is lower than that of matrix controlled flow ability, which is about 56-63%.

## ACKNOWLEDGEMENTS

I want to express my deep felt thanks to my coworkers at State Key Laboratory of Enhanced Oil Recovery, Research Institute of Petroleum Exploration and Development, Beijing, China: Zhang Zubo, Liu Qingjie, Chenxu, Qian Yuchen, and Tan Xiqun at RIED, PetroChina Changqing Oilfield Company, China. Without their help and support, this work could not have been possible.

## REFERENCES

1. Wang Youjing, Song Xinmin, Tan Changbing, et al. Dynamic fractures are an emerging new development geological attribute in water-flooding development of ultra-low permeability reservoirs [J]. *Petroleum exploration and development*, 2015, 42(2): 221-228
2. Xie Jingbin, Long Guoqing, Tian Changbing, et al. Genetic mechanism of dynamic fracture and its influence on water flooding development in extra-low permeability sandstone reservoir: a case of Chang6 member in Wangyao area, Ansai oilfield [J]. *Petroleum exploration and development*, 2015, 22(3): 106-110
3. Fan Tianyi, Song Xinmin, Wu Shuhong, et al. A mathematical model and numerical simulation of waterflood induced dynamic fractures of low permeability reservoirs [J]. *Petroleum exploration and development*, 2015, 42 (4): 497-501
4. Guo Farong, Wang Hongwei, An Mingshen, et al. Dynamic Fractures Change Features and Impact of Ansai Extra-Low Permeability Oilfield [J]. *Journal of Yangtze University (Natural Science Edition)*, Aug. 2015, Vol. 12 No. 23.

# Study of Pore Size Evaluation for Low Permeability Rock Core Sample

Mai SHIMOKAWARA, Yasuyuki AKITA, Yasuyuki MINO and Satoru TAKAHASHI  
Japan Oil, Gas and Metals National Corporation

*This paper was prepared for presentation at the International Symposium of the Society of Core Analysts held in Snowmass, Colorado, USA, 21-26 August 2016*

## ABSTRACT

Characteristics of tight rocks in hydrocarbon reservoirs is important to predict reservoir performance. Especially, it is difficult to accurately evaluate permeability which is affected by pore connectivity.

In this study, we conducted experiments to analyze pore connectivity including the pore shape and network with low permeability rock samples. Low permeability rock samples were collected from the outcrops in Japan. The samples are siltstone and silty mudstone. The permeability of the samples is less than 1nd, whereas the porosity is around 5 %. The N<sub>2</sub> adsorption, Mercury injection and NMR tests were conducted to obtain pore size distributions. The core samples used here contains clays. Special cares were taken to dry the core samples for pre-treatment of the N<sub>2</sub> adsorption tests. N<sub>2</sub> adsorption tests were conducted repeatedly for hysteresis loops. Results shows that the samples have macropores by adsorption process and micropores by desorption process using t-plot analysis. This indicates that the pore of samples has the wide range pore size and the pore shape consists of the slit and cylinder. In addition, we conducted the numerical analysis by BJH and INNES, the pore size is confirmed to be from 0.6 nm to 6um.

## INTRODUCTION

Characteristics of tight rocks in hydrocarbon reservoirs is important to predict reservoir performance. It is difficult to make measurements of properties in low permeability rocks such as shale gas and tight oil formations with conventional experimental methods. Evaluation methods are thus proposed and discussed for low permeability rocks. In this study, we conducted to evaluate characteristics based on the pore size distributions of low permeability rocks.

## EVALUATION OF PORE SIZE DISTRIBUTION

Mercury injection, gas adsorption and NMR methods are often used for evaluating pore throat/size distribution of rocks. In a mercury injection method, pore throat distribution is derived with the Washburn equation using injection pressure and injected volume when mercury is injected into a rock sample. In a gas adsorption method, an amount of physical adsorption of gas is measured at equilibrium pressure as gas is injected into a rock sample under the liquefied point of the injected gas, and pore diameter is calculated from the amount of physical adsorption in consideration of the molecular size of gas and shape of

the pores[1][2]. In a NMR method pore size distribution is obtained from the volume of fluid that contains hydrogen atoms by measuring T2 relaxation time.

In the mercury injection and gas adsorption methods the pores should be connected and the pore size is limited by the atom size of used fluids. The very small pore size cannot be measured with these methods. On the other hand, the NMR method has no limitation of the pore connectivity. The NMR method does not convert pore size distribution from T2 relaxation time directly although it allows us to evaluate hydrocarbons and water in unconnected pores of recovered reservoir rocks. Not only the NMR method but also the mercury injection and gas adsorption methods is thus required to evaluate rocks that naturally have wide variety of pore shape and size. This study describes the results of hysteresis analysis by the gas adsorption method in order to initiate comprehensive evaluation of the pore size and connectivity.

## EXPERIMENT AND RESULTS

A silty mudstone sample obtained from the formation from 200 to 1000m below subsea level was used to evaluate pore size distribution with NMR, mercury injection and nitrogen adsorption methods in this study. The rock sample used here has about 0.05 of porosity derived from a NMR method and less than 1nd of air permeability (Table 1). In the NMR, the mercury injection and the nitrogen adsorption methods, the rock samples were shaped into core plugs in 1cm length, about 5mm debris and particle size less than 250um mesh, respectively. Hysteresis analysis was conducted with decreasing the upper limit pressure in the nitrogen adsorption method.

Fig. 1 shows the pore throat distributions from mercury injection. The pore tt distributions become smaller as the depth increases. The peak of pore throat distribution is 2.9E-02um in No.2 sample, whereas it is 5.1E-03um in No.8 sample. In addition the surface area of the pore throat distribution curves decreases as the depth increases as shown in Fig.2.

Fig. 3 shows the adsorption and desorption isotherms. According to the IUPAC classification of gas physisorption isotherms, these rock samples are categorized as the type IV.

Fig. 4 shows the t-plot[3] analysis based on the isotherms. This suggests that the pore size distributions of the rock samples are relatively wider and the shape of pores is the type of slit. To further understand the shape of the pores, the BJH and INNES[4] analyses were conducted using the adsorption and the desorption isotherms, respectively (Fig.5). By comparing these analyses and NMR measurements it was suggested that the pores that were observed pore size distribution with a single peak from the NMR method comprise of two shapes of slit and cylinder.

## CONCLUSION

We evaluated the shape of pores in silty mudstone rocks that have low permeability using hysteresis analysis based on the nitrogen adsorption method. As a result, the shape of pores was identified to be combinations of slit and cylindrical shapes although the pores represented a single peak pore size distribution from the NMR method. The hysteresis methods used here are useful to better understand flow characteristics of the low

permeability rocks. We will continue to evaluate various types of rocks with a series of measurements presented in this study.

## ACKNOWLEDGEMENTS

We thank Dr. M. Yoshida and M. Nakano of MicrotracBEL Corp. for their technical assistance.

## REFERENCES

1. Kuila et al., 2011, Surface Area and Pore-size Distribution in Clays and Shales, *SPE* 146869.
2. Clarkson et al., 2012, Nanopore Structure Analysis and Permeability Predictions for Tight Gas/Shale Reservoir Using Low-Pressure Adsorption and Mercury, *SPE* 155537.
3. B. C. Lippens et al., 1965, Studies on Pore Systems in Catalysts V. The t Method, *Journal of Catalysis*, 4 (3), 319-323.
4. W. B. INNES, 1957, *Analytical Chemistry*, 29, 1069.

Table 1 Properties of rock core samples.

Core No.	Depth m	Diameter cm	Length cm	Dry weight g	NMR porosity frac.
1	201.05	2.461	5.055	58.74	0.0578
2	201.13	2.464	4.965	57.92	0.0521
3	202.69	2.536	4.891	60.38	0.0599
4	448.79	2.466	4.953	59.60	0.0511
5	753.68	2.521	5.223	66.77	0.0306
6	753.92	2.523	5.061	64.24	0.0305
7	754.71	2.524	5.173	64.00	0.0613
8	998.24	2.522	5.21	67.62	0.0416
9	998.09	2.529	3.221	41.22	0.0533

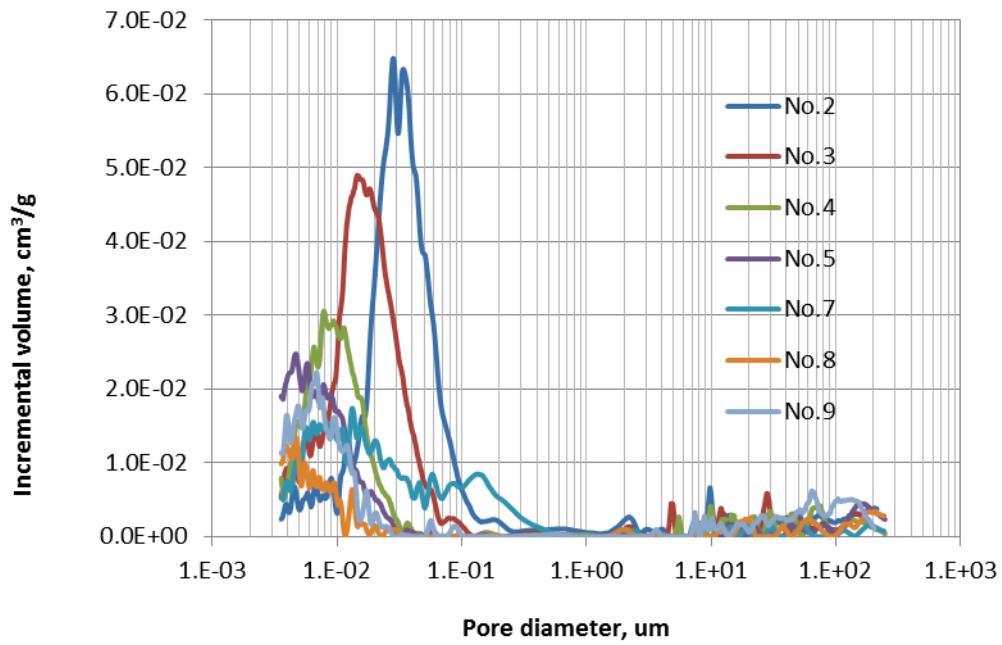


Fig.1 Pore throat distribution by MICP.

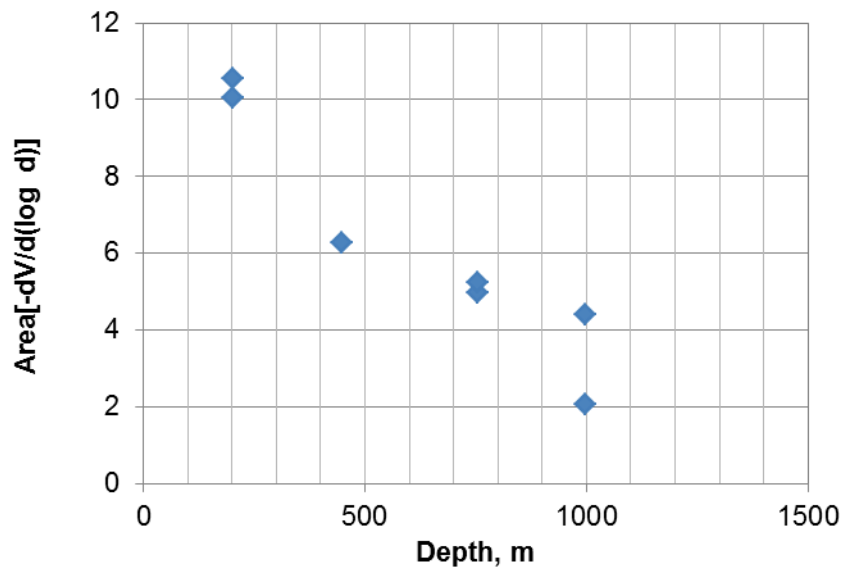


Fig.2 The correlation between depth and surface area.

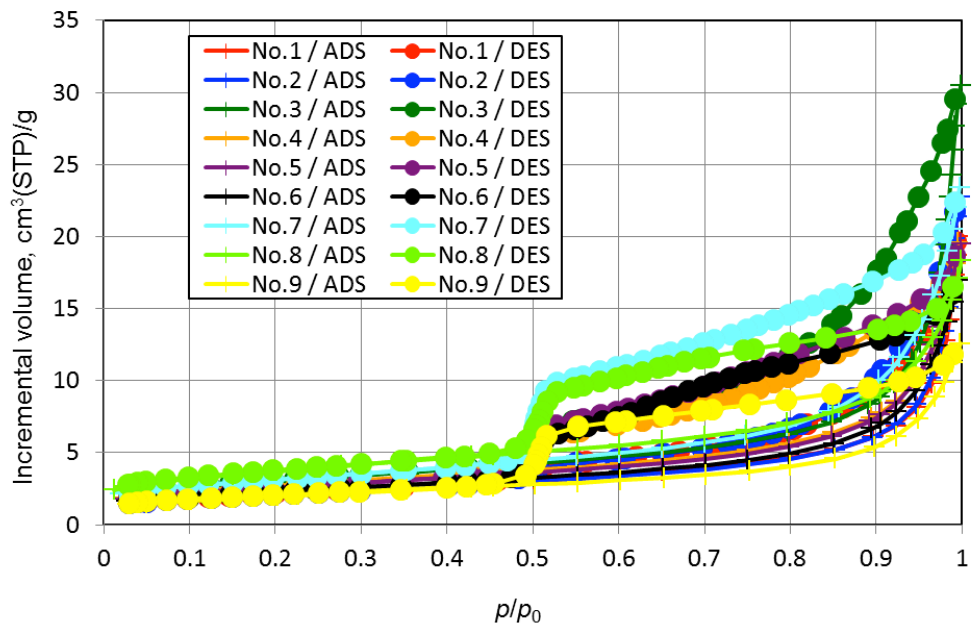


Fig.3 Adsorption and desorption isotherm.

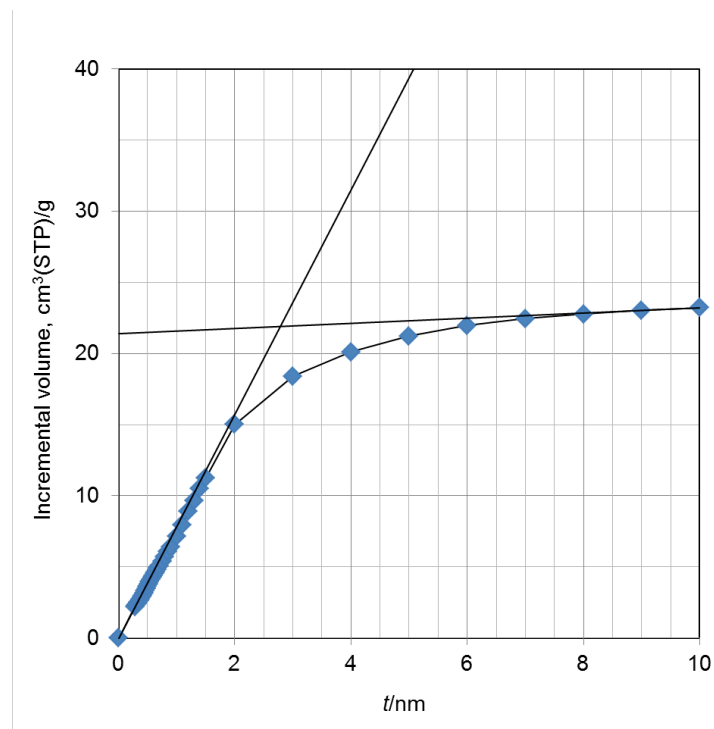


Fig.4 t-plot (Core No. 7).

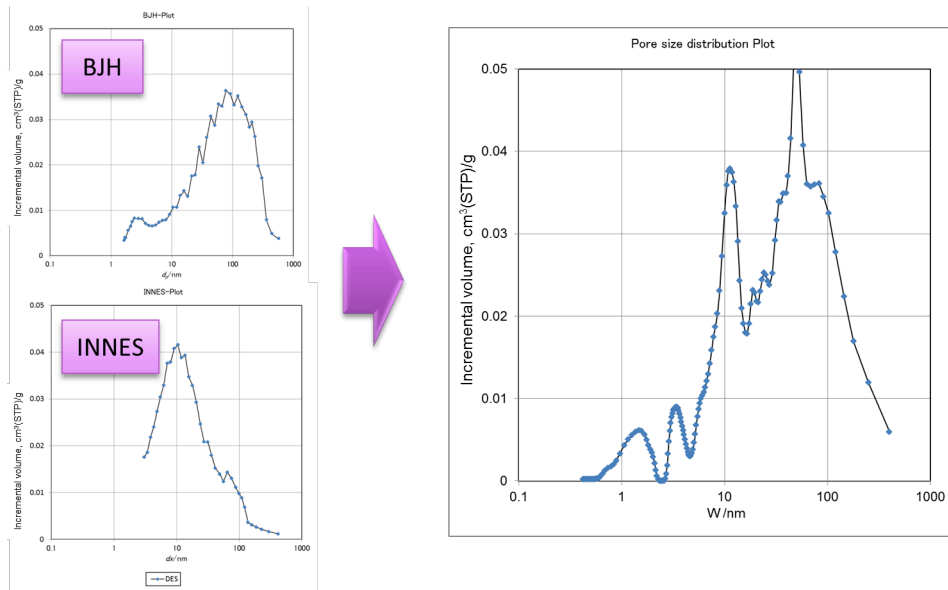


Fig.5 Pore size distribution from BJH and INNES.

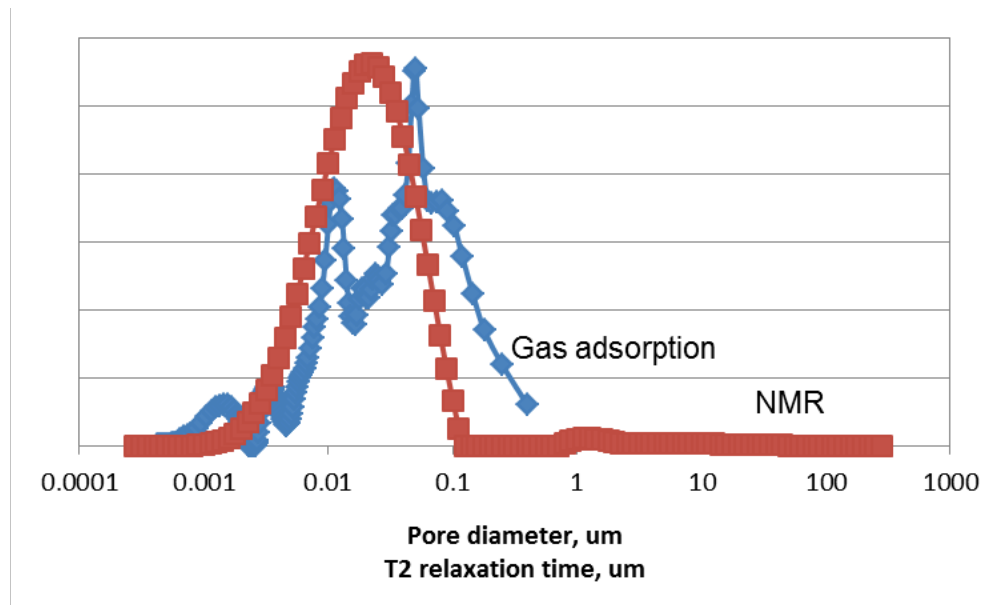


Fig.6 Pore size distribution from BJH and INNES.

## **NEW APPROACH TO EVALUATION OF COAL PERMEABILITY IN UNDERGROUND COAL MINES (CBM)**

Budak P., Szpunar T., Leśniak G., Cicha-Szot R.  
Instytut Nafty i Gazu - Państwowy Instytut Badawczy, Kraków, Poland

*This paper was prepared for presentation at the International Symposium of the Society of Core Analysts held in Snowmass, Colorado, USA, 21-26 August 2016*

### **ABSTRACT**

Laboratory measurements were focused on evaluation of coal permeability at various confining pressure. The investigation shows the distinct relation between coal permeability and overburden pressure which indicate that fracture permeability is a governing factor for methane flow. The petrophysical data (density, porosity, specific surface) measured using the polished sections and thin sections were also analyzed indicating large discrepancy of coal properties. The coal plugs were cut from coal samples collected from walls of underground mine corridors. Our investigations indicated that the coal samples are characterized by the numerous fractures caused by mining operations and stress relief at corridor walls. Such fractures may influence the lab measured permeability of coal. Two hydrodynamic tests were carried out to verify results of laboratory measurements of coal permeability. Such tests are capable to measure the “in situ” permeability in underground conditions. The first test was run in horizontal methane drainage well whereas the second one was run in vertical well which completely penetrated the coal bed. The top of the vertical well was at the overlying mine level. The special equipment constructed in INiG-PIB was used to run the tests (pressure gauge for vertical well and special equipment with two water actuated packers for horizontal well). The data were analyzed using methods invented in INiG-PIB. Results are reproducible and reliable. This paper shows the comparison of laboratory and in situ permeability measurements for coals from one of the Silesian coal mines (Poland).

### **INTRODUCTION**

The methane (CBM) which fills pores and fractures of coal seams can flow to the well in the same way as it does in conventional porous rocks. On the other hand methane is also adsorbed on surfaces at coal grains from where it can be released if the pressure falls below the so called desorption pressure.

Coal is heterogeneous and anisotropic porous rock characterized by two different porosity systems i.e. macropores (cleats) and micropores (matrix). Coal porosity is rather low (some percent) including volume of pores and micro fractures into porosity calculation. Knowledge of permeability, which is the most important factor from the viewpoint of methane production capability, enables evaluation of the potential of methane production from coal. The values of coal permeability are from zero to a few millidarcies, but on average the permeability is rather low.

## LABORATORY MEASUREMENTS OF COALS

Coal samples for laboratory measurement were cut from 2 cores (20 meters long each) collected from 2 wells and from coal blocks.

Collected samples were used to analyse the petrophysical features of the studied rocks, such as: density, porosity and permeability. Petrographical studies were performed for sandstones, siltstones and coals. The thin sections and transmitted light method was used. Coals were analysed using the reflected light.

Some of the collected coal blocks were highly fractured/cleated and showed highly varying lithotypes with maximum thickness of bright and dull coal layers less than 3 cm. It was not possible to prepare cylindrical plugs because they broke either at cleats or at weak bright coal layers. Part of coal blocks was suitable for sample preparation and cylindrical plugs were cut in all three directions. In that coal blocks the cleat network was less dense and lithotypes were thicker than for other seams. The 3 porosimetry analyses were performed for each block. Total porosity of the samples was in range 1.32 – 12.7%, porosities in range 3 – 6% were dominating. The analyses showed large diversity of petrophysical data of analyzed rocks (also within the same coal block). The values of specific surface area were generally high (up to 29 m<sup>2</sup>/g) and changed in a wide range.

We set a special attention to permeability of coal because it is the most important parameter for methane flow. All measurements were performed using Temco<sup>®</sup> relative permeability/coreflooding system at 4 confining pressures – 400, 800, 1200 and 1600 psi for plugs cut in parallel and perpendicular direction to bedding. The strong dependence between the measured permeability and the confining pressure indicates that the fractures are the crucial factor for coal permeability (as well as relatively high permeability values). Results of the coal samples measurements were confirmed using the polished and thin sections – calculated permeability values were similar to those obtained with the use of Temco<sup>®</sup> equipment. Because samples were cut from the walls of mining excavation in our opinion a part of fractures could be the result of mining operations. Also fracture thickness could be the result of coal depressurization.

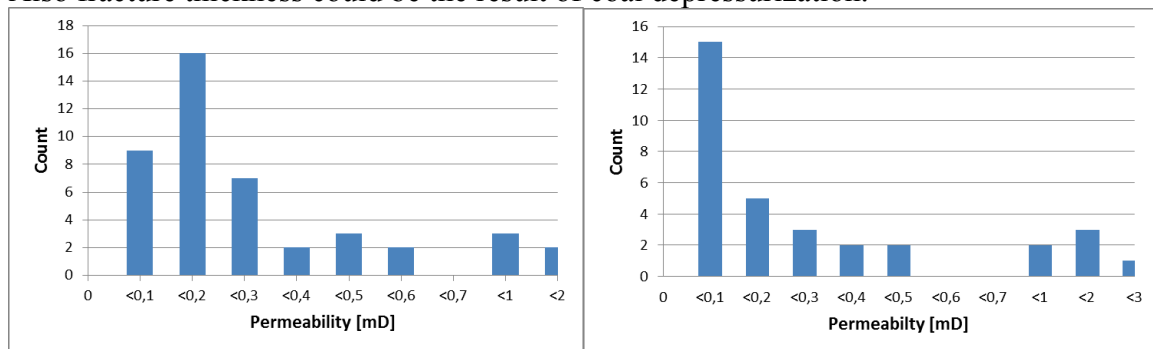


Fig.1. Parallel to bedding (conf.press. 1600 psi) Fig.2. Perpendicular to bedding (conf.press.1600 psi)

## INTERPRETATION OF THE WELL TEST DATA

Two hydrodynamic tests were carried out to verify results of laboratory measurements of coal permeability – one in vertical well and the second in horizontal one. Such tests provide information on the “in situ” permeability in underground conditions.

### Vertical well

The first test was run in vertical well which completely penetrated the coal bed. The well with depth 37 m, was drilled from the overlying mine level. The 5 inch casing was set and cemented leaving open the coal seam with thickness 6 m. The wooden plug was run to the bottom of the well to isolate the coal bed from particles suspended in water. Next the well was left for pressure stabilization. After some days the water table in a well stabilized some centimeters below the surface ( $z_0$ ). No outflow of water was observed which means that the reservoir pressure around the well was equal to hydrostatic pressure of water column. Such a low pressure means that some water was drained off the coal to near about mining excavations located a dozen or so meters from well location. Next, the pressure gauge was run to the mid-point of coal bed and some water was blown off the well ( $z_1$ ) which caused the water table to drop a few meters ( $z_1$ ) below the stabilized level (see Fig.3).

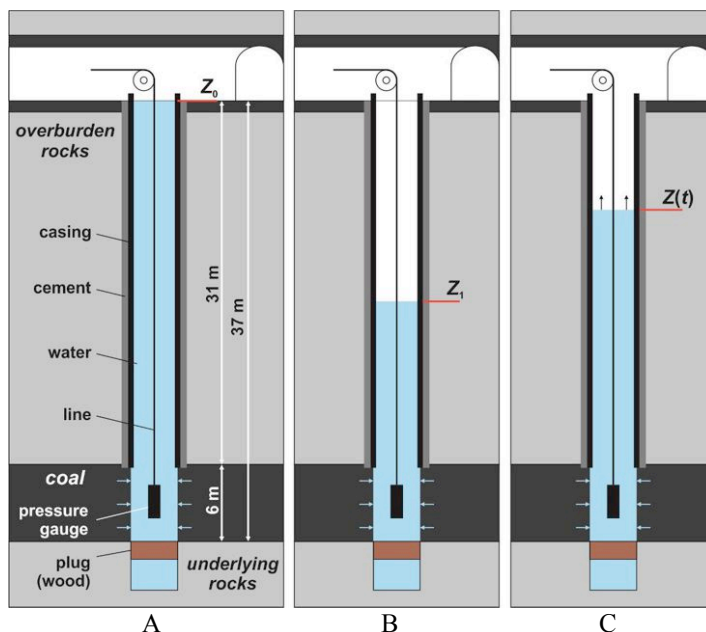


Figure 3: Diagram of the test: A) Hydrostatic pressure balance the reservoir pressure in coal, B) Removal of some fluid volume from the well, C) Monitoring the fluid table behavior



Figure 4: Pressure gauge developed by INiG-PIB

Measurement of water table behavior versus time while the well returned to pressure stabilization was carried out using the INiG-PIB pressure gauge. This equipment (Fig. 4) fulfil the requirements of the restrictive safety regulations for methane coal mine. Time of measurements was around 24 hours. The length of water column above pressure gauge vs. time relation recorded while the well returned to stabilization is shown in Fig. 5 below.

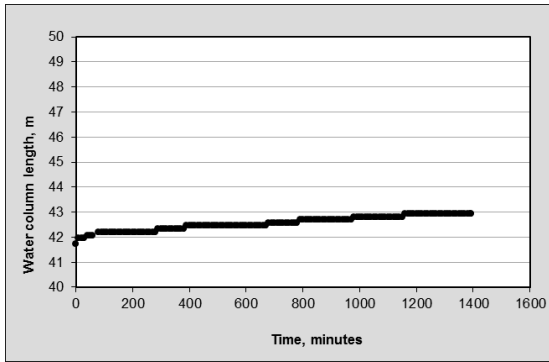


Figure 5: Water column length vs. time curve

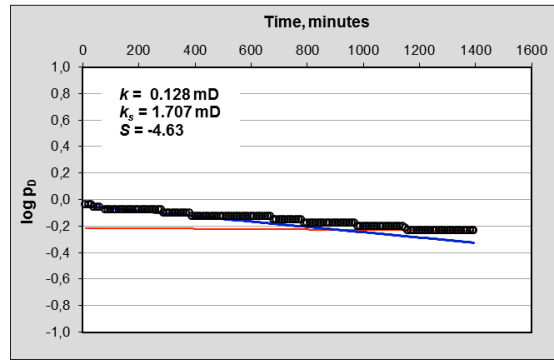


Figure 6:  $\log p_D$  vs. time curve

The recorded data were interpreted using well known “slug test” method which consists in fitting the curve constructed using the measured data to one of curve among family of theoretical curves (Fig. 7) and INiG-PIB method which theoretical background and interpretation procedure are given in papers [1] and [2].

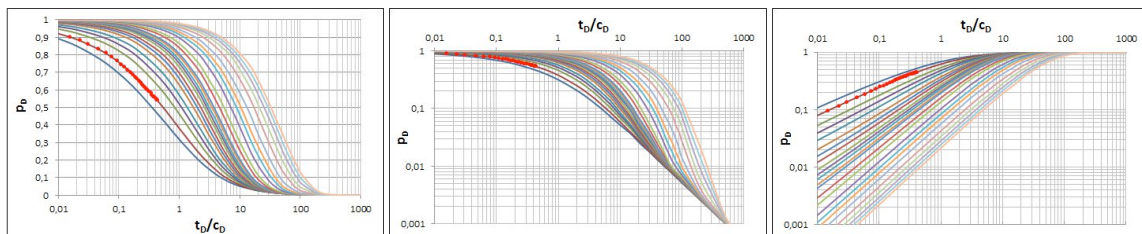


Figure 7. Fitting the whole, initial and final portion of the test curve (red points)

Results of test interpretation using the „slug test” method are given below:

Match of test curve to theoretical curves	Permeability [mD]	Skin effect
Whole curve	0.1771	-5.24
Initial portion of curve	0.1778	-5.24
Final portion of curve	0.1826	-5.24

According to INiG-PIB method relation between dimensionless pressure  $p_D$  and time  $t$  during pressure stabilization is as follows:

$$\log \frac{z(t) - z_0}{z_1 - z_0} = \log p_D = -5.11 \cdot 10^{-7} \frac{Kh\rho t}{r_0 u u} - \log \left( 1 - \frac{S}{u} \right) \quad (1)$$

where  $u$  is a root of the equation  $u = (\ln u - \ln a) / 2$  and  $a = 0.5(r_0 / r_w)^2 h \phi \rho g c$ .

In some circumstances it is possible to calculate permeability of the wellbore zone (fracture permeability), permeability of coal matrix, skin effect and depth of permeability impairment/increase. The relation between  $p_D$  vs.  $t$  is shown in Fig. 6 above. The short time data indicate the fracture permeability (permeability of the wellbore zone) whereas the late time data indicate the permeability of the coal matrix. The following results were obtained: permeability of the wellbore zone (fracture permeability) 1.707 mD, permeability of coal matrix 0.128 mD and skin effect -4.63.

## Horizontal well

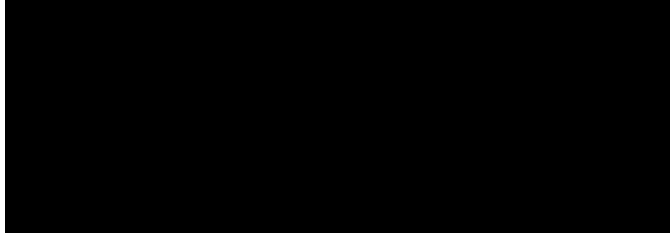


Figure 8. Test in horizontal well

The second test was run in horizontal drainage well (slightly inclined downward to keep it full of water) drilled in the same coal bed. The data were interpreted using INiG-PIB method presented in [3].

The equipment used to run a test (see Fig. 8) consists of pipe with two water-actuated packers placed at distance  $a$  one from the other. The segment between packers is perforated to allow water injection into coal matrix using small water pump capable for maintaining constant injection rate. Relation between injection pressure  $p_{inj}$  and time  $t$  for horizontal drainage well has a following form:

$$p_{inj} = p_0 + 39.81 \frac{Q\mu}{aK} \left( \ln t + \ln \frac{K}{\phi\mu cr_0^2} - 8.912 + S \right) \quad (2)$$

which indicate that plot  $p_{inj}$  vs.  $\ln t$  should be linear with slope  $m$ :

$$m = 39.81 \frac{Q\mu}{aK} \quad (3)$$

permitting calculation of permeability  $K$ . If the straight line is extended to  $t = 1$  min and corresponding injection pressure  $p_{inj lin}$  is read out then the skin effect  $S$  is given by:

$$S = \left[ \frac{p_{inj lin}(t = 1 \text{ min}) - p_0}{m} - \ln \frac{K}{\phi\mu cr_0^2} + 8.912 \right] \quad (4)$$

The recorded relation of  $p_{inj}$  vs.  $\ln t$  is shown below in Fig. 9.

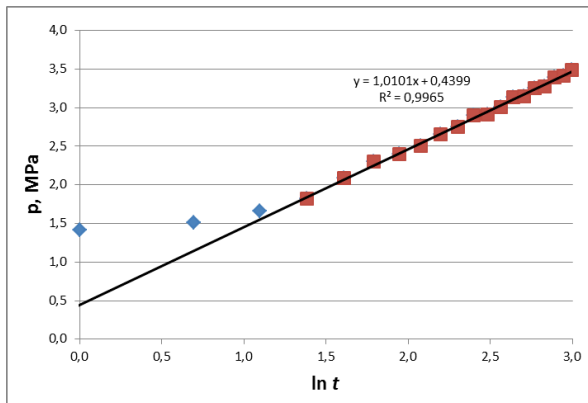


Figure 9. Relation of  $p_{inj}$  vs. time

The length of horizontal interval isolated by packers was 10 m and water injection rate was 2 l/min. The interpreted permeability and skin were  $k = 0.13$  mD and  $S = -4.8$ .

## CONCLUSION

The laboratory data for 1600 psi confining pressure were used to compare results with flow test data. Such a pressure corresponds to overburden pressure prevailing at the coal bed depth.

Table 1. Comparison of permeabilities

Lab tests (at 1600 psi conf.press.)						Test in vertical well				Test in horizontal well		
Permeability samples measured to bedding						"slug test"		INiG-PIB method			INiG-PIB method	
parallel			perpendicular			Average perm. [mD]	Skin effect	Permeability [mD]		Skin effect	permeability [mD]	Skin effect
min	max	average	min	max	average			wellbore zone	coal matrix			
0.02	1.34	0.28	0.02	3.90	0.40	0.179	-5.24	1.71	0.128	-4.63	0.13	-4.81

Table 2. Fracture permeability of coal samples

Permeability [mD]	Macro fracture (>0.1 mm)	Micro fracture (<0.1 mm)
Minimum	1.25	1.32
Maximum	2.08	14.73
Average	1.42	4.37

As shown in Table 1 and 2, the results of laboratory measurements and well test data are in a rough agreement which proved correctness of lab measurements in simulated downhole conditions both as the fracture permeability and permeability of the coal matrix are concerned. Comparing the results of laboratory measurements of coal properties with results of well test data seems to be useful procedure when results of any of those methods are in doubt.

## NOMENCLATURE

$p_{inj}$  – injection pressure, MPa

$p_0$  – reservoir pressure, MPa

$a$  – distance between packers, m

$Q$  – injection rate, l/min

$c$  – total compressibility (coal plus media), 1/MPa

$h$  – thickness of coal, m

$\phi$  – coal porosity

$\rho$  – water density, kg/m<sup>3</sup>

$\mu$  – water viscosity, mPas

$r_0$  – inner radius of casing, m

$r_w$  – radius of the well, m

## ACKNOWLEDGEMENTS

The research leading to these results was partially founded from Research & Innovation Research Fund for Coal and Steel Development of Improved Methane Drainage Technologies by Stimulating Coal Seams for Major Risks Prevention and Increased Coal Output, Contract No.: RFCR-CT -2014-00004

## REFERENCES

1. Szpunar T., Budak P.: How to assess the depth of permeability impairment of the wellbore zone using DST flow period data. JCPT, 2012
2. Szpunar T.: How to assess the permeability and skin of the low pressure water zones. JCPT, July 2001
3. Szpunar T.: Interpretation of well test in horizontal wells. Nafta-Gas, 9, 1992
4. Szpunar T., Budak P.: Simple analytical – graphical method for interpretation of DST flow period data and comparison of results with those obtained using the slug test method, Nafta-Gas, February, 2015
5. Aguilera R., Artindale J.S. et.al.: Horizontal Wells, Gulf Publishing Company, Houston, London, 1999

# **A NOVEL LABORATORY METHOD FOR DETERMINING CAPILLARY PRESSURE AND WETTABILITY WHILE MEASURING STEADY-STATE RELATIVE PERMEABILITY**

Robin Gupta, Daniel Maloney, David Laverick, Robert Longoria, Larry Poore and Jeff Spitzenberger, ExxonMobil Upstream Research Company

*This paper was prepared for presentation at the International Symposium of the Society of Core Analysts held in Snowmass, Colorado, USA, 21-26 August 2016*

## **ABSTRACT**

A novel laboratory method was developed that obtains relative permeability ( $k_r$ ), capillary pressure ( $P_c$ ), and wettability characteristics from a single reservoir-condition steady-state coreflood test. The method uses a modified inlet end-piece that isolates injection phases so that the difference between injection phase entry pressures is measured. Several inlet end-piece designs and related instrumentation are developed that can isolate and precisely capture the pressure difference of injection phases at the inlet. A method is developed to extract the capillary pressure from the difference in flowing injection phase pressures, which has both capillary and viscous pressure contributions. For this method, injected phase pressures are measured for several total flow rates for each steady-state fractional flow. This process enables quantification of  $P_c$  and  $k_r$  at each steady-state fractional flow condition. Rock wettability can be estimated from such measurements using either USBM or Amott-Harvey methods when the steady-state test includes both primary imbibition and secondary drainage cycles. Measured steady-state live-fluid coreflood data is used to illustrate this method of gaining both  $P_c$  and  $k_r$  functions from a single test. An excellent match was obtained between  $P_c$  quantified by the centrifuge method and the new method.

## **INTRODUCTION**

Capillary pressure ( $P_c$ ), relative permeability ( $k_r$ ) and wettability are key special core analysis (SCAL) characteristics used for reservoir performance predictions. Common practice is to measure these characteristics independently via several tests. Ideally, one would like to obtain all of these characteristics for a rock and fluid system from one test, saving time and cost. By doing so, a number of technical issues are avoided, such as mismatched data sets, anomalies from using different samples, test conditions, and fluids in the various tests, and propagation of errors from combining results from different tests.

When a sample (core plug or composite of core plugs) is mounted for a steady-state coreflood test, it is placed between inlet and outlet flow distribution end-pieces. The end-pieces serve as interfaces between the sample and upstream and downstream flow lines. During a two-phase steady-state flow measurement, two fluids are injected into and produced from the sample until steady-state is attained, that is, until saturation and

pressure drop across the length of the sample stabilize. The difference in phase pressures is close to zero at the outlet of the sample because of the capillary end-effect phenomenon (CEE). The difference between phase pressures is non-zero at the core inlet. From independent measures of injected phase pressures, one could conceptually determine capillary pressure as the difference between the non-wetting and wetting phase pressures. This is typically not practical because of phase mixing. This work addresses the mixing issue, enabling measures of phase pressures at the sample inlet face.

In a steady-state test, ability to measure differences in injection phase pressures at the sample inlet and to correct such measurements for viscous effects enables interpretation of capillary pressure. Thus, this work is an effort towards measuring relative permeability and capillary pressure curves on the same core plug (or first of a series of stacked plugs) simultaneously. Wettability can be calculated using established methods such as the Amott and the USBM (US Bureau of Mines) wettability index methods if both imbibition and secondary drainage capillary pressure cycles are available. Combining relative permeability, capillary pressure and wettability measurements into one test can yield a significant reduction in experimental time compared to measuring each separately.

Much of the previous work (for example, Longeron *et al.*, 1995; Richardson *et al.* 1952; Jennings *et al.*, 1988, Virnovsky *et al.*, 1995a, Virnovsky *et al.*, 1995b) relates to independent phase pressure measurements at the sample inlet using hydrophobic (oil-wet) and hydrophilic (water-wet) porous disks or membranes. For such approaches, properties of the disk or membrane allow pressure communication with one phase while the other phase is excluded. Drawbacks include the difficulty of initiating a reservoir-condition live fluid test without exceeding excluded-phase entry pressures of the porous disks or membranes, and uncertainty about whether or not the disk or membrane will perform as desired throughout the test. This work seeks to isolate the injection phases physically for phase pressure measurement rather than isolation via disks and membranes.

Authors including Richardson *et al.* (1952) and Gupta and Maloney (2015) suggested that capillary pressure may be quantified as the difference between non-wetting and wetting fluid phase pressures at the inlet. However, they did not account for the need to correct the viscous flow contribution to the pressure difference, which this work addresses. They also did not describe a practical inlet end-piece design to accomplish phase pressure measurements. Richardson *et al.* (1952) stated that the difference between non-wetting and wetting phase pressures at any point within porous media equals the capillary pressure corresponding to the saturation at that point. They demonstrated the concept by cementing gas (non-wetting) pressure probes to the rubber sleeve and oil (wetting phase) pressure probes made of ceramic porous media to core walls. Their experiments showed that the pressure difference between the non-wetting and wetting fluid phases inside the core is constant away from the outlet end and equals capillary pressure. Cementing probes on a sample is not a preferred approach because the practice might damage the sample or alter its wettability. Further, cementing probes for each test could be time intensive and susceptible to leaks.

Kokkedee (1994) and Pini (2013) proposed that capillary pressure is equal to pressure drop across the core at low rates. No special end-piece is required in this technique. However, this technique assumes that viscous forces are small compared to capillary forces, which may not be true in many test conditions. In this work, a method to correct viscous forces from inlet phase pressure is used to estimate capillary pressure.

## **APPARATUS DESIGN**

Design elements of the proof of concept apparatus are shown in Diagram 1. In this design, end screens at the upstream face of the sample ordinarily used to promote mixing of injection phases are omitted. The inlet face of the sample is directly in contact with the inlet end-piece. To accurately measure difference in phase pressures at the inlet, two differential pressure transducers (high and low pressure ranges) are used in parallel, which can be engaged or disengaged depending upon the magnitude of the pressure difference. Pressures are also measured with Quartz absolute pressure transducers to provide redundancy. Pressure taps are placed as close as possible to the core holder inlet to minimize pressure drops from flow in the tubing and are placed at the same height to avoid gravity head differences. It is preferred to have check valves upstream of the inlet side pressure transducers to prevent back flow, which could result in phase mixing. As in a conventional flow system design, a differential pressure transducer or pair of Quartz absolute pressure transducers is used to measure pressure drop across the length of the sample. Pore pressure is maintained via closed-loop flow or by using a back pressure regulator (BPR). Overburden pressure is supplied by a pump.

## **INLET END-PIECE DESIGNS**

Designing an inlet end-piece that is robust and prevents injection phase mixing at rock and end-piece junction is a challenging problem. Conventional inlet end-pieces have patterns that promote distribution of fluid phases. Examples of several conventional end-pieces are shown in Figure 1. Because test samples are porous, it is challenging to obtain a good seal between a metallic end-piece and a rock sample. Small scale irregularities on the rock surface and the smooth metal pattern on inlet end-pieces seal imperfectly, resulting in mixing of injected fluids and equilibration of their pressures. The challenge of obtaining a good seal and phase isolation exists even for a metal-based inlet end-piece with flow distribution patterns that do not intersect (Figure 1b and Figure 1c). To demonstrate this challenge, steady-state coreflood tests were performed on Cordova Cream limestone (7-9 mD) using helium gas and brine (20000 ppm) at room temperature, 1500 psi pore pressure, and 2400 psi net confining stress. Metal inlet end-pieces like those of Figure 1 were used. Capillary pressure was measured on a companion plug using the centrifuge method with the same net confining stress and temperature conditions. The modified flow apparatus, as discussed above, was used to perform this experiment. The steady-state coreflood was performed with multiple gas-water fractional flows. Pressure and saturation values were recorded at steady-state for each fractional flow. Figure 2 compares difference of inlet phase pressures for each fractional flow with centrifuge capillary pressure data. Clearly, no inlet phase pressure difference ( $\Delta P$ ) at steady-state conditions was measured when using a metal-based inlet end-piece, indicating phase

mixing at the inlet face of the sample. Similar results were observed from a repeat test using a screen between the inlet end-piece and core.

New end-piece designs were tested with the aim of finding a configuration that prevents phase mixing at the core inlet. New designs used machined metal end-pieces and elastomer seals. The metal is used to provide: 1) a desired pattern for fluid distribution, and 2) a rigid base for an elastomer seal that maintains structural integrity at high pressures. The elastomer in the design is used to seal between the inlet end-piece and sample surface to prevent phase mixing. The elastomer and metal/alloy needs to withstand test conditions. Examples of a few end-piece designs are shown in Figure 3.

Although the combination of metal and elastomer can prevent phase mixing, some designs perform better than others. For example, designs with small flow apertures like the O-ring design (Figure 3a) provide excellent sealing between the inlet end-piece and core face, but at the cost of significant additional viscous pressure contribution to the inlet phase pressure. This additional viscous pressure contribution can exceed capillary pressures. It comes from an enlarged region of high injection fluid saturation inside the core near the inlet. Figure 4 shows Cordova Cream limestone results of pressure difference of inlet phases from tests with the O-ring design and metal-based designs. In this test, steady-state was attained with multiple total flow rates for two helium fraction flows (0.5 and 0.8). The pressure difference of helium and brine were non-zero, clearly indicating that the O-ring end-piece provided a good seal. However, helium-brine pressure differences at the inlet were of large negative magnitude compared to centrifuge capillary pressures. This resulted from the additional viscous pressure contribution due to the O-ring design's small inlet aperture. With the O-ring design, phase saturations expanded in a hemispherical pattern inside the core at phase inlet ports. Since brine viscosity is almost two orders of magnitude higher than helium viscosity, the viscous pressure drop near the brine end-piece port is significant compared to that of the helium port. For this reason, the difference in helium-brine inlet pressures makes it seem that capillary pressure is negative in Figure 4. Typical measurement techniques for capillary pressure are performed with no flow and negligible viscous pressure gradients. In this test, the range of measured phase pressure differences match closely with Darcy equation calculations for hemispherical flow in porous media. To remedy this problem, it appeared desirable to have an elastomer-based inlet end-piece with wider flow aperture to reduce the viscous pressure contribution in measured inlet phase pressures.

The use of an elastomer seal that withstands test fluids and conditions is important. Some elastomers may perform well at room conditions, but may lose structural integrity in the presence of hydrocarbons at high pressure and temperature. An example is shown in Figure 5 in which a spiral elastomer pattern made using an incompatible material was destroyed when exposed to live crude oil and brine at high temperature and pressure.

Inlet end-piece patterns with metal and elastomer (e.g., Half-moons and Spiral with gasket in Figure 3) tend to perform better than those with only elastomer between the end-piece and sample (e.g., Elastomer spiral). Elastomers are more compressible

compared to metal. In a 100% elastomer based design, if grooves are not sufficiently deep or wide, there is a risk of pattern distortion under high pressure. During another test with Cordova Cream limestone outcrop at 1500 psi pore pressure and 2400 psi net confining stress, an Elastomer spiral pattern was able to isolate phases at the inlet for the first 4000 minutes (Figure 6), but later failed as evidenced by the reduction in inlet phase pressures to zero as a result of phase mixing. Figure 7 shows post-test pictures of the core and end-piece. The salt residue from brine spreading over most of the inlet end-piece face (Figure 7a) and the brine streak connecting positions of injection ports for both phases on the rock face (Figure 7b) provide clear evidence that fluids mixed at the core face and did not remain isolated. The risk of having the elastomer lose structural integrity under high pressure can be reduced if the end-piece is made of both elastomer and metal.

Based on the above discussion, a good inlet end-piece design contains: 1) a wider aperture or surface area for injection phases to minimize the viscous pressure contribution in measured inlet phase pressures, 2) compatible elastomer material, and 3) face design consisting of both metal and elastomer, or 100% elastomer with sufficient groove width and depth. Examples of such end-pieces are the Spiral with gasket (Figure 3c) and Half-moons (Figure 3d).

From a similar experiment on Cordova Cream limestone outcrop, the Half-moon inlet end-piece successfully isolated both brine and helium phases. Figure 8 shows the difference of phase pressures at steady-state for multiple fractional flows and multiple rates at each fractional flow. Clearly, phase pressure differences at the inlet are non-zero, indicating successful isolation of injection phases at the face of the inlet end-piece. Further, the differences between phase pressures at the inlet are positive, indicating lower viscous contributions to the measurements because of better phase spreading at the core plug face (or wide injection cross section) compared to results from an end-piece with small injection aperture, such as the O-ring design. Though viscous contributions with the Half-Moon design are relatively low, they are not zero, which reflects flow rate dependence in the difference between inlet phase pressures. Because of viscous gradient effects, the difference in inlet phase pressures is lower than the static capillary pressure measured by the centrifuge method in Figure 8. Thus, the viscous contribution must be subtracted from the difference in inlet phase pressures to achieve a measure of capillary pressure from a steady-state coreflood test.

## **VISCOUS PRESSURE CORRECTION**

The difference between non-wetting and wetting phase pressures at the inlet equals  $P_c$  only at a static condition (zero flow rate). However, in a coreflood test (both steady-state and unsteady-state), one or both phases are continuously injected, and the phase pressures at the inlet result from both capillary and viscous forces. Hence, a method is required to estimate and correct the viscous pressure contribution from the difference of phase pressures at the inlet.

In a steady-state coreflood test, corrections for viscous pressure contributions can be determined by performing tests at multiple flow rates for each fractional flow. Steady-

state is achieved at each flow rate. For a given fractional flow, capillary pressure is equal to the intercept of the trend line from a plot of steady-state phase pressure difference at the inlet versus total flow rate (Figure 9). Close to the inlet, fluid saturation does not change significantly with flow rates. Hence, phase pressure difference at the inlet changes linearly with total flow rate for a typical steady-state fractional flow condition, and the intercept of the linear trend equals capillary pressure. The capillary pressure measured using the above method corresponds to the capillary end-effect corrected fluid saturation, which can be estimated using the Intercept Method (Gupta and Maloney, 2015) or through in-situ saturation monitoring. In tests with sufficiently high pressure drop across the core, the correction might be small and within experimental accuracy, and the average saturation across the core can be used.

### **APPLICATION EXAMPLE AT RESERVOIR CONDITIONS**

A water-oil steady-state coreflood test was performed using one of the new inlet end-pieces to demonstrate the concept of obtaining capillary pressure from the difference of phase pressures (after viscous pressure correction) at the inlet. This test was performed on native state core plugs stacked in series to make a composite of 25 cm length. The test was performed at reservoir temperature and reservoir pore and overburden pressures using live fluids. Viscosities of oil and brine were similar. Pressure measurement devices were configured as in Diagram 1. The “Half-Moons” inlet end-piece was used (Figure 3d). The test was an imbibition steady-state test, beginning with a measurement of oil permeability at irreducible water saturation and continuing with oil and water co-injection in steps of decreasing oil fractional flow ( $F_o$ ). For each  $F_o$ , after achieving steady-state conditions, total flow rate was increased several times. With the direction of total flow rate increasing, unwanted hysteresis is avoided. When  $F_o$  is decreased for the next set of steady-state measurements, flow rate can be reduced concurrently with the fractional flow change. Because the change in oil fractional flow coincides with an increase in brine saturation, the reduction of total flow rate between consecutive fractional flows avoids or reduces potential for inadvertently introducing hysteresis because of saturation reversals.

Figure 10 shows phase pressure difference (oil minus brine phase pressure) at the inlet and total flow rate versus time. As discussed above, reductions in total flow rate on Figure 10 coincide with changes in fraction flow. In Figure 10, the difference in phase pressures at the inlet is non-zero and ranges from -10 to +10 psi. The “Half-Moons” end-piece was able to clearly prevent phase mixing at the inlet face during this test.

In theory, the capillary pressure contribution to the difference between measured phase pressures is insensitive to total flow rate. In Figure 10, the phase pressure difference at the inlet changes with flow rate at each fraction flow. This flow rate dependence is the result of viscous rather than capillary phenomena. Figure 11 plots oil phase pressure minus brine phase pressure at the inlet versus total flow rate from steady-state measurements with oil fractional flows of 0.985, 0.9 and 0.3. All three plots show linear trends, as do plots for the other fractional flows that are not shown. Intercepts equal capillary pressure, while slopes are influenced by viscous effects. Slopes are positive for

oil fractional flows above 0.5 (because oil rates are greater than brine rates) and negative for fractional flows below 0.5 (because brine rates are greater than oil rates).

Constructing the capillary pressure curve for the rock at the inlet consists of plotting the intercepts (from the phase pressure difference versus rate plots) versus the corresponding brine saturations. Brine saturation was calculated by applying the Intercept method (Gupta and Maloney, 2015), which corrects the steady-state data for capillary end-effects. Since pressure drops in this test were high, capillary end-effect corrections to brine saturations were small. Figure 12 shows the resulting capillary pressure plot for this test. Saturations at the first and last points represent residual brine and residual oil saturations for this test. In theory, capillary pressure curves asymptote at residual saturations at both ends, but values of 11 psi and -15 psi were used to denote the capillary pressures at these residual saturations. This plot closely matches the centrifuge capillary pressure curves measured on preserved companion plugs of the same rock type (Figure 12), particularly with core sample C1. Figure 13 shows pore throat size distributions for the centrifuge core plugs (C1 to C4) and inlet-plug (S1) of the steady-state test. Clearly, plug C1 pore throat size and imbibition centrifuge capillary pressure data is closest to core plug S1 used in the steady-state test. The  $k_r$  curve obtained in this test closely matched with the curve obtained on samples with similar geology.

Overall, the new method is easy to implement and only requires minor modifications to a steady-state apparatus along with using a modified inlet end-piece. Even if an end-piece fails to prevent phase mixing during a test, quality steady-state relative permeability data is still obtained. However, this method has certain challenges. For example, the inlet end-piece design should be robust and needs to prevent phase mixing throughout the test, the test duration is slightly increased due to multiple flow rates performed for each fractional flow, and viscous pressure correction needs to be added to the test workflow. The application for a gas-liquid system is relatively more challenging compared to a liquid-liquid system because of low gas viscosity. A gas is more susceptible to leaks and phase mixing and generates relatively high viscosity pressure correction compared to a liquid.

## CONCLUSION

Modified inlet end-pieces described in this work successfully isolated injected phases in a coreflood test, allowing measurement of inlet phase pressures. The inlet phase pressures at steady-state conditions were used to estimate capillary pressure of the core after applying viscous pressure corrections. If both imbibition and secondary drainage cycles are performed during a steady-state test, then capillary pressures as well as relative permeabilities can also be measured. Wettability of the core can be inferred from imbibition and secondary drainage capillary pressure curves using either Amott or USBM wettability index methods. Thus, using the described inlet end-piece designs and test methodology, relative permeability, capillary pressure and wettability of a core can be measured simultaneously in a single steady-state test, which may result in significant time and cost savings.

## REFERENCES

1. Richardson, J. G., Kerver, J. K., Hafford, J. A. and Osoba, J. S. (1952, August 1). Laboratory Determination of Relative Permeability. Society of Petroleum Engineers. doi:10.2118/952187-G
2. Longeron, D., Hammervold, W. L. and Skjaeveland, S. M. (1995, January 1). Water-Oil Capillary Pressure and Wettability Measurements Using Micropore Membrane Technique. Society of Petroleum Engineers. doi:10.2118/30006-MS
3. Virnovsky, G.A., Guo, Y. and Skjaeveland, S.M. (1995a, May 15). Relative Permeability and Capillary Pressure Concurrently Determined from Steady - State Flow Experiments. 8th. European IOR - Symposium in Vienna, Austria
4. Virnovsky, G.A., Guo, Y., Skjaeveland, S.M. and Ingsoy, P (1995b, October). Steady-State Relative Permeability Measurements and Interpretation with Account for Capillary Effects. Society of Core Analysts Conference in San Francisco, USA
5. Gupta, R., and Maloney, D. R. (2015, December 1). Intercept Method--A Novel Technique To Correct Steady-State Relative Permeability Data for Capillary End Effects. Society of Petroleum Engineers. doi:10.2118/171797-PA
6. Kokkedee, J. A. (1994, January 1). Simultaneous Determination of Capillary Pressure and Relative Permeability of a Displaced Phase. Society of Petroleum Engineers. doi:10.2118/28827-MS
7. Pini, R., and Benson, S.M.. 2013. "Simultaneous Determination of Capillary Pressure and Relative Permeability Curves from Core-Flooding Experiments with Various Fluid Pairs." Water Resources Research 49 (6): 3516–30. doi: 10.1002/wrcr.20274

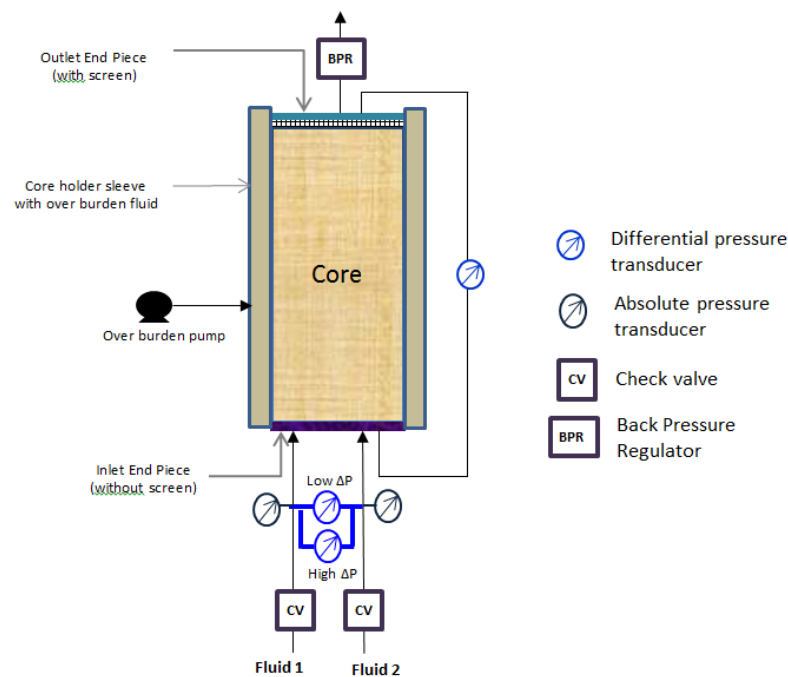


Diagram 1: Schematic of modified core holder assembly

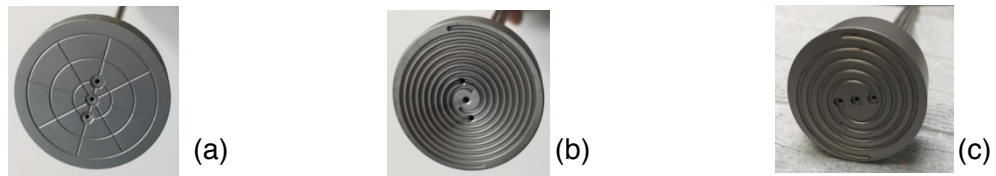


Figure 1: Examples of conventional inlet end-piece designs: (a) Cross, (b) Spiral, and (c) Modified spiral

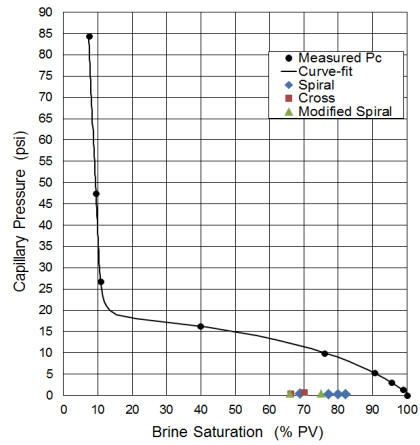


Figure 2: Difference of inlet phase pressure compared to measured capillary pressure for Cross, Spiral and Modified spiral inlet end-pieces

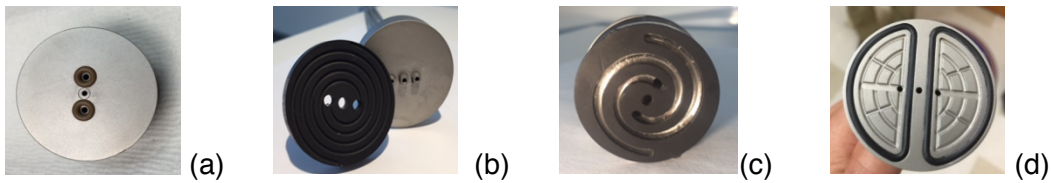


Figure 3: Examples of new elastomer based inlet end-piece designs, (a) O-ring, (b) Elastomer spiral, (c), Spiral with gasket, and (d) Half-moons

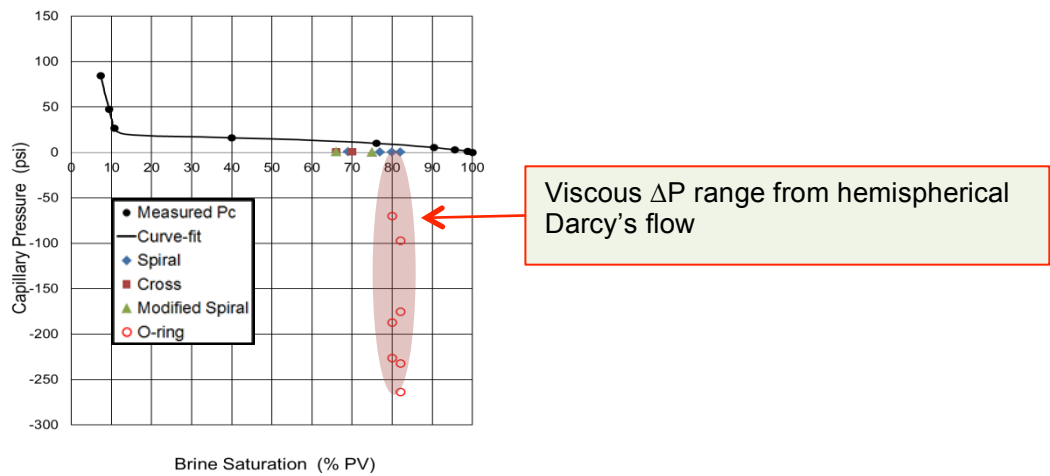


Figure 4: Difference of inlet phase pressure compared to measured capillary pressure for Cross, Spiral, Modified spiral and O-ring inlet end-pieces



Figure 5: Spiral with gasket end-piece after exposure to live crude oil at high pressure and temperature. Incompatible material was used in this test.

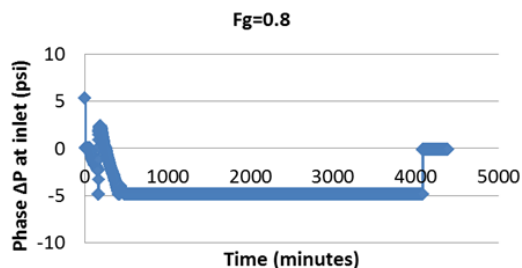


Figure 6: Plot of difference in inlet phase pressures with time for helium-brine steady-state test with Elastomer spiral inlet end-piece



Figure 7: Pictures taken after the test for, (a) face of Elastomer spiral inlet end-piece, and (b) face of the core at the inlet side

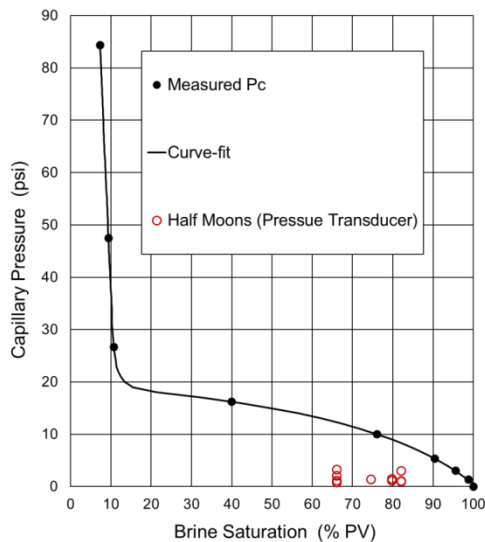


Figure 8: Difference of inlet phase pressures from Half-Moons end-piece compared to measured capillary pressure

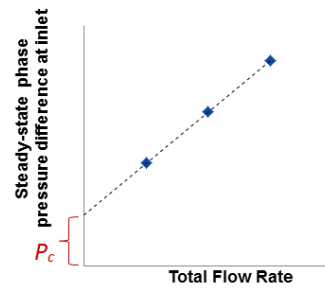


Figure 9: Plot of steady-state phase pressure difference at inlet with total flow rate for a given fractional flow. The intercept of the trend line of this plot equals static capillary pressure.

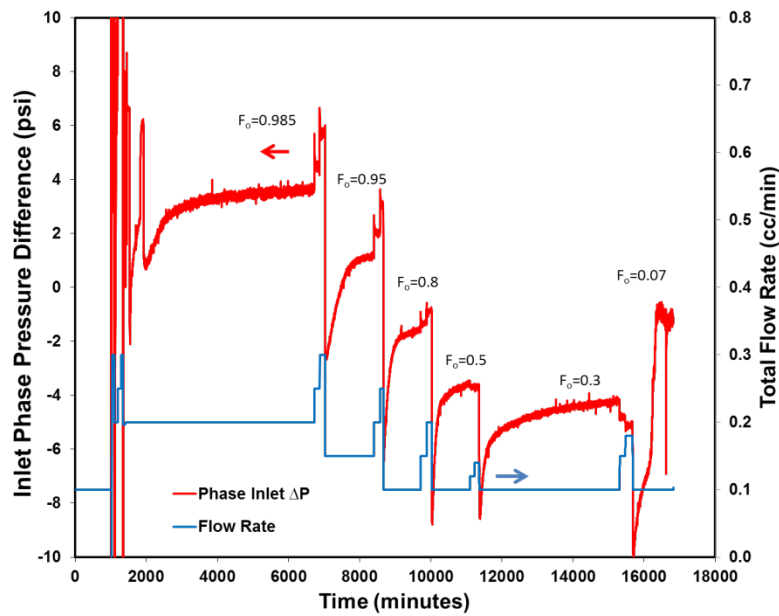


Figure 10: Difference in phase pressure at inlet and total flow rate with time at different oil fractional flow (Fo)

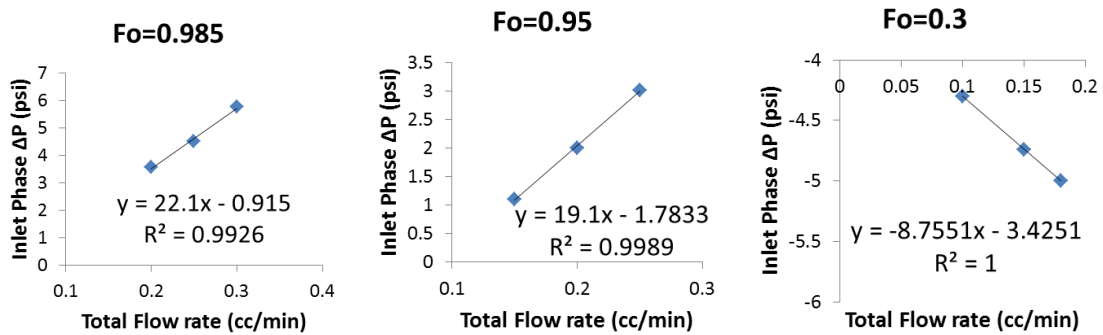


Figure 11: Plot of inlet phase pressure difference at steady-state condition with total flow rate for oil fractional flows of 0.985, 0.95 and 0.3. All three plots have linear trends. Intercepts equal capillary pressures.

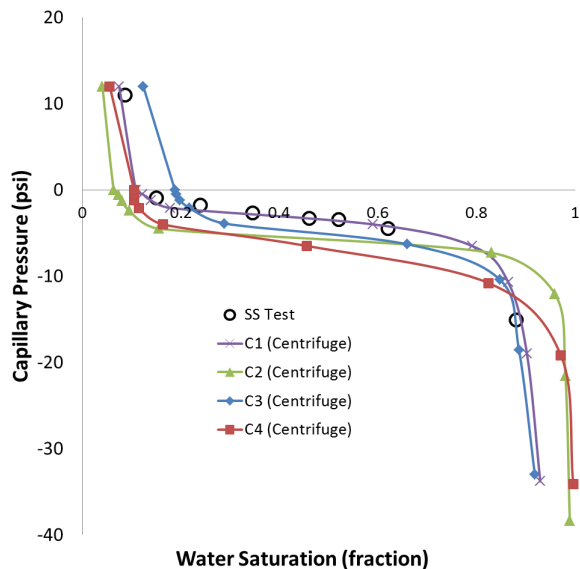


Figure 12: Capillary pressure curve obtained using the new method and compared with centrifuge capillary pressure measured on preserved plugs (C1 -C4) of the same rock type

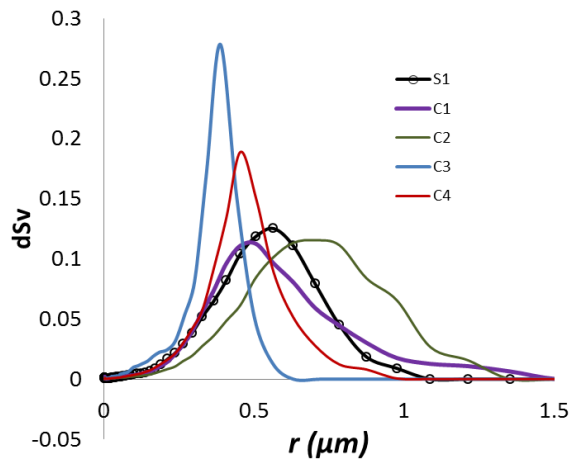


Figure 13: Pore throat size distribution for the inlet core plug used in the steady-state test and the four core plugs for same rock type used in the centrifuge capillary pressure test